

PODDY THE SECOND

Final Design Package



HYPERLOOP
THE UNIVERSITY OF EDINBURGH HYPERLOOP TEAM

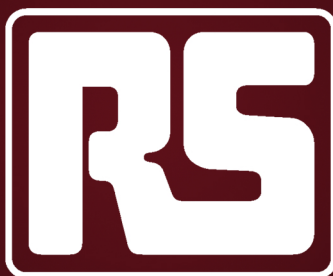
Sponsorship



THE UNIVERSITY
of EDINBURGH



CIRRUS LOGIC®



Indie
SEMICONDUCTOR

COMSOL

SOLIDWORKS

Altium

Contents

1	Summary	7
1.1	Design Philosophy	7
1.2	Top-Level Summary	8
1.3	Team Members and Advisers	9
2	Overview	10
2.1	Predicted Vibrational Environment	10
2.2	Sensor Location Map	11
2.3	Trajectory	12
2.4	Predicted Pod Trajectory with Emergency Braking:	13
2.5	Safety	14
2.5.1	Magnet Safety	14
2.5.2	State 0 Failure, or Pod Stop Command	15
2.5.3	Energy Stored on Board	15
2.5.4	Hazardous Materials	16
2.5.5	Fault Tolerances	17
2.5.6	Vacuum Tolerances	19
2.5.7	Off-Nominal Collision	21
2.5.8	Single Points of Failure	21
2.5.9	Recovery Plan	22
2.5.10	Mitigation of Complete Loss of Power	22
2.5.11	Inhibitions on Braking during Acceleration Phase	22
2.6	Scalability	23
2.7	Testing	23
2.8	Timeline	23
3	Propulsion Module	24
3.1	Halbach Wheels	24
3.1.1	Introduction	24
3.1.2	Summary	24
3.1.3	Considered solutions	27
3.1.4	Simulations	27
3.1.5	Safety	30
3.1.6	Scalability	32
3.1.7	Summary	33
3.1.8	Cost Breakdown	34
3.1.9	Manufacturing	35
3.1.10	Testing	36
3.2	Motors	36

3.2.1	Introduction	36
3.2.2	Summary	38
3.2.3	Chosen Solution	42
3.2.4	Motor Controllers	46
3.2.5	Safety	48
3.2.6	Scalability	50
3.2.7	Cost Breakdown	54
3.2.8	Testing	54
3.2.9	Timeline	55
3.3	Cooling	55
3.3.1	Introduction	55
3.3.2	Summary	55
3.3.3	Chosen solution	56
3.3.4	Safety	59
3.3.5	Cost breakdown	59
3.3.6	Timeline	59
4	Power	60
4.1	Battery Cells	60
4.1.1	Introduction	60
4.1.2	Considered Solutions	61
4.1.3	Chosen Solution	65
4.1.4	Safety & Testing	67
4.2	Battery Management Systems	70
4.2.1	Introduction	70
4.2.2	Chosen Solution	71
4.2.3	Considered Solutions	74
4.3	Power Systems	75
4.3.1	Safety	83
4.3.2	Manufacturing	89
4.3.3	Testing	101
4.3.4	Scalability	103
4.3.5	Timeline	103
4.3.6	Cost Breakdown	105
5	Dynamic Module	106
5.1	Levitation	107
5.1.1	Introduction	107
5.1.2	Summary	107
5.1.3	Considered Solutions	107
5.1.4	Chosen Solution	108

5.1.5	Simulations	109
5.1.6	Safety	111
5.1.7	Scalability	111
5.1.8	Maintenance	113
5.1.9	Cost breakdown	113
5.1.10	Manufacturing	114
5.1.11	Testing	114
5.2	Skis	115
5.2.1	Introduction	115
5.2.2	Summary	116
5.2.3	Considered Solutions	117
5.2.4	Chosen solution	117
5.2.5	Shock Absorbers	117
5.2.6	Wheels	118
5.2.7	Simulations	119
5.2.8	Scalability	120
5.2.9	Cost breakdown	121
5.2.10	Manufacturing Timeline	122
5.2.11	Testing	123
5.3	Emergency Brakes	124
5.3.1	Emergency State	124
5.3.2	Summary	125
5.3.3	Considered Solutions	126
5.3.4	Chosen Solution	126
5.3.5	Simulations	129
5.3.6	Safety	134
5.3.7	Control System	136
5.3.8	Scalability	136
5.3.9	Cost breakdown	137
5.3.10	Manufacturing	139
5.3.11	Testing	141
5.4	Lateral Rollers	142
5.4.1	Introduction	142
5.4.2	Summary	142
5.4.3	Considered Solutions	143
5.4.4	Simulations	144
5.4.5	Safety	145
5.4.6	Scalability	145
5.4.7	Manufacturing	148
5.4.8	Testing	150

5.5	Dynamic Module Plate	151
5.5.1	Introduction	151
5.5.2	Summary	151
5.5.3	Considered Solutions	152
5.5.4	Chosen solution	152
5.5.5	Simulations	158
5.5.6	Safety	159
5.5.7	Scalability	160
5.5.8	Cost breakdown	160
5.5.9	Manufacturing	161
5.5.10	Testing	161
5.5.11	Timeline	161
6	Controls	162
6.1	Introduction	162
6.2	Last Years Design	162
6.2.1	Overview	162
6.2.2	Issues	162
6.3	Control System Overview	163
6.3.1	Microcontroller System	165
6.4	Subsystem & Nodes	166
6.4.1	Master Node	166
6.4.2	Motor Node	167
6.5	Navigation Subsystem	168
6.6	Navigation Node - Master	169
6.7	Navigation Node - Slave 2	170
6.8	Navigation Node - Slave 1	172
6.9	Battery Monitoring Node	174
6.10	Node Protection Circuitry	175
6.10.1	Implementations	176
6.11	Communications	177
6.11.1	CAN Bus	179
6.11.2	Sensor-Specific Protocols	179
6.12	Testing	180
6.12.1	Communications Tests	180
6.12.2	Proximity Tests	181
6.12.3	Photoelectric Test	181
6.12.4	IMU Test	183
6.12.5	Motor Control Test	184
6.12.6	BMS Test	184
6.13	Cost Breakdown	185

6.14 Timeline	186
7 Software Systems	187
7.1 Introduction	187
7.2 Navigation	187
7.2.1 Introduction	187
7.2.2 Summary	187
7.2.3 Conceptual Solution	188
7.2.4 Navigation Algorithm	189
7.2.5 Filtration Technique	190
7.2.6 Scalability	192
7.2.7 Testing	192
7.3 Communications	192
7.3.1 Introduction	192
7.3.2 Summary	192
7.3.3 Considered Solutions	193
7.3.4 Chosen Solution	193
7.3.5 Safety	195
7.3.6 Testing	195
7.4 State Machine	196
7.4.1 Design Constraints	196
7.4.2 Design Decisions	196
7.4.3 State Diagram	197
7.4.4 States	198
7.4.5 Events	199
7.4.6 Testing	200
7.5 Software Development Timeline	200
8 Structure	202
8.1 Carbon Fibre	202
8.2 Chassis	208
8.2.1 Introduction	208
8.2.2 Summary	209
8.2.3 Considered Solutions	210
8.2.4 Chosen Solution	211
8.2.5 Simulations	212
8.2.6 Safety	214
8.2.7 Scalability	215
8.2.8 Cost Breakdown	215
8.2.9 Manufacturing	216
8.2.10 Testing	217

8.2.11	Timeline	217
8.3	Pressure Vessel	219
8.3.1	Introduction	219
8.3.2	Summary	219
8.3.3	Considered Solutions	219
8.3.4	Chosen Solution	220
8.3.5	Simulations	227
8.3.6	Safety	229
8.3.7	Scalability	229
8.3.8	Cost Breakdown	231
8.3.9	Manufacturing	231
8.3.10	Testing	233
8.3.11	Timeline	234
8.4	Shell	234
8.4.1	Introduction	234
8.4.2	Summary	235
8.4.3	Considered Solutions	235
8.4.4	Chosen Solution	238
8.4.5	Mounting	243
8.4.6	Simulations	244
8.4.7	Safety	248
8.4.8	Scalability	249
8.4.9	Cost Breakdown	249
8.4.10	Manufacturing	249
8.4.11	Testing	250
8.4.12	Timeline	250
A	Appendices	251
A.1	Loading Plan	251
A.1.1	Procedure	251
A.2	Propulsion Appendix	252
A.3	Dynamic Module Appendix	257
A.4	Structure Appendix	257
A.4.1	Lamina Properties	257
A.4.2	Seat & Dummy Dimensions	258
A.4.3	Reynolds Number Calculation	258
A.4.4	Previous Nose Cone Iterations & Simulations	259
A.4.5	Crumple Zone Data	260
References		262

1 Summary



1.1 Design Philosophy

Poddy the Second is the next generation of HYPED Hyperloop prototypes with many significant improvements over last year's Poddy McPodface. From last year's design, our team learned the value of a clean, well structured build, and one that enables efficient testing with fast turnaround of prototype iterations. In order to achieve this, a modular platform was developed, allowing for any component on the pod to be removed within ten minutes. Components are therefore housed in various modules which are slotted and fastened to the chassis. Due to the nature of the Hyperloop, each module houses one or more pairs of components that produce virtually equal and opposite forces against the track, enabling these forces to counteract within modules and serve as reactions against each other. This helps make each module structurally self-sufficient, both minimising the loads on the chassis and increasing system reliability, given complete structural failure of any component does not compromise the safety of the system as a whole.

At the heart of our build are the Power, Propulsion, Controls, and Dynamic Modules, all serving essential roles. These, added to the Chassis, Pressure Vessel, and Shells, make up the entirety of our pod, one that pushes the Hyperloop concept ahead. A full-scaled concept has been at the forefront of our minds from the start, leading us to the exciting concept of building a pressure vessel, something that quickly became our leading design driver.

The idea behind this is to seat our dummy in a realistic, comfortable position, while providing her with the luxury of travelling in a liveable environment. Furthermore, implementing carbon fibre in various parts of our pod was also essential in shaping our design with the Hyperloop concept in mind. A commercial design, we believe, would be made from a carbon fibre monocoque, and our goal at the outset was to gain enough experience in working with this material so that we would put ourselves in a position to design and manufacture our own monocoque and integrated pressure vessel within two years.

Beyond the pod's structure, our power source has also been conceived with scalability in mind. In fact, Poddy the Second's battery packs and power systems have been designed to be fully scalable by at least one order of magnitude. This was also done taking serviceability into account, while still providing commercially applicable containment and insulation; in a scaled up pod, a larger number of battery modules would simply have to be added in order to accommodate increased demands in both capacity or power. It is plausible, however, that most systems related to the propulsion would be transferred into the tube for a commercial Hyperloop. The idea is that by doing so, significant weight and power savings would be made on the pods themselves as they are driven by a form of linear induction motor.

1.2 Top-Level Summary

The propulsion and nominal braking is supplied by two pairs of radial flux Halbach wheels each comprising of 20 N55 magnets. They have a radius of 150 mm and a maximum rotational speed of 7000 RPM. Structural integrity at those velocities are maintained through a combination of titanium and carbon fibre reinforced polymer. The power is provided by 756 lithium iron phosphate 26650 battery cells through 4 liquid-cooled Emrax permanent magnet synchronous motors. Together, they allow us to accelerate at up to one g with a payload of a 95 percentile male, carbon fibre pressure vessel and life support systems.

Levitation is provided by 4 skis with linear Halbach arrays utilising passive maglev, chosen for the high reliability and simplicity of the system.

Navigation is primarily handled by a set of 3 IMU's which are continuously calibrated by a set of proximity sensors mounted all around the pod. This serves to reduce the drift in the accelerometers by resetting the gravitational vector when the gyroscopes drift.

The system uses two auxiliary systems for reducing and recalibrating IMU's on the fly. During low speed, the RPM of the service propulsion is measured allowing for extremely accurate readings, and at high speed an optical sensor is used to detect the stripes in the tube, allowing for updates in the positioning.

Should any of the above systems fail, off nominal braking will be provided by a set of normally actuated, self locking friction brakes that will allow the pod to come to a stop at up to 2.5g.

All systems considered, the total system mass is slightly above 500kg including its roughly 140kg payload of a live size and weight passenger and life support systems, with nominal acceleration and braking up to 1g. The on board propulsion gives Poddy the Second with a speed with payload of 80ms^{-1} and without payload 90ms^{-1} . Poddy the Second features no depletable resources and the maximum on board pressure is the atmospheric pressure maintained in the pressure vessel.

1.3 Team Members and Advisers

Hyped is a team of over 100 students from various academic backgrounds who are passionate about the Hyperloop concept, overseen by Professor Win Rampen. Formed in summer 2015, the group participated in the first iteration of the SpaceX Hyperloop Pod Competition and was awarded a Subsystem Technical Excellence Award at the design weekend at Texas A&M University. This was awarded for our modular pod design offering efficient loading and unloading procedures. However, our team did not progress to the first competition weekend.

In 2016, our team participated again in the SpaceX competition and brought our first pod, Poddy McPodface to compete in summer 2017. Of all the contestants, our team was the only one to bring a full size dummy with realistic weight. Unfortunately, due to a software issue our team could not progress to the final stages of the competition.

It is worth noting that HYPED also has a commercial team, which from 2016–2017 participated in and won the Hyperloop One Global Challenge, a competition hosted by Virgin Hyperloop One where 2600 teams presented a route for a Hyperloop along with a plan for its implementation. All other winners were exclusively consulting agencies and governments.

This year, HYPED's technical team consists of over 80 active members working in 6 different subteams: Controls, Dynamics, Power, Simulations, Software, and Statics. Each subteam specialises in different aspects of the design yet almost all work closely together on all the subsystems and modules.

Each subteam in turn consists of a number of projects that relate to a specific subsystem. For instance, the propulsion consists of a Halbach wheel, which was designed by a project team in Dynamics, a motor and power supply designed by the Power team, controlled by hardware made by the Controls team which runs software written by Software team; all held together by a structure made by the Static team while the safety of it all is ensured by the Simulations team.

2 Overview

Module/ Component	Mass (kg)	Peak power consump- tion (W)	Dimensions (mm)	Materials	Cost (£)
Power	105	24*	630x500x200	Aluminium	9,850
Controls	5	50	200x220x720	Aluminium	1,300
Dynamic	69	N/A	730x255x720	Aluminium, Steel, Polymer	13,300
Propulsion	160	~255,000	725x300x315	Aluminium, Steel, Ti- tanium, CFRP	26,000
Chassis	50	N/A	300x750x200	CFRP	5,050- 8,050
Pressure Vessel	50	N/A	2000x750x700	CFRP	6,500
Shell	6	N/A	850x750x916	CFRP	6,000

*power consumption of the electronics used to keep the power systems operating safely; the peak output of the power module is the sum of peak power consumptions in this table

2.1 Predicted Vibrational Environment

A model to simulate the vibrations of the pod during the trajectory was developed using the SIMULINK package in MATLAB. The weight imbalance caused due to acceleration and deceleration was also taken into account. Vertical and lateral displacements as well as pitch, roll and yaw degrees of freedom are simulated. Figure 1 overleaf shows the resulting vibrations for one small bump in the vertical direction and another in the lateral direction as the pod accelerates. More precisely,

the vertical displacement is 0.5mm on the left side and 1mm on the right side, such that the rolling motion is also simulated. The lateral displacement is also 1mm.

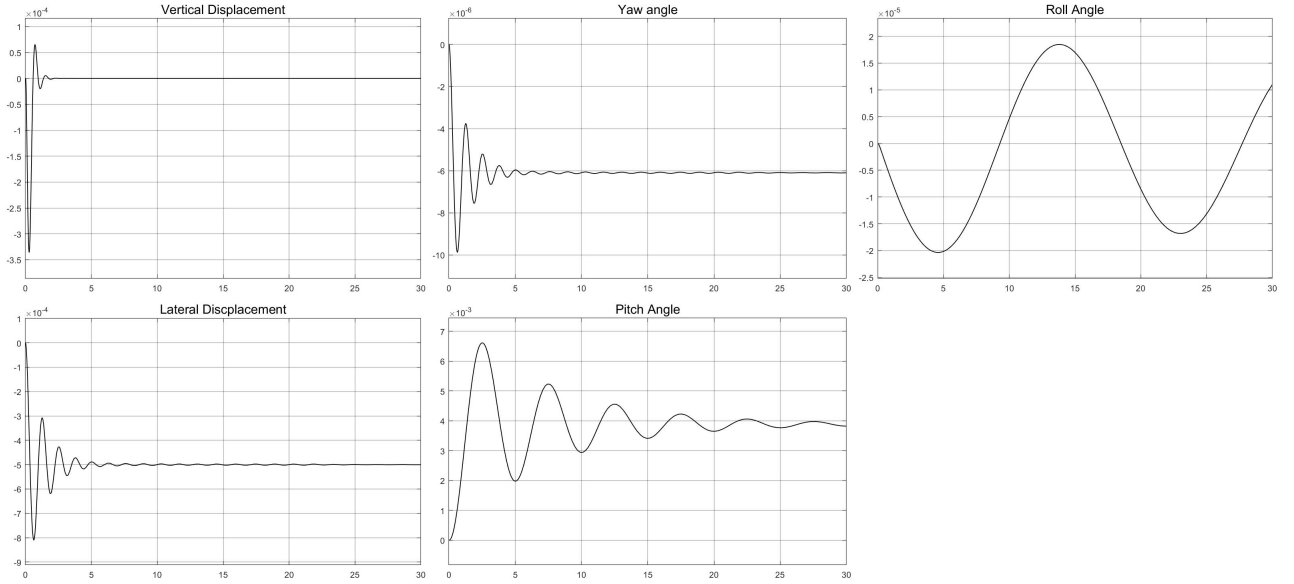


Figure 1: Predicted Vibrational Environments.

2.2 Sensor Location Map

Figure 2 below shows the top view of the chassis with the data acquisition units marked. Microcontrollers are located in the dedicated containers in the front and in the rear of the pod. Proximity sensor clusters are placed on the corners and close to the central rail. Photoelectric stripe counters and IMUs can be found in the front of the pod.

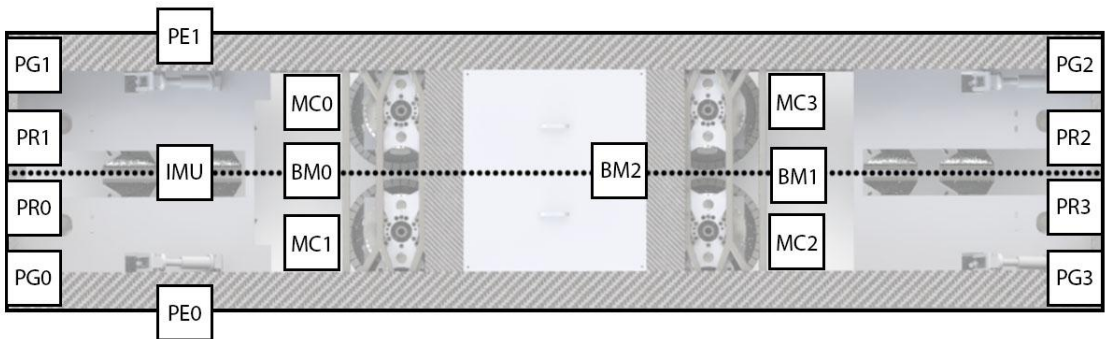


Figure 2: Sensor Location Map (BM - Battery Monitoring System; MC - Microcontroller; PR - Proximity Sensor to the rail; PG - Proximity Sensor to ground; PE - Photoelectric Sensor; IMU - Inertial Measurement Unit)

2.3 Trajectory

A model simulating the acceleration and deceleration from the wheels and the levitation skis was developed in MATLAB in order to predict the trajectory of the pod. The trajectory was simulated twice. The first case corresponds to the pod with the full payload (dummy and pressure vessel), while no payload is present in the second case. Furthermore, the second case includes the use of the emergency brakes during the deceleration phase. The figures below show plots for the predicted velocity against displacement. For the full payload case, as can be seen from the figure below a maximum speed of about 80 ms^{-1} is reached, while in the no payload case, a speed of about 90 ms^{-1} is reached.

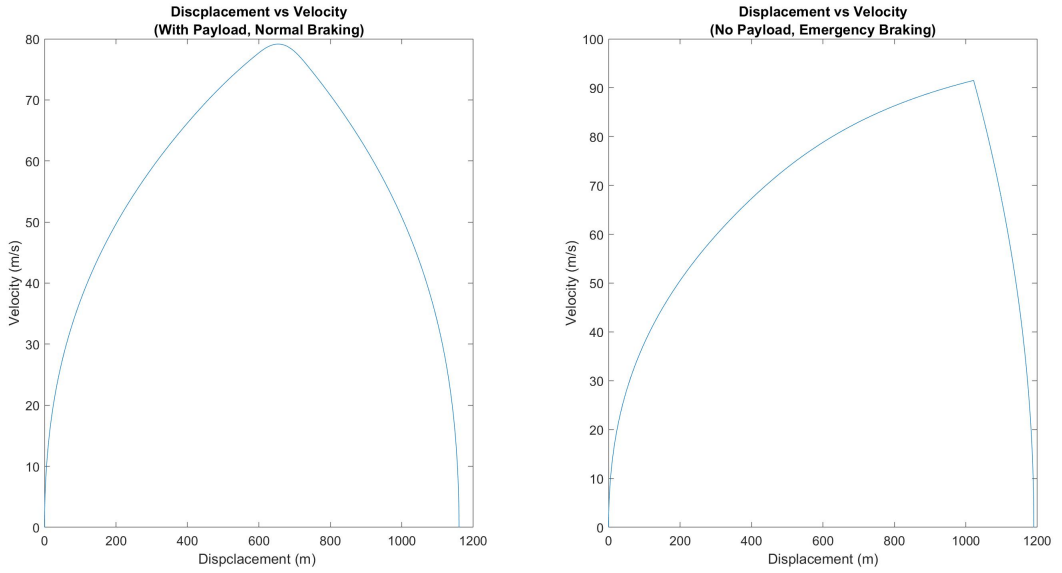


Figure 3: Predicted trajectory with payload and normal braking (left), predicted trajectory without payload and emergency braking (right).

2.4 Predicted Pod Trajectory with Emergency Braking:

The emergency nature of this sub-system calls for a quick and reliable way to stop the pod, while still remaining safe for cargo and passengers. Thus, a deceleration of 2.5g was chosen. The two graphs below show the theoretical velocity against distance and distance against time at different decelerations. The different decelerations are caused by the range of nominal initial brake pad temperatures. Without testing the frictional performance of the frictional pads for the use against the central I-beam, exact values can not be determined and only estimated.

The figure below shows the distance the pod has traveled before a complete stop at the designed deceleration of 2.5g and the theoretical maximum (2.7g) and minimum (1.4g):

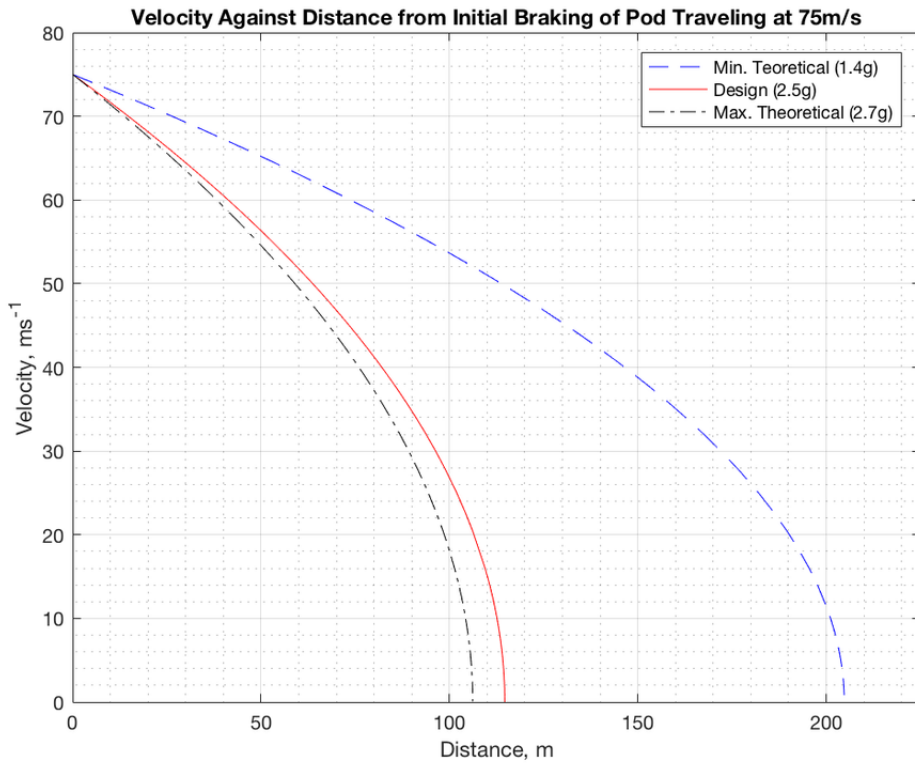


Figure 4: Distance the pod has travelled before a complete stop.

2.5 Safety

2.5.1 Magnet Safety

In order to safely store the magnetic arrays, they will be contained in steel-lined boxes, to contain and reduce the penetration and of the magnetic field. The thickness of the steel-lining required will be experimentally determined, once the team has received the arrays. However the predicted approximate thickness required will be 5mm. Each magnetic array will be separately packaged in its own box, to prevent demagnetisation of the arrays. Once magnets are inside their individual boxes, the field around the storage area will be measured and clearly marked off, with pacemaker warning signs and any other necessity.

Once the magnets have been placed in the skis. Ski-shields will be attached to the skis to safely store and protect the magnet arrays. The ski-shields will consist of a 10mm layer of plastic (facing the skis) and 3mm thick steel. The steel layer

will prevent the magnetic field from propagating, and will allow safe storage and transport of the pod. Similar practices will be carried out for the Halbach wheels.

2.5.2 State 0 Failure, or Pod Stop Command

In the event of a safety-critical error, the on-board state machine — which resides on the *master node* of the control system — is capable of transitioning the pod into the emergency state (state 0). Under this state the high power batteries are disconnected, the motors are no longer driven, and the power-redundant emergency brakes are deployed. Care has also been taken to ensure that the pod does not attempt to accelerate and decelerate simultaneously — in addition to logical restrictions, there is also a hardware mechanism designed to prevent the motors from running and the brakes deploying at the same time. A hardware transition to the emergency state is actuated should a failure in the master node arise.

Our Telemetry and Mission Control system serves to issue real-time emergency signals to the pod, should the operator note that a safety-critical pod parameter (such as battery temperature) has deviated from its safe operating range. Upon receiving a real-time emergency interrupt, the pod will transition into the emergency state. Should telemetry connectivity be lost during the run, the pod will automatically enter the emergency state as a safety precaution.

2.5.3 Energy Stored on Board

Energy Stored in gas springs of the emergency brakes

As gas springs are used, there is energy stored in the form of compressed air. As the gas springs are charged to a pressure of 135bar, they contain an energy of 1.1kJ calculated assuming an isothermal expansion. If an adiabatic expansion is assumed, the energy stored is 0.2kJ. Thus, the entire emergency braking system has 8.8kJ of energy stored.

Battery systems

The primary energy source of the pod is in the form of battery packs. There are a total of three battery packs — a high power one solely for the propulsion system; and two low power battery packs for the electronics and controls of the pod, one of which acts as a redundancy. The high power system consists of 768 A123 Systems ANR26650M1-B LiFePO₄ cylindrical battery cells in a 96S8P configuration, operating at a nominal voltage of 316.8 V with a peak discharge power of up to 300kW. The total energy stored in this system is 22.81MJ. The low power system consists of 28 LG HG2 3000mAh Li-Ion 18650 cylindrical battery cells split across two packs — the main battery pack in a 7S3P configuration; the backup

battery pack in a 7S1P configuration. Both battery packs operate at a nominal voltage of 25.2V, with peak discharge powers of 2.27kW and 0.76kW for the main and backup battery packs respectively. The total energy stored in the low power system is 1.089MJ.

Halbach wheels

Energy is also stored in the Halbach wheels in the form of rotational kinetic energy. This reaches its maximum at the maximum rotational speed of the wheels which is about 7000RPM. Using SolidWorks, the moment of inertia about the rotation axis was computed. The total rotational kinetic energy of the Halbach wheels was computed at 230kJ.

Pressure Vessel

The pressure vessel will be at 1atm and the volume is approximately 1.5m³. Total energy stored in pressure vessel is 150J.

The total energy stored of all systems on the pod is 24.137MJ.

2.5.4 Hazardous Materials

There is a total mass of 60kg in battery cells on the pod, storing 23.891MJ of energy. The majority (98% by mass) of the battery cells are lithium iron phosphate (LiFePO₄) 26650 cylindrical cells made by A123 Systems. As far as lithium-based battery technologies go, these are the safest option available. LiFePO₄ is intrinsically a more stable cell chemistry than other lithium-based battery cell chemistries — the main downside is that LiFePO₄ generally has lower energy density. The rest of the battery cells, used in the low power system, are lithium-ion 18650 cylindrical cells made by LG. This is a well-known battery cell for its reliability. A major reason for using this battery cell is that it has been extensively tested by the team during last year's competition, including passing all battery-related tests at SpaceX grounds.

In both cases, cylindrical battery cells were chosen for their robustness and good vacuum compatibility. These types of cells are much less prone to physical damage than pouch cells. The manufacturers of both battery cells provide detailed information on tests done including physical and electrical attacks.

All battery packs are fused directly at their outputs and continuously monitored by a professional battery management system.

2.5.5 Fault Tolerances

The pod has been designed with safety as the prime consideration; systems have a safety factor of 2 or higher and all systems are designed so that more than one component has to fail before the safety of the pod is compromised. The specific fault tolerances are discussed in each section below.

Pod robustness to tube breach

In the case of a major tube breach, the pod will go from being in a vacuum state to hitting a wall of air at on atmosphere that is approaching it at high speed. The relative speed of contact has been estimated as 430ms^{-1} , where the air from the exterior expands at the speed of sound, and the additional speed is that of the pod as it travels, around 100ms^{-1} . Through simulations, this has given a value for the stresses induced on the pod surface, which have been found to be in the order of a few hundred kPa, well under the material strength, which in this case is carbon fibre. Rapid pressurisation of the tube would therefore not result in catastrophic failure for our pod. However modelling how the pod would move when exposed to such an event is beyond our capabilities and depending on the severity of the tube breach it is possible that the pod would derail.

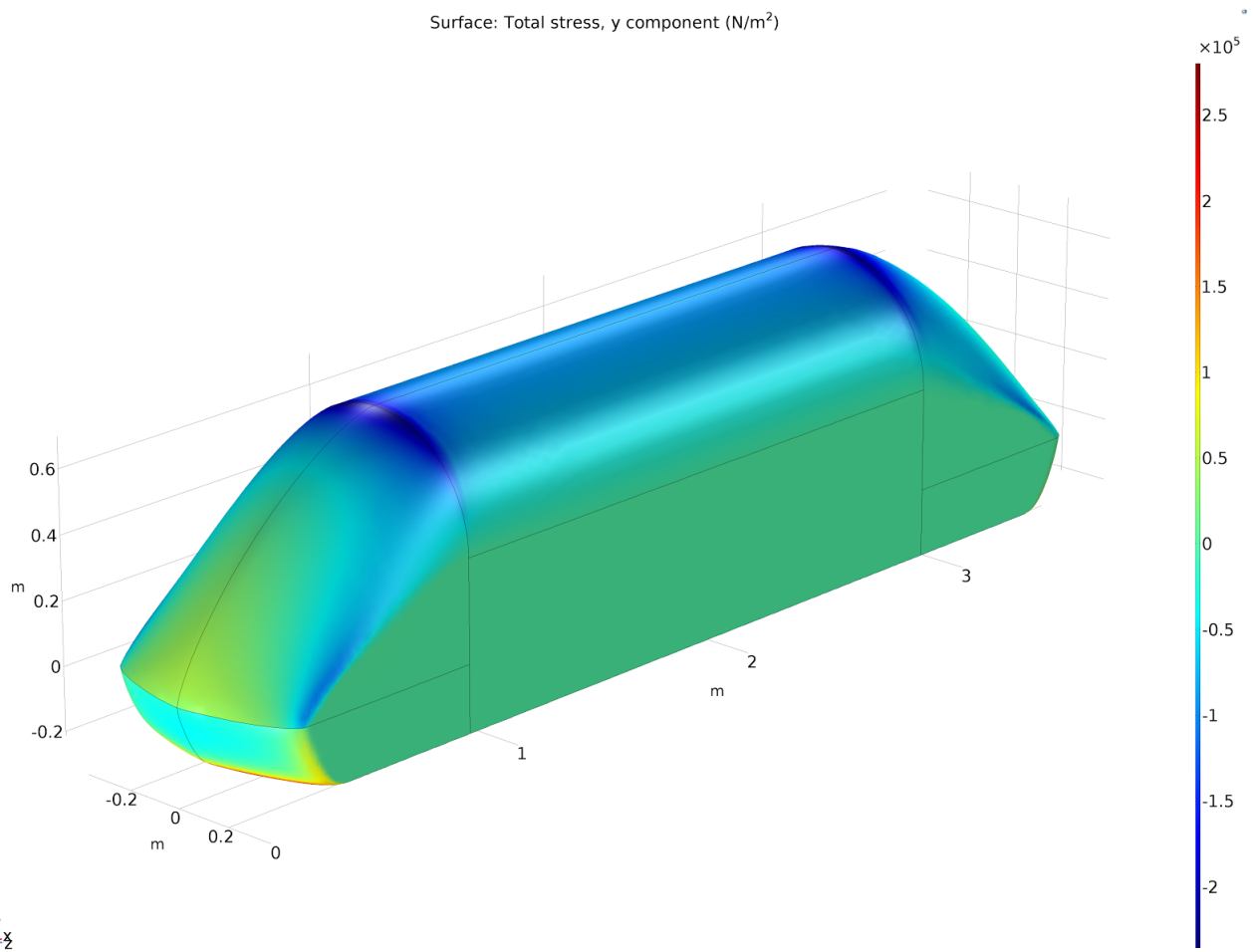


Figure 5: Pod stress simulation.

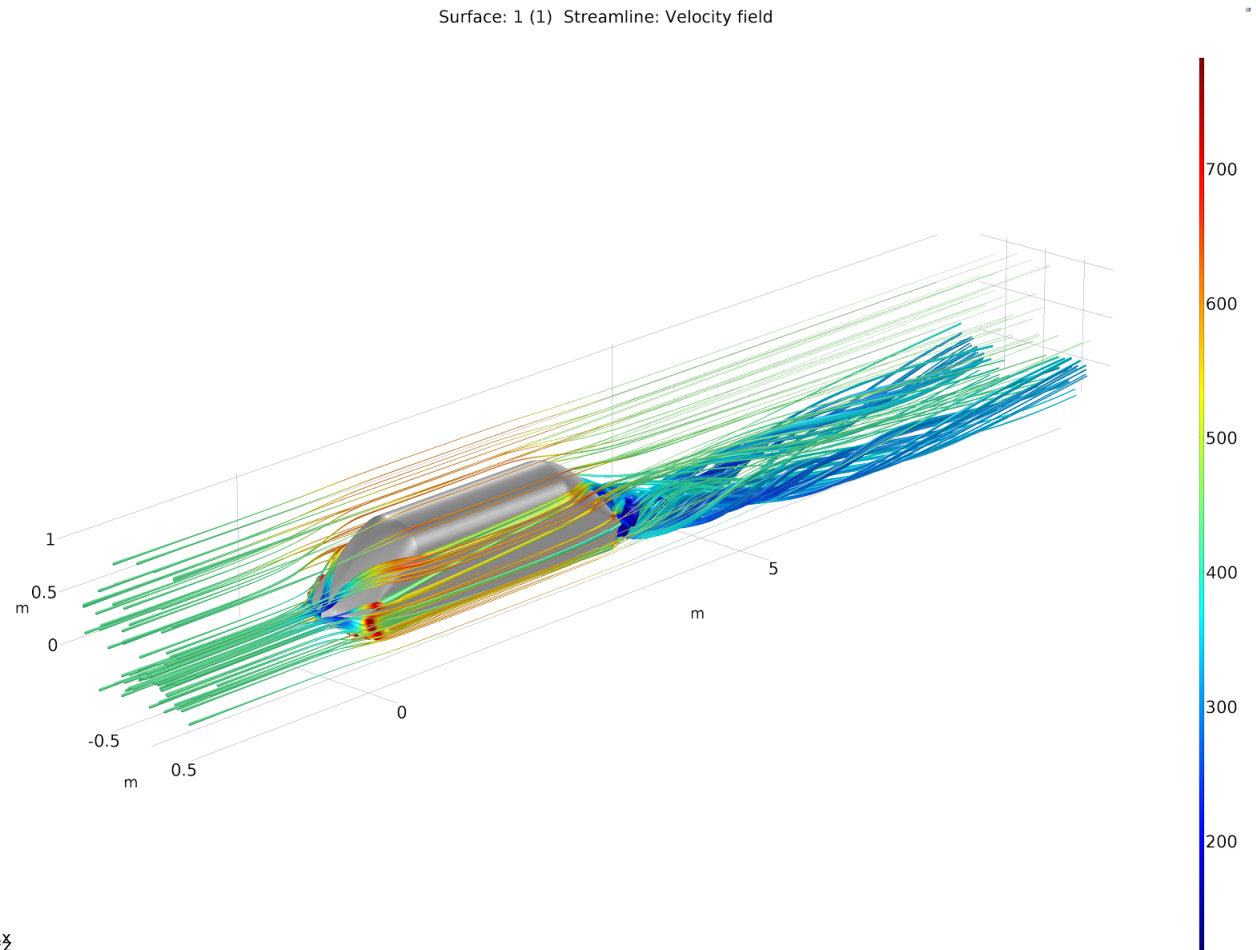


Figure 6: Pod velocity field simulation.

2.5.6 Vacuum Tolerances

Shocks and gas springs

The shock absorber used in the suspension system will be vigorously vacuum tested because it is pneumatic. This is to ensure it keeps its performance in a low pressure environment. We don't expect to encounter any issues concerning pneumatic cylinders in a vacuum as this technology was used on our previous pod and encountered no issues. Nonetheless, it shall be tested again as the shocks are slightly different from last years.

Gas springs will be tested in a vacuum, in a similar fashion to the shocks, to test that they hold their pressure over an extended period of time. The gas spring will

be tested by compressing the spring and ensuring that it exerts the correct force at the different extensions.

Batteries

Cylindrical 26650 LiFePO4 battery cells, the specific cell type used in the high power system, has been researched and approved for use in orbital satellite applications, making it highly vacuum compatible. There was a measured sub-10% decrease in battery cell capacity at room temperature vacuum, with no other measured effects. Individual battery cells have been tested in a vacuum chamber in-house with no measured swelling or power performance drop. A fully assembled battery pack will be tested (with and without a load) in a vacuum chamber as soon as it has been manufactured.

The LG HG2 cylindrical 18650 li-ion battery cells were used in the competition last year, as stated previously. The cells, as well as fully assembled battery packs (electrically nearly identical to the ones used this year) have therefore been vacuum-tested on several occasions in-house, at outside vacuum chambers, and at SpaceX headquarters. Furthermore, this type of battery cell has been research and approve for space mission applications by NASA, making it suitable for vacuum environments.

Motors

The Emrax 208 motors are entirely liquid-cooled and IP65 rated, meaning the presence of air flow is not required for optimal cooling. The manufacturer has been made aware of the vacuum environment application of the motors and agreed to test and manufacture the motors such that the liquid cooling system will hold under vacuum. A slight increase in the efficiency of the motors is to be expected due to non-existent windage losses in vacuum conditions.

Gas springs

The gas spring will be used at a nominal pressure of 135 bar and are rated for pressures of up to 180 bar. Hence the one bar difference won't be significant in adding stress to the the springs. They will however undergo substantial vacuum testing to ensure that the seals don't rely on atmospheric pressure.

Electronics

Photoelectric sensors will be extensively tested under low pressure conditions to make sure the IP65 certified packaging does not deform. Otherwise no components have been identified that are likely to fail in vacuum. Nevertheless, all sensors and microcontrollers will be tested in a vacuum chamber to ensure safe performance.

2.5.7 Off-Nominal Collision

Given that the chassis was designed for bearing the loads from modules specifically, our team chose to give the front shell a structural role so that it could mitigate the loads on the chassis in the event of a frontal collision. As seen in the specific Shell section, the front was structurally designed so that it could bring the pod to a full stop in the event of a 7ms^{-1} frontal crash, before the chassis itself were to hit the obstacle. This avoids any major damage or stresses to be induced on either of the modules or the pressure vessel. Furthermore, a simulation was carried out on the chassis to show that in such a crash it would not fail. This can be seen in Figure 7, where the highest stress is in the direction of the chassis' length, at about 95MPa, whereas material strength stands at a few hundreds of MPa.

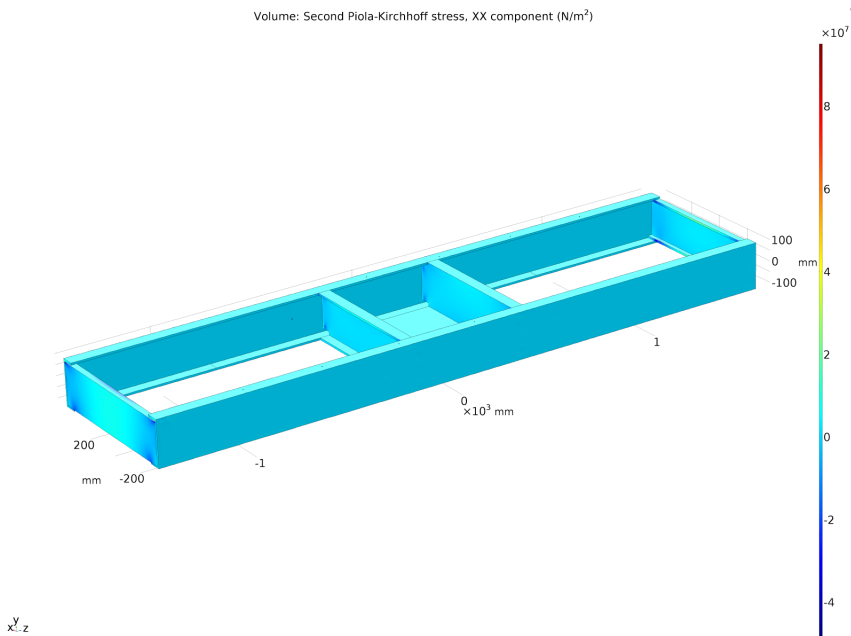


Figure 7: Chassis crash simulation.

2.5.8 Single Points of Failure

As the primary consideration of the design was the safety and reliability of the system. All components critical for the safe braking of the systems have built in redundancies that allow any one of them to fail and still allow for a safe stop. Furthermore, a fault in any safety critical component will trigger a state 0 which releases normally extended brakes and cuts the high power battery, bringing the pod to a safe stop. As a result of this, there are no single points of failure on the pod.

2.5.9 Recovery Plan

Recovery will take two different routes depending on whether or not the emergency brakes were deployed,

1. In the case of actuated emergency brakes, the brakes will have to be manually retracted. The electromagnets will be connected to the power supply (external power supply in case of power failure on board) and switched on to hold the brakes in place. The pod can then be manually moved outside the tube and recovered in accordance with the unloading plan.
2. In the case that emergency brakes were not deployed, it will be ensured that power supply on board is working well and the pod will slowly drive to the end of the tube using on board propulsion where it will exit in accordance with the unloading plan.

2.5.10 Mitigation of Complete Loss of Power

Complete loss of power occurs when the control system of the pod loses power. In this case, communication with the pod and any control of it is lost as well. If this were to happen during the run, emergency braking would automatically activate due to the power loss. However, this scenario is highly undesired, so design considerations have been made to prevent this.

The low power system which supplies the control system consists of two battery packs. If the main battery pack fails for any reason, the backup battery pack takes over without any interruption or need for a control signal (the switch-over is done through diodes). The backup battery pack has its own independent power electronics system, which also provides a backup for the main one. This includes a backup battery management system, temperature sensor, current sensor, physical switch and solid-state relay. Therefore, for complete loss of power to occur, two independent power systems would have to fail.

All battery cells on the pod have been chosen with maximum safety and reliability in mind, rather than just choosing battery cells with highest power or energy density. All battery pack assemblies have their entire surface area, as well as all contacts, once connected, insulated from the outside to mitigate external short circuits.

2.5.11 Inhibitions on Braking during Acceleration Phase

Ensuring that the emergency brakes are not actuated when accelerating is implemented through software, as well as hardware. As the system relies on an

electromagnet to keep the system retracted, the system needs to ensure that constant power is supplied to it. If power is cut from the electromagnet, the emergency brake is released. The power to the magnet can be cut through software by turning off a solid state relay. The terminals of the electromagnet also act as the power supply to a contactor which allows power to flow to the propulsion system. If the electromagnet is no longer active, the power to this contactor is lost and the propulsion system is disconnected. Therefore, we can not brake and accelerate at the same time.

2.6 Scalability

The whole pod was designed on the premise of scalability as our central design philosophy. Going into detail on the scalability of each subsystem is beyond the scope of this section, however a rough estimate of the scale of this pod will $10\text{m} \times 2\text{m} \times 2\text{m} \times (\text{length} \times \text{width} \times \text{height})$. Scalability will be discussed for each subsystem in the following sections.

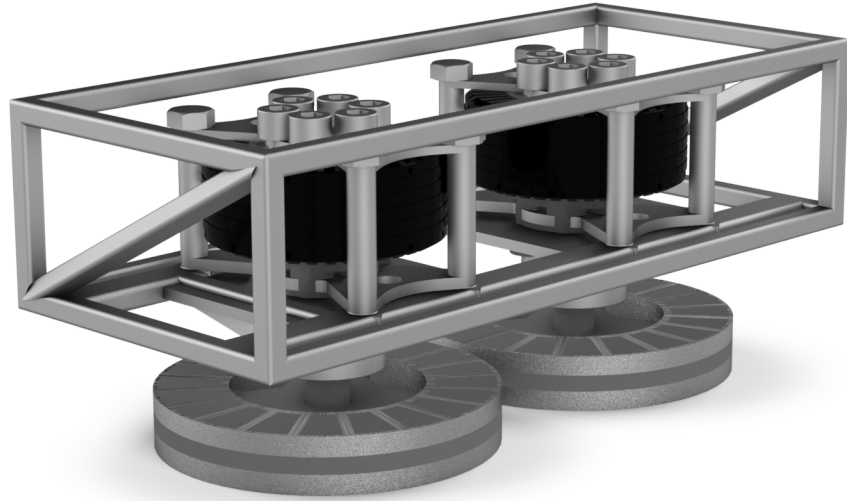
2.7 Testing

Due to the complexity of the Halbach wheel system, a small version of Poddy the Second is being manufactured which will be used to test the physics and control behind the Halbach wheel system before the full implementation. This "prototype prototype" will be used to test the propulsion as well as the control and navigation systems before they are implemented on Poddy the Second.

2.8 Timeline

Discussing a general timeline is also beyond the scope of this section. Currently within the team there is design, testing, and manufacturing work being carried out in parallel. The specifics of this are outlined in subsequent sections.

3 Propulsion Module



3.1 Halbach Wheels

3.1.1 Introduction

The pod is propelled by a system of 4 radial flux Halbach wheels. By controlling the slip of the wheels compared to the central I-beam, both trust and brake force can be produced. Each Halbach module contains two Halbach wheels, arranged on opposite sides of the central rail. The wheels and their auxiliaries, such as the shaft and mounting, the motors used to spin the wheels, the motor controllers and cooling system are described in this section.

3.1.2 Summary

Requirements

The number of wheels that could be used was limited by the size of pod as the interacting magnetic fields of wheels too close to each other cause problems. Given the estimated pod dimensions, and relevant allowances in space for all the other required component modules, a 4 wheel design was proposed. This could provide

a thrust force of approximately 5000N in total or 1250N per wheel for a 6mm air gap from the wheel to the central I beam. With a mass of 500kg a maximum acceleration of just over 1g is expected. When not carrying the pressure vessel, end cones and dummy the mass is 360kg, giving a maximum acceleration of 1.42g. The magnetic performance is shown in the simulations section below, which clearly shows that for a point with 6mm gap to magnets can have a maximum magnetic flux density of 0.7 Tesla. This guaranteed there will be enough force generated from the wheel.

Dimensions and Mass

The Halbach wheels were designed to maximise thrust efficiency, to transfer as much power from the motors into propulsive power. Simulation results showed that the wheels could achieve a maximum efficiency when they have a diameter of approximately 300mm and a pole number between 4 and 6. Magnetic pole number is the number of complete Halbach sections, each section comprising of 4 magnets. We chose to have a pole number of 5, translating to 20 individual magnets. This was chosen due to size of magnets available and size of the wheel. Additionally it gives a high thrust efficiency and a relatively low undesirable radial force. The thickness, limited by the top and bottom flanges of the I-beam, had to be smaller than 60mm, to allow for some vertical movement without entering the no go zones.

Design Parameter	Dimension
Wheel Outer Radius (mm)	150
Thickness (mm)	50
Pole Number (-)	5
Number of Magnets (-)	20
Magnet Grade	N52
Magnets Outer Diameter (mm)	296
Magnets Inner Diameter (mm)	180
Wheel Mass (kg)	15.37
Wheel Moment of Inertia (kg m ²)	0.225

Table 1: Halbach Wheel Dimensions.

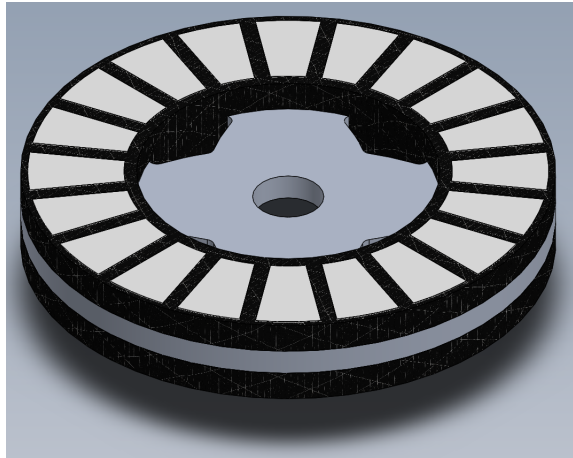


Figure 8: Halbach wheel.

Materials

Due to the requirement of high angular velocity (up to 760rads^{-1}) of the wheel, the stress on the wheel was expected to be high. Finite Element Analysis for stress calculation was performed on wheels made from different materials, such as different aluminium and titanium alloys. To make the wheel as strong as possible, it was decided to structure it with a titanium plate in the middle, to transfer the stress and torque from the motor while the magnets would be attached along the perimeter of the plate. To further improve design robustness, it was decided to fix all the magnets by carbon fibre reinforced epoxy. This would aid in withstanding the significant centripetal forces expected during operation.

Halbach Wheel Stability

The Halbach wheels are expected to contribute to lateral stability of the pod as the Halbach wheels supply spring and damper like properties. As there are wheels on either side of the rail, these properties serve to centralise the pod. Additionally, as the magnitude of the lateral force is inversely exponentially dependent on the air gap, when the pod translates horizontally towards the rail, the decrease in air gap will lead to significant increase in force whilst the opposite occurs on the opposite wheel. This force difference can create a negative feedback and force the pod back to its centre position.

However, due to the uncertainties inherent in magnetodynamic simulations, this is only considered to somewhat smoothen the ride while the lateral stability system is designed to single handedly handle all nominal vibrations of the pod without considering the Halbach wheels.

Motor-Wheel Assembly

Each wheel has its own independent motor (seen in following sections). The motors will be connected to the Halbach wheels via EN24T driveshafts. The shaft length is 100mm, to make the wheels central to the rail. To ensure the safety of the shaft, its diameter is calculated to be 40mm. Simulations for this can be found below.

3.1.3 Considered solutions

We considered linear induction motors in the past, but have deemed them unsuitable for the specific environment of the competition. We also have avoided the system of clamping wheels on the rail to provide thrust, as one of our main objectives is to produce a contactless, scalable system. Additionally the pod levitates, so a clamped wheel would act against any vertical movement, creating conflicts when the pod reaches lift off speed.

3.1.4 Simulations

Wheel Simulations

Based on the simulation results, under 760rad/s rotational velocity and the gravitational force, the Halbach wheel will have a maximum stress of 250MPa, using titanium material, the Halbach wheel can have a safety factor of 4.

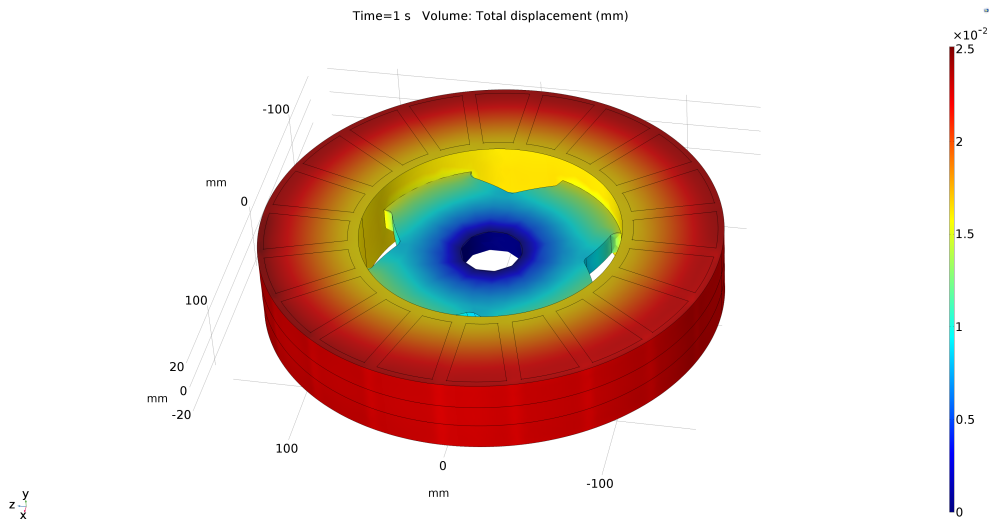


Figure 9: Deformation simulation on Halbach wheel.

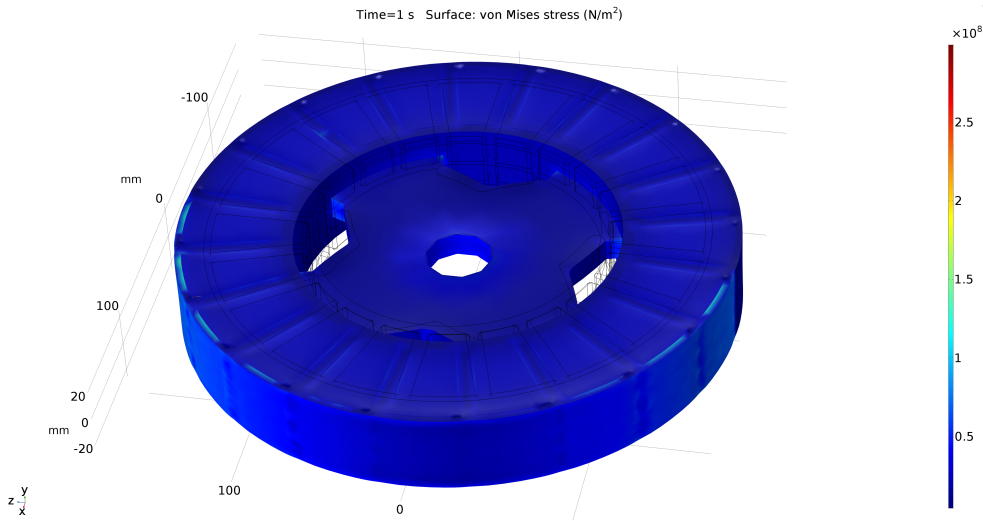


Figure 10: Stress simulation on Halbach wheel.

Coupling Shaft FEA

For the use case of the Halbach wheel shaft, a radial force of 10kN is expected to act on the bottom end of the shaft, this will yield a maximum stress of 200MPa, which for EN24T means a safety factor of 3. The shaft is displaced approximately 0.01mm, this is deemed insignificant in this scenario, especially as this simulation includes a safety factor.

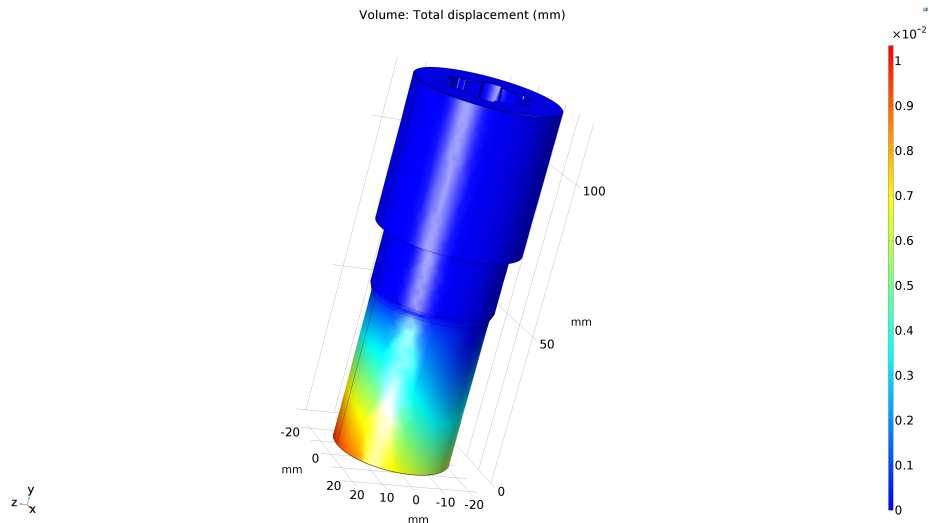


Figure 11: Coupling Shaft Von Mises Stress simulation.

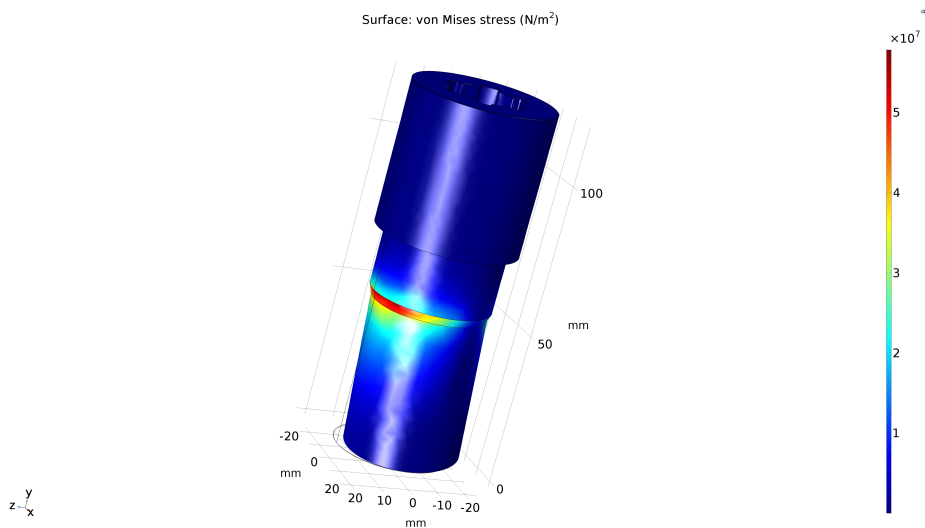


Figure 12: Coupling Shaft deformation simulation.

Magnet Performance of Halbach Wheel

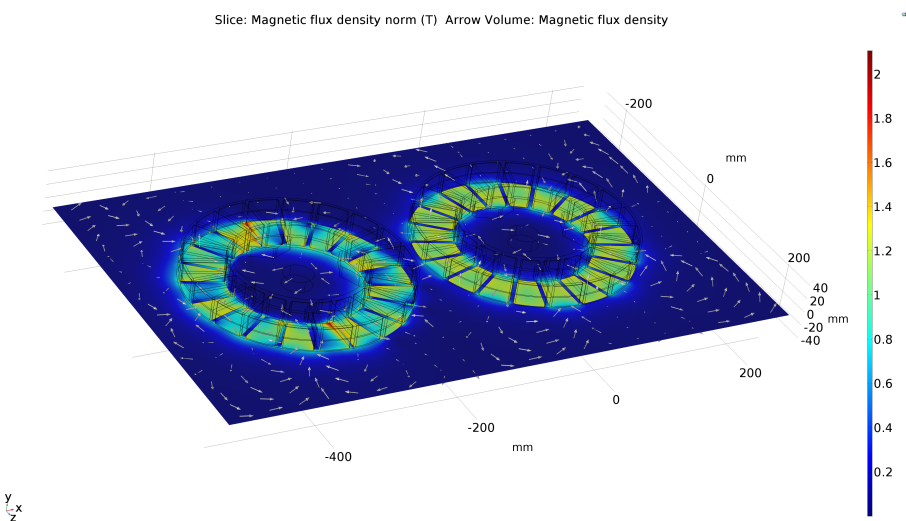


Figure 13: Halbach wheel static field simulation.

3.1.5 Safety

Fault tolerances

See the table below for possible failures of Halbach wheels.

Failure	Effect	Risk	Detection Method	Solution
Motor Failure	Loss of rpm synchronisation in one pair of Halbach wheels	Loss of lateral stability. The whole pod might shift to hit the rail with the fragile Halbach wheel	Rpm sensor should detect the difference	Turn off both motors in the pair to reduce drift. Built in emergency system of rollers will make sure that the wheel will not move closer than 1mm from the rail. Emergency brakes can be used to stop the pod.
Controller Failure	Loss of Rpm synchronisation in one pair of Halbach wheels	loss of lateral stability. The whole pod might shift to hit the rail.	Rpm sensor should detect the difference.	Cut off the power to both motors. Built in emergency system of rollers would make sure that the wheel will not move closer than 1mm from the rail. Emergency brakes can be used for stopping the pod.
Wheel Structural failure	Destruction of wheel. Possible damage to surrounding pod and tube.	Loss of stability, the whole pod might shift. Parts of the wheel might damage sensors/motors/ other systems/rail. They may pollute the testing tube.	Motor speed analysis. Motor speed should run away without wheel present.	If titanium form fails to hold the magnets. All the motors are stopped and activate emergency braking. the motors will shelter the above structures of the pod from the explosion impact.
Wheel hit the rail	Wheel gets damaged	Damage to pod and rail. Further loss of stability. Loss of velocity control.	Accelerometers and distance sensors.	Roller wheels added that hit the rail before the Halbach wheel.

16

Broken sensor	Sensor gives false readings	Loss of control of pod subsystems due to lack of information.	Multiple sensors in groups to highlight erroneous readings.	Multiple sensors take the same readings, and the readings are compared to check for discrepancy. If the value of a sensor is outside of the acceptable range, the measurement is classed as faulty.
Loss of power	Halbach wheels slow to stop	Loss of lateral stability. Slowing of pod.	Motor speed sensors. Voltmeters located around pod.	Emergency braking system activated. Pod stopped.
failure of cooling	Motor or motor controller overheating	Damage caused to motor	Temperature sensors located around motor, controller and rest of pod.	Emergency braking system activated
Bearing failure	Slowing/stopping of Halbach wheel	Loss of lateral stability and velocity control. Slowing of pod.	Motor speed analysis measured from distance sensor and accelerometers.	Motor controller is manipulated to control the motor speed, along with the safety features of the controller. Emergency braking system activated.

3.1.6 Scalability

There are three main possible scalable factors of the Halbach propulsion system, they include: magnet strength, air gap and number of wheel pairs.

Stronger magnets could be employed in the wheel construction in order to create a greater propulsion force generated by each wheel. This would however greatly reduce the practicality of construction and maintenance due to the increased magnetic fields that would have to be dealt with. The magnets used are already the strongest commercially available. So increasing the magnets strength alone would not be a viable method, however, it could be utilised alongside other methods to provide a scaled up propulsion system.

In our pod, an air gap of 6mm between the Halbach wheel and the rail is used. This could be decreased in order to increase the thrust force produced. However, this is the distance between the magnets and the rail. So in reality, including the thickness of the wheel housing, the air gap between the rail and wheel is 5mm. This, in addition to the tolerance in the rail and slight variations in pod trajectory, means that the air gap cannot be decreased whilst maintaining safe operation.

Another method of scaling up the propulsion system to accommodate larger pods, and so passengers or cargo, would be to increase the number of Halbach wheel pairs present on the pod. This seems to be the most viable of the suggested options. It requires no further advances in the technology presented in this report, merely a replication of the already devised systems.

Size/Mass

In the design presented by this report, 2 pairs of Halbach wheel are used to propel a pod of 500kg. With an 8000kg estimated mass of a passenger-carrying pod, and assuming linear scaling, 32 pairs would need to be employed for propulsion. This demonstrates the lack of scalability inherent in the on-board propulsion design.

The addition of onboard propulsion also adds the requirement of batteries. The batteries in the design are very massive and greatly limit the speed and runtime of the pod. Unfortunately this is a problem inherent in current battery technology. The batteries in the design are heavy and are only designed to run the pod for short periods before recharging is required.

The majority of the pod mass is a direct result of the propulsion system. This is the main factor in limiting the scalability of the pod. The total mass of the propulsion system, including the motors, wheels, batteries and controllers is 220kg

If one assumes linear scaling once again, this would mean an 8000kg pod would have a propulsion system of 3520kg.

The addition of propulsion built into the pod is advantageous over the propulsion being provided by the tube as it allows for more future proofing. As technology advances, the pods can be updated with little to no system downtime (i.e. pods updated one at a time). However, if the propulsion mechanism were to be built into the tube, updating the system would be exceedingly costly and require a complete shutdown.

Onboard propulsion greatly increases the weight of the pod. The total weight of the Halbach wheels, motors, controllers and batteries that must be added to provide the propulsion is quite a large portion of the total weight of the pod.

Cost

If the costs were linearly scaled with the number of wheels, the total cost would simply be 16 times the costs presented below. In reality, with large scale production costs would be reduced.

Maintenance

The modular design of the pod allows for much greater ease of maintenance. This is due to the design allowing the Halbach wheel module to be removed from the pod, and so it can be worked on separately outside the pod. Whilst this module is out for repair or maintenance a secondary module can be installed meaning the pod downtime is reduced. Maintenance on the module includes checking for wear or structural defects in the wheel and housing. Additionally, the remnant field of the permanent magnets should be checked. Any structural damage or wear should be fixed and if the field has dropped significantly the magnets should be replaced. These issues are rather major and may result in the complete replacement of wheels or shafts.

3.1.7 Summary

On board propulsion, with current technology, is not a viable option for a full scale Hyperloop system. This is due to a number of factors. The mass of the propulsion system is a very large part of the final pods mass. This drastically inhibits the acceleration and speed of the pod.

3.1.8 Cost Breakdown

Component	Quantity	Estimated Cost for 4 wheels (£)
Magnet	80	2500
Titanium plate	4	1200
Carbon fibre reinforced epoxy	-	50
Connection shaft	4	400
Flange housing for plate	4	400
Flange housing for bearing	4	400
Bearing	4	800
Framework	2	200
Overall	-	5950

Table 2: Cost breakdown for Halbach wheels.

3.1.9 Manufacturing

CC

	January	February	March		April		May		June		July	
Parts	1st-15th	1st-28th	1st-15th	16th-31st	1st-15th	16th-30th	1st-15th	16th-31st	1st-15th	16th-30th	1st-15th	16th-31st
Magnets				Assembling the halbach wheels / testing methods of assembly	Testing the wheels for uniformity / making corrections	Finishing any corrections						
Housing for the Magnets												
Housing for the whole system				Assembling the frame								
Shaft												
Motors				Assembling the motors and all of the relevant connections	Testing the motor assembly and taking profiles of heat							
Bearings/Connections/etc.												
Final Assembly			Halbach Wheels Made	Motor Assembly Made		Begin final assembly	Final assembly is finished / testing	Testing		Make any necessary repairs / changes	Parts are tested and ready to go	

Figure 14: Manufacturing timeline for Halbach wheels.

3.1.10 Testing

To confirm the simulations and model of the Halbach wheel match reality well, a small scale prototype of the pod is currently being manufactured with one pair of Halbach wheels (diameter 94mm, 16 cubic magnets per wheel, motor max power of 2200W, torque of 2.9Nm). It will prove assumptions behind used theoretical model, and give insight into any manufacturing problems that may occur. This prototype is scheduled to be finished by the middle of January 2018. At that point in case of any discrepancies between used theoretical model and reality there should be enough time to fix the calculations.

Full scale, manufactured Halbach wheels will be tested in two different ways:

Firstly, each wheel balance and strength would be checked mounting it to the motor and rotating with rpm increased in small steps up to ~ 8000 . It will make sure that there are no internal defects (those could result in shattered magnets) and our design is strong enough to sustain intended operation (which should not go above 7500rpm).

Secondly, we will confront the theoretical predictions with the real performance of the system. Each wheel will be fixed to the ground alongside the block of aluminium acting as a rail. Sensors will measure achieved lateral and propulsion forces at different rpms and air gaps.

These tests will be done in an enclosed, safe environment to protect everyone involved in case of critical failure of the system. They should finished by the end of June 2018.

3.2 Motors

3.2.1 Introduction

Propulsion and primary braking of the pod are achieved by electric motors driving the Halbach wheels. It was decided that each Halbach wheel would be powered by its own motor. As there are four Halbach wheels, this means there are four motors as well. In this way, there is no need for a complex drivetrain, which could be a critical point of failure. Furthermore, higher performance can be achieved in a smaller physical size using modern high power density electric motors.

Requirements The main required specifications for the motors to reach the desired maximum speed for a 520kg pod at 1g acceleration and deceleration, based

on pod trajectory analysis are:

- Peak torque of 180Nm (per wheel)
- Rotational speed of 7000rpm at 16 seconds into the run
- 35kW continuous output power (per wheel)

The required torque-speed relationship to achieve optimal performance as calculated by the simulation team can be seen in the figure below:

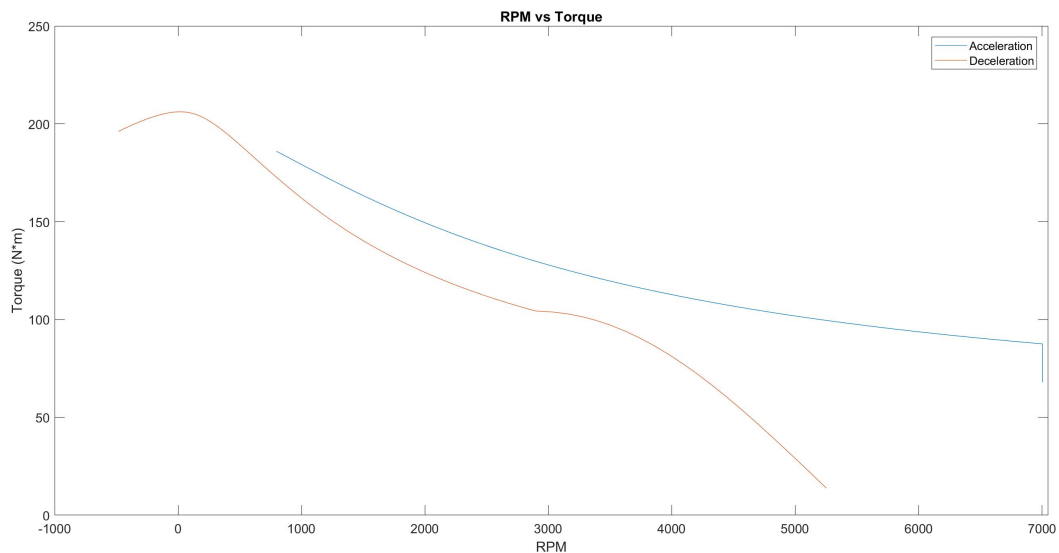


Figure 15: Required torque-speed relationship to achieve optimal performance.

While it is likely that a realistic electric motor would keep a more constant torque output at higher speeds, that does not constitute a major problem — the additional torque will just not be translated into useful forward movement of the pod. This will then be quickly corrected by the control system to minimise energy losses from the battery pack.

The pod uses rotating magnetic fields to induce currents on the aluminium test track, thereby generating a current, and, consequently, an opposing magnetic field in the track. By Faradays law, the magnitude of the current (and therefore the opposing magnetic field) is proportional to the velocity between the initial magnetic field (from the Halbach wheels) and the track. This difference in velocity is known as the slip ratio, and it decreases with time (see graph). Therefore, for 1g acceleration and deceleration, the values of the graph above reflect the required torque

value for the motor in relation to Halbach wheel rpm. The systems maximum usable torque, at a steady rpm (instantaneously), is governed by this slip ratio. This explains the decreasing torque requirement as shown by the graph above. To compare with traditional wheel-based propulsion devices (cars, for example), the torque requirement is limited by the static frictional force between the tyres and the road. Any more torque will result in the wheels spinning and not doing work on the car.

Furthermore, for good system integration, it is required that the motors fit inside the C-beam of the chassis — in other words, that the motors do not stick out of the chassis in any way. This is a significant limitation, as height of the usable space inside the chassis is only 191mm. It is also necessary for the motors to be liquid-cooled due to the vacuum environment where no air cooling can occur, requiring additional space for coolant tubing.

3.2.2 Summary

For the propulsion of the pod, four liquid-cooled Emrax 208 permanent magnet synchronous motors are chosen. Each of the motors can provide a peak torque of 180Nm and peak speed of 7040rpm - the maximum continuous power rating is 40kW, and the maximum 2-minute cold-start power rating is 80kW. The motors achieve state of the art power density, with a mass of only 9.4kg per motor. Each motor is controlled by an emDrive H300 liquid-cooled motor controller.

Analysis of choices available

There are four main electric motor types that were considered: brushed DC, induction, brushless DC, permanent magnet synchronous.

Brushed DC Motor

The only truly DC motor that was considered. Since the pod is powered only by batteries, which operate on DC, it makes sense to consider a DC motor to avoid complex and expensive inverters/controllers. However, brushed motors are inefficient and large compared to other options. They are generally not used in the power range required by us, for good reason. This option was therefore abandoned before picking a specific brushed DC motor model.

Induction Motor

These are very rugged motors that perform well at a large range of powers. However, the size and weight of induction motors does not work well with our physical

requirements. Particularly, the long cylinder shape most common in induction motors simply does not fit inside the C-beam of the chassis at the required rated motor power. Furthermore, to control the speed of an induction motor, a large, complex and expensive variable frequency sinusoidal inverter controller is required. While full-load efficiency of induction motors is rather good, part-load (slip-dependent) efficiency is poorer compared to motors of the synchronous type. For the purposes of the this competition and Halbach wheels in general, where full-load only constitutes a small fraction of the total runtime, poor part-load efficiency is undesired. The HPEVS AC-35 induction motor was considered as a potential viable motor option if an induction motor were to be used. See Section ??.

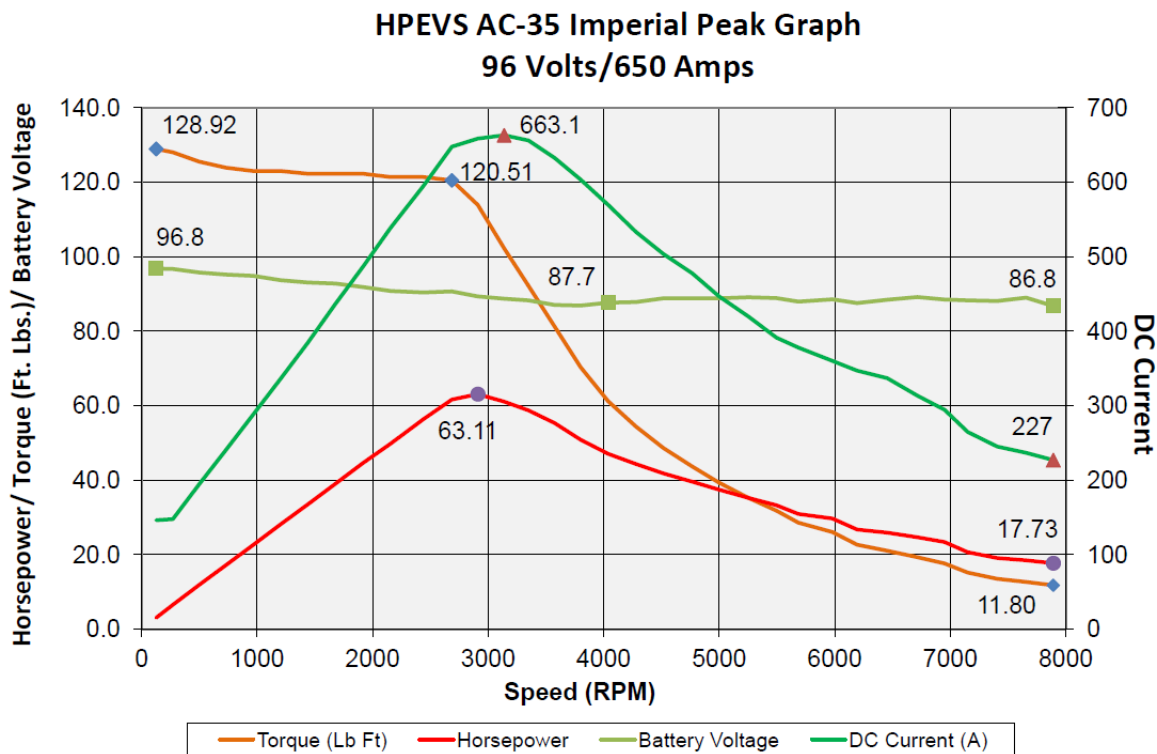


Figure 16: Graph for the motor torque, speed, power, voltage and current.

Brushless DC Motor (BLDC)

When supplying power from a DC source, the controller required for a brushless DC motor can be significantly simpler than those required for AC motors such as induction or synchronous. This is because a brushless DC motor only requires a trapezoidal/square voltage and current waveform, whereas traditional AC motors require a sinusoidal waveform. However even the highest power commercially

available BLDC motors do not comfortably meet our torque requirements without the use of a gearbox (considering a peak speed of 7000rpm is also required). Furthermore, due to the trapezoidal voltage waveforms, there is a more significant ripple current and therefore ripple torque with BLDC than other AC motors, slightly reducing vehicle stability and efficiency. The main BLDC option considered was the Alien Power Systems 20080 Outrunner Paramotor, see Appendix A.2.

Permanent Magnet Synchronous Motor (PMSM)

Much like regular synchronous motors, but the field windings are replaced by neodymium permanent magnets - this achieves significantly smaller size and does not require two different voltage sources, but comes at an increased cost. Permanent magnet synchronous motors have been expanding their presence in the industry for high performance applications due to their notably high efficiency (96%+) and small size (comparable to BLDC). It is not as simple to control these motors as BLDC however, as they require a sinusoidal voltage and current - meaning a variable frequency inverter controller is required, much like for an induction motor. Permanent magnet synchronous motors are also not quite as robust as induction motors, mostly due to the volatility of neodymium permanent magnets. However this is an issue that can be designed for so that, for example, the safe temperature range of the permanent magnets is not exceeded.

PMSM was the most widely considered option and several viable choices were found. Initially, the option of having a single motor powering all four Halbach wheels was also considered - in this case, PMSM was truly the go-to choice, as brushed and brushless DC motors are not commercially available at the required torque-speed range, and induction motors are generally larger in size.

The top choice for the single-motor configuration was the locally based Equipmake APM200 traction motor with an integrated inverter/controller, gearbox and liquid-cooling. See Section A.2.



Figure 17: Equipmake APM200 motor Performance Curves.

A two-motors configuration was also considered, as in the preliminary design briefing (one motor powers two out of four wheels). This would simplify the drivetrain required and would allow for more space within the chassis, however a completely custom drivetrain would still have to be developed. For this option, the also-local YASA-400 motor was considered, see Appendix A.2.

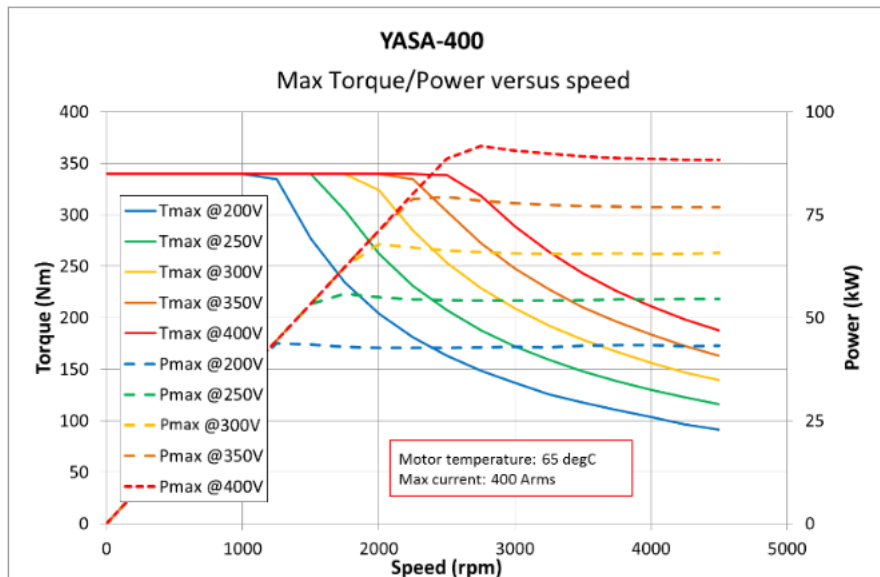


Figure 18: YASA-400 motor performance curve.

3.2.3 Chosen Solution

The previous sections concluded that the ideal motor configuration would be one where there is one motor for each Halbach wheel, or four motors in total - and that this motor would be a low-height permanent magnet synchronous motor. The final choice is the Emrax 208 axial flux permanent magnet synchronous liquid-cooled motor.



Figure 19: Emrax 208 motor.

This is a very high power density motor at only 9.4kg of dry mass that is primarily used in powered gliders and small airplanes. The motor has the typical pancake shape, which is desired in applications with limited space available. Two motors will comfortably fit side-by-side within the C-beam of the chassis, which is the main reason the motor was chosen.

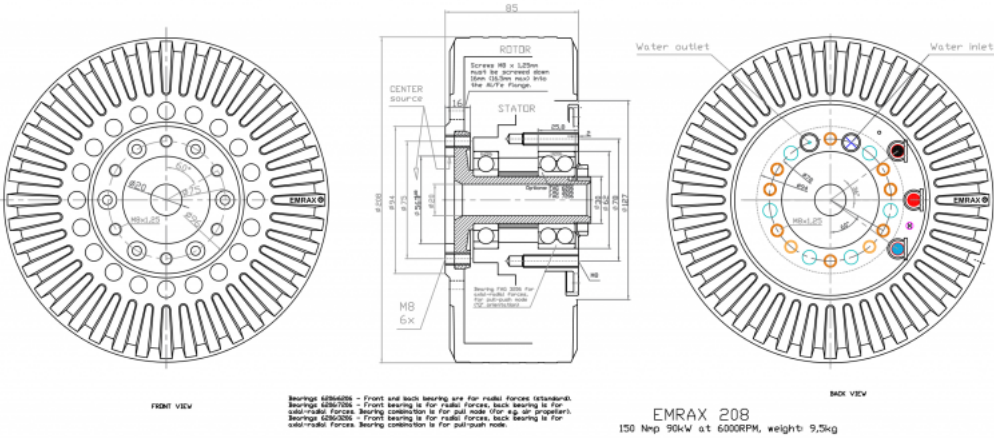


Figure 20: Emrax 208 motor diagram.

The motor also meets our required specifications perfectly with:

1. 180Nm of peak* torque (80Nm continuous)
2. 7040rpm maximum peak* speed (6000rpm maximum continuous speed)
3. 80kW of peak* power (40kW continuous)
4. Entirely liquid-cooled and IP65 rated (water-glycol cooling)
5. Very high efficiency of up to 98%
6. Not low cost, but affordable at £3,200 per motor

*for 2 minutes at cold-start, or 10 seconds at hot-start

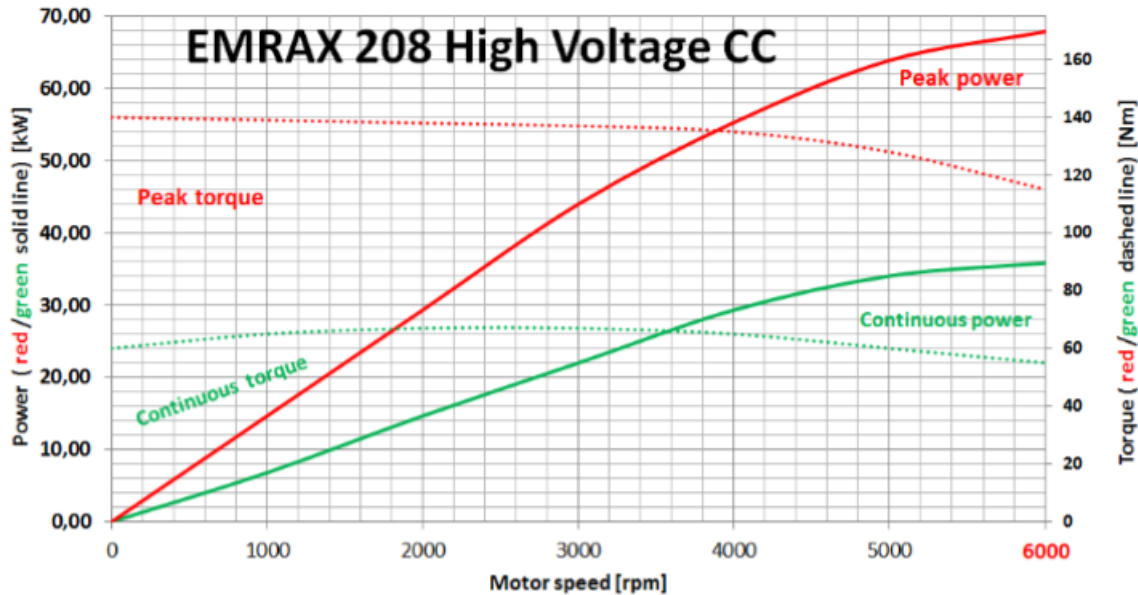


Figure 21: Emrax 208 motor performance curve.

The manufacturer offers three different winding options: low voltage (125V), medium voltage (320V) and high voltage (470V). It was decided that the 320 V medium voltage option would work best to optimise battery sizing within the chassis, lower the current that needs to flow in the system, but also keep high voltage dangers such as arcing to a manageable degree. Furthermore, there are three cooling options: air cooled; combined air and liquid cooled; and liquid-cooled. Because of the low pressure environment in the tube, the purely liquid-cooled version was chosen - additionally, Emrax have been made aware of the vacuum environment that the motors will be used in and agreed to manufacture the motors to fit for this purpose.

The cooling system passes liquid coolant around the motors and through the controllers and then pumps it around the chassis of the pod. This allows the heat to be removed from the motors and controllers and then dissipated throughout the pod in order to keep the motors at a safe and efficient temperature range during the operation.

The temperature range of the motor is from -40°C to $+120^{\circ}\text{C}$. There will be 8 litres of liquid coolant consisting of a 50/50 room temperature (30°C assumed) water/glycol solution flowing through the system per minute.

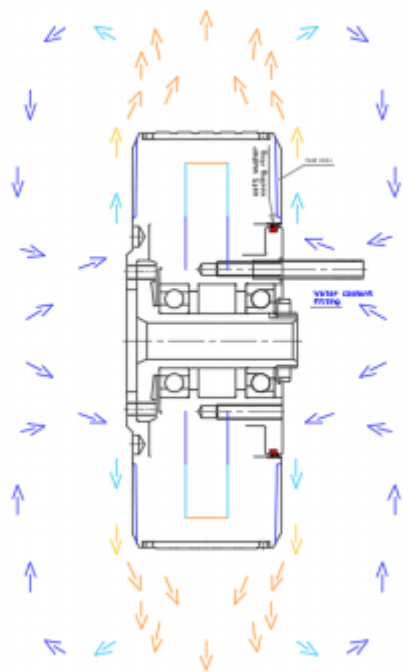


Figure 22: Emrax 208 motor cooling system.

The performance of the motors will be controlled by the emDrive H300 controllers, as recommended by the manufacturer. There will be one controller for each motor. More detail on the controllers is discussed in the motor control section.

The table below compares the motor choices discussed in this document to further clarify the reasons that the Emrax 208 motor was chosen.

Table 3: Table comparing motor choices.

	AC35	APS 20080	APM200	YASA- 400	EMRAX 208
Type	Induction	BLDC	PMSM	PMSM	PMSM
No. of motors	4	4	1	2	4
Torque per wheel (Nm)	175	71 (gearbox required)	112/618*	180	180
Peak speed (rpm)	8000	6000	10000	7500	7040
Rated power per wheel (kW)	47	45	55	45/90**	40/80**
Total rated power (kW)	188	180	220	180/360**	160/320**
Liquid cooling	Only on custom order	No	Yes	Yes	Yes
Power density (kWkg ⁻¹)	2.47	5	6.875	3.75	8.5
Peak efficiency (%)	86-90***	Unknown	Unknown	95-97***	96-98***
Price per wheel (£)	2500	1400	Unknown	5000	3200
Fits inside chassis C-beam	No	Yes	No	Yes	Yes

*without/with gearbox **continuous/peak ***depending on conditions such as ambient temperature and coolant composition, assuming coolant flow rate is as specified by the manufacturer

3.2.4 Motor Controllers

The team has chosen to use one motor for each of the four Halbach wheels, and there will be one motor controller for each of the four motors. The motor con-

trollers will be controlled with one microcontroller which will send a CAN bus signal to each motor controller.

The motor controller we have decided to use is the emDrive H300. The team chose this motor based on beneficial protective features and compatibility with our requirements. It is optimized for up to 120kW continuous and it is CAN bus compatible.

The system uses negative feedback to control and synchronize the motors. When the state machine is in the acceleration or deceleration phase, the navigation system will relay translational velocity data to the motor control microcontroller. The control system will use the data to calculate the optimal slip ratio, and from that the desired rpm. The system will then use rpm feedback from the motor sensors to calculate adjustments for each individual motor, and factor this into the desired rpm calculation to ensure the motors are synchronised. These calculations will be carried out continuously on the microcontroller which will also calculate the voltage parameter, and it will be fed through the CAN bus to each motor controller which will control the motor torque and speed.

The motor controller has built in thermal protection for both the motor and controller itself. It also has motor stall protection, low and high battery voltage protection and hall sensor failure detection and safe shut down. We will add other safety features that will transmit a critical error to the state machine if certain criteria are not met, such as: motors are not synchronised to a certain degree, loss of connection to any motor or any other loss of connectivity in the system.

If the system receives a critical fault message i.e. state of the system changes to “stop”, we will kill all power to the motor contactor.

The graph below shows the rpm against displacement, which shows the acceleration and deceleration phases of the motors. The motors will be in the acceleration phase until 7000rpm, at which point the system will change to the deceleration state by sending the appropriate signal to the motor controllers and the slip speed will become negative.

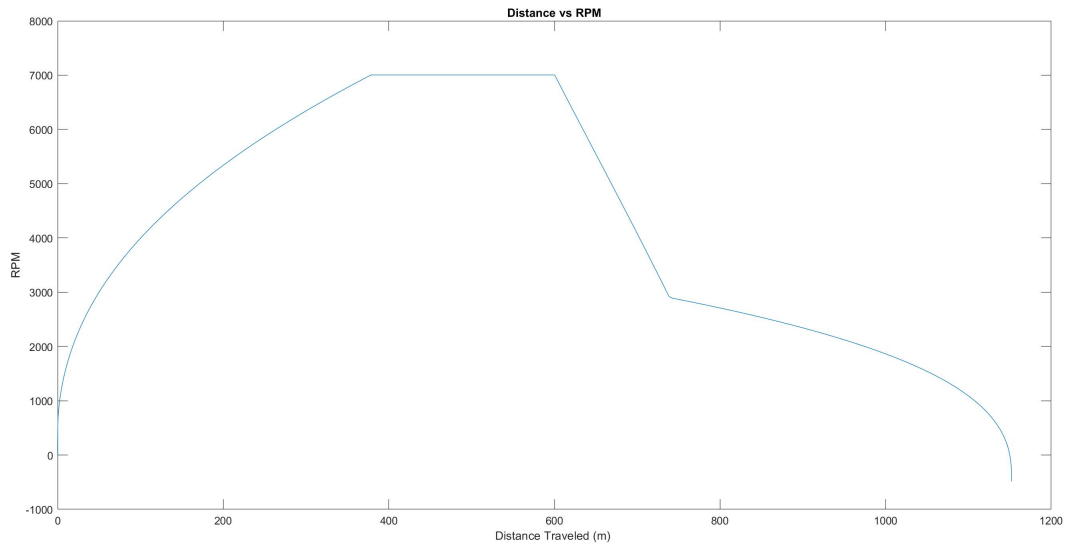


Figure 23: rpm against displacement.

Each controller takes up 230mm × 245mm × 126mm of space and weighs 7.5kg.

3.2.5 Safety

When any of the four motors, control or power systems fail, the emergency braking system will engage. General emergency breaking scenarios are the following: overheating of motors or controls, physical warping or breakage, control system malfunction and desynchronization of the motors, dislodging of the motor from the chassis and complete loss of power.

Overheating

The primary issue of overheating in any motor is short circuiting of the windings. The Emrax 208 is tested at a maximum amperage of 320A. A high current fuse will prevent a short circuited motor from drawing too much current. Detection of the fuse breaking will result in immediate loss of power and therefore application of the emergency brakes.

Physics Warping or Breakage

Physical warping of the rotor of any motor will result in oscillations that can be detected using 3-axis accelerometers that can be placed on the stator. Warping in

the stator can be detected using thin-film strain gauges. These can be planed at critical points around the stator as well as all around the motor. Detection of rotor warping will be based on data from the controller. Data such as inductance and back-EMF will be useful in this regard. The Emrax 208 is an axial flux synchronous motor where the stator electromagnets are wound on a plane that is perpendicular to the motor axle. Many such layers of electromagnets are sandwiched between similar planes that house permanent magnets. When an inductor of any kind (such as an electromagnet) is placed inside a magnetic field, the inductance of the coil lowers by a predictable amount (this depends on the physical aspects of the coil and the strength of the magnetic field). When warping occurs in the rotor, the oscillations may move the rotor (and therefore the permanent magnets along with it) closer or farther from the electromagnets. Such movement can potentially change both inductance and back-EMF readings from the baselines that were set during testing. While this method should not be used as a primary means of determining when to brake, it can be used in tandem with the accelerometers and strain gauges. Furthermore, for post-scenario analysis where vibrations occurred, recorded back-EMF and inductance data can be used to determine whether the motors were at fault or whether the vibrations occurred by some other means.

Control System Malfunction and Desynchronisation

The high power system will be fitted with high amperage fuses. In the case of semiconductor breakdown in the controller, the fuses in place will trigger the emergency brakes to engage, while cutting power to the motors. In the event of malfunctioning sensors, contactors will allow for power to be cut to the motors by a control signal. Sensor malfunctions can be identified through software readouts (on rpm, accelerometer) in correlation with motor warping or breakage. In the event of complete power loss to the control system, power to the main contactor will also be lost, which will result in power loss to the propulsion system as well - emergency braking is activated in this case.

Dislodging of motors from chassis

It is possible that the motors may dislodge themselves from the pods chassis while still being able to spin freely. Gyroscope data can be used to tell the orientation of the motor in such a situation. What can also be used (as this does not require the addition of a gyroscope sensor), is load detection through back-EMF readings from the controller.

Vacuum compatibility

The motors are fully liquid-cooled and sealed, therefore do not require the presence of airflow for optimal operation. Due to the partial vacuum in the tunnel, windage losses within the motor are expected to significantly reduce, somewhat improving the efficiency of the motor. The manufacturer has been made aware of the environment that the motors will be operated in and promised to deliver motors that will be able to perform in this environment as specified in their datasheet. Care will be taken when installing liquid cooling piping so that a solid seal is kept. The motor controllers connect to the control system with an anti-vibration, waterproof locking connector to ensure the connection does not get interrupted. The connector is detailed below.

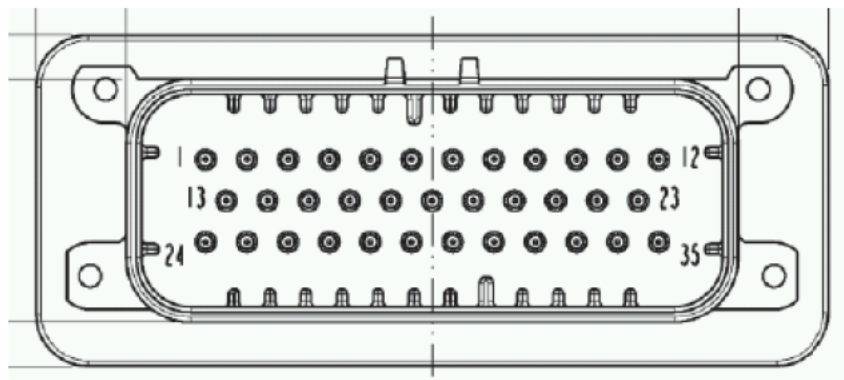


Figure 24: Motor to controller locking connector.

3.2.6 Scalability

In a commercial full-scale pod, a custom motor designed specifically for use with Halbach wheels in a vacuum environment is likely to be developed. The following section begins the design and prototyping of such a motor - although this motor prototype will not be used in the competition this year due to limited time to reliably develop a motor that could compete with the Emrax 208.

Custom Motor

Hyperloop pods require very specific properties from their motors. As seen previously, the torque requirement for 1g acceleration follows a steadily decreasing torque curve (and an increasing curve for deceleration). While the Emrax 208 does meet all these criteria, a motor specifically designed for Hyperloop can be

conceived — one that better meets the specification criteria while optimising for simplicity in design. The Hyperloop calls for motors that are ideally flat or pancake shaped, with high torque, midrange peak rpm, and designed with a vacuum environment in mind. Particularly the vacuum environment allows for a different design mindset - motor efficiency and acceleration would actually become higher due to no windage losses, but heat dissipation to the environment is also non-existent. Initial specifications can be found below:

1. Outrunner configuration
 - (a) Rotor on the outside — for torque and easy attachment to H-wheels
2. Input wattage: $\sim 40\text{kW}$
 - (a) 114A @ 350V
3. 3-phase winding configuration
 - (a) WYE (STAR)
 - (b) AaABbBCcCAaABbBCcC
4. Rotor and Stator:
 - (a) 20 rotor poles — 40 magnets for Halbach configuration
 - (b) 18 stator armatures
 - (c) Winding factor: 0.93301 (closer to 1 is better, and this is very good)
5. Permanent Magnets for Rotor:
 - (a) $40 \times$ Grade N52, 1.44T, 12.7mm \times 12.7mm \times 12.7mm.
6. Motor Physical Dimensions:
 - (a) Rotor Inner Radius: 8.09cm
 - (b) Rotor Outer Radius (excluding gearing and rotor assembly): 9.36cm.
 - (c) Height:
 - i. Of stator core: minimum 3cm
 - ii. Total (Including rotor): Depends on stator — stator height + at least 4cm for mounting
7. Wire specs:

- (a) Wire diameter: < 0.812mm (< 20AWG)
- (b) Braided wire: To deal with high current and the fact that the internal resistance will have to be fairly low (due to input current and voltage being very close to each other), winding with 4 or 5 wires in parallel to the source will allow for better handling of the high current

Such an electric motor can be made so that the stator armatures are towards the outside leaving the inside empty. The following images shows an example of what such a motor would look like (though does not exactly match the specifications listed above and all components are not to scale;). The green components represent stationary ones, and the red components represent rotating ones. To leave the inside exposed, large ball bearings would be required. The stationary and rotating parts of the ball bearing are represented in dark green and dark red.

Cooling ducts can be attached to the exposed area of the stator, and control devices can potentially be put in the same area. This is an outrunner configuration motor — where the rotor spins on the outside of the stator. For Hyperloop applications, attaching a Halbach wheel on the outside of the rotor means that this kind of motor can be mounted directly underneath the I-beam, without the need for separate mounts for the motor and Halbach wheel. See Section A.2 for figures.

Prototype Motor

As a proof of concept and for testing various types of wires and winding configurations, a prototype electric motor was designed using 3D printed parts. This prototype is an outrunner motor similar to the planned full-size motor; however, it is smaller and more compact. The design is also modular, allowing for the stator to be completely swapped, as well as the stacking of multiple motors on top of each other so as to test a variety of stator designs. The rotor consists of 10mm cube N48 magnets arranged in a Halbach array — similar to the Halbach wheels used for propulsion. This motor has 12 stator armatures and 14 rotor poles (28 individual magnets). The frame for the Halbach wheel is made from five 2mm laser-cut acrylic sheets sandwiched together. The rest of the frame was 3D printed using PLA. The stator armatures include permeable steel cores and are wound with 30 turns of 20AWG wire each. The winding configuration is WYE (star). The stator rod is stationary and is made from a 8mm outer-diameter hollow aluminum rod with 2mm walls. The windings have a line resistance of roughly 0.33 ohms. See Section ?? for a further figure.

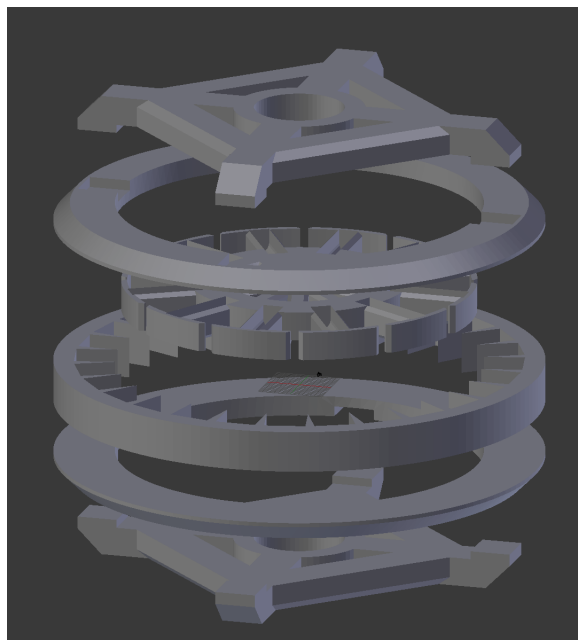


Figure 25: Prototype Motor CAD Assembly.



Figure 26: Prototype Motor Rotor Magnets.

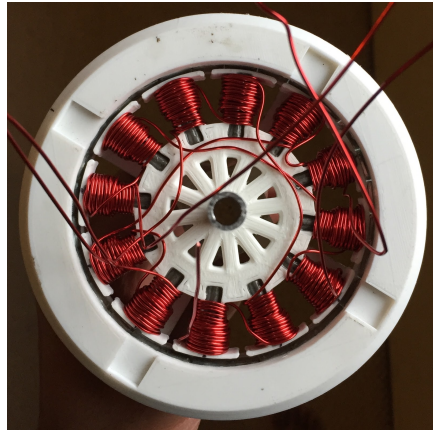


Figure 27: Prototype Motor Full Assembly.

3.2.7 Cost Breakdown

The Emrax 208 motors are purchased to order directly from the manufacturer. The standard cost of the Emrax 208 motor with liquid-cooling, shaft position sensor, motor shaft and angled coolant fittings is 3800. After communication with the manufacturer, a 5% discount was offered, bringing the price down to 3610 - at the current exchange rate, this is approximately £3200 per motor.

The team has contacted the manufacturer of the controllers, emDrive asking for a quote, as well as sponsorship. The price quoted per controller comes out to approximately £2000 per controller.

3.2.8 Testing

The majority of motor testing will be done alongside motor controller testing, as the two components are mutually required.

The first tests done will be simple off-load speed control tests. The motor will be spun up and the ability of the control system to control the speed of the motor is tested. Next, the same tests will be done with motor, controller and cooling system in a vacuum chamber. The performance and efficiency of the motor will likely change under vacuum conditions and the control system will have to be optimised so that the real speed of the motor will reflect the control system calculations.

The power engineering laboratories at the University of Edinburgh will be utilised to perform load testing of the propulsion system. The motors will be connected

to a generator to measure their maximum power output, maximum torque output and maximum full-load speed. Once ample load testing has been done, the same tests will be performed, but the power input will be rapidly cut at various speeds of the motor - any potential damage to the controllers or motors will be observed.

3.2.9 Timeline

Lead times on the Emrax 208 motors are 6 to 8 weeks according to the manufacturer. Two motors have been ordered as per submission of this document, with an exact shipping date to be still confirmed - however this should be early in March at the latest. The majority of in-house testing can be done with just two motors - the latter two will be ordered once the real-world suitability of the motors has been confirmed. Expect arrival of the next two motors in early May.

Testing will be first done on controlling the speed of the motors with no load connected. Next, the same tests will be performed with the motors in a vacuum chamber - any measured difference in performance can hence be accounted for. Following will be careful tests of the liquid cooling system in a vacuum chamber. Next, load and torque testing will be performed at the University of Edinburgh's power engineering laboratories. Once ample testing has been done, the motors can be mounted on the chassis of the pod. All motors are expected to be mounted on the chassis of the pod by early June.

3.3 Cooling

3.3.1 Introduction

Due to state of the art power density of the motors and motor controllers used, a liquid-cooling system is required even for the short runtime of below 30 seconds. All four of the Emrax 208 motors, as well as all four of the emDrive H300 controllers need to be continuously cooled when running. Both the motors and the controllers are fitted for liquid-cooling — they simply need to be attached to a system of hoses, pumps and reservoir.

3.3.2 Summary

A coolant flow rate of 8 litres per minute is supplied to each motor and controller. The coolant composition is a 50/50 water/glycol solution. Coolant tubing with a diameter of 10mm is used - it is assumed that the length of tubing to each component is 2m. It has been calculated that to stay within the coolant temperature limit specified by the manufacturers, a total coolant volume of 12.6 litres is required. This coolant will be delivered at the desired flow rate of 8 lmin^{-1} to each component

by a 12V DC pump. With a total of 8 pumps (4 motors, 4 controllers), the power consumption of the cooling system comes to 96W.

3.3.3 Chosen solution

Following the recommendations of Emrax for their 208 motor, a coolant flow rate of 6 to 8 litres per minute is required, with a 50/50 water/glycol composition, assuming a coolant temperature below 50°C. The maximum rated temperature the Emrax motors is 120°C and there is a built-in temperature sensor. Similarly for the emDrive H300 controller, a coolant flow rate of 8 to 10 litres per minute is required - however this is specified for a coolant temperature of below 60°C for a 50/50 water/glycol solution. The controller monitor the temperature of the motors.

Following the flow rates specified by the manufacturers, a flow rate of 8 litres per minute is chosen for every component that requires cooling (4 motors, 4 controllers).

A worst-case assumption is made that the cooling tube length to each component is 2 m long at 10 mm inner diameter. This is the maximum tube length that the manufacturer's specifications hold for. In reality, the length of the tubes will be tested and optimised while testing and fitting the propulsion system. The tubing used can be seen on the figure below.



Figure 28: Cooling tube.

The largest limitation to the cooling system is the volume of coolant carried on-pod. It is simple to cool all components adequately if a large volume of coolant is available, however, any additional coolant increases the weight of the pod, thereby reducing acceleration. Furthermore, space on board is limited and liquid coolant takes up a large volume. The cooling system is therefore designed such that in the worst-case power draw (and therefore heating) of the motors, the coolant heats

up by approximately 30°C - assuming an ambient temperature of 30°C during the competition, this would mean a peak coolant temperature of 60°C, or the same temperature that the motor controllers have been tested for.

The worst-case scenario assumes that the battery pack outputs the maximum power it can supply continuously for 30 seconds - this means a continuous discharge current of 800A for 30 seconds, or 200A per motor. This supplies each motor a power of approximately 63kW for this 30 second run. A motor efficiency of 92% is assumed, which is the lowest value according to the manufacturer. The specific heat capacity of a 50/50 water/glycol solution at 30°C ambient temperature is approximately 3200J/g°C. Taking the above into consideration, a coolant volume of 1.575 litres is required per motor and per motor controller. The total coolant volume required is therefore 12.6 litres. With the longest possible tubing length, approximately 1.2 litres of this would be spread in the tubing, as well as some extra within the internal cooling pipes of the motors and controllers. Taking into account that the coolant tubing may be cut shorter in the future, two coolant reservoirs with a volume of 6 litres each are chosen - this is so that there is a separate reservoir for each physical Halbach module.

To meet the coolant flow rate requirements, a small DC pump is used for each component that requires cooling. These pumps will be powered from the low power system, so that cooling continues even as the propulsion system loses power. As such, a small DC water pump with an operating voltage of 12V, power consumption of 12W and maximum flow rate of 12 litres per minute is chosen, as shown on the figure below. As there are a total of 8 such pumps, the total power consumption of the cooling system is 96W.



Figure 29: Cooling pump.

Real-world testing with the motors and controllers will allow us to optimise the cooling system further and minimise the coolant volume carried. It is likely that tests with real motor loads and pre-cooled coolant (that has been allowed to rest in the reservoir for 30 minutes before a vacuum is applied, as could happen during the competition) will reveal that a lower coolant volume will keep the system operating within the 60°C coolant temperature limit. Such tests will be performed with thermal cameras, as well as temperature sensors in the coolant. However, the higher ambient temperature of California compared to Scotland has to be taken into account. Thus, the optimal coolant volume calculated from tests done in Scotland will be increased by 50%.

The manufacturer states that the DC pump is waterproof, and is therefore sealed. However, the vacuum compatibility of the pump has not been proven. As of the submission of this document, the pump has not been delivered to us. As soon as it arrives, the pump will be tested in a vacuum chamber to pump water through a closed loop pipe and observed for any leaks or malfunctions. If any problems are found, another model has to be tested and researched until a compatible model is found.

3.3.4 Safety

The cooling system is integral to the propulsion system. If a fault at any point in the cooling system is found when doing a pre-start check-up, launch will be halted. Failure of the cooling system during the run would not have immediate catastrophic results, but would damage the motors and controllers if left uncooled for more than a few seconds. If the cooling system were to fail very soon after the pod takes off, it is possible that due to excessive heating of the motors and controllers, primary braking can no longer be performed adequately. The control system is able to detect that deceleration of the pod is not happening, or that communication with the motor controllers has failed — in this case, emergency braking is activated through software. Furthermore, the Emrax 208 motors have a KTY81-210 temperature mounted into the stator. This allows the control system to easily detect if a motor is heating significantly - motor temperatures of above 110°C constitute a critical failure that will result in emergency braking. In the case that both the cooling and control systems fails, emergency braking automatically activates due to complete power loss - as the emergency braking is activated, the propulsion system power is disconnected through an automatic contactor shut-off.

3.3.5 Cost breakdown

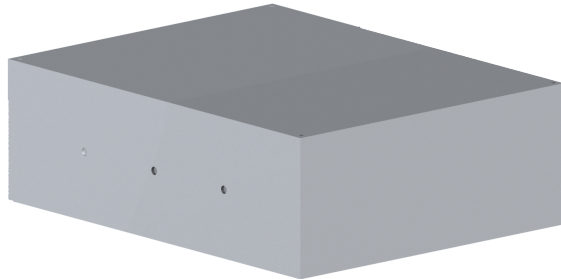
Table 4: Cost Breakdown for cooling system.

Component	Amount/Quantity	Cost
Tubing	16 m	£32
12V DC pump	8	£184
12 litre reservoir	1	£23
Total		£239

3.3.6 Timeline

The cooling system follow the same timeline as the motors, as it cannot be tested effectively without them. Components for the cooling system have been ordered together with two of the Emrax 208 motors in early January. Testing will likely begin in early March at the latest, when the motors are expected to arrive - half of the cooling system can be tested at this time. The rest of the cooling system can be put to a test in early May at the latest, when the other two motors are expected to arrive.

4 Power



Power systems are responsible for safely and efficiently providing power to components on the pod that require it. All energy on the pod is provided in the form of battery packs. The pod is designed in a way that there are two isolated power systems — low power, which is used for powering electronics; and high power, used solely for powering the propulsion motors. There are a total of three battery packs, as there is a redundancy backup battery for the critical low power electronics power system. There is no redundancy high power battery pack due to its large size and weight — a failure in this system results in activation of emergency braking.

4.1 Battery Cells

4.1.1 Introduction

There are several important factors to take into account when choosing the battery cells used in the pod, mainly:

- **Safety:** As the Hyperloop is ultimately a transportation medium, it is crucial that a high standard of safety is met when choosing the battery cells.
- **Vacuum compatibility:** The cells should be able to operate in a vacuum environment, so that it is not necessary to create a pressurised vessel for them. This is not only more economical, but also safer, as the pressurised battery vessel is a point of failure. Putting the battery packs in the passenger pressure vessel would be a potential safety hazard for the passengers.
- **Durability and reliability:** The battery cells do not only need to survive in a vacuum environment, but also operate under considerable vibrations

during rapid acceleration and deceleration. For the reasons of scalability, it is desirable that the battery cells will sustain their performance for several demanding cycles without significant losses.

- **Working temperature range:** The Hyperloop will need to be able to operate in different climates, in different seasons. Ideally, the same battery cells could be used on Hyperloop pods across the globe. Furthermore, heat dissipation does not work as well in a near-vacuum environment, so the battery cells will heat up faster if no cooling is provided.

Due to the different nature of their application, it makes sense to choose different battery cells for the high power and low power systems.

4.1.2 Considered Solutions

High Power

Besides the above mentioned requirements, the main requirement for the high power system battery cell is maximum power density. Generally, electric vehicles aim for high energy density, so that the propulsion system can be powered for the longest time possible given minimum battery space. For the purposes of this competition, and arguably Hyperloop in general, power density takes priority. Our pod will need to provide a large burst of power to the propulsion system for a short time during rapid acceleration, after which the pod coasts at an efficient passive levitation velocity, not supplying any power to the propulsion system (only the control system). The pod keeps coasting until its velocity drops out of the desired range, at which point another burst of power is supplied to the propulsion system. In the SpaceX competition, the pod will accelerate to its maximum velocity, then proceed to brake to a stop.

To minimise the size and weight of the high power battery pack, it is desirable to use the minimum volume of battery cells that can supply the peak power of the propulsion system with a safety factor of 20% or higher. Research has shown that any commercial lithium-based battery cell will have enough energy capacity to power at least two full runs in the SpaceX Hyperloop tunnel if it can supply the peak power requirement of the pod.

Lithium Polymer Pouch Cells (LiPo)

The most common choice for high power density battery cells are lithium-polymer (LiPo) pouch cells, which are popular in radio-controlled drones and airplanes. While the power density of LiPo pouch cells is hard to beat, they are extremely volatile. Being pouch cells, they are prone to punctures and other physical damage

if additional heavy-duty casing is not provided. A punctured or otherwise damaged LiPo cell will almost certainly no longer provide power, but there is a good chance of internal short circuit occurring due to the layered structure of pouch cells. An internal short circuit will cause rapid heating and expansion of the cell, potentially resulting in fire or a minor explosion. Without protection circuitry (or with faulty protection circuitry), an external short circuit would have much the same result. Furthermore, LiPo pouch cells have not been proven to be vacuum compatible. As all the materials are only sealed in a pouch, it is possible that the cell would expand once under vacuum, as the pouch is not strong enough to contain the expansion pressure. Test results by NASA show high variance between the performance of LiPo pouch cells from different manufacturers under vacuum conditions. However, four out of five cells tested did not pass vacuum chamber tests to a degree acceptable by NASA — where one of the tested cells expanded and stopped working after the first test [1].

Test	A	C	D	F	G
Vacuum	x	x	x	✓	x

Figure 30: Tests on LiPo pouch cells done by NASA.

Therefore in order to utilise lithium polymer pouch cells for Hyperloop applications, it is necessary operate them under atmospheric pressure, in a pressurised vessel. It was deemed that the additional weight and complexity associated with the pressure vessel would make LiPo (and other lithium-based) pouch cells a poor choice for Hyperloop.

Lithium-Ion 18650 Cylindrical Cells (Li-Ion)

The most widely used lithium-based battery cells in many industries. These are very well proven, scalable and vacuum-compatible battery cells that are significantly more robust than LiPo pouches due to their cylindrical metal casing. However, 18650 Li-Ion cells are generally optimised more for energy density than power density and have a much lower power density than comparable LiPo pouch cells. As a rule of thumb, it was found that LiPo pouch cells are roughly twice as power dense as equivalent Li-Ion 18650 cells. The decision was made to pursue other options further in order to find a battery cell with higher power density.

Prismatic Lithium Cells

Whether lithium-ion or lithium iron phosphate, prismatic cells are larger, higher capacity and higher current (therefore higher power) than the other types of cells looked at previously. Prismatic cells are very rugged and have been the standard for electric vehicles in the past. However, due to their increased size and ruggedness, they contain a lot of extra material in the form of casing and terminals. This makes their power density (per unit mass in particularly) poorer than the other choices looked at. This choice was therefore not pursued any further.

Lithium Iron Phosphate 26650 Cylindrical Cells (LiFePO₄)

Further research revealed a type of cylindrical cell often used in jump starters and high performance electric vehicle racing. It was previously discussed that there are several advantages to cylindrical cells that make them optimal for Hyperloop applications, except the problem previously was that the power density of Li-Ion 18650 cells is rather low. This type of high power density cylindrical cell is the lithium iron phosphate (LiFePO₄) 26650. 26650 denotes the dimensions of the cell — 26 mm in diameter, 65 mm in height. So these cells are the same height as 18650, just wider. Unlike Li-Ion, LiFePO₄ has a lower nominal voltage per cell — 3.3V instead of 3.6–3.7V; as well as a lower energy density — making LiFePO₄ uncommon in modern commercial electric vehicles. However with well manufactured cells, it is possible to safely get higher charge and discharge rates from LiFePO₄, as the internal chemistry is less volatile than Li-Ion. Furthermore, LiFePO₄ battery cells have a more consistent voltage throughout their discharge cycle. This specific type of battery has also been proven to be vacuum-compatible, with less than 10% worse performance under room temperature vacuum conditions, making them a strong choice for Hyperloop [2].

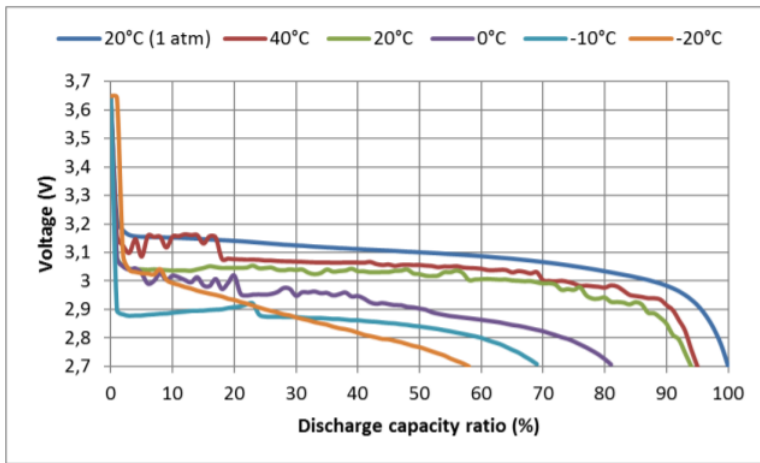


Figure 31: Battery cells performance in a vacuum chamber at different temperatures.

Several battery cell models with nearly identical specifications were looked at, the most trustworthy and well-known of which was chosen.

Low Power

The choice of the low power system battery cells is less critical than in the high power system, as size and weight are not a significant concern due to the low amount of total energy required. The total peak power consumption of all electronics on the pod is below 200W, with nominal power consumption at under 100W. For the sake of simpler battery management electronics, it is desired to minimise the number of battery cells in series — therefore, a higher voltage per cell is optimal.

In the case of the low power system, power density is of little concern if a lithium-based battery is to be used. The energy density or energy capacity is also not of extreme importance considering the time taken for a single run in the competition. However, as a convenience feature and to show a more realistic implementation of a Hyperloop power system, the capacity of the low power battery system is significantly oversized, so that frequent charging is not required. Also, in a real Hyperloop, the control electronics would be required to run without interruption, so a higher capacity makes sense. Considering the statements above, the lithium ion 18650 cylindrical battery cell type makes sense, as it is both higher voltage and higher capacity than the battery cells used in the high power system, while still retaining the vacuum compatibility and reliability associated with cylindrical cells.

4.1.3 Chosen Solution

High Power

This is the A123 Systems ANR26650M1-B LiFePO₄ Nanophosphate Cylindrical 26650 cell. This is a battery cell well known for its high power density and used by, for example, Porsche in their hybrid racing competitions.



Figure 32: A123 Systems ANR26650M1-B LiFePO₄ Nanophosphate Cylindrical 26650 cell.

The cells have a very impressive rated continuous discharge current of 70A, and 10-second peak discharge current of up to 120A. A table of specifications provided by the manufacturer can be seen below.

ANR26650M1-B Cell Specifications	
Cell Dimensions (mm)	Ø26 x 65
Cell Weight (g)	76
Cell Capacity (nominal/minimum, Ah)	2.5/2.4
Voltage (nominal, V)	3.3
Internal Impedance (1kHz AC typical, mΩ)	6
HPPC 10 Sec Discharge Pulse Power 50% SOC	200 W
Recommended Standard Charge Method	1C to 3.6V CCCV, 45 min
Recommended Fast Charge Method to 80% SOC	4C to 3.6V CC, 12 min
Maximum Continuous Discharge (A)	70
Maximum Pulse Discharge (10 seconds, A)	120
Cycle Life at 10C Discharge, 100% DOD	>1,000 cycles
Operating Temperature	-30°C to 55°C
Storage Temperature	-40°C to 60°C

A technical drawing showing three views of the cylindrical cell: top view, side view, and bottom view. The top view shows the diameter Ø12.90. The side view shows the height 65.15 with tolerances +0.50 and -0.00, and the diameter Ø25.85* with tolerances +0.30 and -0.30. The bottom view shows the diameter Ø15.00. A note at the bottom right says "DIMENSIONS IN MM". Below that, it says "* with sleeve 25.96 +/- 0.50 mm".

Figure 33: A123 Systems ANR26650M1-B LiFePO₄ nanophosphate cylindrical 26650 cell specifications.

The cells are available for purchase worldwide, have a power density not very far from lithium polymer pouches and high safety standards, which are arguably better than those of lithium ion. The team is confident that the A123 ANR26650M1-B will make an optimal battery cell for the pod.

Low Power

It was decided that the LG HG2 Li-Ion 18650 3000mAh 3.6V cylindrical cells would be used for the low power system. These are the same battery cells that were used by the team in the SpaceX Hyperloop Pod Competition II last year and were tested and approved by SpaceX engineers present at the competition.

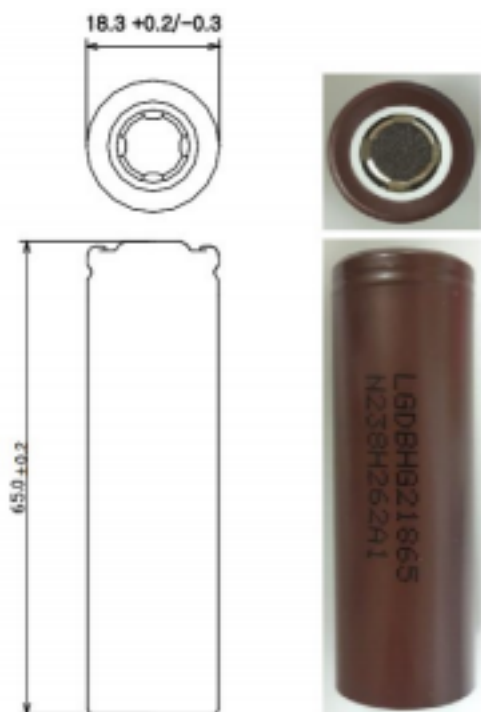


Figure 34: LG HG2 Li-Ion 18650 3000mAh 3.6V cylindrical cells.

Detailed specifications provided by the manufacturer can be seen below in Figure 35.

Type	Specification	Actual
Chemistry	Li[NiMnCo]O ₂ (H-NMC) / Graphite + SiO	
Dimensions (mm)	Diameter	18.3 +0.2 / -0.3 mm
	Height	65.00 ± 0.2 mm
Weight (g)	Max. 48	44~45
Initial IR (mΩ AC 1kHz)	Max. 17	14~16
Initial IR (mΩ DC)	Max. 30	24~26
Nominal Voltage (V)	3.6	
Charge Method	Nominal : 1.5A 4.2V, 50mA End-current (CC-CV)	
	Fast : 4A 4.2V, 100mA End-current (CC-CV)	
Charge Time	Nominal (min)	165min
	Fast (min)	85min
Charge Current	Nominal Current (A)	1.25A
	Max. Current (A)	4A
Discharge	End Voltage (A)	2V
	Max. Current (A)	20A (Continued discharge current)
0.2C Capacity	Nominal (Ah)	3.0 Ah
Energy Density	Nominal (Wh/kg)	240

Figure 35: LG HG2 Li-Ion 18650 3000mAh 3.6V cylindrical cells specifications.

4.1.4 Safety & Testing

High Power — A123 ANR26650M1-B

The manufacturer provides results from abuse tests including nail penetration, external short circuits, over-discharge, physical crushing of the cell and thermal stability. All the tests resulted in a pass, as shown in the figure below.

Abuse Test	Result
Nail Penetration	Pass—EUCAR 4
Over-discharge	Pass—EUCAR 3
Thermal Stability	Pass—EUCAR 4
External Short	Pass—EUCAR 3
Crush	Pass—EUCAR 3

Figure 36: Abuse tests on A123 ANR26650M1-B cells.

Other available test results show the full-cycle performance of the battery cell at various continuous discharge currents, up to 60A.

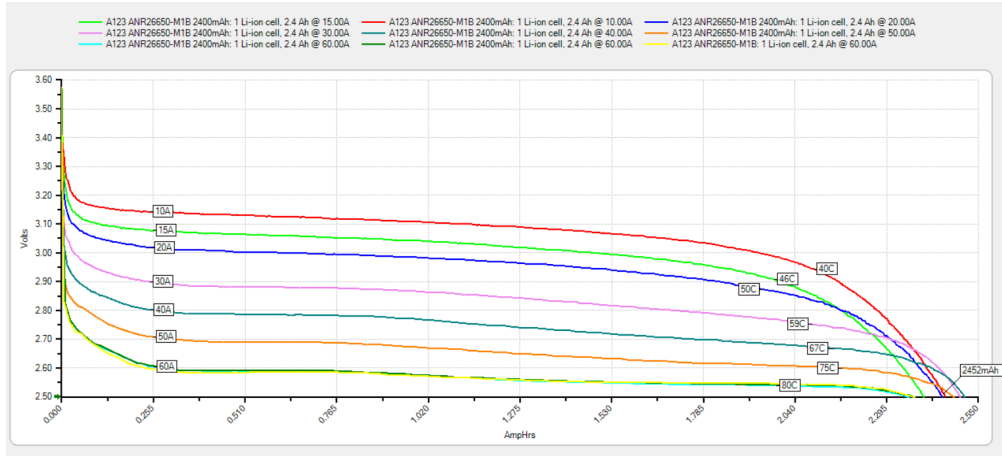


Figure 37: Full-cycle performance of the A123 ANR26650M1-B cells.

It can be seen that the consistency of the cell's performance does not suffer significantly with higher discharge currents, but there is an increased voltage drop at high discharge rates, which is to be expected and can be accounted for in further calculations. Similarly with pulsed discharge currents, performance remains consistent, but voltage drop increases with discharge rate, as in Figure 38.

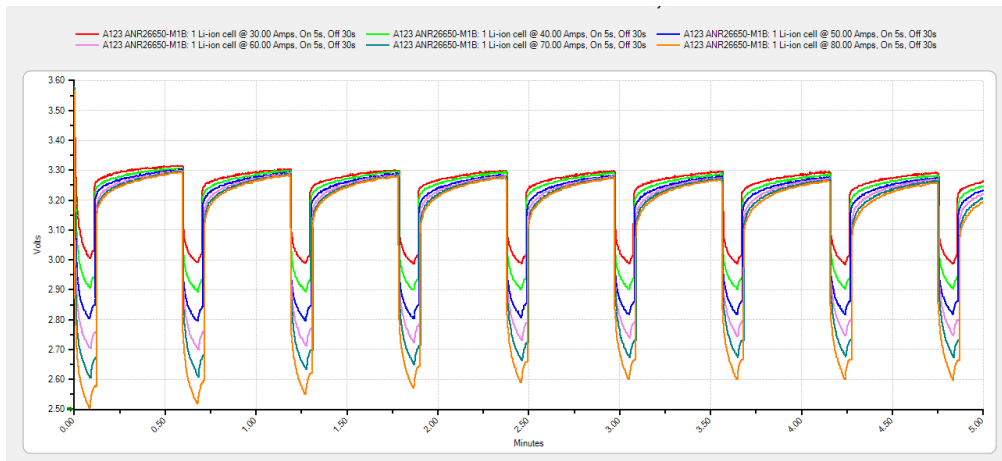


Figure 38: Pulsed discharge current performance of the A123 ANR26650M1-B cells.

The manufacturer states an internal resistance of $10\text{m}\Omega$ and a maximum discharge current of 120A for 10 seconds. Tests done in-house with power resistor loads and clamp-on ammeters show that a discharge current of 100A can be sustained for up to 1 minute while satisfying the recommended operating temperature and cell voltage. In our calculations, 100A is assumed as the maximum available discharge current to provide a safety factor on the stated 120A. During the run, peak power will only be drawn for the first few seconds when starting the motor, then at a later time, for a few more seconds when rapid deceleration braking is activated.

Considering the paragraph above, a worst-case temperature increase of a battery cell is approximated for the following scenario: 100A is drawn from each battery cell continuously for 30 seconds, where 30 seconds is over the maximum expected runtime of the propulsion system. Using the manufacturer's data, this would result in a temperature increase of at most 18°C above a 25°C ambient temperature on the aluminium casing of the cell, assuming there is zero heat dissipation to the environment (perfect vacuum) — still well within the operating range of up to 55°C . Furthermore, the actual continuous load on the battery cells will be significantly lower and the cells will be able to dissipate some heat into the environment (partial vacuum), as well as the copper plates used to interconnect them.

Low Power — LG HG2 18650

The team feels confident in the reliability and Hyperloop compatibility of these battery cells following the experience of using them as our primary energy source during last year's competition.

It was previously mentioned that there will be a backup battery pack for the low power system — this battery pack will utilise the same battery cells and operate at the same pack voltage.

Seeing as in the main low power battery pack, there will be 3 cells in parallel → there will be less than 2A drawn from any cell at any time. This is far below the maximum rated current of the cells, so heating of the low power battery cells during the run is not an issue. Test data from the manufacturer shows a highly efficient discharge curve at this load level, as shown in the figure below.

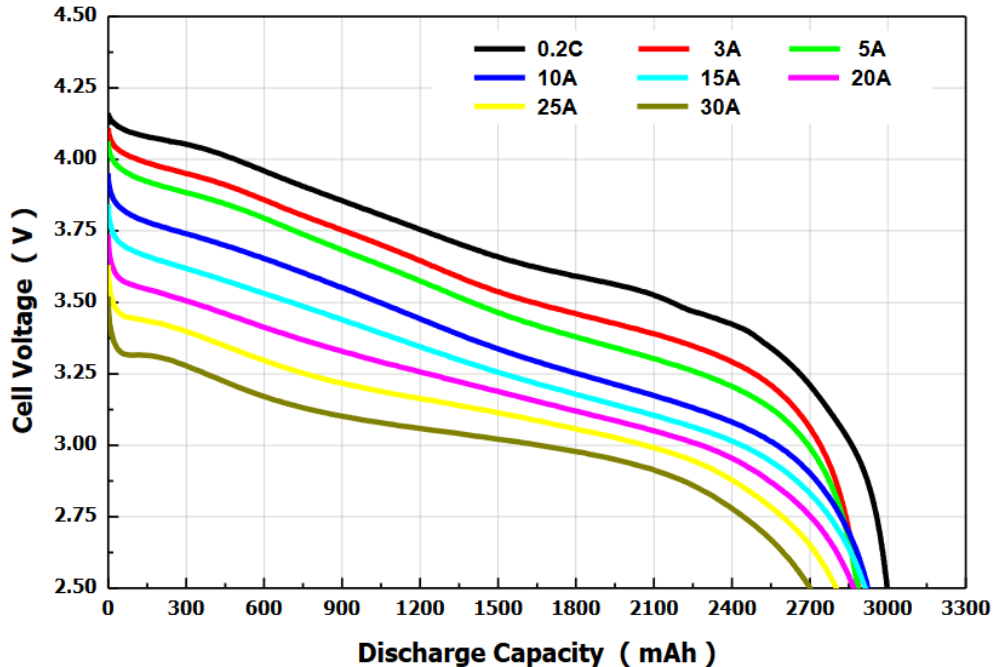


Figure 39: Discharge curve of LG HG2 18650 cell.

The manufacturer has tested the battery cells for high temperature storage (60°C), thermal shock — -20°C to 65°C and vice-versa), drop test (3 drops from 1m height), vibration test (90 minutes with frequency sweep), overcharge (3 times maximum charging current at 4.2 for 7 hours), external short circuit (0.1 Ω wire across terminals for 1 hour), overdischarge (to 250% of minimum capacity), high temperature (130°C oven for 10 minutes), crush test and impact test. None of the tests resulting in explosions, fire or leakage. After the tests, some battery cells experienced a drop in capacity.

4.2 Battery Management Systems

4.2.1 Introduction

When using lithium battery packs, it is necessary to consider some kind of security mechanism to protect the cells. This is where the Battery Management System (BMS) comes in. This is a system that monitors individual battery cells, as well as the battery pack as a whole, and manages the safe charging and discharging of the battery pack.

The team has chosen three separate BMSs as there are three battery packs. The pod will have two small BMSs for the two low power battery packs that will provide power to all the electronics (the second battery pack is a backup), and a bigger BMS for the high power battery pack that will provide power to the propulsion system.

A quick reminder:

The main battery pack that will power the electronics will contain 7 cells in series and 3 cells in parallel. As it is important that the electronics must not encounter any alimentation problems, there will be a backup battery pack composed of 7 cells in series and 1 cell in parallel. There will only be one battery pack to power the propulsion system. It will have 96 cells in series and 8 cells in parallel.

Data Managed

Data managed by the BMS includes the total pack voltage which varies between 19.6 volts and 29.4 volts for the small battery packs and varies between 259.2 volts and 345.6 volts for the big battery pack, as well as the voltage of each individual cell in series in all battery packs. Next, the total output current of each battery pack is measured through a current sensor rated at the maximum output current of each battery pack — this is 30A for the backup low power battery pack; 90A for the main low power battery pack; and up to 960A for the high power battery pack. Surface temperature of the battery cells in all battery packs is also monitored. Finally, the state of charge of each series cells, as well as the battery pack as a whole is continuously monitored.

4.2.2 Chosen Solution

Low Power

The BMS chosen for this battery pack is the 12-cell Lithium BMS Module, provided by ZEVA (Zero Emission Vehicles Australia), an innovative technological company that develops a range of custom electronic devices for electric vehicles.

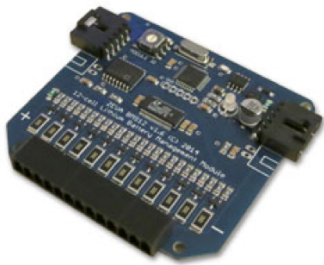


Figure 40: ZEVA BMS

Some important features:

- Cells managed: 4-12 lithium cells per module
- Maximum total voltage: 60VDC
- Compatible chemistries: LiFePO₄, LiCo (LiPo), LiMn
- High, low and shunt voltage thresholds: Configurable, 0-5000mV
- Accuracy: Within 0.25% (>10mV)
- Operating temperature range: -40°C to 85°C
- Pack balancing: Timed 30Ω shunts (~120mA, up to 1hr)
- Temperature sensing: Dual 100KΩ NTC thermistors
- Cell quiescent current draw: 1.6mA (idle) 2.2mA (when sampling)
- CAN power supply: 12V nominal (7-16V range), 20mA
- CAN bus specification: 250kbps 29-bit IDs (CAN 2.0B)
- Dimensions: 72 x 66 x 10mm (plus plugs)
- Weight: 35g
- Price: AU\$145.00

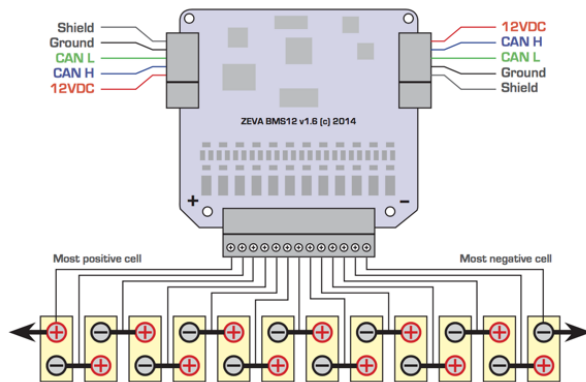


Figure 41: Typical wiring for BMS module

This particular BMS was chosen for our purposes because of its small dimensions, 72mm×66mm×10m, its light weight of 35g and it's CAN 2.0b interface which allows for central monitoring of battery status. Finally, it's designed for li-Ion and 7s configurations.

High Power

As the previously chosen BMS is not good enough to monitor the high power battery pack, another BMS is considered. The Orion BMS, designed and manufactured by Ewert Energy Systems, inc which is a research and development company focusing on developing solutions for plug-in hybrid and electric vehicles, is a much more professional BMS.

Some important features:

- It is capable to measure up to 108 cells in series based on the configuration.
- It performs passive cell balancing.
- It calculates the state of charge.
- It calculates the discharge current limit and charge current limit.
- It can measure the cell voltages between 0.5 volts and 5.0 volts.
- It can monitor the temperature of the cells.
- It uses Dual CANBUS 2.0B interfaces.
- Price: \$1,285



Figure 42: Orion BMS

The Orion BMS is able to adequately monitor all the series cells of the high power battery pack simultaneously. It is able to monitor all the required data discussed previously, as well as send it all through CANBUS 2.0B. In addition to this it performs passive cell balancing. However, it standard enclosure's dimensions are 240mm×174mm×82mm, and it weighs 2.427 kg.

Therefore, because of its size and price, this BMS was not a viable option for

the small battery pack. But it will be needed for the battery pack that powers the propulsion system.

4.2.3 Considered Solutions

VRUZEND, 36V 10s Battery Management System:

This BMS would have been ideal for the small battery pack if it had a CAN-BUS communication protocol. It is designed for Li-Ion cells, it is only 10.9 cm x 5.9 cm x 0.9 cm big, it only weights 0.15 kg and only costs USD\$29.99. Not very trustworthy-looking, and the seller would not respond to messages for over a month. A more reliable options was pursued.

JTT Electronics, S1 BMS Controller:

The reason why the team did not choose this BMS is because of the price: USD\$650. Otherwise it would have been a good option as it has CANBUS communication and allows Li-Ion cells in a very small and lightweight package, while also offering professional protection features.

TYVA Moduloo, TYVA BMS 6-25S:

Once again, the reason why the team did not choose this BMS is because of the price: 550€. This BMS would have been a great option because it is ultra-lightweight (50 grams), is very small (11cm×6.2×cm×1.5cm), and allows CAN-BUS communication.

Custom BMS

In last year's competition, the team used a custom battery *monitoring* system developed in-house, based on an Arduino Mega. This system monitored all the same data that above mentioned battery management systems do, but did not include management features such as cell balancing, and therefore required a balance charger to be used. When using a balance charger without a BMS, it is required to feed each series cell tap into the charger for balancing. This quickly becomes messy due to having to feed so many wires out of the pod — it was easier to simply take the entire battery pack out of the pod for charging. Last year, the largest battery pack had 7 Li-Ion cells in series, much fewer than this year's 96. Therefore, using an external balance charger is highly undesired.

Furthermore, the team is aiming for a more professional design. While last year's Arduino-based system worked in the end, it could not match the reliability of professionally made BMSs — though this is likely due to the fact that it was built in a protoboard, rather than a PCB. On another note, the number of battery cells the

Arduino-based system can monitor is limited by the number of analogue inputs of the Arduino Mega — therefore, this system is not suitable for the high power battery pack of this year's design.

If time allows, last year's monitoring system will be expanded to include cell balancing, then soldered onto a professionally made PCB. Rather than using a full Arduino Mega, an equivalent Atmel chip would be put on the PCB with the rest of the system. This system will be carefully tested against the ZEVA BMS used for the low power battery system. The custom BMS will only be used if it is able to perform as consistently as the ZEVA BMS, and it will only be used in the low power battery system.

4.3 Power Systems

High Power

As discussed in previous sections, the A123 Systems ANR26650M1-B LiFePO₄ battery cells will be used, in a 96S8P configuration. This battery pack powers the propulsion system of the pod, consisting of 4 electric motors and controllers. The table overleaf summarises the critical specifications of the high power battery pack.

Battery Cell	A123 Systems ANR26650M1-B
Cell Chemistry	LiFePO4 (Lithium Iron Phosphate)
Cell Nominal Voltage	3.3V
Pack Configuration	96S 8P (96 series, 8 parallel)
Total Number of Cells	768
Pack Nominal Voltage	316.8V
Pack Capacity	6336Wh
Pack Maximum Discharge Current	560A / 800A / 960A (continuous / 30 second peak / 10 second peak)
Pack Maximum Output Power	177.4kW / 253.3kW / 304.1kW (continuous / 30 second peak / 10 second peak)
Maximum Expected Load to Supply	160 kW / 224 kW (continuous, sub-5 second peak)
Pack Weight	100kg
Pack Dimensions	619mm×464mm×174mm

Table 5: Critical specifications of the high power battery pack.

The battery pack can provide more than the maximum expected load power which was a requirement as there is an expected drop in battery cell performance under vacuum conditions. The battery pack can output its maximum rated continuous power for approximately 130 seconds, or approximately 4 runs, before running out of charge. Note that if more space becomes available on the pod at any point in the future, another string of battery cells will be added in parallel, bringing the peak 10-second power to 342.1kW. While this amount of power is not necessary to meet the simulated pod trajectory in the SpaceX tunnel, it allows the team to push the Emrax 208 motor to, and slightly above their rated peak power during in-house tests. For this reason, the additional 96 cells are purchased for use in tests where the battery pack is out of the pod.

This battery pack will have its output voltage, output current, individual cell voltage, state of charge and temperature continually monitored by the Orion BMS discussed previously. In the event of over-voltage, under-voltage, critically high current (over 900A), low battery state of charge, high battery pack temperature, or if the BMS fails to send information altogether, the control system disconnects all loads from the high power battery pack and emergency braking is engaged. A diagram of the high power system can be seen in Figure 43 below.

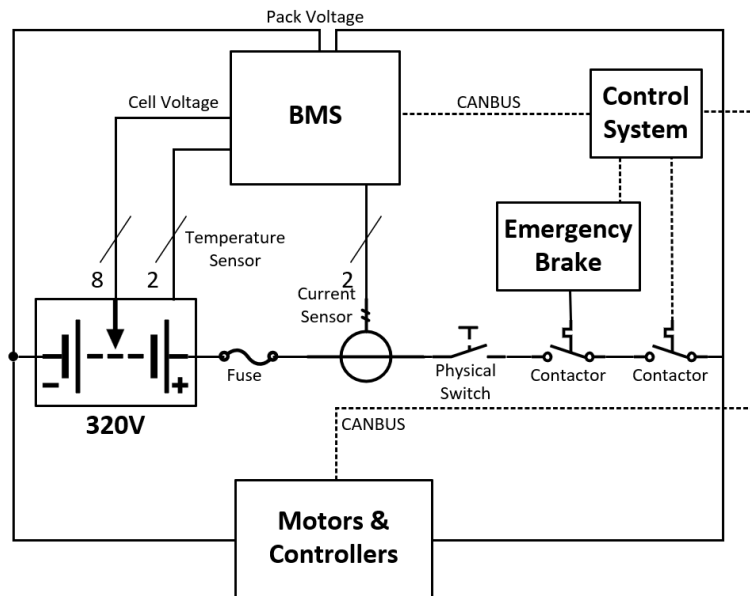


Figure 43: System diagram of the high power system.

Before connecting to anything else, the positive terminal of the battery pack is connected to a 900A slow-blow fuse to provide critical short-circuit protection that does not need to rely on the control system to be functional. A blown fuse means there is an open circuit on the positive terminal of the battery, therefore a loss of power to the propulsion system which means that emergency braking is automatically activated. There is a small chance the fuse will fail in a short circuit, rather than in an open-circuit as desired. The chances of this can be minimised by using physically larger fuses, with a larger gap between terminals. However, if in some way the fuse does not perform its function, the resulting high current can still be measured on the BMS through the current sensor. If an off nominal current is measured for a period of over 3 seconds, the loads will be disconnected from the battery pack and emergency braking will be engaged.

Loads are connected to the battery pack through two switches in series. The first switch is a physical switch that has to be turned on manually — the purpose of this switch is safe storage and transportation of the pod → the switch will be turned on before the pod enters the tunnel. It is highly unlikely that a manual switch would fail, but if it would, it would result in an open circuit → loss of power to the propulsion system. In this case, emergency braking is automatically activated.

Finally, there are two high power electromechanical DC contactors in series. The rightmost contactor is turned on by the control system by applying a 12V potential difference across its control terminals. With no voltage applied, the contactor stops conducting, which also works as a safety feature if power to the control system is lost. Similarly to the manual switch, the main way for a DC contactor to fail is an open circuit failure during the run → in this case, power to the propulsion system is lost and emergency braking is engaged. It is theoretically possible (though highly unlikely) for the contactor to fail such that it is permanently shorted. To further reduce this risk, as well as to provide a hardware-level insurance that emergency braking and propulsion cannot be active at the same time, another contactor is added. This contactor gets its control signal from the terminals across the electromagnet of the emergency braking signal. When this electromagnet loses power, it releases the emergency brakes. Therefore, if the emergency brakes are released by intentional or unintentional power-down of the electromagnet, this contactor is open and the propulsion system no longer receives power.

All solid-colour single wires (e.g. ones that do not include a line stating the number of wires) are 1/0 AWG power wires. All other wires are generic signal wires.

The running power consumption of the system (not including the primary load) is:

Component	Quantity	Power consumption	Total power consumption
Orion BMS	1	3W	3W
Contactor	2	2.8W	5.6W
Total			8.6W

Table 6: Running power consumption of the high power system.

Low Power

As discussed in previous sections, the LG HG2 3000mAh 18650 Li-Ion cells will be used. There will be a total of two battery packs — the main pack, in a 7S3P configuration; and a backup pack, in a 7S1P configuration. The low power systems powers the control system of the pod — therefore, it requires a high standard of safety and reliability, hence the redundant backup system. All power to the control system is supplied through an automotive-grade 12V regulator. Table 7 below summarises the critical specifications of the low power system:

Battery Cell	LG HG2 3000mAh 18650
Cell Chemistry	Li-Ion (Lithium-Ion)
Cell Nominal Voltage	3.6V
Pack Configuration (Main)	7S 3P (7 series, 3 parallel)
Pack Configuration (Backup)	7S 1P (7 series, 1 parallel)
Number of Cells (Main)	21
Number of Cells (Backup)	7
Pack Nominal Voltage (Main & Backup)	25.2 V
Pack Capacity (Main)	226.8 Wh
Pack Capacity (Backup)	75.6 Wh
Pack Maximum Discharge Current (Main)	60 A / 90 A (continuous / 30 second peak)
Pack Maximum Discharge Current (Backup)	20 A / 30 A (continuous / 30 second peak)
Pack Maximum Output Power (Main)	1512 W / 2268 W (continuous / 30 second peak)
Pack Maximum Output Power (Backup)	504 W / 756 W (continuous / 30 second peak)
Maximum Expected Load to Supply	<200 W
Pack Weight (Main)	1.5 kg
Pack Weight (Backup)	0.5 kg
Pack Dimensions (Main)	147 mm x 73 mm x 61 mm
Pack Dimensions (Backup)	147 mm x 73 mm x 23 mm

Table 7: Critical specifications of the low power system.

The expected nominal load of the control system is under 100 W. However, taking into account the peak ratings of components used and making room for possible future expansions, approximately 200 W is assumed for the peak load power draw of the control system. Battery packs constructed from modern lithium-ion battery cells can easily provide more power than this, as seen on the table above. The reasons that the main battery pack has additional parallel cells is to provide a larger capacity — the control system will be turned on before the pod gets loaded into the tunnel, therefore requires a much longer runtime than the high power system, as pressurising the tunnel takes several minutes. The main battery pack is designed to last approximately an hour at the maximum expected load, taking into account the 10% decrease in average capacity that lithium-based battery cells suffer in vacuum environments. Furthermore, the additional parallel cells in the main battery pack provide another layer of redundancy, as a failure of any two parallel strings in the pack will not stop it from functioning at the rated voltage.

The backup low power system only has a single parallel string, as this can provide more than enough power to the control system. Having only a single parallel string reduces the size and cost of the battery pack. The backup lower power system can supply peak load power for approximately 23 minutes, more than enough for the pod to stop and the tunnel to pressurise. The battery packs will have their output voltage, output current, individual cell voltage, state of charge and temperature continually monitored by the Tyva BMS discussed previously. In the events of over-voltage, under-voltage, critically high current, low battery state of charge, high battery pack temperature, or failure to receive information from the BMS on both battery packs → the control system engages emergency braking of the pod and once at a stop. In the event that critically high currents or temperatures still continue, the control system disconnects all loads from the system, including itself.

A diagram of the low power system can be seen in Figure 44 below.

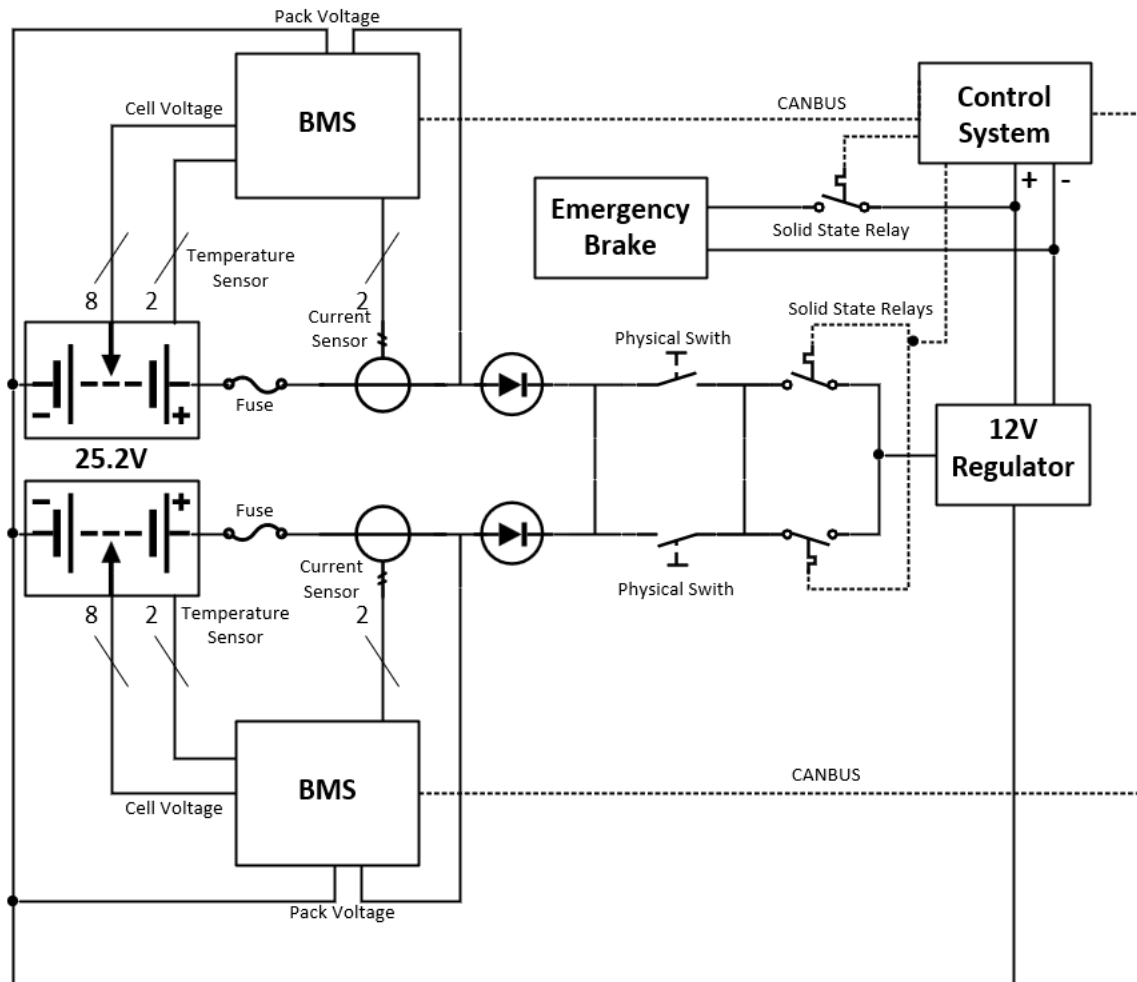


Figure 44: System diagram of the high power system.

Before connecting to anything else, the positive terminals of the battery packs each go through a 20 A quick-blow fuse to provide critical short-circuit protection that does not rely on the control system. In the event that any one of the fuses blows, the system will remain operational as normal. If both fuses were to blow into an open-circuit shortly after one another (highly unlikely), all power to the control system would be lost, which results in automatic activation of emergency braking. The ways fuses can fail were discussed in the high power system overview.

The two separate battery packs connect to the load in parallel through series forward diodes. In this way, current will always flow from the battery pack with higher voltage. This is an analogue solution that does not require a feedback loop from the control system (which has more potential points of failure). If any one of the diodes fail, the system will remain operational as normal. Power diodes are generally very rugged, but if both were to fail into an open circuit (due to physical damage for example), all power to the control system would be lost, resulting in emergency braking of the pod.

The load is first connect through two parallel manually-operated physical switches. These are present for long-term storage and transportation safety. The physical switches are turn on prior to entering the tunnel. As switches are a potential point of failure, two in parallel are used so that if one fails, current can still flow through the other with no interruption to system operation. In the unlikely scenario that both switches fail shortly one after the other, emergency braking would activate due to all power lost to the control system.

After the physical switches, normally-on solid state relays are used in case of an emergency when all loads from the low power battery packs need to be remotely disconnected. As these relays are unlikely to be put to use, but act as additional point of failure, two in parallel are used in case one were to fail. The unlikely failure of both solid state relays would result in emergency braking of the pod.

As the control system operates entirely on 12V, all power supplied to the control system goes through an automotive-grade 12V regulator. This is the main reason that the chosen battery pack voltage is 25.6V, as many automotive regulators are optimised to take an input voltage of around 24V (generally 18–36V). Industrial voltage regulator packages already contain several smaller regulator ICs inside, as well as safety features that safely connect them together. A regulator with a rating of 400W is chosen, so that if 50% of the internal ICs fail, peak load power can still be provided. Therefore, a second regulator is not put in parallel as with the switches → simply putting two regulators in parallel can cause undesired current spikes, which could ultimately lower the reliability of the system. Failure of the regulator (therefore failure of over 50% of the internal regulator ICs) would result in power loss to the control system, followed by emergency braking of the pod. Experiments of using several regulators in parallel will be performed and compared with using a single regulator in a stress-load scenario. If extensive testing shows that parallel regulators (with some added capacitors) perform as well, then two such regulators will be used for extra redundancy.

Finally, the electromagnet of the emergency braking system is powered from the same 12V regulator as the control system, so that if the entire regulator were to fail, both the emergency brake and the control system would lose power simultaneously. Note that a loss of power to the emergency brake electromagnet means triggering of emergency braking. All solid-colour single wires (e.g. ones that do not include a line stating the number of wires) are 12 AWG power wires. All other wires are generic signal wires.

The running power consumption of the system (not including the primary load) is shown in the table below.

Component	Quantity	Power Consumption	Total Power Consumption
ZEVA BMS	2	0.24W	0.48W
Solid state relay	2	0.09W	0.18W
Diode power loss at 200W load	1 (as currently only flows through one diode at a time)	4.7W	4.7W
Power loss in regulator at 200W load (95% efficiency)	1	10W	10W
Total			15.36W

Table 8: Running power consumption of the low power system.

4.3.1 Safety

This year's design demands a significant increase in power compared to last year's. Such an increase in both voltage and current requires a heightened awareness of safety. Each aspect of the design has been implemented with this in mind. Special considerations have been made for the type of battery chosen as the designs safety under conditions approaching near vacuum will be highly dependent on the cell chemistry. The team prioritizes safety at every level, from design to manufacturing. For the power systems, protection features focus on three main systems: batteries, motors and connections.

Battery

Safety Advantages of Li-Ion and LiFePo4

In the process of selecting the battery cells for the design, attention was paid to the durability and safety features, so that the cells can withstand the harsh environment within the tunnel. The team has decided to use LG HG2 Li-Ion batteries for the low power battery packs and the A123 ANR26650M1-B LiFePO4 cells to be used for the high power battery pack. Lithium ion technology has been validated by NASA for use in vacuum condition [3]. The LG HG2 cells used have been put to vibration, impact and crush tests by the manufacturer with no runaway action detected. Furthermore, these battery cells in a very similar configuration were used in last year's competition, where they managed to pass all battery-specific tests given by SpaceX. More information on the tests done on the battery cells and battery packs can be found in the testing section.

Connections and Insulation

Every cell will be fully insulated from the external environment. The compact battery design is centred around a rectangular tube structure which has a reliable interconnection system that avoids exposed contacts and eliminates the risk of external short circuiting. The design comprises of an outer structural steel box and an inner insulating housing. Internal cells are connected with a copper plates within the tube. The battery modules do not end in screws/pins, but instead solid copper plates, such as in those between the cells. The plates would then be faced with a plastic cover which had cutouts so external pins could connect directly to the copper plate. In this design, the short circuiting hazard is significantly reduced as there are no accessible conductors.

Complete Loss of Power

In order to prevent the pod from losing all the power, multiple measures have been deployed. As mentioned above, the team will be using three battery systems. A high power one to power the motors, and two low power ones to power the electronics — one of which will be redundant. Complete power loss would occur if the low power system were to fail to provide power for the control system. In which case, the communication with the pod would be lost along with any measurements and actions. To avoid this scenario, two prevention methods have been implemented. Firstly, the three parallel strings within the small battery are going to be connected. In the case any two string fail, one would be still capable of powering the control system. Secondly, in the chance the entire main battery pack or related components break down, the redundant battery system would power the electronics. Figure 45 shows a diagram of the two small batteries configuration.

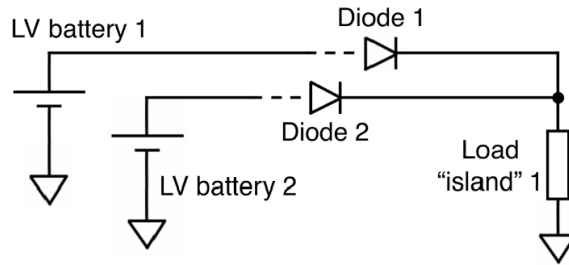


Figure 45: Configuration of the main and backup battery packs.

The diodes will allow the flow of current only from the higher potential battery and will prevent a catastrophic failure caused by an internal short to ground caused by the battery or due to insulation failure.

If the voltage on the first battery pack drops below a threshold, the redundancy battery pack is connected by default. Therefore if there is a fault in the main battery pack, power to the control system will appear uninterrupted, and braking can still be implemented.

Motor

The emDrive H300 Motor Controller will be used to control each electric motor on the pod. The following built-in protection functions are included:

- Maximum motor current protection
- Thermal protection of motors (input for temperature sensor in motor). Gradual decrease of maximum motor current when motor temperature reaches limit.
- Controller thermal protection. Gradual decrease of maximum motor current when controller temperature reaches limit
- Hall sensor failure detection and safe motor shut down.
- Low battery protection with battery voltage measurement. Gradual decrease of maximum current when battery voltage indicates empty battery.
- High voltage battery protection. Prevents over voltage situations when regenerating with full or damaged battery.
- Motor stall protection – limits motor current if motor is blocked for certain time
- Optional throttle out of range detection for detecting of damaged throttle or broken wire.

- High pedal protection: Disable operation if power up with non-zero throttle.
- Full self test at start. Check all IGBT-s, motor connection and battery connection.

Connections

High Voltage Circuit Shut Off

- Main contactor – controlled by the small battery, this relay shuts off the high voltage battery by an external command (given by the master control unit on board).
- Fuse – a fuse is blown disconnecting the high power battery if unexpectedly high currents occur.

Reducing Risk of Electrocution

High voltage components have bright orange coverings on their terminals that provide complete external insulation and easy identification that these should not be touched without care.

Protection Circuitry

All power sources and loads are fused; include reverse polarity and reverse current protection through a simple diode; and are constantly monitored by reliable BMS and motor controller.

Charging

For this year's design, the team has decided to power the pod with a custom built battery pack made up of several lithium battery cells connected together. Unfortunately, there is a problem with building a battery pack this way: each individual cell could have a different state of charge. This may cause the cells to overcharge or undercharge which prevents the battery pack from being utilised to its fullest capacity, and this may also reduce the overall lifespan of the whole battery pack. More importantly, it is crucial that lithium battery cells are not overcharged or undercharged, as this is a safety hazard. For these reasons, it is essential to ensure that the battery pack is charged properly by ensuring that each cell will have the same state of charge.

The main components needed for a balance charging system are:

- Battery Monitoring System (BMS): The BMS that will be used to monitor the battery packs in the Hyperloop pod are discussed in greater detail in the 'Battery Monitoring System' section. Basically, the BMS is used to protect the battery pack, and it achieves this by performing multiple tasks such as: reporting and calculating data, monitoring the voltage, current, state of charge and temperature.
- Lithium Smart Charger: These chargers will be used to charge the battery packs by converting AC from the power supply into DC which is needed to charge the battery cells. The team has also decided to specifically use a lithium smart charger because the charger needs to be able to work and communicate with the BMS of the battery pack to ensure more precise and safe charging.

Based on the different requirements, we will need different chargers and BMS for each individual battery system. Besides these requirements, another thing that is important to note will be the dimensions and weight of the components more so for the BMS because the BMS will be built into the pod where space is limited. As for the charger, it is not so important because the team plans to charge the pod externally so the size requirements are that the charger not be too big and to accept the standard AC mains voltage of both the UK (230V) and the US (120V).

Low Power

Since the voltage and power levels of the control system battery packs are relatively low, the requirements needed for balance charging will not be as great compared to the other, high-power battery pack. The nominal voltage of the low power battery packs is 25.2V.

BMS Used:

ZEVA 12-cell BMS module. Performs passive balancing. Chosen for its performance and small size and weight at a reasonable price. More in depth information can be found in the BMS section.

Charger Used:

Smart Charger 1.0A for up to 8S Li-ion/Polymer Rechargeable Battery Pack. The specifications and reasons for choosing this charger are stated below.

Key Specifications:

- Designed for up to 8S lithium ion batteries
- Dimensions: 63.5 x 31.75 x 25.4 mm
- Weight: 386g
- Input voltage: 110V-240V
- In built protection circuitry to prevent: over voltage, short circuit and reverse polarity
- Price: \$49.95

Based on these specifications, this charger is chosen because it has the capabilities to safely and reliably charge the battery pack. Another reason is this charger is affordable and can work for both UK and US main supply and finally, this charger is small and lightweight, which makes it easier to bring around.

High Power

This battery pack will be used to power the propulsion system of the pod. Since this battery pack contains many more cells, it has a much greater power and voltage level. The high power battery pack operates at a voltage such that it is suitable to charged with battery chargers designed for electric vehicles — the nominal voltage is 316.8V.

BMS Used:

Orion BMS. Passive cell balancing is performed. Although this unit is much pricier, larger and heavier, it is required because of the much larger battery pack. This is a professional BMS used in electric vehicles, containing many protection features. See the BMS section for further detail.

Charger Used:

Elcon PFC1500 Charger. The specifications and reasons for choosing this charger are stated below.

Key Specifications:

- Output voltage range: 24–320V
- Input voltage range: 90–260V, 50–60Hz
- Output current range: 5–40A
- Input current range: 0.2–15A
- For Li-Ion and LiFePO₄ battery cells

- Programmable through CANBUS
- Dimensions: 137.5mm × 172.5mm × 340mm
- Weight: 7kg
- Protection from: over voltage, short circuit, reverse polarity and high temperatures
- Price: \$569

This charger can provide enough voltage and power to reliably charge the battery pack, while being able to run on both mains voltages used in the US and the UK. It provides built-in protection features and is programmable through CANBUS, which makes it highly compatible with the Orion BMS. The price and size are reasonable — and while the battery cells could technically be allowed to charge at a higher power than the maximum output of this charger, it is more important that the charger is portable.

4.3.2 Manufacturing

In total 3 different battery packs will be used in the pod. Two smaller low-voltage battery packs will be used to power the electronics. The voltage for these batteries is 25.2V (nominal) and the primary battery will have a capacity of 9.0Ah with the backup battery at 3.0Ah. To provide the chosen voltages and capacity the cells will be arranged in a 7 series (7S) 3 parallel (3P) and 7S1P configuration respectively.

The required voltage for the motor battery was set to approximately 320V which with the chosen ANR26650 LiFePO4 battery cell would require a 96S configuration. The capacity of the battery will ultimately be limited by the space available for the battery within the chassis, but achieving a 8P (20Ah) capacity is the desired minimum requirement, after accounting for safety factors.

High Power Propulsion Battery

The primary battery of the pod provides power to the propulsion motors. It is a self contained unit that has its own BMS which provides information to the other systems.

Low Power Electronics Battery

The electronics battery is a separate low voltage, high capacity battery. It is completely isolated from the main motor power system and has its own backup.

Summary of Manufacturing

The final design for the high power propulsion battery makes use of a modular design to achieve the required configuration within the available space. The battery assembly is made out of three types of components. 1. the battery modules are sealed and insulated tubes containing the individual cells in a 8S8P configuration. All cells are connected in series via copper plates, acting also as heat sinks for the high currents. Each end of a module is faced by an insulation cover with holes for connectors. 2. the connectors to link the modules with each other are available as four separate types to accommodate the chosen assembly configuration. When 3 modules are connected together they become a battery section. Four battery sections connected together make up the final assembly. 3. the structural frame or harness is a steel structure designed to keep the assembly connected and structurally sound. By creating a compression fit, the frame ensure good electrical connection between the modules and connectors.

Through insulated access holes, a wiring loom can be connected to the internal battery terminals allowing for monitoring of the voltage levels within the battery using a BMS. External cables can be connected to the battery via terminal connectors on one face of the assembly. The total size of the high power battery pack is 619mm×464mm×174mm, with a maximum estimated weight of 100kg.

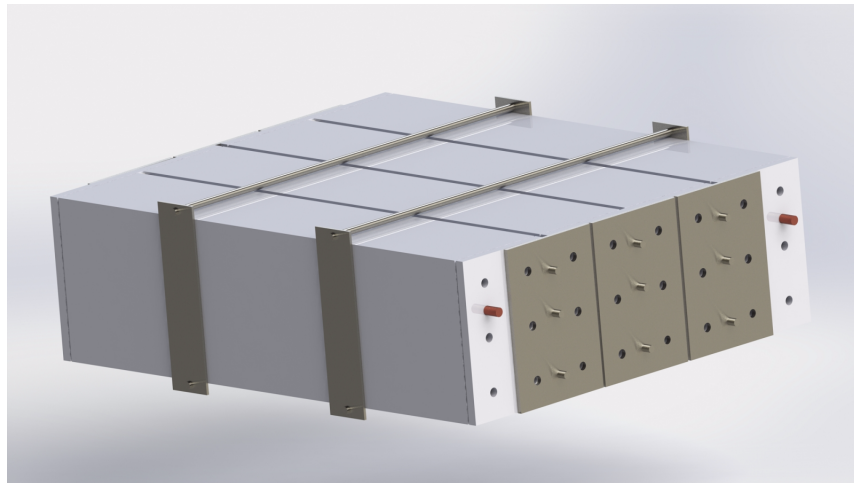


Figure 46: High power battery pack.

The design for the low power electronics battery uses two shells that slot into each other insulating the poles of the cells from each other. Connections between serial cells are made using copper plates and sense wires for a BMS are connected to these plates using small access holes. The dimensions of the main low power

battery pack come out to 147mm×73mm×61mm, with an estimated weight of 1.5kg. External cables can be attached to the last copper plate on either end of the battery. The back-up battery is designed in the similar but slimmer way — dimensions are 147mm×73mm×23mm with an approximate weight of 0.5kg.

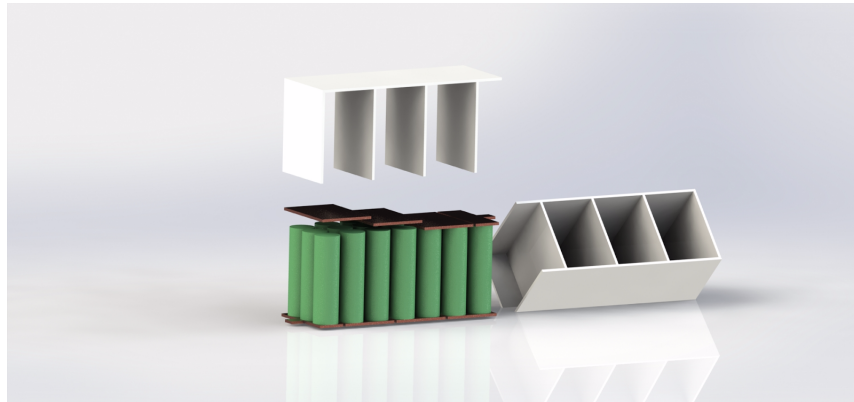


Figure 47: Low power battery pack.

Housing

Design Consideration and Process

To build the complete high power battery pack, the individual cells will have to be connected in series and parallel with good connections that allow for high current flow. Further the cells will also have to be fully insulated from the outside. To achieve the interconnects the battery blocs [4] connector system used in last year's competition was initially considered. Due to safety concerns, especially concerning short circuits and exposed terminals, this idea was soon abandoned and an alternative had to be found.

An initial idea was to use 1-inch PVC pipes to connect the cells in series with a screw cap to allow for good connections. In this design, short lengths of pipe would be used to construct a larger cell-pipe which then could be connected in series or parallel to achieve the desired battery configuration. Heavy duty brass screws would connect the cells through the end caps with external connectors.

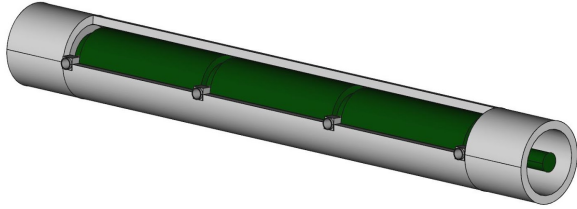


Figure 48: Battery tube concept.

This design was later extended to arrange 6 pipes in a hexagonal shape around a centre pipe which would act as a conduit for monitoring wires. In this configuration a 6P battery module could easily be manufactured and more parallel tubes could be added by altering the diameter of the centre pipe for efficient packing ratios.

A main driving point for this design was its inherent modularity and potential for hot-swapping. In an ideal set-up the tubes could be replaced in case of cell failure or all discharged tubes could be replaced with fully charged tubes. A point of contention though were the connectors on the ends of the tubes. As they were fully exposed, the risk of short circuiting still remained. A mitigation for this was the use of shrouds that extended the tube beyond the contacts on either end. Both solid shrouds and flexible rubber shrouds were considered to suit a connector system for the tubes which still had to be developed.

In the end the tube design was replaced by a rectangular design due to space restrictions within the pod and the less optimal packing geometry of cylindrical tubes. But the tubes are still used as a modular prototyping and testing design.

In the next overall design iteration the battery compartment inside the chassis of the pod became a solid steel box with an access hatch at the top. As this box provides structural support it cannot be made of an insulating material, without significant material cost. Therefore the chosen design comprises of an outer structural steel box and an inner insulating housing. It will be made of PVC tubing or ABS plastic and is designed to be modular and potentially hot-swappable.

The modular design chosen makes use of individual battery modules which contain a set number of cells in series and parallel. These modules can then be connected together using a modular interconnect system to build the desired battery configuration.

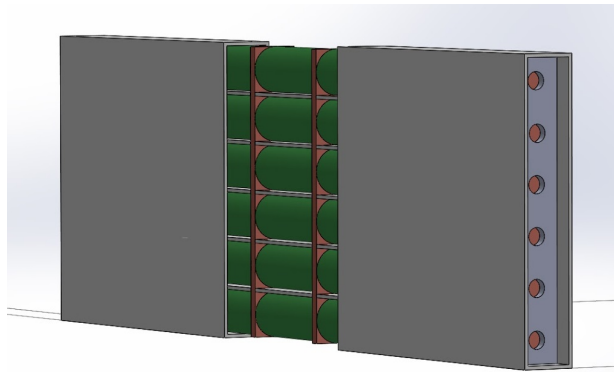


Figure 49: Flat pack concept.

In the first design of this kind, each module will contain 6 parallel cells and as many series cells as the space allows or we chose to use. The general design of a module can divided into internal, ends and shell. The shell is a custom extruded PVC tube (or similar) with a rectangular cross-section. Internal dimension is set to 26mm by 166mm, with a wall thickness of 2mm. The internals of the tube are filled by 6 cells in parallel, separated by 2mm plastic plates to space the cells apart in order to avoid thermal conductivity between cells. Each row of parallel cells is connected on either end by a 26mm×166mm×5mm copper plate which also acts as a connector to the next parallel row. In this manner all series cells are connected to each other by a copper plate. The ends of the cells on either end of the tube are faced by a copper plate and a 3mm thick plastic cover containing holes so plug pins can make contact with the copper plate. The tube extends beyond the ends of the cells by a few mm to act as an insulating shroud. The purpose of this shroud is to limit the access to the terminals and therefore reduce the risk of shock to people and reduce the risk of short-circuiting when the battery module comes into contact with conductive materials.

A further feature which might be included, would be to key the ends of the tubes, so that positive terminals can only be connected to negative terminals. There is no direct design as of yet, but as a preliminary precaution, the ends of the tubes would be coloured corresponding to their polarity with the connectors having matching colour coding.

Final Chosen Design

As this design did not meet the requirements of the motors chosen and did not fit into the available space, a modification was made to the design. The new design keeps the essential features, but modifies the geometry of the cell arrangement from a 1×6 to a 2×4 arrangement. This allows for an 8P configuration to be achieved which is critical to the supply for the motors. The general design stays the same, but the internal dimensions of the module tube are now $54\text{mm} \times 112\text{mm}$. There is a single dividing plate of 2mm thickness between the two cells and 3 dividing plates between the 4 cells, with the middle plate having 4mm thickness and the other two, 2mm. This is needed as otherwise the external dimensions would not be in a 2:1 ratio, which is required for efficient stacking.

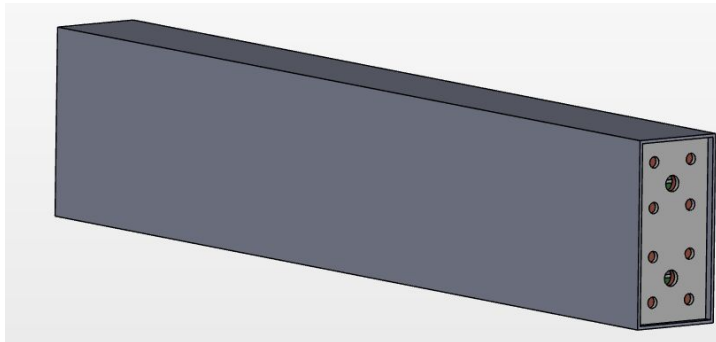


Figure 50: Diagram of final flat-pack battery pack.

The stacking of the modules is such that three modules are always grouped together into a battery section, two in a vertical arrangement and one horizontally on top. By connecting 4 of these battery sections together a full battery can be assembled. This design allows for a 8P configuration and makes efficient use of the space available.

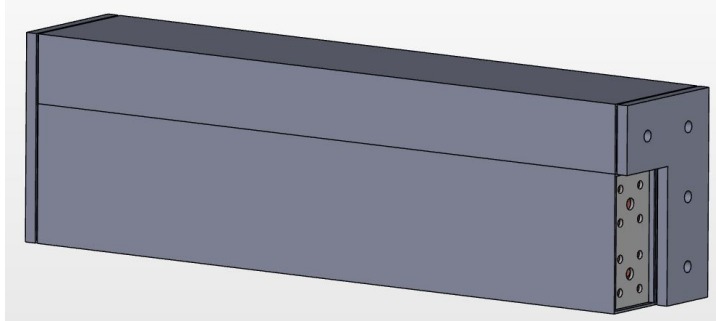


Figure 51: Diagram of final flat-pack battery pack stacking.

In this design a 96S8P battery will be able to fit into a 619mm×464mm×174mm space with a nominal voltage of 316.8V and a capacity of 20Ah with 768 cells in total. Not all cells will be monitored due to cost and space limitations, instead to maintain adequate safety standards, each set of parallel cells is monitored. This allows accurate monitoring of the cells state-of-charge after an initial complete balance charge to bring all parallel cells into harmony. Connections for monitoring the cells are made through small contacts/holes in the shell allowing access to the copper plates. These contacts can then be connected to sensor wires for the BMS.

BMS sensor wiring is achieved by having a wiring harness connect through the end plates to the copper plates inside, which is illustrated in Figure 52. An insulated hole feeds the wire from the inside to the outside. A simple 8-pin EPS connector or similar is used to extend the wire onwards to the BMS. Inside the module the sensor wires attach to the copper plates between the cells.

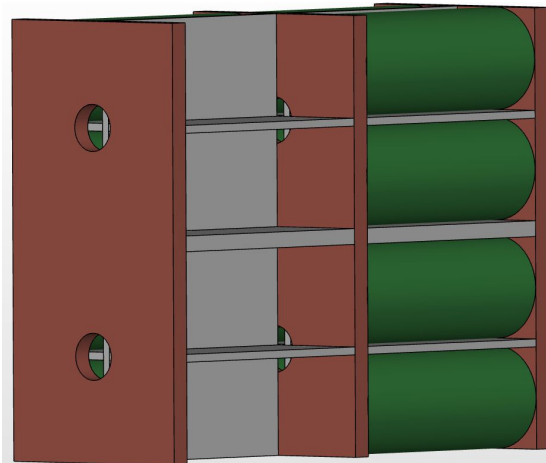


Figure 52: Detail of the inner structure of a battery module, showing the conduit holes in the copper plates to pass the sense wires for the BMS.

Connections

Design Consideration and Process

A major driving factor in the design for the battery and the connectors was safety. The battery blocks were very intuitive and easy to use, creating compact battery structures with reliable interconnects, but were lacking in most aspects of safety with its exposed terminals. So the teams design had to prioritise the safety aspect and to this end aspired to design an interconnection system that avoided exposed contacts and therefore reduced the chance for short circuits.

Taking inspiration from existing high voltage connectors (such as: Kostal HV connector, Rosenberger HV connector), the initial design with the battery tubes was to use a connector that slotted over the battery tube end to seal the connection in. Electrical connections would then be made using spring loaded contacts gripping onto the terminal from the battery. The contacts could then be connected to a bus bar to transfer the power along to another connector or to a terminal. A difficulty in this design were the spring loaded connectors (similar to household sockets) as they would have to be designed to handle very high currents.

The second revision of the connectors was then made when the battery module design switched to rectangular tubes. In this version the battery modules do not end in screws/pins, but instead solid copper plates, such as in those between the cells. The plates would then be faced with a plastic cover which had cutouts so external pins could connect directly to the copper plate (see Figure 49). In this design, the short circuiting hazard is significantly reduced as there are no easily accessible connections.

Connections between battery modules would then be made via external module connectors. These are designed in such a way that there are multiple pins (currently one per cell parallel) which are attached to a backing plate. The backing plate is encased in a plastic housing (which could be 3D printed) and the pins are covered by a facing plate with cutouts and enclosed by a small shroud. The shroud for the pins is manufactured in such a way that it has a perfect fit inside the battery module tube. So when the connector is slotted into the module housing, no live connections are accessible.

To build up the final battery from the modules and connectors, they can be attached in a staggered fashion allowing a series connection between the modules. In case two modules were to be connected in parallel, a connector twice as wide could be used to connect four modules together.

Final Chosen Design

In the second design iteration using the 2×4 arrangement, the connector design increased in complexity and required some L-shaped designs. In total, 4 different connectors would be required, with one type being terminal connectors. Two would have either a left or right L-shape and the last type would be a double connector to connect two modules next to each other.

With precise enough manufacturing processes, it should be possible to produce these to high enough tolerances so much so that a perfect friction fit between the connector and the module can be achieved. Though some external support is still required to ensure good connections in case of vibration loosening, this is discussed in the next section.

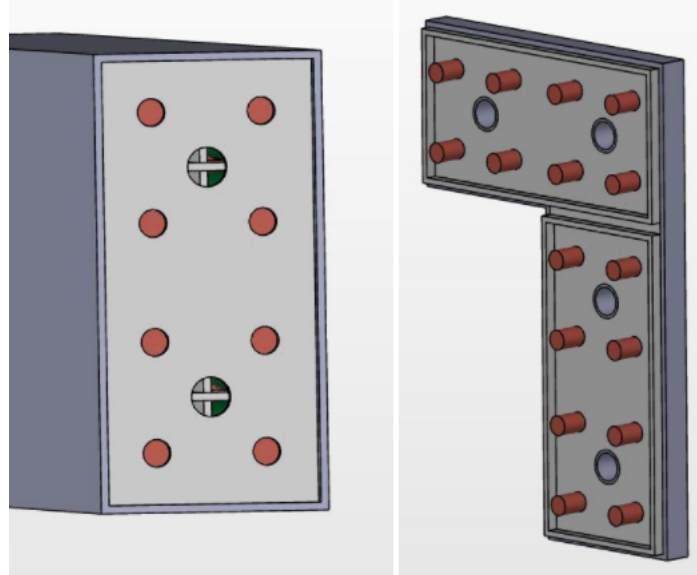


Figure 53: Diagram of L-type connectors.

Structure and Stability Mechanism

Design Considerations and Process

Previous designs features a base plate on which the modules are mounted. The purpose of this base plate is to securely hold the modules when connected as well as act as a conduit for the Sensor wires and pins. If the design with all modules next to each other had not been made infeasible by the space restrictions in the chassis, a proposed idea for hot-swappable modules would have included a RAM-DIMM style connector. In this design the base plate would have contained pins sticking up, onto which the modules would be slotted to make connections with the plates inside. At the ends of the base plates, hinged connectors could clip onto the module to seat it securely onto the base and connect two modules together in series. To swap out a module, the two hinged connectors at either end would have to be loosened and the module could be pulled out and replaced with a spare module.

As the newer design now no longer places all modules on a common surface, the idea of a base-plate became redundant. Further, the desired hot-swapping will have to be discarded for the time being as it is a bit too ambitious and not feasible with the space available. While not exactly hot-swappable, the design is still very serviceable and quick to disassemble.

Final Chosen Design

To provide structural stability in the new design, a combination of face-plates and threaded rods will have to be used. The challenge in providing structural integrity in this design is that fact, that there is very limited space available. Therefore with the design limitations in mind, two methods were chosen preliminarily to provide structure to the battery. The primary structure mechanism also doubles as a mechanism to ensure good electrical contact between the battery modules and connectors. As such it is based on threaded 4–8mm rods passing between the four sections and terminating in face plates (steel or aluminium) which can be tightened with locking nuts to ensure the entire battery assembly does not fall apart under vibrations. By compressing the connectors onto the modules we can ensure good connection and reduce chances of loosening the connectors.

The secondary mechanism has to ensure that there remains structural integrity between the different modules and they do not break apart. For this it should be possible to either weld/glue the modules together into the sections, but this would reduce the modularity of the design. A more efficient approach would be to use an outer structure of rods, plates and locking nuts to secure the entire assembly using a cage around the battery assembly. Alternatively as the battery assembly is housed inside a structural steel box, this could be fabricated to provide a close fit limiting any lateral movement of the assembly and keeping all the parts together. In the case of a loose fit, dampening and padding materials would be used to fill any gaps which in turn would also help with reducing vibrations.

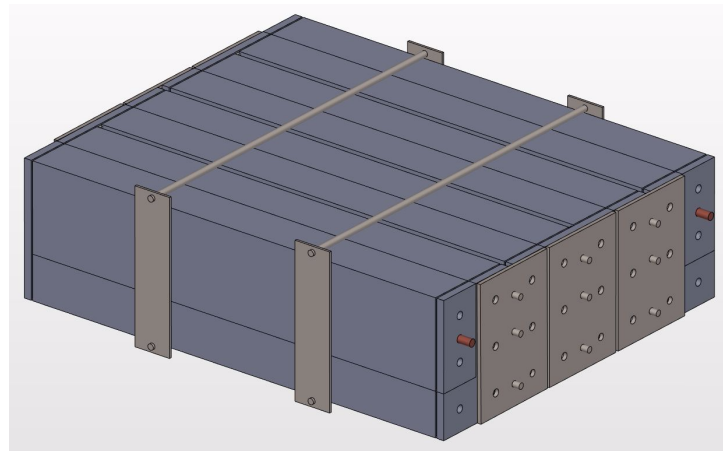


Figure 54: Final Battery Assembly.

Final projected dimensions for the entire high power battery come to $619\text{mm} \times 464\text{mm} \times 174\text{mm}$ for the battery assembly itself with a estimated total weight of maximum 100kg.

Fabrication

To produce the custom PVC tubes, a plastic extrusion company would have to be commissioned to produce enough tubes for the entire battery. By using an out of house company, industrial standards and tolerances can be adhered to. Alternatively, material alternatives include acrylic, fibreglass or 3D printed ABS.

Acrylic can easily be procured and cut in a workshop, the pieces can then be cemented together to create the tubes. A downside of acrylic is that it can easily shatter upon impact.

Although out-of-house fabrication of the module housing is more professional, the option of 3D printing all the required housing parts is an option open to us. At least two of the dimensions of all the parts are within the printable sizes of many 3D printers and the third dimension can be made up of multiple parts which are then welded together. This is currently the preferred fabrication method, as it would make the entire battery pack (except battery cells, of course) manufactured in-house.

All the copper parts of the battery can be cut out of 5mm sheet stock in the workshop and the pins for the connectors can be made of 7mm diameter copper rods. Any plastic dividers or plates can be cut in the workshop out of sheets of the

required thickness and by using CNC machines, fabricated to precise dimensions.

Assembly

The assembly of the battery pack will proceed in stages. Once all the parts are available each module can be assembled individually and tested for conductivity. A charging and discharging rig has been made to aid in the testing of each module. When a module passes all safety tests, it can be permanently assembled (though disassembly will be possible) and connected to two further modules to build a three module pack. Further safety tests can then be carried out in this configuration before finally 4 packs are connected together to make up the final battery pack.

Low Power Battery Housing

For the electronics battery a simpler design could be used due to the much reduced size. To keep the design compact, the cells are arranged 3 in parallel and stacked 7 in series, with connections made between the cells by thin copper plates. To isolate the poles of the cells from each other a thin plastic wall is placed between them. The entire assembly is further encased by a plastic housing to keep the connections isolated. The sense wires for the BMS are passed through small access holes in the outer housing side. They are situated at the top and bottom to line up with the copper plates inside to which the wires can be soldered. Exact mounting options are to be finalised as the spacing of other electronics becomes clearer, however, the battery packs will be held together by the same nuts and bolts that are used to mount them.

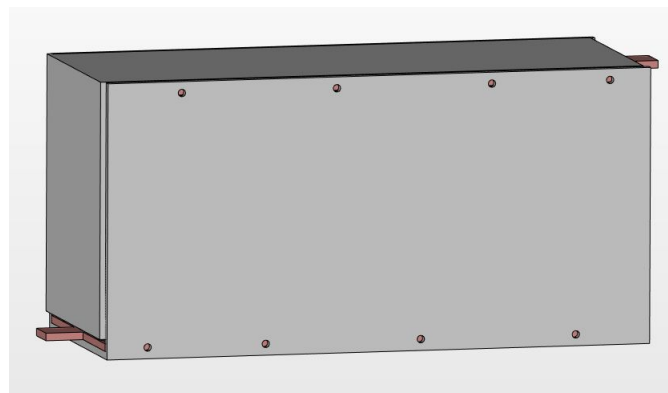


Figure 55: Housing for the small battery, with power tabs on either side and sense wire access holes.

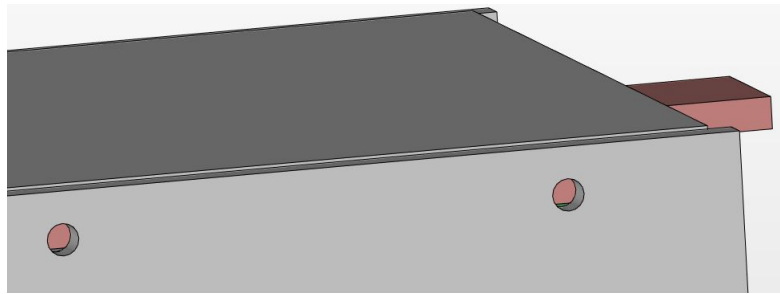


Figure 56: Detail of the sense wire access holes.

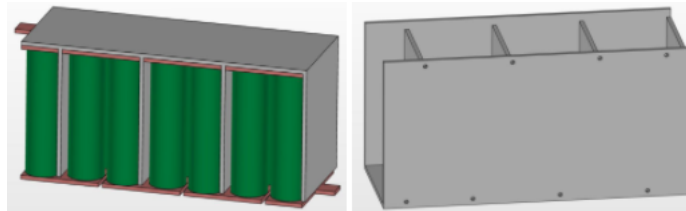


Figure 57: View of the internal structure and outer housing.

Tabs on either end can be used to connect cabling and will have to be further insulated for safety. Sensor wiring is achieved by soldering wires directly onto the copper plates, then feeding them out of the battery pack through a small hole on the plastic casing. Final dimensions for the electronics battery are expected to be **147mm×73mm×61mm** with an expected weight of **1.5kg**. The backup electronics battery can be manufactured in a similar way and will have dimensions of approximately 147mm×73mm×23mm and a weight of approximately 500g.

4.3.3 Testing

Lithium ion technology has been validated by NASA for use in vacuum conditions. The LG HG2 cells used have been put to vibration, impact and crush tests by the manufacturer with no runaway action detected. Furthermore, these battery cells in a very similar configuration were used in last year's competition, where they managed to pass all battery-specific tests given by SpaceX.

The technology used in the LifePO₄ cells the team has selected have better thermal stability, enhanced safety and are more tolerant of mechanical and thermal stresses than the Li-Ion cylindrical cells, all while providing a significant increase in power density, but at the cost of lower energy density. The LiFePO₄ cells have been

rigorously tested and approved by the manufacturer in case of nail penetration, over-charge/discharge, thermal instability, external short circuits and excessive compression. Further tests performed by David Balaguer Escolano on the thermal analysis of a LiFePo4 showed that [2] in near vacuum conditions under ambient temperatures of 20°C, the LiFePo4 cells performed adequately with an expected 10% decrease in capacity — the cells did not sustain damage.

Rather than just counting on research data, the battery cells and battery packs are also vacuum-tested in-house. The low power battery system, which uses the LG HG2 Li-Ion cells was used in the competition last year and had already undergone extensive vacuum testing in-house, as well as during the competition under SpaceX supervision. No significant power performance loss was measured, only an expected 10% capacity drop. The A123 ANR26650M1-B LiFePO4 cells used in the high power battery system have so far been tested individually in a vacuum chamber, with no measured swelling, voltage loss or performance reduction. Single-cell load tests, as well as tests done on individual cells by the manufacturer can be found the Battery Cells section. Load-testing of the full battery pack in vacuum conditions will be done as soon as it has been manufactured — this will include constant loads, motor loads and rapid switching of loads.

The power system as a whole will be tested in a vacuum chamber under conditions much like in the SpaceX tunnel to look for any performance difference. One of the most important electronics to vacuum-test is the BMS, as it is a complex system that was not necessarily developed for use in vacuum. Experience from last year's competition suggests that no difference is likely to be measured when operating the BMS under vacuum, but tests on any newly bought component will be performed regardless.

Fuses used in the power systems will be attempted to be blown in a vacuum chamber to test whether their blow time changes in these conditions. Components such as switches, relays and contactors will be tested under vacuum as well, although no observable effect is expected. More importantly, switching components will undergo vibration and rapid full-load switching tests.

4.3.4 Scalability

The power systems follow a highly modular approach, which can be seen in the similarity between the high and low power systems.

For the high power battery pack, more modules would simply be added. For a full-scale model, it is likely that a higher voltage would be required for good system efficiency. As this is a half-scale model, the full-scale model would optimally contain twice the series battery cells, giving a nominal pack voltage of 633.6V — in this way, the output power of the battery pack is doubled as well. Furthermore, a full-scale model will have to travel a significantly longer distance than that of the SpaceX tunnel. For longer travel distance, a higher battery capacity is required — this is achieved by putting more battery cells in parallel. The specific number of additional parallel cells can be optimised for the required travel distance — adding too many extra cells would increase the pod weight far too much, so careful optimisation is necessary.

The extended Orion BMS, used in the current high power design, could be used for full-scale high power battery pack described above. Switches and contactors used in the railway and aerospace industries would have to be used in a full-scale design that comes with a significant power increase.

For the low power battery pack, the current design would likely suffice for a full-scale model, with the possibility of adding more parallel cells for longer capacity in case of lengthy travel time.

For the same number of series battery cells, the same BMS, in this case the ZEVA BMS, can be used without additional components. Switching components used would be very similar, as a significant increase in the power of the control system is not expected. For high long-term reliability, solid-state relays would still be preferred.

4.3.5 Timeline

Testing of individual battery cells and prototypes of the low power battery system has been done during the design stage. This allowed the team to become familiar with power electronics equipment such as balance chargers, clamp-on ammeters, battery management systems and switching equipment. This will allow the team quickly begin testing in the coming weeks as design stage is nearing its end.

In mid-December, an 8S1P PVC pipe prototype of a high power battery module

was constructed, as described in the manufacturing section. The prototype has been tested for structural stability and pack voltage, but shipping delays of the BMS have not allowed for extensive electrical tests. Load-testing of this prototype will begin in mid January, with vacuum chamber load-testing expected in early February at the latest. The low power battery packs will be vacuum chamber load-tested at this time as well, as these battery packs are ready to be assembled. Components such as the BMS, fuses, contactors, solid state relays, diodes and regulators will be vacuum tested at this time also.

Construction of the 8S8P high power battery pack modules will begin in late January and is expected to take up to a month for the whole battery pack, mainly due to 3D printing times. The modules will be tested one at a time as they are made, then the battery pack size under test will be increased one module at a time.

High power testing of the battery pack will commence once the motors have arrived, which is expected in early March for the first two motors. The other motors are expected to arrive in early May at the latest, which is when the full high power battery pack can be tested at its maximum peak power rating. However, even with two motors, a smaller number of battery cells can be tested to their peak limit.

Functional testing is expected to finish in early June at the latest. Any additional time will be spent on structural improvements, weight reduction and neatness.

4.3.6 Cost Breakdown

Component/Material	Quantity/Amount Required	Cost (£)	Total Cost (£)
A123 ANR26650M1-B battery cell	768	9	6912
LG HG2 18650 3000mAh battery cell	28 (available from last year)	(5)	(140)
Orion BMS	1	950	950
ZEVA BMS	2	85	170
900A 600VDC ABB fuse	2 (at least 1 to break)	100	200
1000A manual disconnect switch	1	50	50
Gigavac 1000A 400VDC EV contactor	2	100	200
90A 48VDC fuse	2	1	2
30A 48VDC fuse	2	1	2
90A power diode	2	10	20
100A manual disconnect switch	2	3	6
90A solid state relay	2	50	100
5A solid state relay	2	10	10
24V to 12V automotive regulator	1	20	20
Surface temperature sensor	3	3	9
1/0 AWG power wire	7.5m	20	20
1/0 AWG ground wire	7.5m	20	20
1/0 AWG ring terminals	50	0.6	30
Assorted 12 AWG wire	20m	25	25
ABS filament	15kg (spare 20kg)	25	375
Copper sheet 5mm	1050mm×900mm×5mm	90	90
Copper rod 7mm	3.5m	12	72
Steel threaded rod M6	6.3m	9	27
Steel sheet 3mm	1000mm×600mm×3mm	60	60
8S LIthium Smart Charger	1	37	37
Elcon EV Charger	1	420	420
Miscellaneous (incl. nuts, low power terminals, etc)		20	
Total			9847

Table 9: Power cost breakdown.

5 Dynamic Module

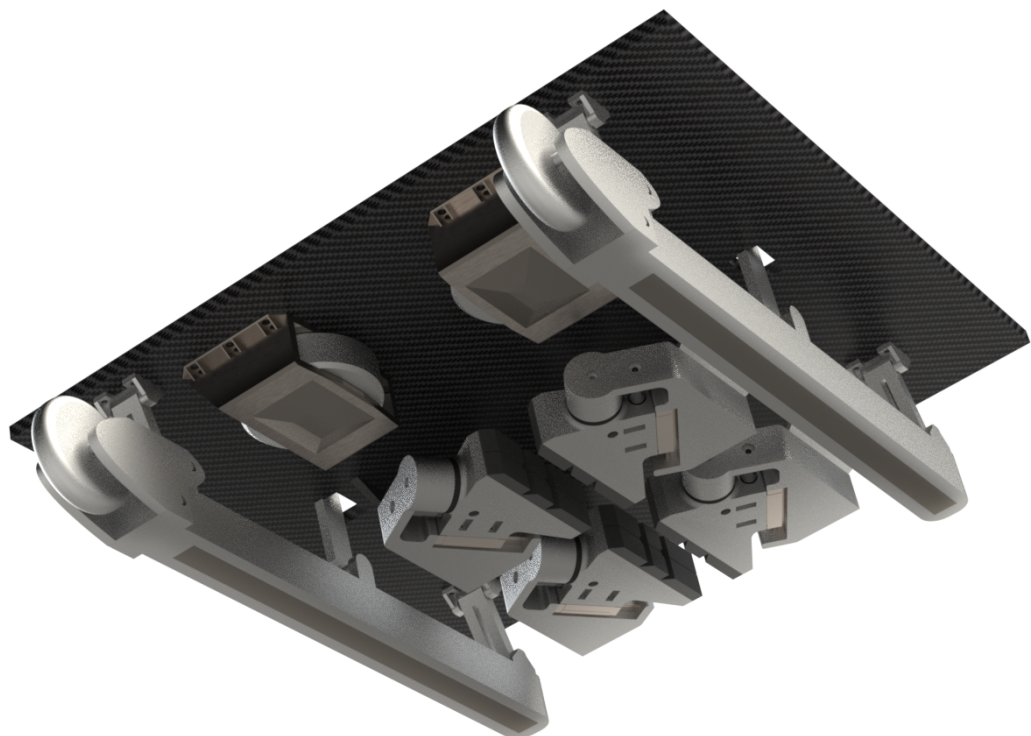


Figure 58: Bottom view of the dynamic module.

5.1 Levitation

5.1.1 Introduction

Passive levitation is used in our system which exploits the horizontal velocity of the pod by inducing an opposing magnetic field in the aluminium sub-track of the tube. This sub-track can be modelled as a conducting slab, which unfortunately does not produce the most efficient lift-to-drag ratio compared to other possible track designs due to a shallow skin depth. However, this issue is lessened at high velocities since the lift-to-drag ratio is proportional to \sqrt{v} .

Other considered factors were the cost of the magnets, mass of the pod (payload), manufacturing and safe implementation of strong magnets. Since it is impractical to have a single strong magnet, Halbach arrays are used instead. These arrays can be fitted into skis, so that they are held together and easily mounted to the pod.

5.1.2 Summary

The levitation mechanism will use 4 linear Halbach arrays, each with 21 N52 25mm³ magnets, coming to a total mass of 2.46 kg excluding the 0.357 kg of the mounting steel plates. Each of the arrays will be contained within a ski, with two skis mounted on each side of the chassis. This arrangement allows for optimal stability of the pod.

To achieve the desired levitation height of between 7.5-9.5 mm above the sub-track, this configuration can lift a range of pod masses between 490-630 kg. With current estimates for a pod mass of 500 kg and a top speed of 75 ms⁻¹ the equilibrium levitation height will be 9.4 mm. This is a passive levitation mechanism as it requires no power or active control, making it very favourable in this application where safety is the primary concern. This also means that in the event of loss of power or control, the pod will simply come to a rest on its auxiliary wheels once slowing down to the transition (take-off) velocity.

5.1.3 Considered Solutions

During the early design process the first decision to be made was regarding the optimal type of levitation that should be used. Broadly speaking, the options available were active levitation using air bearings or electromagnets, or passive levitation using permanent magnets. The latter was chosen because it does not require power or active control, so the system design is much simpler and therefore much safer.

5.1.4 Chosen Solution

A Halbach array is a specific arrangement of permanent magnets that enhances the magnetic field on the desired side, in this case facing the aluminium track, and decreases the magnetic field on the opposite side to a magnitude of almost zero. Linear' implies that the magnetic array is in straight line arrangement, as opposed to a circular Halbach array (as used for the propulsion). The augmented field on one side is created by arranging the magnets in a particular pattern: the North pole is rotated by 90° from one magnet to the next consecutive one, and this can be repeated indefinitely. Halbach arrays are highly convenient for a system of this kind as they offer the possibility of having a stronger magnetic field on one side, providing a higher efficiency per magnet and a stronger lifting force, while almost cancelling the magnetic field on the opposite side - minimising any risk for items within the pod.

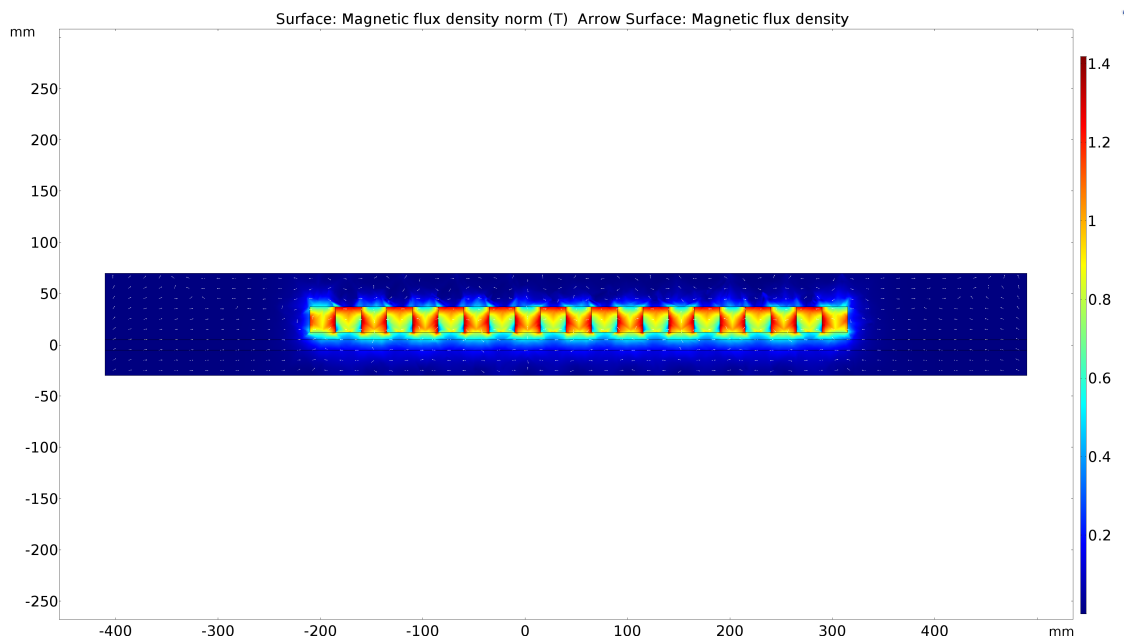


Figure 59: 2D Flux Density of Halbach Array

Faraday's Law is the principle that allows the pod to be levitated magnetically. It describes how a current is induced as the result of changing magnetic field. The magnetic field change is given by the relative movement of the arrays relative to the tube track. As the magnetic field changes, a current is induced in the underlying conductive aluminium track. The induced current flow creates a magnetic field, defined by Lenz's Law.

This induced magnetic field is in the opposite direction to that created by the four Halbach arrays, resulting in magnetic repulsion and hence a lift force on the magnets and pod. The pod can levitate once the upwards magnetising force is greater than the pod's weight. Except of the lift force the induced magnetic field creates a drag force as well which opposed the motion of the pod which is high at the beginning but as the velocity of the pod increases the drag force decreases.

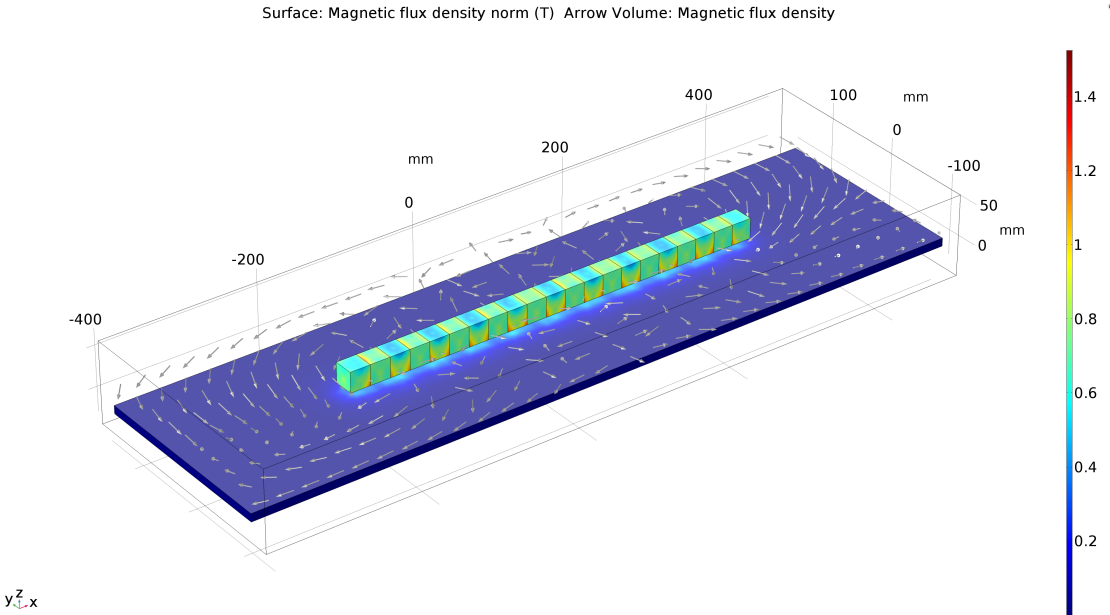


Figure 60: 3D Flux Density of Halbach Array

5.1.5 Simulations

Thermals

For the conditions that the pod will meet, thermal heat dissipation is insignificant. The passive levitation system can be assumed to withstand the thermal transfers, and it can also be concluded that there will not be any significant heating generated and transferred into the sub-track. This conclusion was based on information provided by Arx Pax [6] on their Hover engine, a powered device, which states:

$$\frac{\Delta T}{m_p} = \frac{0.056^\circ C}{kg - min} \quad (1)$$

This implies the approximate temperature rise of the pod will be of 0.056°C per kg of the pod per minute. Whilst this considers dissipation by convection, which will not be possible in the excavated tube, the pod will not be at a standstill but in continuous movement, and during standstill no eddy currents can be induced by the permanent magnets. Additionally, no cooling of the Halbach Arrays for levitation is required, as the thermal heat capacity of the magnets and surrounding chassis (aluminium) will store the excess heat for the short 1.5km test run.

Magnetic

The 3D flux variation of Halbach array above, confirms the theory behind Halbach arrays. The flux on the bottom side of the array is maximised, whilst the flux above the array is minimised.

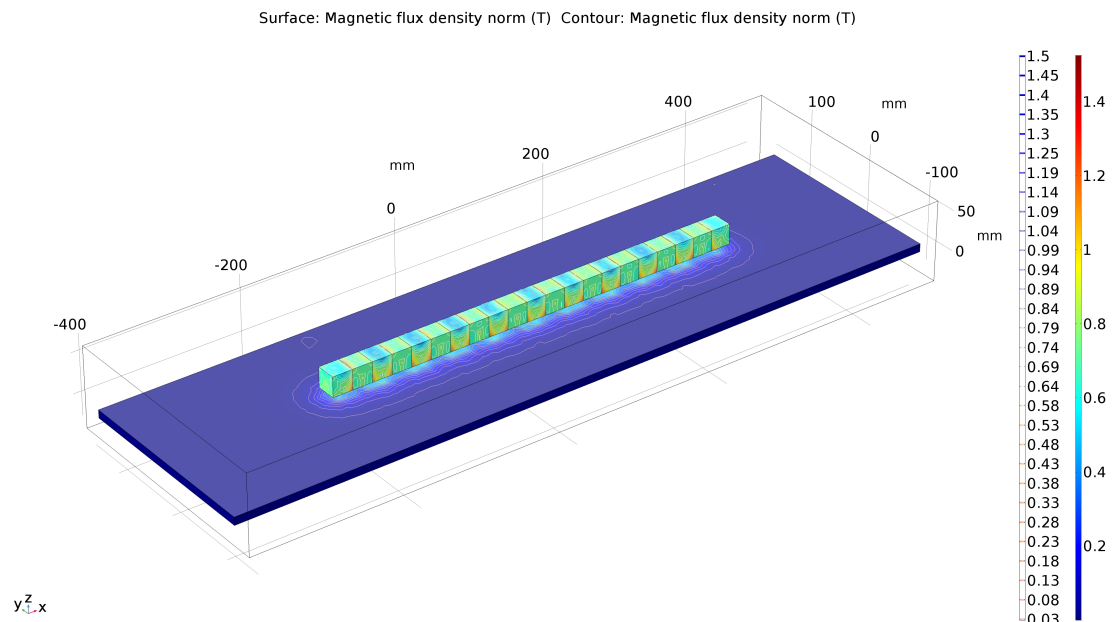


Figure 61: Flux Density of Linear Halbach Array.

5.1.6 Safety

Fault Tolerances

Careful design was developed in such a way to prevent as many failures as possible. However, there are still 2 potential problems to be discussed; demagnetisation and overheating. Demagnetisation of the arrays can occur at several stages: manufacturing, transportation, testing, and general use. Manufacturers of the Halbach arrays must be aware of possible demagnetisation and take measures to avoid damaging the magnets.

As mentioned previously, several precautions are taken, such as implementation of steel ski shields to prevent demagnetization during transportation. In order to protect magnets, they should not be tested directly. Instead, magnets from last year will be tested using the design described in the “Testing” section. This will confirm how accurate simulations are, allowing the team to make more adjustments if needed. Lastly, demagnetisation due to general use is not considered significant; a problem may only occur if magnets are hit directly.

Even though the probability of failure is low, it must be addressed regardless. In the cases of magnet damage or demagnetization of a single (or several magnets), the issue is not of extreme relevance, since there is a total of 84 working magnets. Depending on the extent of damage, lift force would decrease and levitation height would decrease. For the system to stop functioning optimally, the remanent field of the magnets would have to decrease to 1.25T, instead of the initial 1.45T. This would only mean that the pod would still levitate, but to a height of under 7.5 mm and above 5 mm.

5.1.7 Scalability

Size & Mass

The mass of the full-scale pod was estimated to be 10 tonnes (fully loaded): this is approximately 20 times the mass of the team’s prototype pod. Therefore, if the same levitation system were to be used for the full-scale pod, it would require 20 times the number of magnets and arrays that are in the team’s prototype pod meaning it pod would have to accommodate a total of 80 linear Halbach arrays of dimensions used in the prototype, which would require a lower surface area of 1.05m^3 . In addition, the full-scale pod will travel at higher speeds than the prototype pod; 340ms^{-1} rather than 75ms^{-1} . This means the number of arrays required to lift the pod to the required levitation height will be less than the calculated value 80, as the drag force decreases as speed increases.

Our MATLAB simulations show that the number of magnets required to lift the 10,000kg pod at the desired levitation height (approximately 9mm), when travelling at maximum speed of 340m^{-1} is 1407. This would require a total lower surface area of 0.88m^3 . Although the lower surface area of the scaled up pod would be sufficiently large, it would be more efficient to increase the magnet strength to grade N55, to reduce the number of arrays required to lift the pod.

Additionally, the efficiency of the levitation system would be increased if a system was designed to retract the wheels on the skis. This would reduce the required levitation height, thus reducing the number of arrays required. If N55 magnets were used, and the levitation height was reduced to 5mm, the full-scale pod travelling at 340ms^{-1} would require 819 magnets.

	Prototype Pod (500kg)	Full Scale Pod, travelling at 340ms^{-1} , levitation height 9mm, N52 grade magnets	Full Scale pod, travelling at 340ms^{-1} , levitation height 5 mm, N55 grade magnets
Mass	500kg	10,000kg	10,000kg
Maximum speed	75ms^{-1}	340ms^{-1}	340ms^{-1}
Levitation height	9mm	9mm	5mm
Magnet grade	N52	N52	N55
Number of magnets	84	1407	819
Number of arrays (21 magnets each)	4	67	39
Mass of magnets	10kg	165kg	96kg
Cost of magnets (excluding production costs)	£3,500	£58,400	£34,000

Table 10: Magnet Scalability

Unlike with active levitation systems there is no power input required for the pod to levitate, making the system economically efficient, and more reliable as it cannot fail due to a power supply failure. Another benefit to using passive rather than active levitation, such as air-bearings, is that it will take up a smaller proportion of the pod, reducing its total size and mass, thereby increasing efficiency.

The system can be relatively easily scaled up, as this can be done simply by increasing the number of magnets.

Although few, there are a number of disadvantages associated with the use of a passive magnetic levitation system. Neodymium-boron magnets are expensive and brittle, and their high magnetic strength makes them difficult to handle. As previously mentioned, it is likely that after repeated use, the magnets will degrade over time - increasing maintenance requirements and expenses of the pod. In addition, if a passive levitation system is used for a full-scale pod, and for long-distance travel, a cooling-system would be required to handle the increase in temperature of the magnets due to eddy currents.

Cost

Production costs for the Halbach arrays should not increase proportionally to the number of arrays required to be produced. This is because once the necessary equipment and machinery is obtained for production of the arrays there will be no significant extra production costs, thus increasing efficiency with scale of production.

5.1.8 Maintenance

Maintenance of the levitation skis will simply require the removal of the arrays and shielding to check the arrays are still intact. The remnant field of the arrays should also be checked regularly.

5.1.9 Cost breakdown

Having spoken to magnet suppliers, the team has received a quote for the price of the magnets. Each magnet is expected to cost £41.50. Therefore, the total cost of all the magnets, excluding production costs, would be £3,500. An estimate of the total cost of the arrays, including production and coating, is £8,000 maximum.

5.1.10 Manufacturing

Manufacturing of the arrays will be outsourced to guarantee quality and specs.

January	February	March	April	May	June	July
Finalise magnet suppliers by the end of January	Magnets will be manufactured		Testing			Ship magnets

Table 11: Manufacturing Schedule

5.1.11 Testing

To ensure the theory used in our simulations matches the experimental data, testing for the levitation mechanism will be carried out . The setup of the experiment will include a slab of conducting material, ideally the same material that is being used in the track (Al 6101-T61), and a rotating arm holding the magnetic array in its end. One end of the rotating arm will be fixed to the ground, above the slab of conducting material, the other end holding the array with the field pointing downwards (towards the conducting material). This arm will also have hinges that will allow the arm to move vertically about the centre. The spinning arm will give the array a certain tangential velocity, which is analogous to the linear velocity of the arrays relative to the tube, and by the mechanisms explained in the description of our levitation system, the array will levitate.

When magnetic repulsion is not considered, the spinning arm would be at 90 degrees to the vertical. Due to the magnetic repulsion between the arrays and the induced magnetic field in the aluminium sheet, there will be an upwards force on the array, causing the spinning arm to levitate at an angle θ_2 greater than 90 degrees. The vertical displacement from the horizontal can be measured, and used to calculate the lift force due to the magnetic repulsion of the arrays and aluminium sheet.

These numbers will be compared with those generated by the MATLAB simulations used, with different parameters to suit those in the experiment. It should be noted that this experiment begins to break down when the angle becomes large as the array is no longer parallel to the conducting surface. As our designed levitation height is 7–9mm we can make sure that the angle remains small, and the experiment will hold.

5.2 Skis

5.2.1 Introduction

The ultimate aim regarding the ski design was to provide suitable housing for the Halbach array along with providing a suspension system to mitigate any abnormalities in the track.

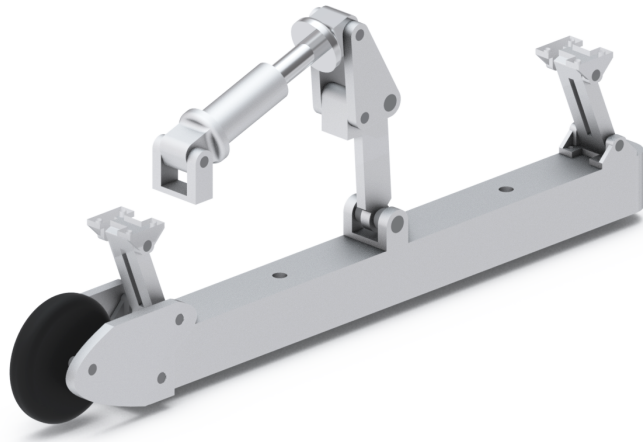


Figure 62: Proposed Ski Design

Almost all suspension systems are designed with the focus on keeping a wheel in contact with the ground. This obviously makes designing a suspension system for a levitating vehicle a challenge as many pre-established designs do not work and have to undergo changes to be able to be applied to the system.

Although a challenging experience, this is vital to maximising the longevity of the pod throughout the journey and ensure it does not undergo unnecessary fatigue due to vibrations caused by track imperfections.

5.2.2 Summary

The ski has a length of 600mm, width 50mm and height 50mm. The constraints of the ski dimensions are to reduce weight as much as possible whilst still providing a strong support for the levitation array. The material used to manufacture the ski will be the 6061 Aluminium alloy, which was chosen for its high strength to weight ratio, relatively low manufacturing costs, and its paramagnetic properties.

Torque on the aluminium skis is insignificant because the lift force acting on the skis is uniform, therefore the skis will not deform. The skis will be manufactured based on our SolidWorks models using CNC. No electromotive force (EMF) is induced as the magnetic arrays are bolted into the ski and therefore there is no relative motion between the two, meaning no currents or forces are induced in the ski.

Force applied on the skis from the levitation arrays is uniform, therefore there is only compression on the aluminum resulting in only minor deformation. Therefore, we have designed the system to have a maximum angle of 70 degrees (between the ski and the arm) and a minimum angle of 60 degrees, this will allow the ski to translate vertically without restriction. This restriction along with having a maximum distance between ski and chassis of 100mm and a minimum height of 95mm resulted in having a pushrod length of exactly 75mm. The wheels have a diameter of 110mm and a width of about 30mm, with a mass of around 250g each.

Everything regarding the suspension sub-system will be made out of a high tensile alloy steel, which is stronger and more cost-effective than an aluminium alternative. High tensile strength is especially important in the bell crank and arms holding the push rod and wheels, since they support the weight of the pod. The disadvantages regarding this particular choice of material are: weight; corrosion; and difficulty in manufacturing specific designs in this material using CNC machines. These issues should be minor when considering them for our uses and short service life, especially since steel can be coated to prevent corrosion.

Each ski will have a 110mm wheel, which will be made of Polyurethane (PU) and have an aluminium hub, in order to combine the elasticity of rubber with the durability and resistance of metal wheels. The high load-bearing capacity, mechanical resilience and vibrational damping properties render Polyurethane a suitable material for the team's chosen design.

5.2.3 Considered Solutions

Initially in the design process a suspension system similar to that of a ski mobile was chosen - where it would have a vertical shock absorber inside of a simple suspension system. However, this design was found to be unsuitable and instead a push rod suspension system was chosen. The initial design had many benefits such as being simple to manufacture and test. However, there were drawbacks to this design that meant it was not the best option, such as difficulty in ensuring the shock absorber would work effectively in the system, and be correctly sized. However, the final decision was made due to a lack of space available for the vertical shock absorber (less than 100mm), which would make the shock, a pneumatic rear shock from a mountain bike with length of roughly 200mm, unable to fit into this space. Therefore, the final design is now based on the push rod suspension, which translates the vertical displacement of the ski into a horizontal travel through the shock absorber, via a bell crank system.

5.2.4 Chosen solution

The final design for the suspension system is loosely based around that of an F1 car: there is one main pushrod through which the majority of the force acts and then two pivot points on either side of the push rod control the motion of the vehicle/ski. As the pod will experience much smaller bumps than a conventional vehicle, a bell crank system has been used to translate vertical displacement into a larger horizontal displacement which then relays through the shock absorber. A crank ratio of 5:2 has been used meaning that for 2 mm of vertical change the shock will experience a 5 mm change. This ratio is included due to the relatively small step changes in the track. Displacements in shocks of only 1mm, renders very small damping forces. Including this ratio means distances and therefore interactions are more meaningful. As the spring and damping forces are increased by the square of this ratio we are careful to not make it too large as this will result in too stiff suspension.

5.2.5 Shock Absorbers

The shock absorber is used in the suspension system of the ski to help dampen any imperfections of the track that will result in vertical displacement of the ski. The shock absorber is a pneumatic rear shock from a mountain bike of length 200mm and mass 400g. For setting up the shock absorber, a fast rebound speed will be required as the pod is expected to cover a large number of small imperfections (roughly 1mm) many times a during the run, and therefore the shock needs to return to its initial setting as rapidly as it can.

For the compression settings of the shock, it needs to be setup to ensure that shock is not too rigid to not allow travel in the vertical displacement, as expected travel of the system is expected to be a maximum of 5 mm (2mm vertical travel turning into 5mm from the 2:5 bell crank ratio), as the shock has a maximum stroke of approx. 50mm we will not be in danger of reaching the end of this stroke. Therefore, high compression resistance is unnecessary.

5.2.6 Wheels

To transport the pod and to assist it during the first phase of travel before levitating, the pod will be provided with a set of four wheels. They will be attached to the skis and ensure the skis rest 5mm above the track. After having reached the take-off speed, the pod will start levitating and reach a maximum levitation height of 9mm, this means that the wheels will be 4mm above the floor level. Therefore, the system can use static wheels rather than retractable wheels, saving on mass, complexity and power consumption.

5.2.7 Simulations

Structural

As shown in figure 63, maximum deflection is 0.4mm in compression on the ski and occurs in the ski itself when the shock is fully collapsed.

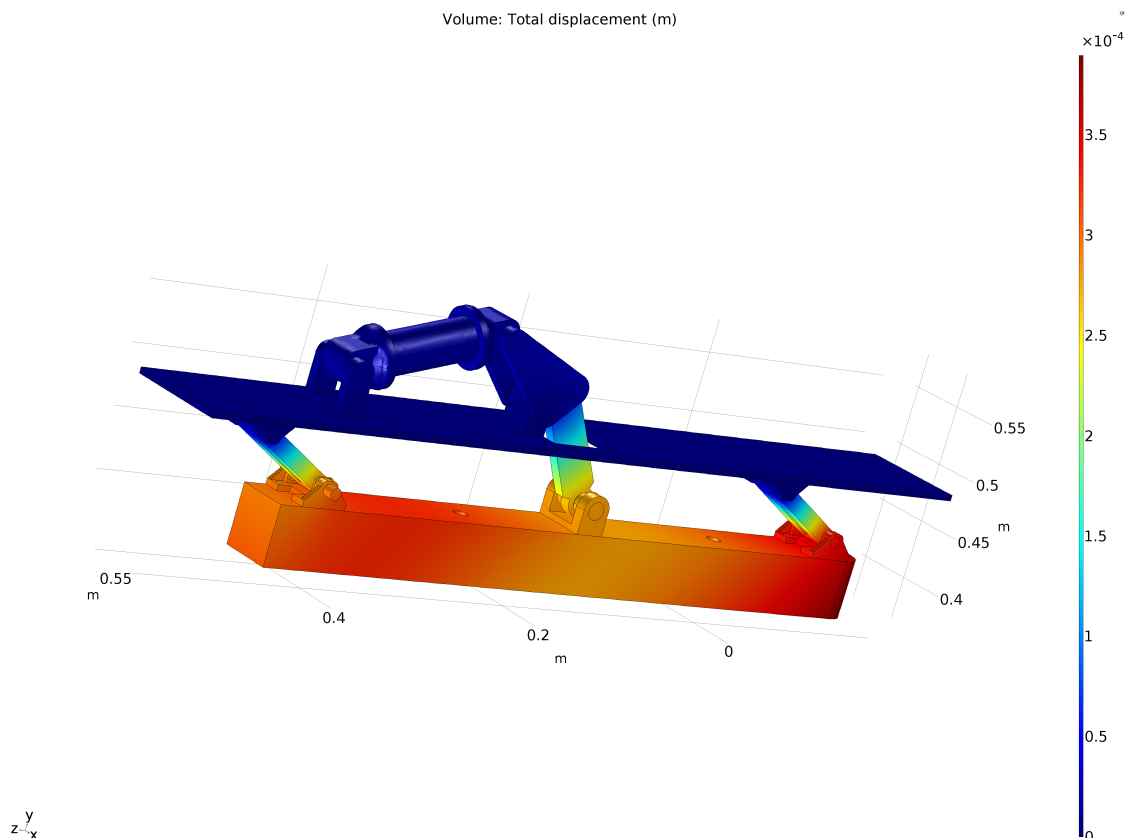


Figure 63: Displacement of ski when suspension is bottomed out

Fault Tolerances

By design, the system employs previously tested technologies and is simple so is expected to be highly reliable. As long as maintenance of the suspension components is not neglected there should be no possibility of them failing during the run. If the shock absorber is off-nominal, the oscillations of the pod would be affected but it would not result in a crash. This is due to the levitation system relying on passive levitation which will successfully keep the pod levitating.

Vacuum Tolerance

We have previously tested shock absorbers in a vacuum, and incurred no issues. Nonetheless, we shall still vacuum test the new shocks, but we expect no issues. We shall test that the shocks hold their pressure in a vacuum for an extended period of time. We will then repeat by holding the shock compressed (or simply upping the pressure to simulate compression) to double check that the higher pressures can also be maintained.

5.2.8 Scalability

Size & Mass

As the scale of the pod increases, so does the levitation/suspension sub-system. However, if the theoretical mass of the full-scale pod is approximately 8 tonnes, that would mean a sixteen times increase in the weight of the pod hence a proportional increase in the force acting on each shock absorber, as the force acting to counteract the weight of the pod is almost linearly related to the weight. Thereby the spring constant would also increase about sixteen times if we want to retain the same length contraction as before. The bell crank would increase in size accordingly, retaining the 2:5 ratio. The skis and the wheels would of course increase proportionally as the rest of the system to accommodate for the increase in the magnets needed per ski and for the increase in the tensile forces within the skis. Also the fact that the wheels will have to increase in size means possible changes in the design of the mounting of the wheels on the ski if the same levitation height is to be retained.

Cost

The ski system scales with mass to accommodate for the larger forces involved. This includes both the physical dimensions of the ski and the number of magnets required for levitation. Therefore, the shock absorbers will have to be replaced with larger and more expensive shocks to accommodate for this increase in mass.

Maintenance

The maintenance of the scaled version will need to consider the same cases as the original version i.e. wear on the wheels and possible wear on the suspension, hence the methods employed for the maintenance of the original pod will be identical for the scaled version. Of course larger and more complicated components required in the scaled version, will have higher maintenance costs.

5.2.9 Cost breakdown

Component	Part	Quantity	Cost	Total Cost
Ski	1220*70*70 Aluminium bar	2	£95.88	£191.76
Various Components	Steel Sections	4	£100	£400
Shock Absorber		4	£500	£2000
Wheel		4	£35	£140

Table 12: Estimated Ski Cost Breakdown

5.2.10 Manufacturing Timeline

122

	January		February		March		April		May		June		July		
	1st half	2nd half	1st half	2nd half	1st half	2nd half	1st half	2nd half	1st half	2nd half	1st half	2nd half	1st half	2nd half	
Ski					CNC job is complete. All necessary drilling/cutting jobs are made										
Suspension arm and connectors			Job request to the University for CNC		CNC job is complete. All necessary drilling/cutting jobs are made										
Bell crank system			Order materials/parts	Laser Cut Request	Laser cut complete	Testing (by applying forces)									
Shock absorbers					Testing (Applying forces and in vacuum chamber) to investigate spring constant, rebound										
Brackets			Job request to the University for CNC		Assemble to relevant arms/brackets										
Joints/pins															
Total system									Completion of the assembly		Testing		Repair in case of testing failure		

Figure 64: Ski Manufacturing Timeline

5.2.11 Testing

Testing will be done on the system and components prior to competition. Especially on the shock absorber because as it is pneumatic, it needs to be tested in a vacuum to ensure it keeps its performance in this environment. We do not expect to encounter any issues concerning pneumatic cylinders in a vacuum as this technology was used on our previous pod and encountered no issues.

Scale model testing will be undertaken on the ski system using one of the four skis in a vacuum environment, which will try to model the expected conditions that will be faced by the ski during the competition. This will look into the fine tuning of the shock absorber settings in detail to produce the most effective results; mainly investigating the effect a near vacuum will have on the chosen shock absorber.

Additionally, the wheels will be spun up to their rated speeds and have maximum speeds confirmed.

5.3 Emergency Brakes

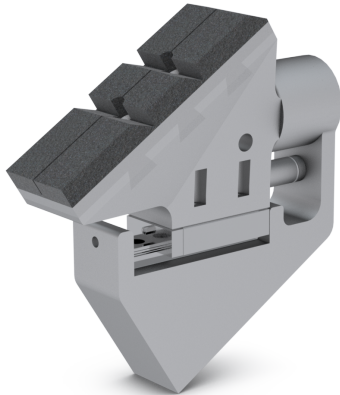


Figure 65: Emergency Brake Design

The majority of frictional braking systems that have been widely adopted throughout society rely on the braking against a rotating drum or disk. This is because of how friction pad materials and the drum or disk bed together to minimise wear and maximise braking performance. As the use of frictional braking against a linear system is not widely researched and implemented, the design needs to tolerate the much higher than normal wear rates and degraded performance.

Furthermore, as a result of how the tube and I Beam have been manufactured and assembled, the braking system needs to be able to tolerate up to a 1mm lip between each 3.84m section of the central tube I beam. This further increases the wear rate of the frictional pad material, as the lip will effectively cut material off the pad and preventing uniform braking performance.

5.3.1 Emergency State

An emergency state can be constituted as a navigation or positioning problem such as the loss of the position of the pod within the tube; stability problems such as excessive movement of the pod towards or away from the rail; insufficient braking distance for the Halbach brakes to prevent a crash; total loss of power to the pod or to any subsystem within it or a propulsion (primary braking system) issue.

5.3.2 Summary

The emergency braking system will use a total of 8 wedge brake modules, arranged in four pairs (one on each side of the track I beam). Each brake module is 190 x 150 x 50 mm (LWH) in size and weighs a total of 3.165 kg. The weight distribution is shown below:

Part	Mass (g)
Gas Spring	70
Brake Pad	840
Linear Rail	336
Electromagnet & counterpart	393
Brake Wedge	736
Brake Mount	790
Total	3165

Table 13: Estimated Ski Cost Breakdown

In aims to minimize weight and allow the system to operate unhindered in the magnetic environment, aluminium 6082 alloy was used in as many parts as possible. As shown in the simulations section, the finite element analysis of the brake wedge and brake mount are seen to withstand the forces exerted on them with a safety factor of 2 without any major risk for damage.

As this is an emergency braking system, it is required to have a power-redundant actuation system. This is done in each module through the use of a pre-compressed gas spring that is held back by an electromagnet.

During the idle state of the emergency braking system (when the pod's systems are operating normally and they are not in use), the electromagnets use 6.5W each to hold the brakes retracted, summing up to a total of 52W to keep all 8 brakes retracted.

5.3.3 Considered Solutions

Throughout the initial stages of designing an emergency brake system, the concept of a pneumatically actuated brake system was our main focus. The original idea consisted of four pivoting arms, each individually actuated by a pneumatic piston operating at 7 bar. With a total system mass of under 9kg and the dimensions of a brake unit being 265 x 295 x 75 mm, this seemed like a viable system. However, with further research into frictional materials, we came to a realisation that we had greatly underestimated the amount of frictional brake pad material needed. Because of this issue, other designs of frictional braking were investigated.

As our knowledge of how friction brake systems worked and the technical difficulties in that arise from the friction pad material itself, a wedge brake design was chosen. This new design allowed us to greatly increase the frictional pad contact surface area from 12.5 cm^2 to 75 cm^2 per brake module, while also allowing us to input less force into the system.

5.3.4 Chosen Solution

Wedge brakes work by using the kinetic energy of the vehicle to mechanically amplify the braking pressure applied to the brakes. Doing so allows for smaller actuation forces to be applied for the same braking pressure in the system.

Shown in Figure 66 is a free body diagram representation of the wedge block during braking where the velocity of the central I Beam relative to the wedge block is given by V_I .

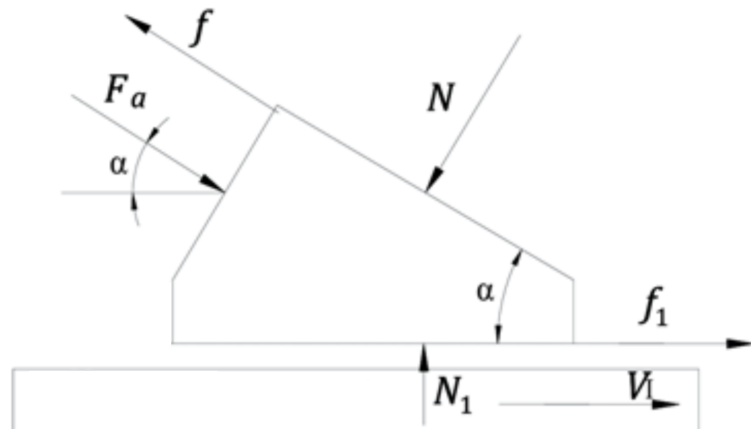


Figure 66: Free Body Diagram of Wedge Block [7]

F_a = actuating force

N = normal force between wedge and roller support

f = frictional force of roller support

μ = frictional coefficient of roller support

N_1 = normal force between wedge and I-beam

f_1 = frictional force between wedge and I-beam

μ_1 = frictional coefficient between wedge and I-beam

By evaluating the forces in both the x direction (tangential to the I-beam) and y direction (perpendicular to the I-beam), the equilibrium forces are as follows:

$$X : \quad F_a \cos \alpha + f_1 = f \cos \alpha + N \sin \alpha$$

$$Y : \quad F_a \sin \alpha + N \cos \alpha = f \sin \alpha + N_1$$

Solving the equations simultaneously by using the fact that $f = \mu N$ and $f_1 = \mu_1$ and rearranging in terms of f_1 expresses the frictional force provided by a wedge brake:

$$f_1 = \frac{F_a \mu}{\cos \alpha (\tan \alpha - \mu) + \mu_1 \cos \alpha + \mu \mu_1 \sin \alpha} \quad (2)$$

To achieve a 2.5g deceleration of the 500kg pod, a 12.3kN frictional force is required. Splitting this force between the 8 brakes, results in a 1.5kN frictional force per brake. Working with the specifications of the Wilwood PolyMatrix Q brake pads, that have a frictional coefficient range of 0.38 to 0.47 dependent on temperature (as shown in the section ‘Frictional Pad Material Choice’), the wedge angle and applied force were chosen to be 0.555 radians (31.8°) and 460N. An angle closer to the arctan of the highest frictional coefficient (the point at which the wedge brake is most effective) was not chosen due to the desire to have a more linear deceleration characteristic across the operating temperature range of the pads. Using the angle and force combination above, at a pad temperature of 35°C , the deceleration will be 1.4g. At a pad temperature of 250°C , the deceleration will be 2.7g.

If the system would be operating in an ideal and theoretical scenario, the maximum deceleration would be slightly above the maximum designed deceleration of the pod. However, the frictional pads will not achieve a frictional coefficient of 0.47 in the applied system, as the value was achieved in a system with a rotating disk, where a third body layer would form between the disk and the pad, increasing performance while decreasing wear rate.

Friction Pad

This system also allows for the frictional performance to be easily adjusted based on the performance of the frictional pads. This is done by changing the angle, the applied force, or both in unison through testing and optimisation to reach the desired performance of the braking system.

The emergency braking system has been designed and analysed using Wilwood PolyMatrix Q brake pads as they fulfil all necessary requirements set on frictional braking systems. The team is working on optimizing the design through the optimization of the brake pads. This work is happening alongside a respected frictional brake company to try to get the best pads designed for our specific use and design.

Properties of Wilwood Polymatrix Q:

The pad material has, according to Wilwood, been produced with consideration of being used against aluminium with a low wear rate at low to mid temperatures and medium friction. The frictional coefficient variance with temperature is shown below, where the frictional coefficient for Compound Q is seen to vary between 0.38 and 0.47 depending on temperature. [7]

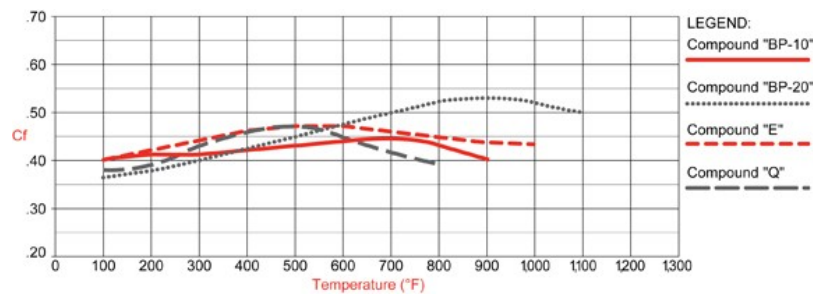


Figure 67: Compound Comparison

5.3.5 Simulations

Structural

To ensure that the components would operate as designed, a finite element analysis was made to ensure that they were operating within the material parameters. Below are the FEA's of the wedge block and the mount, showing both the material deflection and the von Mises stress plot. The analysis was performed with a safety factor of two, meaning that the forces applied to the model are twice as large as what is expected during operation. It is seen that both components are safe to use as designed. Furthermore, it shows that work can be done to minimize weight by removing material in the structurally strongest parts.

Wedge block:

As seen in Figure 68 overleaf, the wedge block experiences a maximum deflection of 60 micrometres and a von Mises stress of 25MP, which is well within the material limits of aluminium.

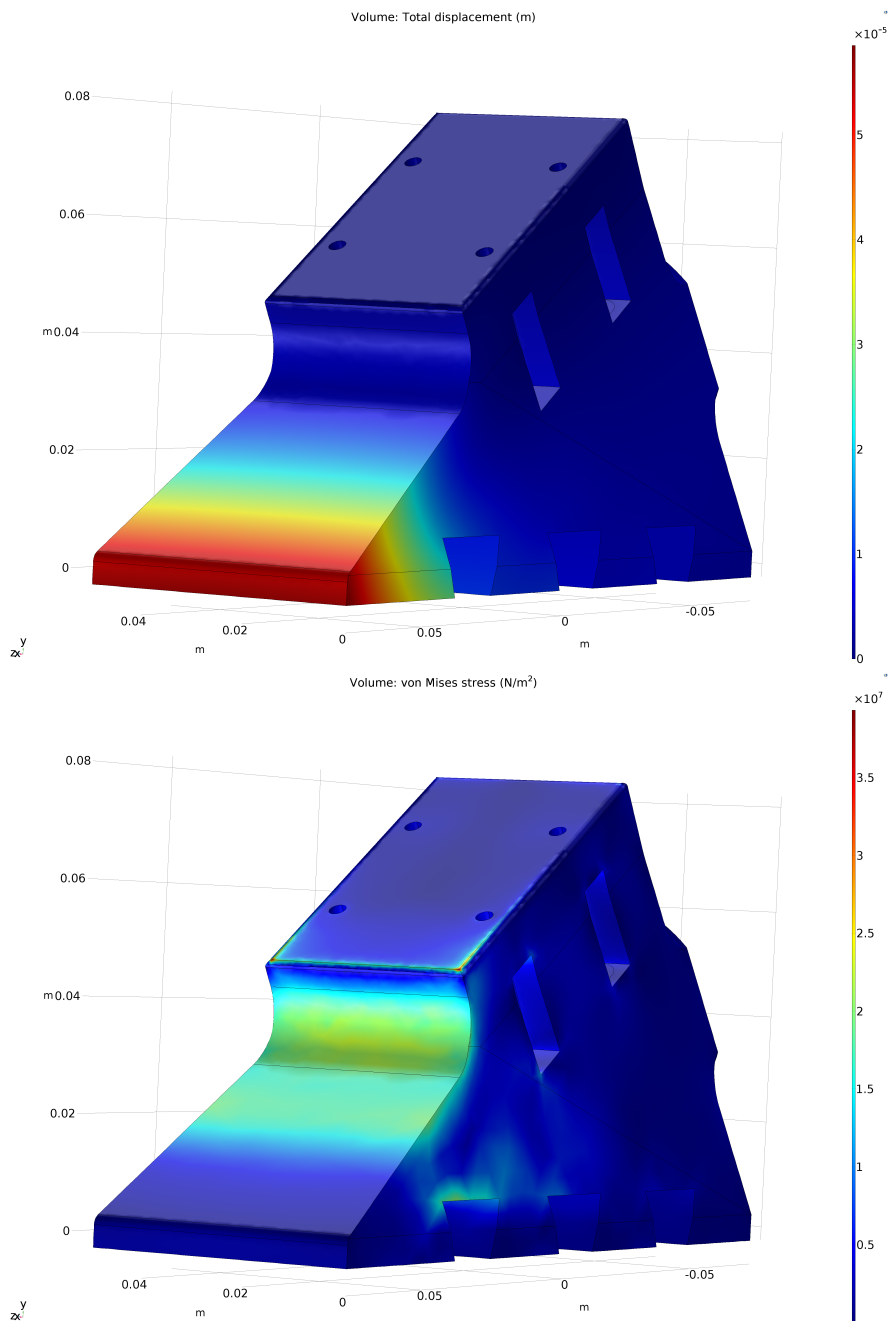


Figure 68: Deformation (top) and Stress (bottom) Wedge Simulations

Mount:

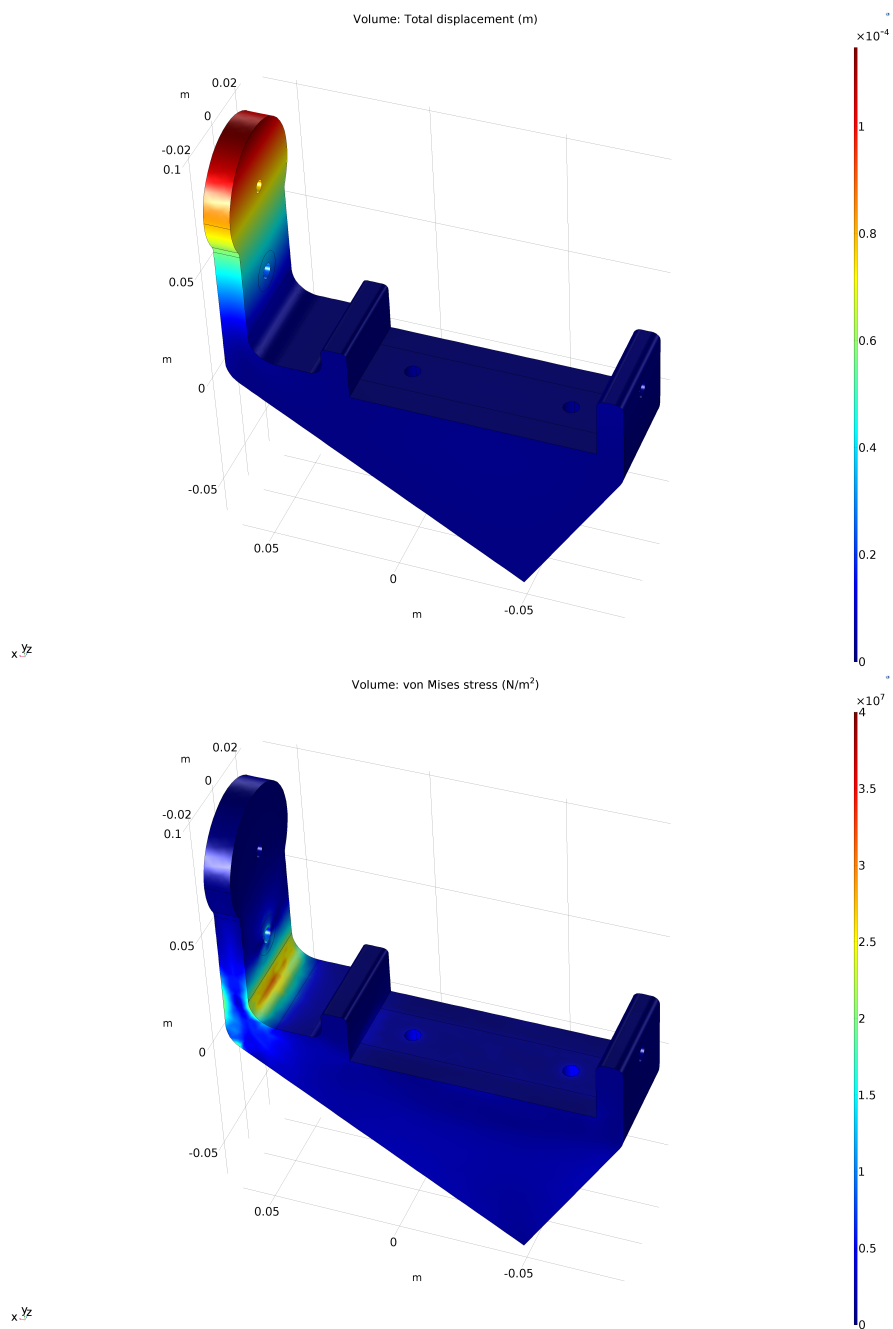


Figure 69: Deformation (top) and Stress (bottom) Mount Simulations

As seen in figure 69, the mount for the brake experiences a maximum deflection of 0.1 millimetres and a von Mises stress of 30MP, which is well within the material limits of aluminum.

The mechanical hold will make use of a pin design which can be inserted into the wedge to hold it in place. The mechanical hold will be made of 4340 steel to ensure a safe and reliable method of keeping the brakes retracted. The mechanical hold is shown below alongside its finite element analysis which shows that with a safety factor of 2, the mechanical hold is well within its material limits with a maximum deflection of 0.6mm and a maximum von Mises stress of 300 MPa when evaluated with a safety factor of 2.

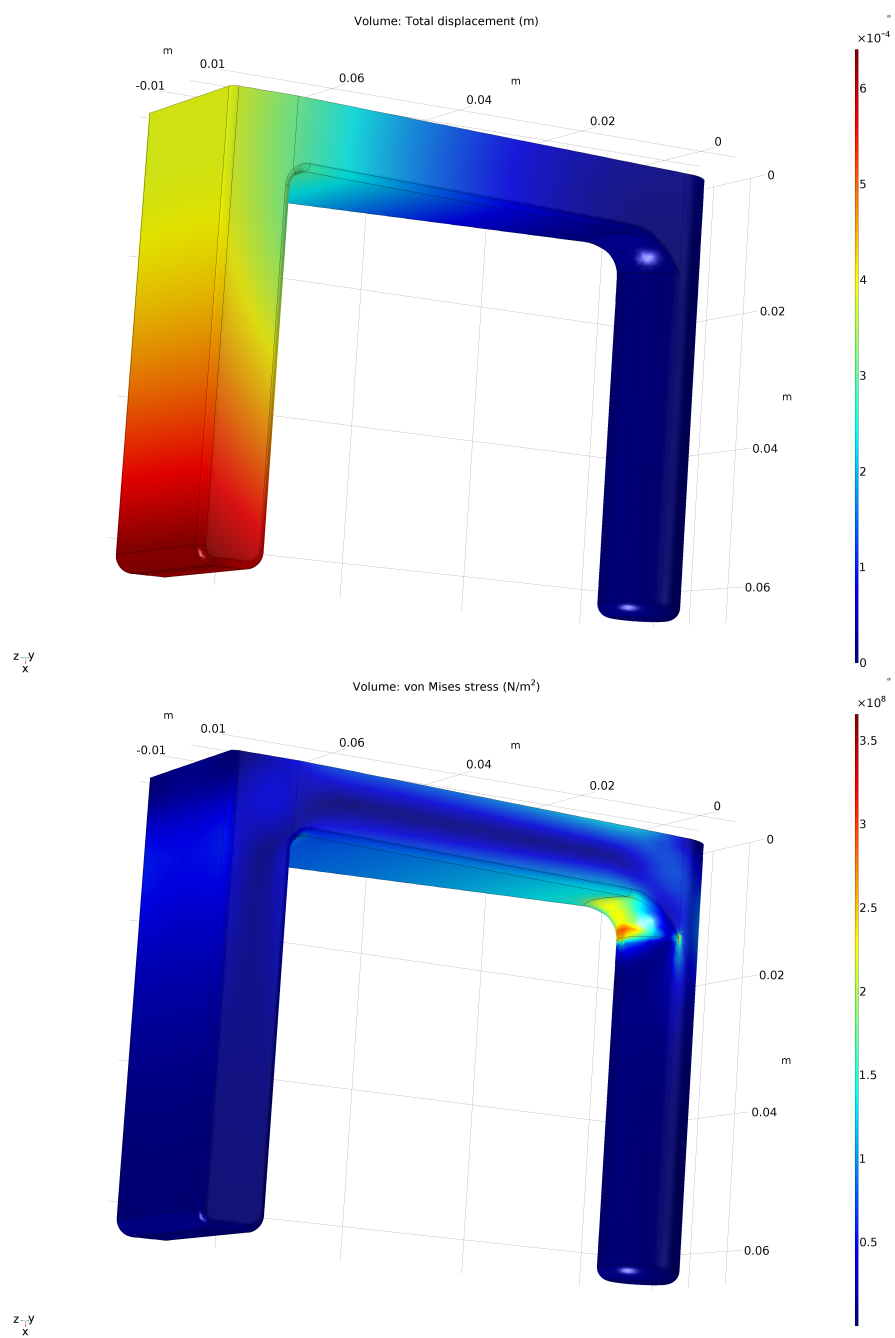


Figure 70: Deformation (top) and Stress (bottom) Mechanical Hold Simulations

5.3.6 Safety

Fault tolerances

As the frictional coefficient of friction brakes is dependent on the temperature of the brake pads and the brake force has a positive feedback as the brake force is used to drive the brakes into the rail amplifying the brake force, a small change in the initial temperature of the brake pads have a significant effect on the braking profile. The graphs below illustrate this effect with the minimum and maximum expected operating temperatures of the brakes.

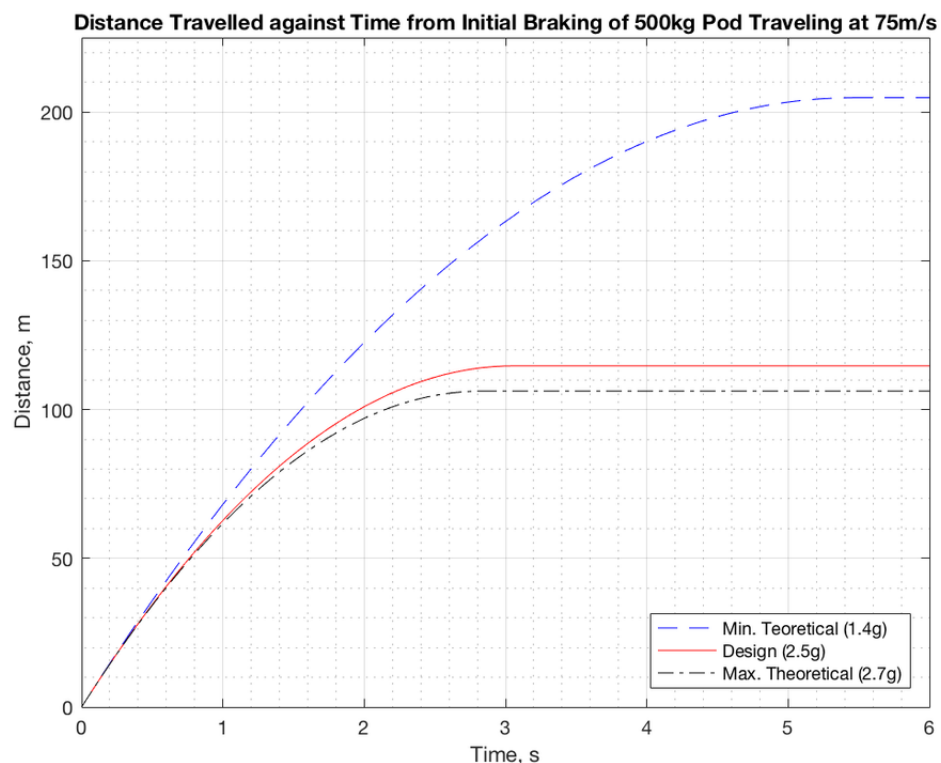


Figure 71: Distances Traveled After Braking

Figure 71 shows the distance the pod has traveled before a complete stop at the designed deceleration of 2.5g and the theoretical maximum (2.7g) and minimum (1.4g).

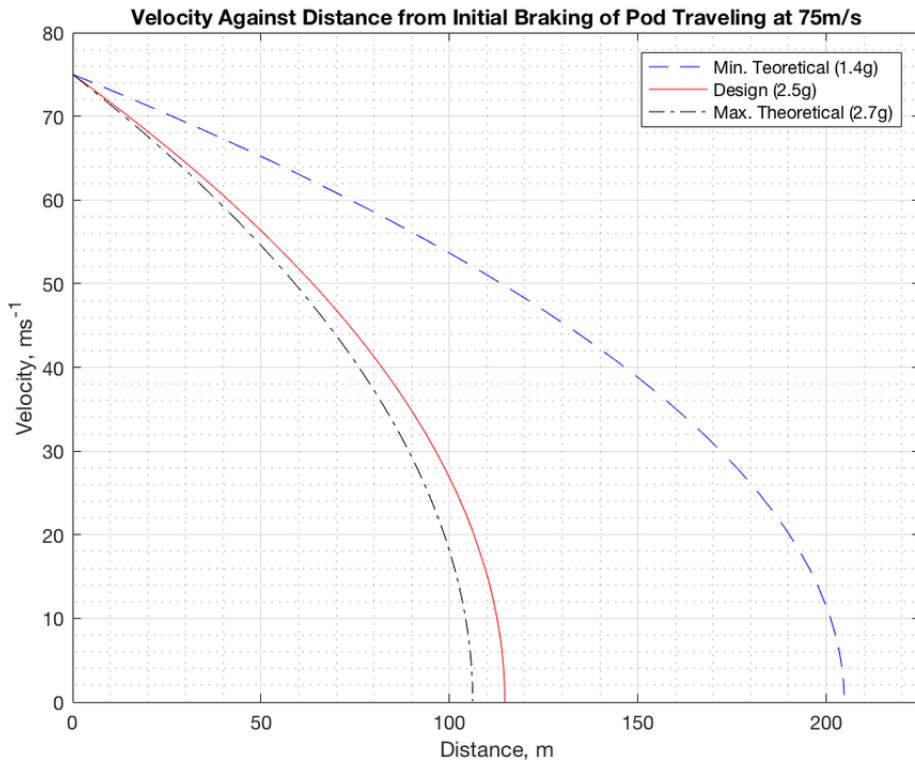


Figure 72: Velocities After Braking

Figure 72 shows the distance the pod has traveled before a complete stop at the designed deceleration of 2.5g and the theoretical maximum (2.7g) and minimum (1.4g).

The design of the system is such that each brake module is independent from each other. As a result, even if all but one fail, the pod would still decelerate to a stop. However, this deceleration will be massively degraded.

To prevent simultaneous braking and acceleration, the power supply to the electromagnets that hold the brakes back is also connected to the signal wire of a normally open contactor which connects the motors to their power supply. In the event that the emergency brakes are deployed, either as a result of a fault or manual trigger, the motors will be automatically disconnected, preventing the possibility of braking and accelerating at the same time.

Vacuum Tolerance

Gas springs will be tested in a vacuum, in a similar fashion to the shocks, to test that they hold their pressure over an extended period of time.

5.3.7 Control System

The emergency braking system will be controlled directly by a normally open solid state relay such that if power is lost, the electromagnet preventing emergency braking is demagnetised causing the emergency brake to activate. Simultaneously, the same signal that disconnects the electromagnet will also disconnect power to the motors such that a scenario where both the brakes and the motors are active is avoided. Figure 73 describes the hardware implementation of the emergency braking.

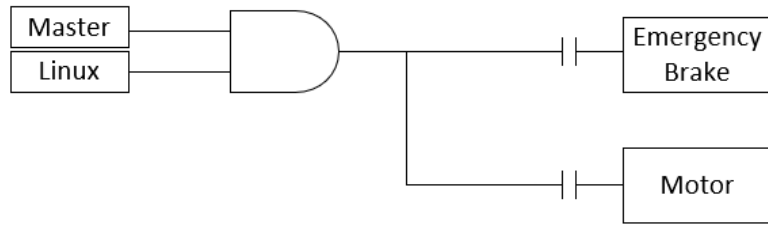


Figure 73: Emergency Brakes Control System

5.3.8 Scalability

Size & Mass

Working with the assumption that the scaled-up HypED Hyperloop system has a mass of 8 tons when empty and between 10 to 12 tones when loaded, the feasibility of a scaled up version of the current emergency braking system can be determined. Assuming that the structural design of the pod allows for a maximum deceleration of 2.5g (when empty), the emergency braking system would need to exert 196200N of frictional force. Using the designed system, this would require 128 wedge brakes.

As the system makes use of the same brake module throughout the length of the pod the system is easy to scale up by adding more brake modules to the system. Despite the system being easily scalable, it is in practice impractical and costly

at large scales. With a total system mass of 405 kg and 16m on each side of the I-beam, it will add a lot of mass to the total pod for a system that should ideally never need to be used.

On top of the mass and length limitations of this emergency braking system when scaled up, the electromagnets would draw a total of 832W from the battery of the pod. Not only does this add mass through the need of a larger battery to accommodate the extra power draw, but it also vastly increases the needed power for longer distances. The system would draw 0.14 kwh of energy every ten minutes of operation, causing it to waste a lot of energy.

Cost

As discussed above, we would need 128 wedge brakes to work in a full scale system. Therefore, if the costs are linear, then to implement the system would cost north of £36,000. In full scale development the economies of scale would reduce this figure per pod.

Maintenance

The maintenance of the system would also be costly both in terms of repairing broken parts and the amount of time required to do so. Regular maintenance checks would be required to ensure that all linear rails are properly lubricated, all electromagnets function properly, the gas springs are not damaged in any way and that the braking pads are not damaged and need replacing.

Furthermore, if the emergency brakes would have required to actuate and stop the pod, all brakes would need to be retracted before being able to move the pod. All of the brake pads would also be required to be replaced as they are designed to be used for a single stop.

5.3.9 Cost breakdown

Shown below is a bill of materials required to build the emergency braking system outlined. Machining and labour costs are not included in this calculation. Conversions of other currencies are done with the exchange rate on 30/11/17. The total system cost is the total cost of 8 brake units.

Item	Units	Manufacturer	Part number / Identification	Source	Per Unit Cost	Total System Cost
Gas Spring	1	Special Springs	M70-038-A-RD	Berger Tools LTD	£25.81	£206.48
Frictional Material	1	TMD Friction	-	TMD Friction	60€ (£52.88)	480€ (£423.03)
Brake Pad Back-plate	1/8	Steel Express	EN24T 1360mm - 60mm - 30mm	Steel Express	£14.70	£117.50
Linear Guide	1	IKO	MLG 20C1 HS2	IKO	£33.59	£268.72
Linear Rail	1	IKO	LWL20R95BHS2	IKO	£17.84	£143.52
Electromagnet	1	Magna-C	81050	Magna-C	54.87€ (£48.36)	438.96€ (£386.86)
Electromagnet Counter Surface	1	SCG Industries	2" – 500mm	SteelCityGav (Ebay)	£3.73	£29.85
Brake Wedge	1	Aluminium Droitwich	2 $\frac{1}{2}$ – 7 – 100mm	Alum - Droitwich (Ebay)	£35.04	£280.32
Brake Mount	1	Aluminium Droitwich	2 $\frac{1}{2}$ – 8 – 150mm	Alum - Droitwich (Ebay)	£50.68	£405.52
				Total	£282.73	£2261.80

Table 14: Emergency Brakes Cost Breakdown

5.3.10 Manufacturing

Manufacturing Details

1. The frictional material will be mounted to a custom manufactured steel backplate which will allow the brake pad assembly to easily slide into the wedge and be easily replaced.
2. Wedge and brake foundation will be made using CNC to ensure the high accuracy of all dimensions and avoid big tolerances.
3. Slider, gas cylinder, electromagnet and all fixings will be purchased.
4. The important advantage of this design is that no abrasives will be used except for the friction pad, which will be manufactured by the supplier. Friction pad will however be tested to ensure that it can handle the temperatures and forces in this application.
5. Steel core will be attached to the wedge with the screws
6. Slider, gas cylinder and electromagnet suppliers specify the installation methods and these methods will be followed in brakes manufacturing.

Manufacturing Timeline

140

	January		February		March		April		May		June		July	
	1st half	2nd half	1st half	2nd half	1st half	2nd half	1st half	2nd half	1st half	2nd half	1st half	2nd half	1st half	2nd half
Wedge			Latest material arrival		CNC job is complete. All necessary drilling/cutting jobs are made		Part is complete							
Friction pad			Job request to the University for CNC		Cutting to the correct size									
Slider					Testing (temperature, pressure, wear)									
Gas Cylinder					Testing (by applying forces)									
Iron Core					Testing (under pressure)									
Electromagnet					Cutting to the correct size	Part is complete								
Supports (connection to the chassis)			Ordering all parts needed for connection to the chassis		Testing with a power supply									
Total assembly					Latest Parts arrival	Finishing the parts i.e. drilling, cutting to the size, welding	Assembling together							
					Assemble the wedge: assemble wedge, friction pad, slider and all fittings together		Assemble gas cylinders and electromagnet with a wedge and an iron core.		Completion of the assembly		Testing		Repair in case of testing failure	

Figure 74: Emergency Brake Manufacturing Timeline

5.3.11 Testing

Component Test

The testing of the components will be both tested independently and as a complete assembly. This is to ensure that not only the individual components work as advertised, but they also work in unison as desired.

1. The electromagnet will be tested by applying the operating voltage and power and ensure that it can hold the rated force of 830N.
2. The linear rail will be tested by applying the rated load and ensure that the rail functions.
3. The gas spring will be tested by compressing the spring and ensuring that it exerts the correct force at the different extensions. They will also be tested in a vacuum to ensure that they operate as expected.
4. The testing of the brake pad is difficult as implementing a linear testing system is difficult and costly. As a result the pads will use a rotating spinning disk of the same material and thickness as the I-beam in the tube. This will provide a rough indication towards the performance and wear of the pads, however these results will need to be compared to theoretical simulations to provide more accurate data.

Component testing will occur in March – April, while the total assembly testing will occur in June.

Functional Tests

Right before the launch two tests will be performed to ensure that the system is functioning:

1. Measure the current and voltage delivered to the electromagnets to ensure that they are operating at the correct power and thus exerting the correct force.
2. Ensure that the mechanical switch is active. The switch is installed in such a way such that it is activated when the wedge is retracted and makes contact with the electromagnet.

5.4 Lateral Rollers



Figure 75: Proposed Design

5.4.1 Introduction

Several systems are employed to improve pod stability in multiple directions. Halbach arrays used in the levitation skis provide little suspension but vertical stability is further improved since this system is also mounted onto shocks. Attached to these skis are low speed rollers which allow the pod to be moved and loaded into the tube but will lift off during high speed operation.

As mentioned earlier, the Halbach wheels create lateral forces away from the rail that reduce lateral movement. To prohibit the Halbach wheels from making contact with the rail, lateral rollers keep the pod in line with the track, they contact with the upper part of the rail to minimise the contact area.

Together these systems significantly improve the overall stability of the pod.

5.4.2 Summary

Four lateral rollers made of hard polyurethane are rigidly attached to the far front and back of the chassis. They provide lateral stability and also to prevent the Halbach wheels from hitting the rail. There is a 2mm gap between the rollers and the rails.

5.4.3 Considered Solutions

Material Selection

Key properties for the wheel material during the selection process were hardness, impact resistance and abrasion resistance.

Material	Shore Hardness	Static Coefficient of Friction	Notes
Styrene Butadiene Rubber (SBR)	50	c.0.6	Like natural rubber but harder and with better abrasion resistance
Polyurethane	95	c.0.3	Hard polymer with excellent abrasion and impact resistance

Table 15: Hardness and Coefficient of Friction of Materials

The Steady State Wear Equation is $V = K \frac{PL}{3H}$, where:

V = volumetric wear (equal to Residue Deposited)

P = normal load (mg)

L = length that material slides for, calculated from time for wheel to spin up to speed

H = Shore Hardness

K = Standard Wear Coefficient

$$\therefore V \propto \frac{1}{H\sqrt{V}}$$

Increasing both hardness and friction coefficient will reduce residue deposited.

\therefore If SBR is used approximately 1.3* more material will be deposited on the track than polyurethane.

All things considered, polyurethane was chosen for the lateral rollers' material.

5.4.4 Simulations

Structural

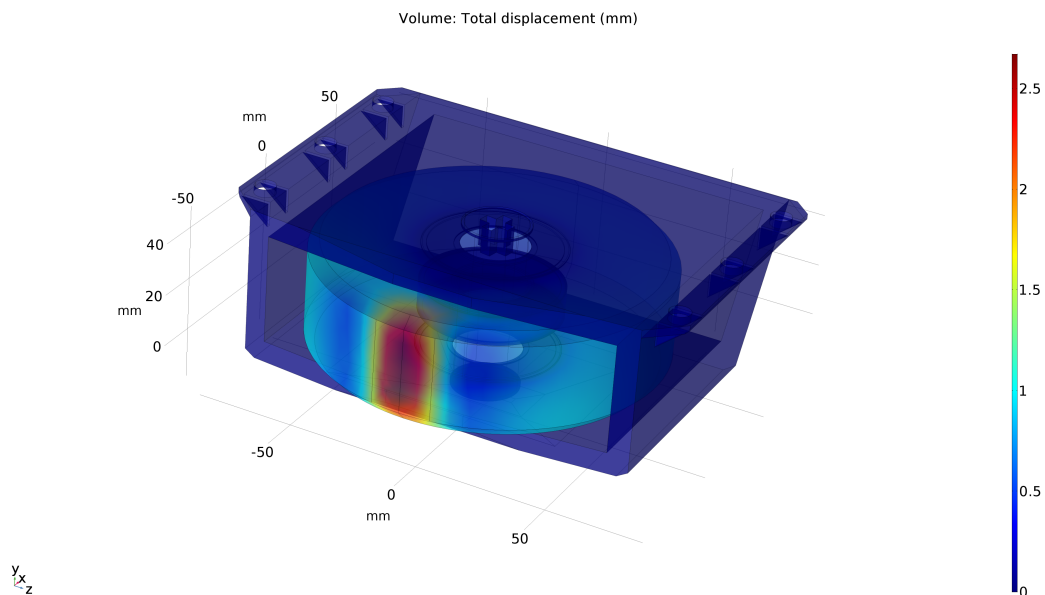


Figure 76: Insert caption

The above simulation shows that the wheel will deform much more than any of the structural components. This makes sense as the wheel is made from relatively soft plastic. This deformation adds to the “spring/damper” of the stability mechanism whilst remaining structurally sound.

5.4.5 Safety

Fault tolerances

The table below shows failure modes and how they can be avoided.

Failure	Mitigation
Bearing attachment failure that allows the wheel to become loose or detach from the pod	All the components are housed inside a box so that the rest of the pod and the rail are undamaged if a component becomes loose
Bearing failure which prevents rotation of the roller	The hard polyurethane will allow the roller to skid on the rail when contact is made
The wheel attachment structure deforms so that the assembly is intact, but the wheel may be in the wrong position.	Tests will be done to make sure that neither the metallic structure or the plastic surface of the wheels will deform more than allowed under operating conditions.

Table 16: Failure Modes of Lateral Rollers

5.4.6 Scalability

Size & Mass

The lateral stability system is custom designed for a 500kg pod and the same materials may not be able to be used on an 8-tonne full size Hyperloop pod travelling over 1000km/h. This is mainly due to mass constraints that would become an issue for larger rollers with large inertia that would slow down the pod if they made contact with the rail.

With refinement in the design of a Hyperloop pod, we would ideally want to remove the lateral stability wheels from the design altogether. Instead one would implement an emergency brake system that could also be used to laterally stabilise the pod if the lateral stability became compromised. This system could use similar technology as the levitation skis - where arrays of magnets are used to create a lift (or repulsion) force. Clamping the pod onto the rail with these arrays would passively stabilise the pod when it started veering off the axis of the track. A simple wheel setup will not be appropriate when at 1000 km/h.

Mass and dimensions of the lateral rollers are shown in table 17

Part	Dimensions (LxWxD in mm)	Mass	Materials
Lateral rollers	D130x40	3.6 kg	Aluminium and Polyurethane
Roller housing	260x60x202	2.8kg	Steel
Shaft	25D	0.3kg	Steel
Bearings	52Dx25dx15	0.13kg	Steel

Table 17: Lateral Roller Dimensions

Cost breakdown

A bill of materials for the lateral rollers is shown below. This is excluding labour and machining costs.

The total system cost is for 4 rollers.

Item	Units	Manufacturer	Part number / Identification	Source	Total System Cost
Bearings	8	RS Pro	6205-2RS	RS Components	£25.68
Shaft	1	SKF	LJM25X1000ESSC2	RS Components	£48.84
Steel tube	1				£50
Liquid Polyurethane	12kg	Polycraft	7536	MBFibreglass	£192
Total					£316

Table 18: Bill of Materials for Lateral Rollers

5.4.7 Manufacturing

Procedure

The roller will be made using an inner aluminium plate for support and an outer mould. Any sized wheel can be made to our specification by using the moulds to set the inner and outer diameter of the wheel as well as the diameter. Additionally, back up wheels have been selected to fit the purpose if our self-manufactured wheels are not up to standard. The shaft will then fit through the centre of the aluminium plate. This has holes throughout so that the plastic hardens round the support and is held firmly in place.

This part will be manufactured by cutting 130mm off a standard rectangular steel tube at a 33° angle. Protruding sections used to attach the housing to the module will be made using small steel plates with triangular pieces for support welded onto the casing. An additional plate may be placed between the housing and the module to deal with any alignment issues.

Supports must be added above and below the housing the fix in the shaft in place and prevent them from making contact with the wheel. The bottom support will be threaded so the shaft can screw into place.

Buying a standard shaft off the shelf and cutting to our requirement will suffice. The shaft will be threaded at one end and bearings will be press fit onto it — all separated in the middle by a 10mm spacer. There will be additional spacers above and below the wheels to prevent vertical movement. A slot must be cut into the unthreaded end so that the shaft can be tightened and loosened.

Our method of attaching the module to the shaft will provide some flexibility for positioning the subsystem. Using bolts sliding into slots then filling the gaps with wedges to position the roller will allow this. Washers above the wedges should keep everything locked in place.

Manufacturing Timeline

149

		January		February		March		April		May, June and July	
		1st half	2nd half	1st half	2nd half	1st half	2nd half	1st half	2nd half		
Roller		Test ratios and setting conditions of the 2 part mix to maximise strength and abrasion resistance		Job request to the University for CNC		CNC job is complete. All necessary drilling/cutting jobs are made	Make a complete wheel with the optimal polyurethane mix from the testing stages				
Housing								Weld support sections to the main housing part			
Shaft		Order Parts		Cut shaft to size, thread one end and make hole at top to screw into the housing							
Bearings & spacers			Cut spacers from a small diameter pipe					Check alignment of all parts	Complete Assembly	Testing	Time allocated for any changes or repairs that are required
Total Subsystem											

Figure 77: Manufacturing Timeline for Lateral Rollers

5.4.8 Testing

1. Test melting point heat conduction properties of the wheels. This is important as a super-hot skin layer may be formed on the surface of the wheels as they spin. Need to ensure that a hot surface layer that prevents nominal performance of the wheels cannot occur.
2. Change in material strength with temperature will be checked with high temperature tests to validate the expected heat expansions.
3. Impact tests on wheel to simulate the pod colliding with the central rail.
4. Testing will be conducted to test wheel balance. The imbalance will need to be corrected.
5. The rollers will be spun at high speeds on a drill press to check for any unwanted deformations that might occur during operation, repeat at raised temperature.
6. Combine the high rpm test with an impact test as a final design test.

5.5 Dynamic Module Plate

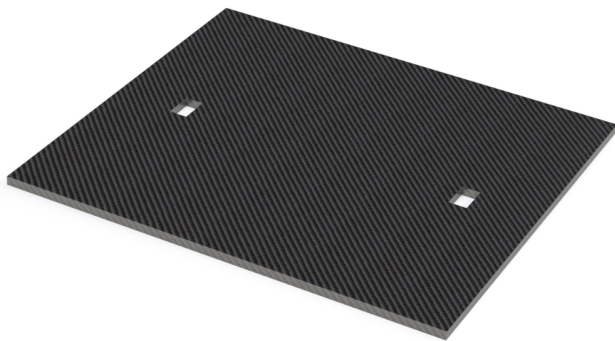


Figure 78: Dynamic Module Plate

5.5.1 Introduction

The levitation skis, emergency brakes, and lateral rollers will all be attached to a same module, the Dynamic Module Plate. These components will be bolted to the plate, so as to be easily assembled. Two of these plates will be mounted onto the pod by bolting the sides to the lower flanges of the chassis. These two plates will be at the extremities of the pod, respectively ensuring the lateral rollers and levitation skis are as far apart as possible to best prevent yaw of the pod and ensure good stability. As can be seen in the figure, the plate is fairly crowded, and houses many essential components of the pod, making its role critical. Various forces and moments will be acting through it, from each component; the skis provide longitudinal shear forces (loading perpendicular to the plate), the lateral rollers primarily cause transverse shear (parallel to the plate) and distributed moments; and the brakes all cause transverse shear forces and moments as well.

5.5.2 Summary

The plate will have dimensions 730x650x30mm, and will weigh about 1.5kg.

5.5.3 Considered Solutions

This module must be able to withstand bending caused by upward forces from skis and bending from lateral rollers and secondary breaks, as well as transverse and longitudinal shear from these components. A full metal construction from aluminium, steel, or even titanium was dismissed on the basis of suboptimal weight. A honeycomb structure sandwiched between aluminium plates was then considered, as honeycomb plates are very good in bending while keeping a low mass, due to their high second moment of area offered by the very light honeycomb structure. However, sandwich structures are notorious for being poor in transverse shear, that is shear parallel to the surface of the plate, and this option would not have fared well due to the loads coming from the brakes of over 1kN that would have caused even a carbon fiber honeycomb to fail.

5.5.4 Chosen solution

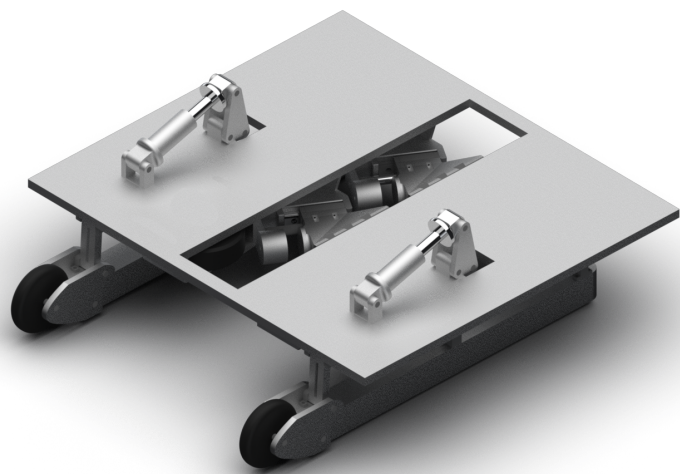


Figure 79: Dynamic Module Proposed Design

Levitation Skis

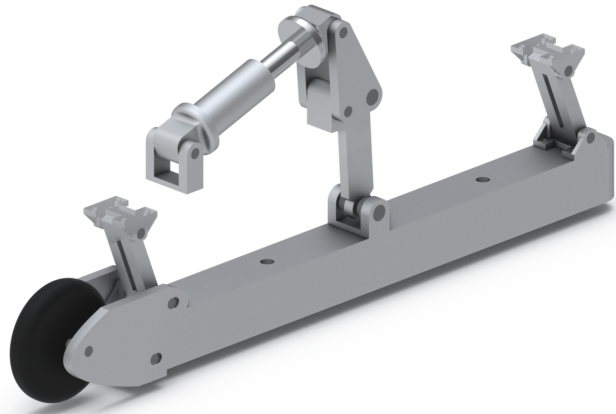


Figure 80: Skis With Mounts

The skis are integrated to the dynamic module, with two attachment points for each ski on the underside of the plate. A hole in the dynamic module plate allows for the suspension system to be mounted to the top of the dynamic module. The skis take up most of the length of the dynamic module plate, but drop low enough so that the other dynamic components such as the lateral rollers and secondary brakes can fit between them and the plate. The wheels that are part of the levitation skis are for runs within the tube, but for everyday transport there will be a set of castor wheels that we will use so as to avoid unnecessary wearing of the skis' wheels, and raise the pod clear of any debris that could scratch or otherwise damage it.

Emergency Brakes



Figure 81: Emergency Brakes With Mount

To attach the secondary brakes to the dynamic module, the brake body is extended creating two angled supports as seen in Figure 81. The supports will bear the parallel and perpendicular loads to the brake pad caused by the friction and reaction forces respectively. The most probable yield point of the supports when the forces are applied during braking will be where the support meets the dynamic module. To address this, the depth of each support increases with distance from the break, forming a triangular shape. The increase in cross section increases the maximum bending moment and shear stress that the attachment material can withstand.

To streamline the manufacturing process, since the brake housing is made from aluminium, the mount will be made from aluminium as well so that it can be milled from a single block if reasonable.

Lateral Rollers

The lateral roller housing is meant make these contact the upper flange of the track's 'I' beam, and bear the moment generated were these to contact the rail. To work against this moment, the lateral roller housing is at an angle, becoming larger as its distance from the rail increases.

With a wheel size of 250mm diameter, it was once again realised that there was not enough space for all the dynamic modules on the plate therefore meaning the wheel size had to be reduced. A new wheel of 130mm diameter allowed for a smaller housing and for it to be closer to the rail therefore creating more space for the new push-rod suspension system to mount through the dynamic plate.

Given the intended distance between the centre rail and the Halbach wheels is are 5mm, the rollers need 2mm clearance between the top of the rail and the wheels, therefore preventing yaw motion as well as the Halbach wheels from clashing with the rail. Figure 82 shows the lateral roller housing will easily withstand the stresses it will undergo, as these will be under 20MPa.

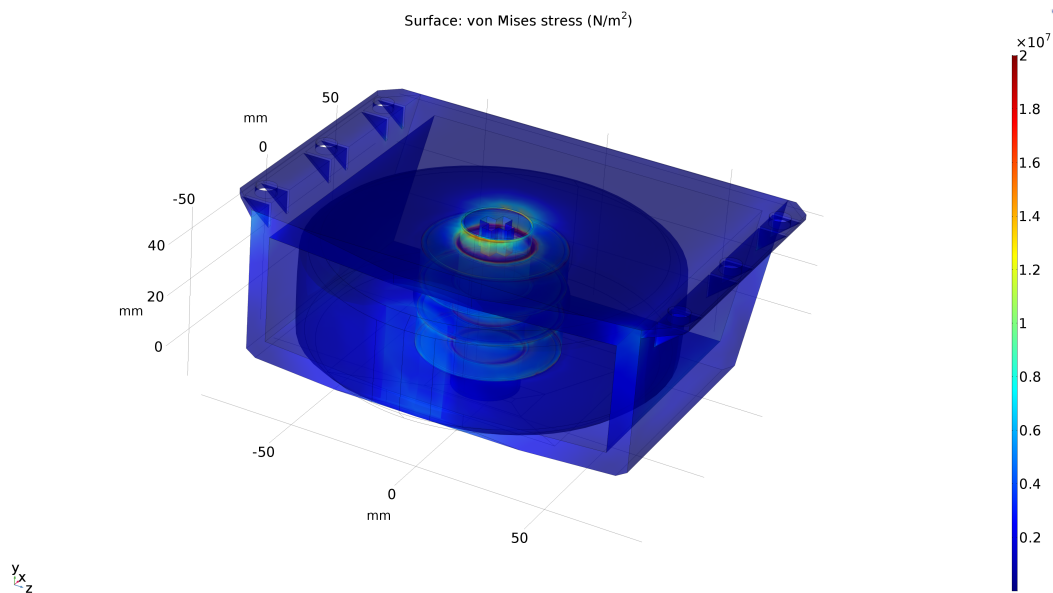


Figure 82: Stress on Lateral Roller Shaft

Dynamic Module Plate

Sandwich plates perform remarkably well in bending and longitudinal (vertical) shear, yet are notorious for premature failure in transverse shear. Extensive research on the topic led to a paper by Han B. et al [8] who have specifically explored a particular sandwich construction that fares remarkably well in transverse shear loading. The sandwich in question is based on a regular corrugated geometry, with the specificity of having high quality foam inserted in it, as seen in Figure.

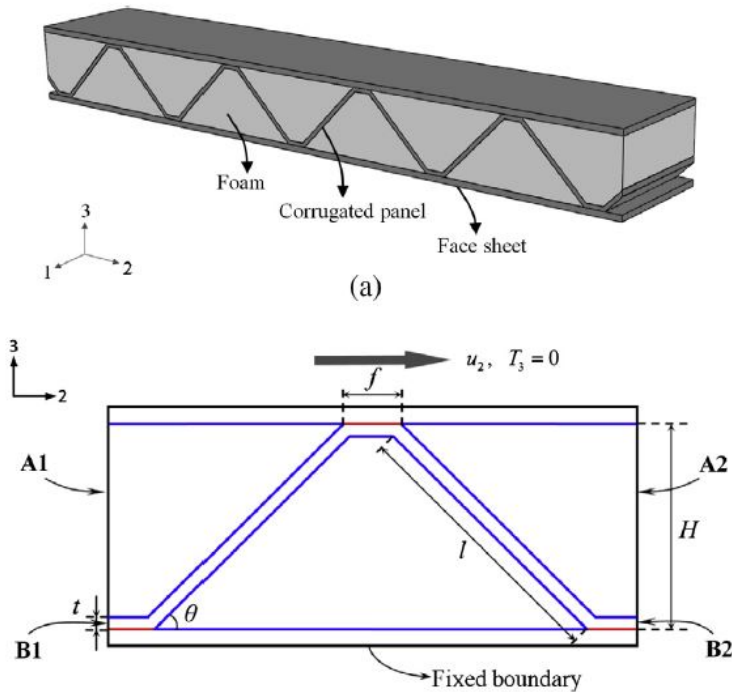


Figure 83: Sandwich Plates [8]

The foam holds the corrugation into place like a cast and enables it to withstand higher transverse loads before these corrugations buckle. This sandwich plate can be made from various different materials, but in the paper some base materials mentioned are 304 steel, and both GFRP and CFRP. Different foams used in testing were Rohacell 31, 51, and both Divinycell H100 and H200 foams; further information on these can be seen in the appendix. Furthermore, Figure 84 shows the performance of various sandwiches made from different base and foam materials, comparing these with high end ‘conventional’ sandwiches such as CFRP honeycomb.

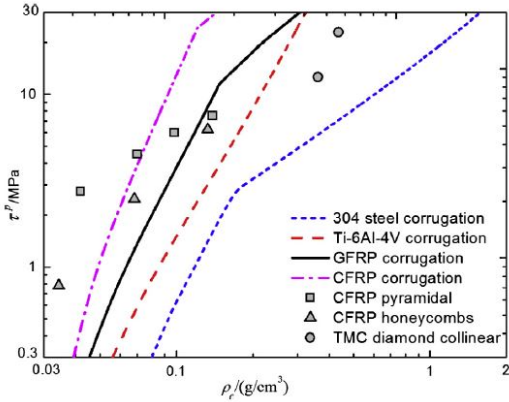


Figure 84: Stress Comparison

In Figure 84, τ^p is the transverse shear stress. Comparison of minimum weight designs of foam-filled corrugated sandwich cores made of different strut parent materials. 304 steel, Ti-6Al-4V, GFRP and CFRP corrugation denote separately Rohacell 51 foam-filled versions of these corrugations. [8]

Noting that both x and y axes are logarithmic, it can be seen that a properly manufactured corrugated sandwich plate from carbon fiber and Rohacell 51 foam can withstand up to 30MPa in transverse shear, while a carbon fiber honeycomb could withstand a maximum of about 7MPa. Accounting for little manufacturing experience in making corrugated sandwiches with foam infills, but the ability to use higher quality foams, it is reasonable to assume that a sandwich corrugated plate made at our university may withstand up to 10MPa in transverse shear, which is a good performance compared to what we may achieve by manufacturing a CFRP honeycomb plate. The simulation section will show how this is a good result, and would serve its function in our pod design.

In addition to housing the levitation, brakes, and rollers, each plate will have two closed hooks at their bottom through which straps will be able to be run so that the pod can be lifted with a crane.

5.5.5 Simulations

As mentioned previously, the major concern for this plate is how it acts in transverse shear, given sandwich plates perform very well under longitudinal shear and high moments. Finite element analysis has been done on the plate to obtain both maximum displacement, and maximum transverse shear. This has been done in the case of maximum braking with the reaction forces from levitation.

The force from the lateral rollers does not need to be added in this model given the brakes produce larger moments and shear than the lateral roller would, and when the brakes are actuated the lateral rollers could not touch the rail. Figure 85 shows that the maximum displacement of the plate in our worst case scenario is a fraction of a millimetre, and therefore would not affect the performance of the components attached to it.

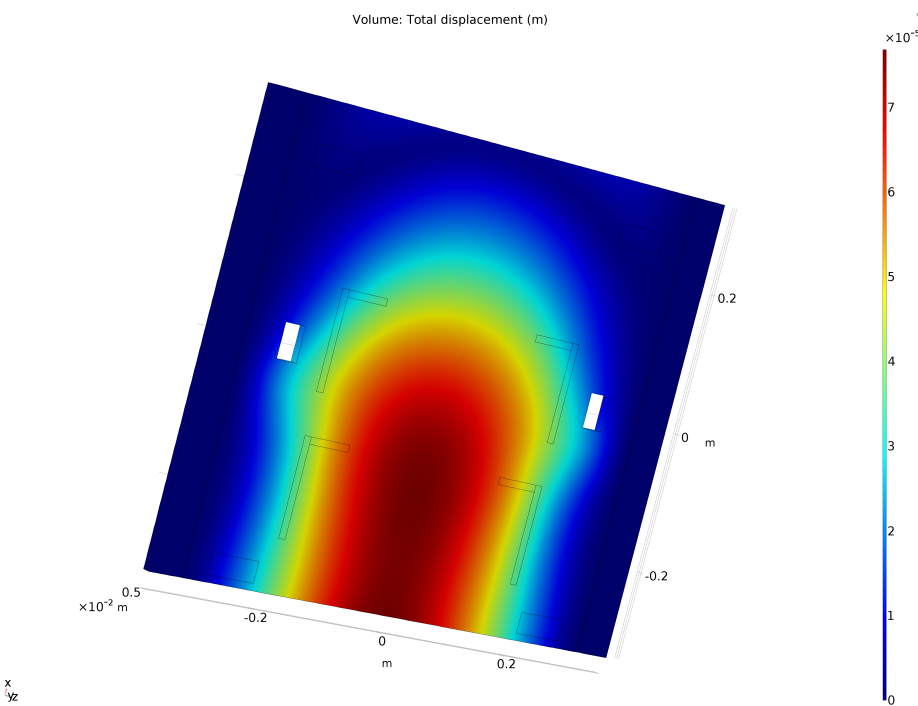


Figure 85: Deformation of Plate Under Load

On the other hand, Figure 86 Shows that the maximum transverse shear stress would be just under 9MPa, making our part capable of withstanding it without failure.

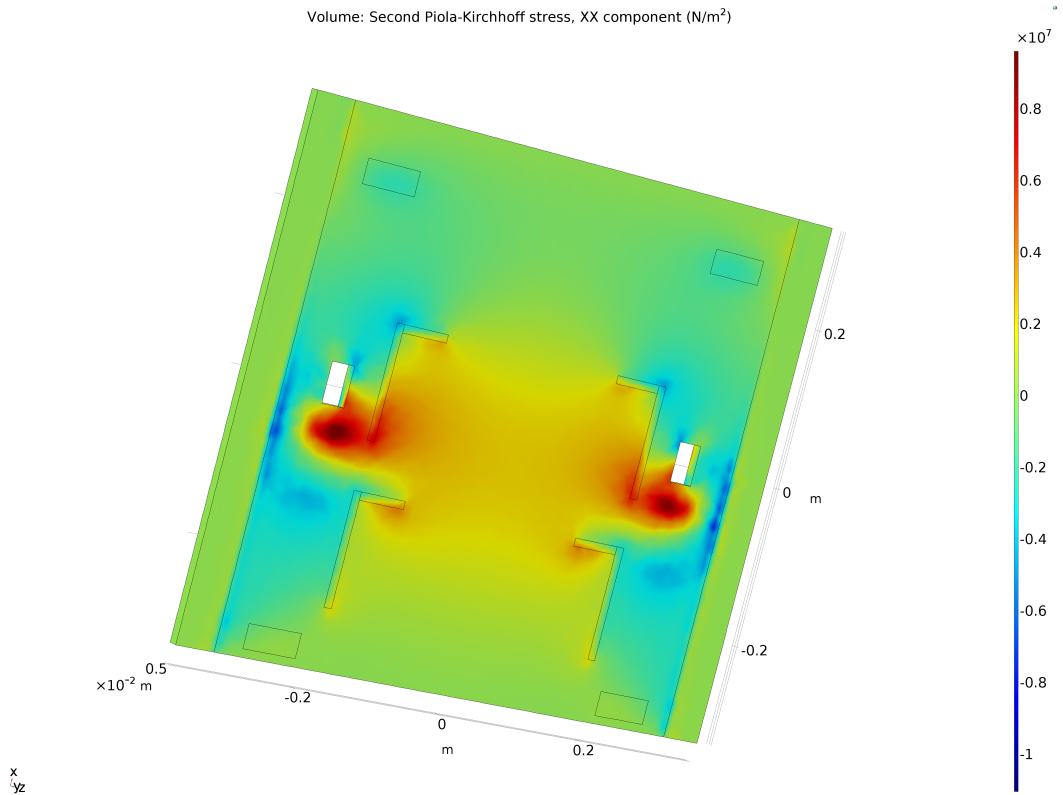


Figure 86: Shear Stress on the Plate

As all other simulations, these have been made with a safety factor of two. A honeycomb sandwich would not have been able to withstand such stresses, making the exact construction of this part crucial to our design.

5.5.6 Safety

Bolting through a composite sandwich plate repeatedly may cause the fibres to start fracturing at the bolt point. A washer that can spread the contact area and stop the nut from directly touching the carbon can circumvent this issue.

Vacuum tolerance may not be an issue, but as this part depends on foam it will be tested in a vacuum chamber to ensure this. The likely outcome is that the foam will be porous enough for a vacuum environment not to cause any issue.

5.5.7 Scalability

The Dynamic Module plate would not be used as is in a full scale Hyperloop given it is very specific to our chassis geometry, and the components in our pod. However, corrugated sandwiches are widely used due to how easy they are to manufacture and therefore how inexpensive they are. As a consequence, the relative breakthrough from this new manufacturing technology will likely see wide applications in the transport industry, including the Hyperloop.

It is possible, for example, that a scaled Hyperloop may have its pressure vessel made from such a sandwich plate, or have parts of its monocoque made this way. Maintenance of such a part would have the same drawback as all composites: once fibres are fractured the part is irretrievably weakened. It is therefore important to engineer parts with this in mind.

Due to these reasons, detailing a size, mass, or cost of a scaled version of this component is irrelevant.

5.5.8 Cost breakdown

Following is the cost breakdown to manufacture both Dynamic Module Plates, in terms of raw materials.

Material	Price (£)
CFRP	200
Rohacell 51	50
Epoxy	50
Total	300

Table 19: Material Costs

5.5.9 Manufacturing

A similar paper to that from Han B. et al [8] details foam-filled corrugated sandwiches in compression, and explains the manufacturing procedure, which is summarised in Figure 87.

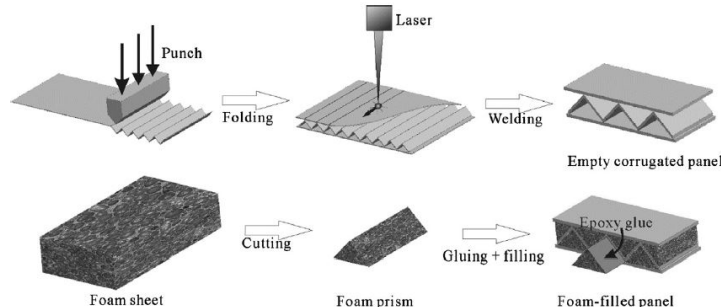


Figure 87: Plate Manufacturing Technique [9]

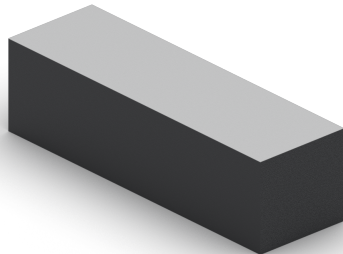
5.5.10 Testing

If time and resources allow, two or more test plates will be manufactured combining different materials to test their relative performances. Testing will be carried out by inserting bolts into the plates and applying the forces to these bolts that will occur when the maximum braking force is applied, and the pod is levitating - the two largest forces that act on the plate.

5.5.11 Timeline

As CFRP supplies are obtained, this part will be able to be manufactured and tested as soon as in February. From this point onwards it will be possible to improve upon the design, either by making it sturdier or lighter, depending on the test results. The part will be finished by May at the latest.

6 Controls



6.1 Introduction

The purpose of the controls modules is to gather data from sensors, perform calculations and determine the appropriate action to initiate. In order to allow all this, the underlying hardware will be designed as a number of module nodes on a CAN bus network similar to that of in an automotive application. These are the master, motor, battery and navigation nodes. The benefits of designing the modules ourselves is that it allows us to include all the desired protection circuitry, hardware interfaces and connectors necessary while also reducing unnecessary power consumption caused by several unutilised components found on development boards.

6.2 Last Years Design

6.2.1 Overview

Control system of Poddy McPodface consisted of 5 Raspberry Pi's (4 Slaves and 1 Master) placed in different locations on the pod with multiple sensors connected to each control unit. The decision concerning which sensors were connected to which Pi was mainly based on the principle of shortest distance. The Master Pi was in charge of all the on-board calculations, brake control and other vital functions of the pod. Additionally, it could communicate with the staging area using the provided Network Access Panel (NAP). The communication between the Raspberry Pi's was implemented using Ethernet. To achieve that, a network switch was placed in the pod, where all the system nodes were connected. Networking within the pod was based on TCP protocol, whereas UDP was used for Pod-to-SpaceX data streaming.

6.2.2 Issues

During the last SpaceX Hyperloop Pod Design competition, multiple weaknesses of the main control system were identified.

As it was outlined before, the sensors were spread between the nodes based on their location. This eventually resulted in higher complexity of data exchange between nodes and master. This was especially complicated for the Navigation data acquisition. Proximity sensors to the rail and to the ground were split between four Slave nodes. At the same time, all IMUs and photoelectric sensors were connected to the master. Consequently, data from every node had to be collected to acquire navigation readings. Moreover, great care had to be taken to synchronise all the incoming data packets.

Raspberry Pi's also appeared to be a suboptimal solution for data acquisition when multiple sensors are connected. This is mainly due to the overhead incurred by the background processes relating to the Linux operating system as well as limited GPIOs. This resulted in instability in certain systems and unreliable functionality of I2C bus used in multiple sensors. Additionally, Linux offers a relatively limited level of control over hardware interfaces such as SPI, I2C buses and system latencies which made synchronisation of data even more difficult.

Finally, two single points of failure were identified at SpaceX Design Weekend. The first one, Network Switch, was inevitable with chosen system architecture. Its failure would lead to complete loss of communication both within the pod and with the outside world. Internal communication failure would also lead to inability to use both hydraulic brakes . The second issue was the relay board that was used to control the solenoids for hydraulics control. This was the most crucial downside of the system as there was no efficient way to duplicate this element. Its failure would result in inability to use the hydraulic brakes as intended. If it were to fail, the brakes would deploy causing problems if the failure occurred during the acceleration phase.

The SpaceX competition gave the team an opportunity to identify the weak points of the system. Those drawbacks have been analysed carefully to be resolved in the new generation of the pod.

6.3 Control System Overview

This year, the team's aim is to optimize the latency and reliability of the Pod Main Control System (MCS). Therefore, multiple Control Unit (CU) options have been investigated considering last years' experience. Eventually, the team decided to use a series of microcontrollers and a Linux powered machine. Microcontrollers are responsible for the data acquisition and internal controls while the Linux machine will serve as a communication interface between the pod and base station. It will also register the base station commands and forward them to internal control

system. Sensors are now associated with the nodes based on their purpose instead of their location. Therefore, several subsystems were identified. Those subsystems are:

- Navigation
- Battery Monitoring
- Motor Control
- Master

Each subsystem consists of one or more nodes and several sensors. All the subsystems will be discussed in detail in the corresponding sections. Figure 88 shows the high level system layout and the internal connections.

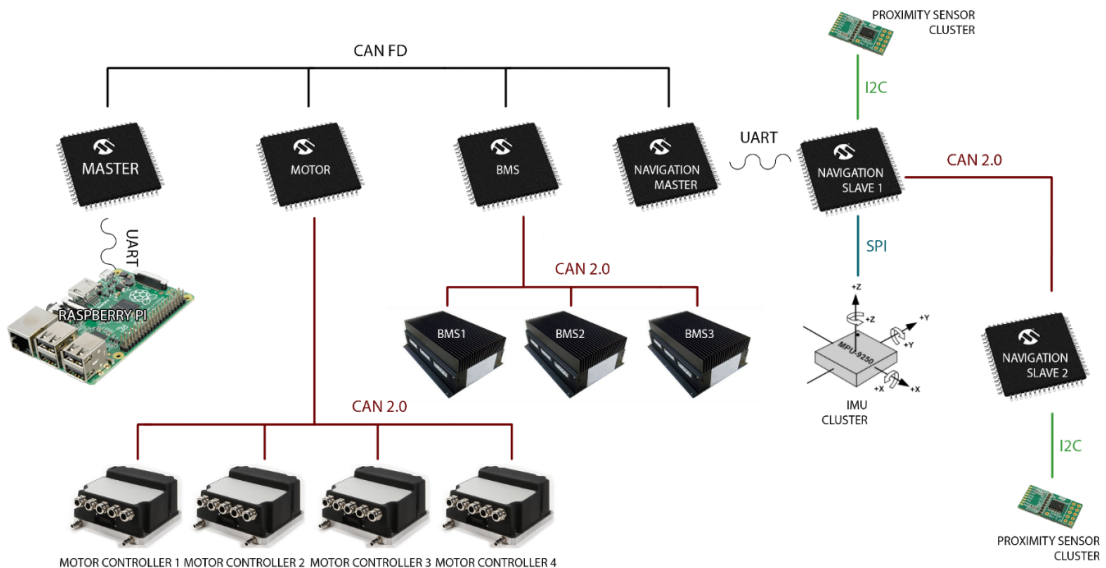


Figure 88: Overall system architecture (BMS – battery monitoring system; IMU – inertial measurement unit).

Another major change is the replacement of the Ethernet interface for communications with CAN. Automotive industry is viewed as a reference due to a number of similarities. CAN is a very robust interface with excellent noise immunity and sufficiently high data rates. Moreover, all nodes can be interconnected and exchange all the data. CAN also allows to transmit safety critical messages based on their priority and the arbitration process.

Since sensor location is immovable for most cases, the relevant nodes will be placed according. This year's design will adopt the following sensor positioning as seen in Figure 89.

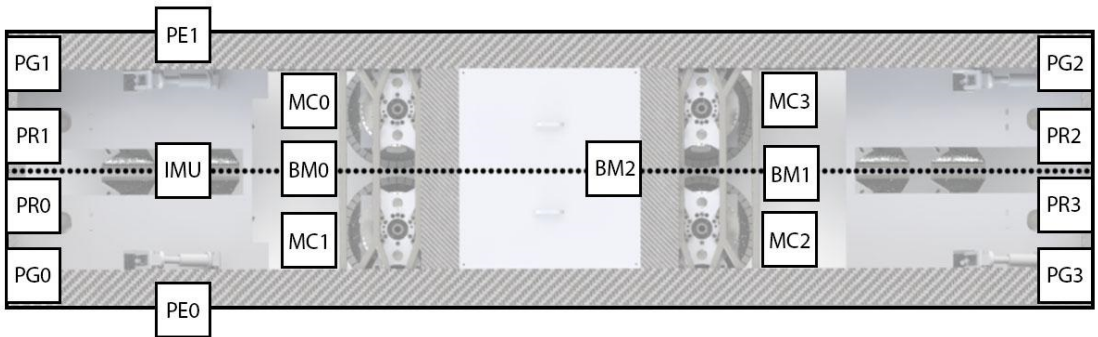


Figure 89: Sensor layout (BM battery monitoring system; MC microcontroller; PR proximity sensor to the rail; PG proximity sensor to ground; PE photoelectric sensor; IMU inertial measurement unit).

6.3.1 Microcontroller System

The system requires a robust and reliable system for data collection and processing. This means having a microcontroller that can collect data from several sensors using various interfaces such as:

- SPI
- I2C
- UART
- CAN
- GPIO
- Analog

As described in the Section 6.3, the CAN interface will improve noise immunity of communication and allow us to transfer safety critical real-time messages (such as emergency stop) over the network using arbitration.

The microcontroller chosen for the control network is the ATSAMC21J18A which has the following specifications:

- ARM Cortex M0+ at 48MHz
- Eight 16-bit timers
- CAN 2.0A/B built in transceiver
- CANFD built in transceiver
- Six Serial Communications Interfaces, each able to handle:
 - UART
 - SPI
 - I2C

- LIN
- Two 12-bit Analog to Digital Converters with 12 Selectable channels each
- One 10-bit Digital to Analog Converter
- Integrated Temperature Sensor
- Up to 52 I/O pins

This new microcontroller architecture will also allow us to eliminate the overhead created by the Linux OS and have much tighter time critical control loops.

6.4 Subsystem & Nodes

6.4.1 Master Node

The master node in the electronics control system will be at the centre of all data collection and processing. The purpose of the master node will be to process all relevant information from the navigation master node and algorithmically decide on a suitable action to perform and transmit to the motor control and BMS nodes. This is described by the state machine of the pod. From the hardware perspective, the master node will consist of an MCU, a CAN FD interface to the remaining nodes as well as a direct UART connection to the Raspberry PI main computer. This will allow the master node to both act independently of the Pi by collecting measurements and acting accordingly or by receiving an asynchronous signal from the Pi (such an Emergency braking command) and having that supersede any other instructions.

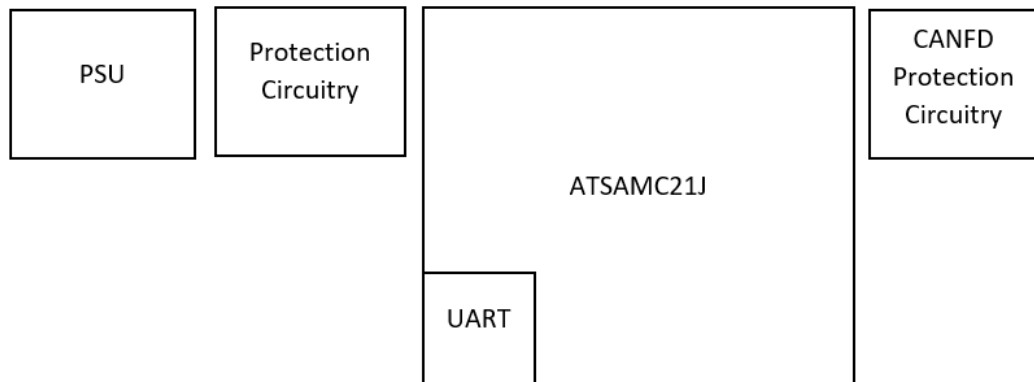


Figure 90: Master node block diagram (PSU – power supply unit).

Power supply requirements for this node are summarised in Table 20.

Operating Voltage	5V
Maximum Current Consumption	20mA
Maximum Power	0.1W

Table 20: Power supply requirements.

Signal	Description	Analogue/Digital	Input/Output/ Bidirectional
UART RXD	UART Receive	Digital	Input
UART TXD	UART Transmit	Digital	Output
CANH	CAN High	Digital	Bidirectional
CANL	CAN Low	Digital	Bidirectional
Emergency Brake	Emergency Brake Enable	Digital	Output
Temperature	Cabin Temperature Measurement	Analogue	Input
Pressure	Cabin Pressure Measurement	Analogue	Input

Table 21: Primary incoming and outgoing signals.

6.4.2 Motor Node

The scope of the motor node is to collect position, torque, temperature, voltage and current values over the CAN2.0 network and send them over to the master node over the CANFD network. This node will therefore need a CANFD and CAN2.0 interface, both available within the ATSAMC21J. Additionally, this board will also require that the standard connector (35 POS AMP SEAL) be available for each motor controller. Since we will be using four motors in total, four connectors must be available on the motor node PCB such that the bus can be connected in a star configuration and allowing more reliable cabling. Additionally, this board will be interfacing to a magnetic field sensor such that there is no degradation of the Halbach wheels magnetic field strength.

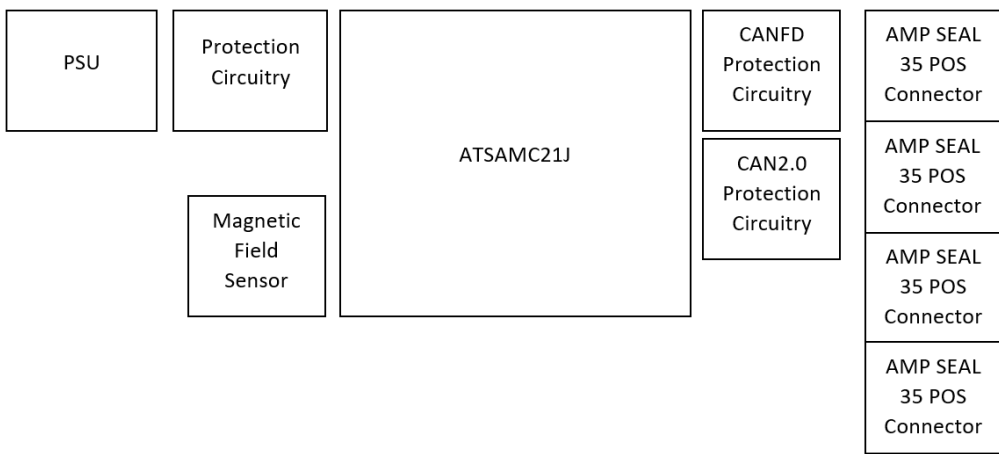


Figure 91: Motor node block diagram.

Power supply requirements for this node are summarised in Table 22.

Operating Voltage	12V
Maximum Current Consumption	830mA
Maximum Power	10W

Table 22: Power supply requirements.

Signal	Description	Analogue/Digital	Input/Output/Bidirectional
CANH	CAN FD High	Digital	Bidirectional
CANL	CAN FD Low	Digital	Bidirectional
CANH	CAN 2.0 High	Digital	Bidirectional
CANL	CAN 2.0 Low	Digital	Bidirectional
Emergency Brake	Emergency Brake Enable	Digital	Output

Table 23: Primary incoming and outgoing signals.

6.5 Navigation Subsystem

This is one of the most resource critical subsystems on the pod because it requires the reading of 22 sensors. Multiple Inertial Measurement Units (IMUs) (accelerometers and gyroscopes) are used to determine the current velocity and displacement of the pod in between the stripes. Two photoelectric sensors supplied by Keyence are used to detect the stripes and reset the displacement drift from accelerometers each time the stripe is passed. This guarantees increased reading accuracy and

better representation of pod orientation. Finally, eight pairs of proximity sensors are placed on the pod to measure the distance to the rail at four points and the levitation height at four points as well. The algorithm that combines all those readings and determines Pod's current velocity, displacement and acceleration in three axes is described in full detail in Section 7.2.4.

6.6 Navigation Node - Master

This is the node where all the computations for the navigation subsystem of the pod will be performed. From the hardware perspective, the data from the other two Slave navigation nodes is gathered using UART from Navigation Slave 1. Connection diagram for the system is depicted in Figure 92.

Only two UART connections on the microcontroller (TX and RX) are required to collect sensor readings from all over the pod. To eliminate data synchronisation issues, Navigation Slave 1 will collect proximity data from Navigation Slave 2. Navigation Slave 1 will then forward the data in its totality (i.e including IMU measurements and its own proximity sensors) to Navigation Master for processing. This also reduces the computation required by Navigation Master, since it will receive the data through a single interface instead of multiple ones allowing it to be focused solely on the navigation algorithm calculations. Navigation readings are sent through the main pod CAN network to the Master Node.

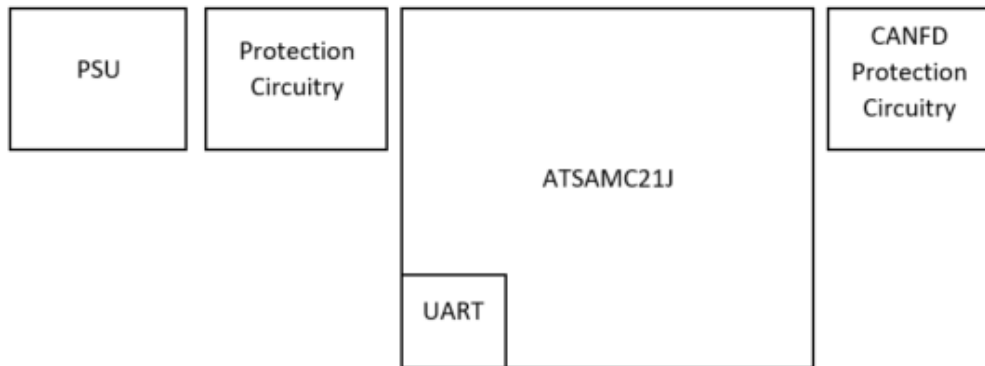


Figure 92: Navigational master node block diagram.

Power supply requirements for this node are summarised in Table 24.

Operating Voltage	5V
Maximum Current Consumption	20mA
Maximum Power	0.1W

Table 24: Power supply requirements.

Pin	Description	Analogue/Digital	Input/Output/ Bidirectional
TXD	Serial Transmit	Digital	Output
RXD	Serial Receive	Digital	Input
CANH	CAN FD High	Digital	Bidirectional
CANL	CAN FD Low	Digital	Bidirectional

Table 25: Primary incoming and outgoing signals.

6.7 Navigation Node - Slave 2

Eight proximity sensors from the rear of the pod are connected to this node using I2C. Those readings are then transmitted further to the front of the pod, where the Navigation Master is located. Therefore, the reason for these nodes to be separate is the limitations of I2C in terms of noise immunity over long distances. To reduce the chances of errors and data losses, it was decided to place the microcontroller as close as possible to the proximity sensors where CAN is used to send the data to Navigation Slave 1.

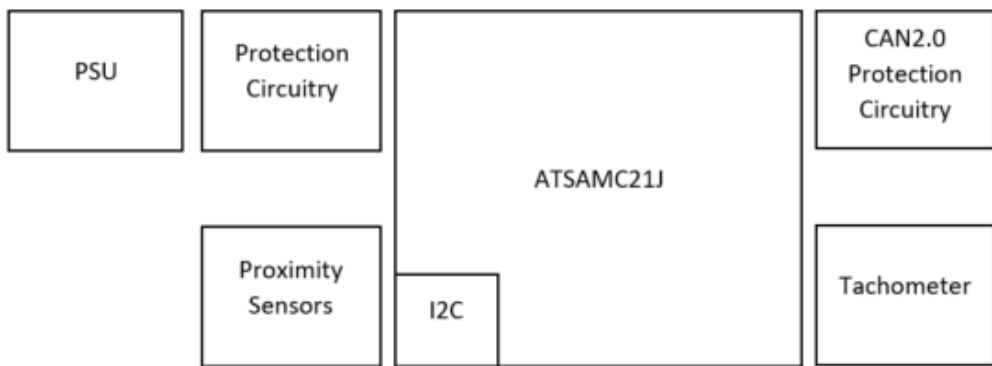


Figure 93: Navigational slave 2 node block diagram.

Power supply requirements for this node are summarised in Table 26.

Operating Voltage	5V
Maximum Current Consumption	20mA
Maximum Power	0.1W

Table 26: Power supply requirements.

Pin	Description	Analogue/Digital	Input/Output/ Bidirectional
CLK	I2C Clock	Digital	Bidirectional
DATA	I2C Data	Digital	Input
RST0	Proximity sensor 0 reset pin	Digital	Output
RST1	Proximity sensor 1 reset pin	Digital	Output
RST2	Proximity sensor 2 reset pin	Digital	Output
RST3	Proximity sensor 3 reset pin	Digital	Output
RST4	Proximity sensor 4 reset pin	Digital	Output
RST5	Proximity sensor 5 reset pin	Digital	Output
RST6	Proximity sensor 6 reset pin	Digital	Output
RST7	Proximity sensor 7 reset pin	Digital	Output
CANH	CAN 2.0 High	Digital	Bidirectional
CANL	CAN 2.0 Low	Digital	Bidirectional

Table 27: Primary incoming and outgoing signals.

6.8 Navigation Node - Slave 1

This node has two main functions. Firstly, it serves as an intermediate point between Slave 1 and Navigation Master. Secondly, it acquires the readings from eight proximity sensors and four IMUs. Readings from both sensor clusters are then sent to the Navigation Master using UART.

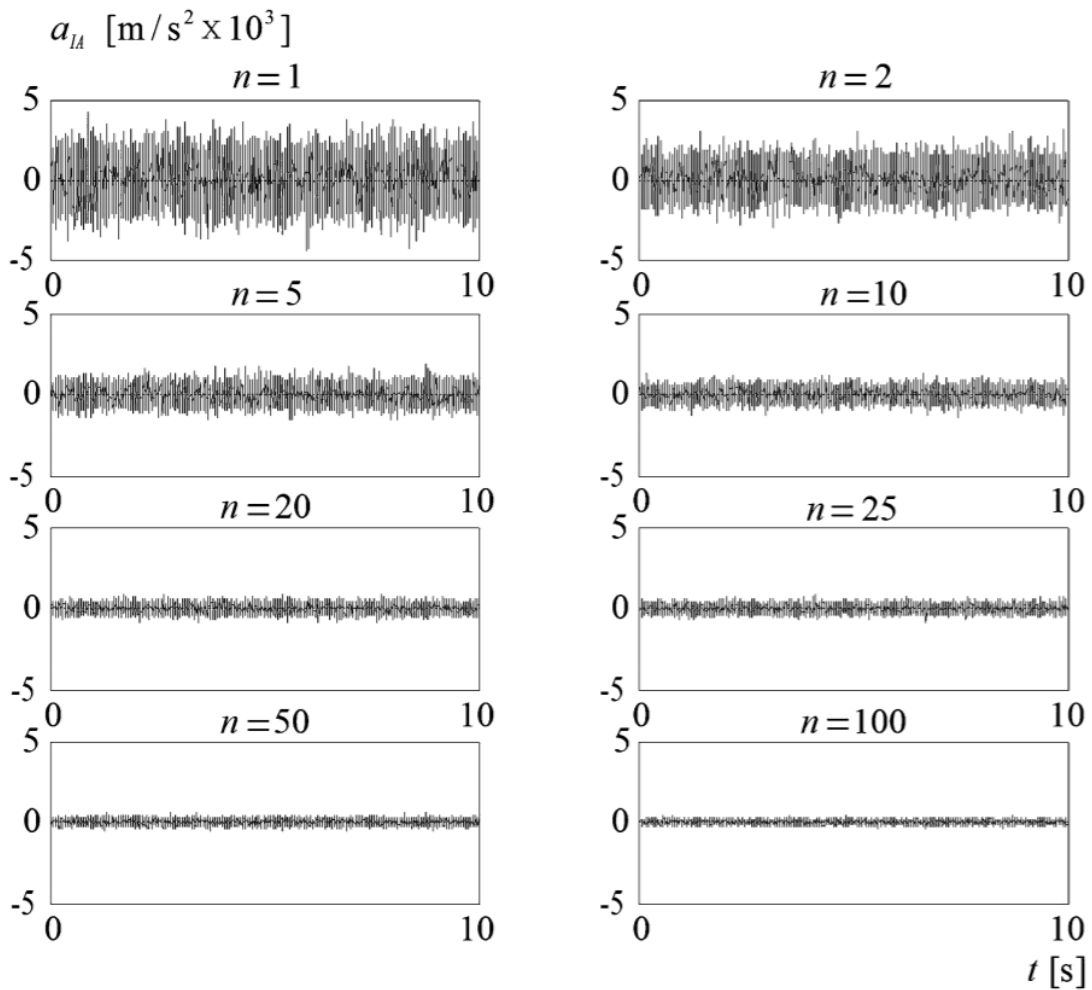


Figure 94: Acceleration noise with increasing number of accelerometers [10].

Multiple IMUs are included to achieve higher accuracy of the acceleration readings. As it can be observed from Figure 94, increasing n (number of accelerometers) leads to the reduction of noise which improves overall performance of the system. Acceleration data is then integrated to obtain velocity and displacement values.

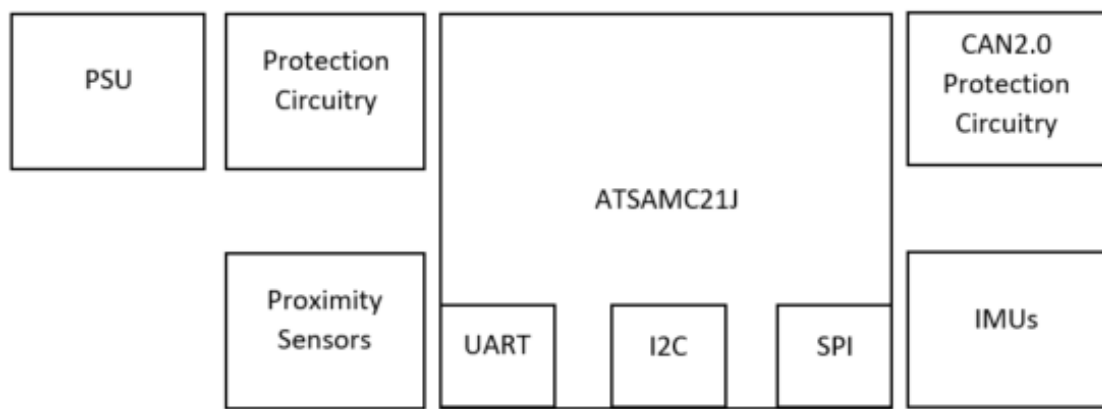


Figure 95: Navigation slave 1 node block diagram.

Power supply requirements for this node are summarised in Table 28.

Operating Voltage	5V
Maximum Current Consumption	20mA
Maximum Power	0.1W

Table 28: Power supply requirements.

Pin	Description	Analogue/ Digital	Input/Output/ Bidirectional
CLK	I2C Clock	Digital	Bidirectional
DATA	I2C Data	Digital	Input
RST0	Proximity sensor 0 reset pin	Digital	Output
RST1	Proximity sensor 1 reset pin	Digital	Output
RST2	Proximity sensor 2 reset pin	Digital	Output
RST3	Proximity sensor 3 reset pin	Digital	Output
RST4	Proximity sensor 4 reset pin	Digital	Output
RST5	Proximity sensor 5 reset pin	Digital	Output
RST6	Proximity sensor 6 reset pin	Digital	Output
RST7	Proximity sensor 7 reset pin	Digital	Output
CANH	CAN 2.0 High	Digital	Bidirectional
CANL	CAN 2.0 Low	Digital	Bidirectional
CX	Serial Transmit	Digital	Bidirectional
RX	Serial Recieve	Digital	Bidirectional

Table 29: Primary incoming and outgoing signals.

6.9 Battery Monitoring Node

This node will gather data from all batteries located on the pod and use it to determine the health and remaining capacity of the batteries. Measured parameters include overall battery voltage, output current, state of charge and temperature. It was decided to use Orion BMS that is equipped with CAN 2.0 interface. Development time is reduced, since the same drivers as for Motor Node can be utilised. Three control signals are required from the microcontroller to be able to disconnect each of the batteries from the system in case of emergency (command received from the base station, battery temperature is critically high, voltage is too low/high).

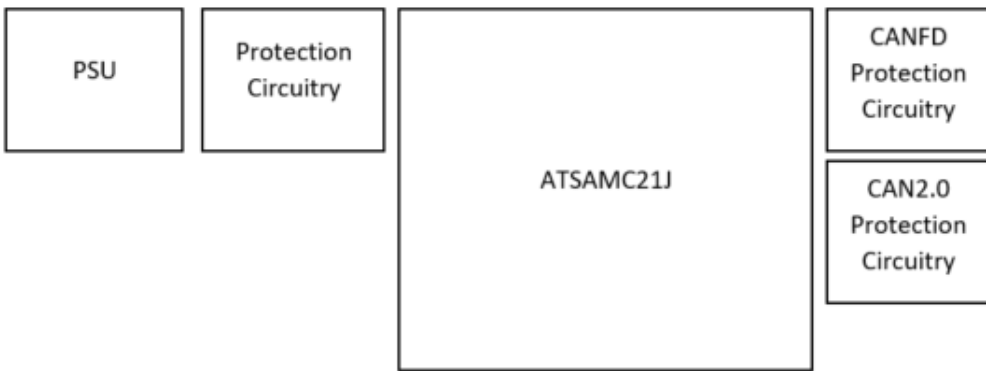


Figure 96: Battery monitor node block diagram.

Power supply requirements for this node are summarised in Table 30.

Operating Voltage	12V
Maximum Current Consumption	290mA
Maximum Power	3.48W

Table 30: Power supply requirements.

Pin	Description	Analogue/Digital	Input/Output/ Bidirectional
EN	Enable Signal for Charging	Digital	Output
DSC	Disconnect High Power Batteries	Digital	Output
CANH	CAN 2.0 High	Digital	Bidirectional
CANL	CAN 2.0 Low	Digital	Bidirectional

Table 31: Primary incoming and outgoing signals.

6.10 Node Protection Circuitry

Electronic design reliability and robustness is at the forefront of our targets this year, particularly due to the safety critical nature of the motor control communication. For this reason, each Node on the network will be outfitted with substantial protection circuitry. Each node on the network will contain the following electronic protection circuitry as a precaution:

- Power Supply Protection
 - Transient Voltage Suppression
 - Over Current Protection
 - Thermal Shutdown Protection
 - Reverse Voltage Protection
- Communications Lines
 - Transient voltage suppression
 - Series over current protection

6.10.1 Implementations

Transient Voltage Suppression

This type of protection will be implemented by having an input TVS diode. This will be able to clamp any large voltage spikes such as that generate by the Electromagnetic Interference (EMI) from the motors. This is particularly important due to the extreme electromagnetic noise environment the nodes will be functioning in.

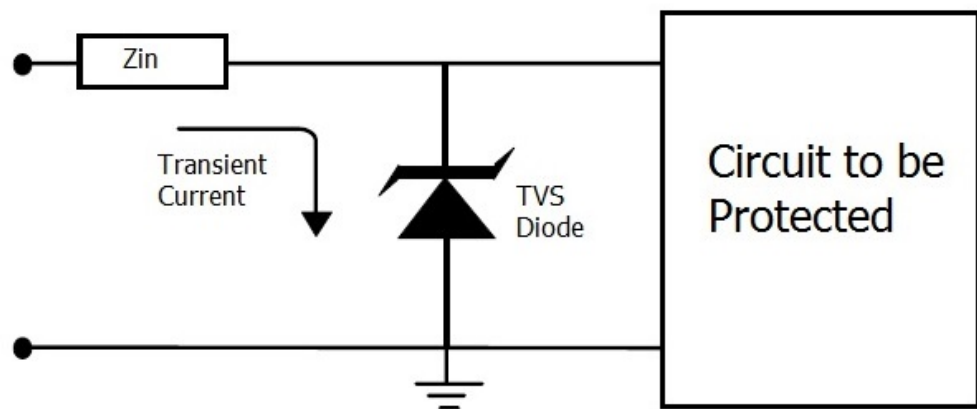


Figure 97: TVS protection[11].

Over Current Protection

This will be implemented in the form of a positive temperature coefficient (PTC) resettable fuse. When the current passing through this electronic device exceeds its rating, the temperature will begin to rise. This in turn will cause the PTC's resistance to rise and thus limit the current. However, PTC fuses only limit current to a certain amount by their resistance ($\approx 4\text{--}20$ when active). To further ensure that a high current event does not occur, a series fast blow non-resettable fuse will also be included.

Thermal Shutdown

Due to the nature of the vacuum environment under which the electronics will be operating, heat dissipation management is crucial for nominal operations. Each node will be outfitted with a switching buck converter as opposed to a linear regulator such that the thermal power dissipation (TDP) may be further reduced. Further to the previously mentioned protection circuitry, each buck converter will be chosen to have built in protection for a thermal shutdown event.

Reverse Voltage Protection

Although this is unlikely to come into play once the pod is correctly wired, reverse voltage protection allows each node to be more forgiving to installation errors. Reverse protection is provided by a series Schottky diode in the node's power supply rail. This prevents any current to pass in the reverse direction should the supply lines be flipped.

6.11 Communications

As previously described, the pod will be utilising several different communications interfaces and protocols. In this section, we will briefly specify why certain communication interfaces are used over others. When choosing a communication interface, several compromises must be made between complexity, speed and reliability.

No.	Name	Connection	Direction (Read/Write)	Connection Description
1	Master	UART	RW to Raspberry Pi	Speak to Host computer and SpaceX server
		CAN FD	RW to 6 R from 3	Refresh BMS data from 6 Receive Navigation Summary data from 3
2	Motor and Battery Management System	CAN FD	RW to 1 R from 3	Receive velocity refreshes from Navigation (3) Send and receive STOP and KILL signals to and from 1 Send and Receive instructions and motor data to Master
		CAN 2.0	R/W from 4 MCs	Secondary CAN 2.0 Network for networking Motor Controllers
3	Navigation Master	CAN FD	RW to 1 W to 2 R from 5	Proximity readings from 4, 5 Velocity stream to 2 Navigation data refreshes to 1
		UART	R from 4	Proximity readings from 4, Condensed accelerometer and gyro readings from 4
		GPIO Interrupts	R from stripe counter	Stripe counter interrupts every time a stripe is passed
4	Navigation Slave 1	UART	W to 3	Send Proximity readings to 3, Send condensed accelerometer and gyro readings to 3
		I2C	R from 8 Proximity Sensors	Proximity readings from 8 proximity sensors
		SPI	R from 8 IMUs	Gyro and accelerometer readings from 8 IMUs
5	Navigation Slave 2	CAN 2.0	W to 3	Send Proximity readings from 8 proximity sensors to 4
		I2C	R from 8 Proximity Sensors	Proximity readings from 8 proximity sensors
6	Battery Management System	CAN FD	W to 1	Send BMS data to Master
		CAN 2.0	R from BMS	Secondary CAN 2.0 Network for networking with Battery Management System

Table 32: Communication connections.

6.11.1 CAN Bus

It is important that our communication is resistant to interference, especially because we are dealing with high magnetic fields and significant motor noise. Long wire connections are particularly exposed to such problems. To minimize the risk of data corruption, we decided to use Control Area Network (CAN) protocol commonly used in automotive industry. All the node MCUs and the main MCU will be connected to the same CAN bus to achieve a reliable way of data transfer even when the nodes are distant.

CAN bus has several advantages including broadcast capability, priority arbitration and error checking to ensure on time, priority based and reliable communication.

For the main bus we decided to implement the latest CAN Flexible Data-rate (CAN-FD) standard that has up to 8 Mbps Data Bit Rate making the communication as fast as possible without sacrificing reliability. Because our motor controllers and BMSs support CAN 2.0 standard with a fixed Bit Rate of 1 Mbps, a dedicated node MCU with dual CAN support creates a bridge between the two data lines. Thus, the main bus will be free of low speed data transactions.

6.11.2 Sensor-Specific Protocols

Standard digital interfaces like I2C and SPI are prone to interference, hence we want to keep these connections as short as possible. Due to frequency and data resolution differences it is necessary to unify data formats in node MCUs.

Although inexpensive and widely used, SPI and I2C are not as noise immune as CAN bus. However, these are suitable for short distance applications such as interfacing with the IMUs or proximity sensors. The buses provide cheap, simple and efficient methods of communication to nearby sensors.

- I2C
 - Two lines: data and clock
 - Address-based sensor communication
 - 400kHz fixed bitrate
- SPI
 - Two data lines and a clock line
 - Controller selection based communication, requiring extra digital connection per sensor
 - Flexible bitrate, up to 20MHz

- Digital I/O
 - Interfaced directly from microcontroller's GPIO pins

6.12 Testing

6.12.1 Communications Tests

Objectives:

- Functionality
- Noise Immunity
- Distance
- Data Rate

All of the described tests are applicable to each and every communication protocol being used within the pod unless stated otherwise. This includes UART, CANFD, CAN2.0, I2C and SPI.

Functionality

The integrity of the communication protocols will be tested by pinging each node on the network respectively to ensure that each node is responsive over the CAN bus. In addition, the heartbeat signal will intentionally be suspended to ensure that the pod successfully transitions to the emergency state in the event of a communication break-down. Sensor-specific IO such as I²C will be tested by extension of the sensor hardware tests outlined in their respective sections of this report.

Noise Immunity

Since the worst case of electromagnetic interference will mainly be caused by the motors and Halbach wheels, an appropriate test would be to run data transmission while the motor is operating at peak speed and peak torque. In this test, the nodes will be mounted in their appropriate position on the pod such that the test conditions represent the expected environment. The test will consist of sending several thousands of packets and counting the rate of corruption.

Distance

It is useful to determine the limits of reliable data transmission against range for different communication interfaces. Each interface will be tested for a difference range in accordance with their expected application.

Interface	Distance Range (m)
UART	1
CANFD	5
CAN 2.0	5
I2C	0.75
SPI	0.3

Table 33: Expected operating ranges for communication protocols on the pod.

Data Rate

Since we will be utilising each protocol at a distance much less than the theoretical limit, we seek to achieve the ideal theoretical transfer rate. E.g. I2C Full Speed should operate at 400kbits^{-1} .

To test data rate, we will create test programs which continuously send data packets over the network. The continuous data rate will be measured at the receiving end. Maximum data transfer should be sustainable indefinitely for ideal communication.

6.12.2 Proximity Tests

Accuracy & Range

A series of laboratory experiments will be conducted to determine the actual range and the accuracy within this range for the proximity measure of the pod. The set up will include a bar of Aluminium 6061-T6 such that real-world reflectance conditions are tested since we will be using time of flight proximity sensors. In this test set up we will be able to compare measured distance against actual distance.

6.12.3 Photoelectric Test

Translational Speed, Stripe Count Rate & Range

The photoelectric sensors are a crucial part of the pod's navigation system. The team intends to keep the Keyence LR-W500 sensors that were used in the 2017 competition. To prove the sensor's suitability, a test was designed to verify its capability of recognizing the red stripes at the required frequency.

The test station can be described using the scheme below in Figure 98:

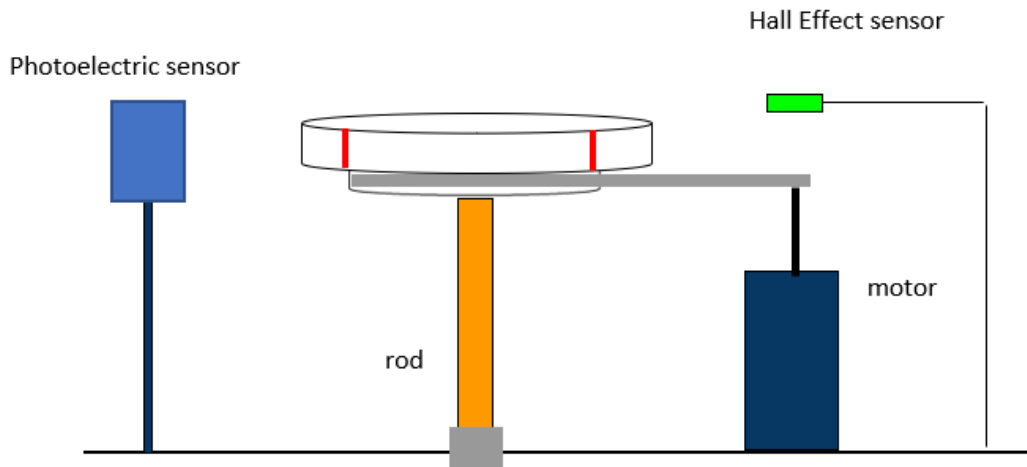


Figure 98: Test station scheme.

The motor should be driving the disk through a belt and pulley system. The 3D printed disk will be mounted on a rod through a bearing allowing it to rotate. The speed of rotation will be measured by a Hall Effect sensor, and will be compared to the data from the photoelectric sensor. This will allow the functionality of the photoelectric sensor to be verified. An Arduino will be used to control the system.

To keep the dimensions of the disc and its speed of rotation manageable the test station had to be scaled down. As that the width of the stripes in the actual tube is 10cm, it was decided to reduce the width to 5mm, allowing the speed to be reduced from 140 ms^{-1} to $v=7\text{ms}^{-1}$, whilst keeping the frequency of the stripes constant.

Choosing a $r=10\text{cm}$ radius for the disc, the angular velocity needed was:

$$\omega = \frac{v}{r} = \frac{7}{0.1} = 70\text{Rads}^{-1}$$

Estimating the time needed by the motor to reach its full speed at approximately $t=10$ seconds, the angular acceleration that had to be provided was calculated:

$$\alpha = \frac{\Delta\omega}{\Delta t} = \frac{70}{10} = 7\text{Rads}^{-2}$$

Assuming the density of the 3D printer filament is similar to the density of nylon, the required torque, τ , can be calculated:

$$\tau = \left(\frac{1}{2}mr^2\right)\alpha = 0.066\text{Nm}$$

where m is the mass of the disc. Thus, the required power of the motor was:

$$P = \tau\omega = 4.61\text{W}$$

6.12.4 IMU Test

Objectives:

- Velocity drift under 0.1ms^{-1} in 9s.
- Reasonable distance drift (max few meters in 3s).
- Tune the algorithms to achieve and exceed the above two goals.

Stationary

This test will verify that velocity and distance drift can be sufficiently small to be corrected by the stripe counter. IMUs will be kept completely stationary. The navigation algorithm will be run for 20 seconds and its outputs will be recorded. Ideally, both velocity and distance would remain 0 throughout the test but in reality, there will be non-zero numbers indicating the drift. This is the best-case scenario as there are no physical movements that could distort the results.

Vibration

Same as Stationary test but some vibration will be applied to the IMUs during the test. Ideally, the results would be the same as for Stationary test, but they are expected to be slightly worse. This test is to verify that the effect of vibrations is small and the drift remains within the limits.

Small Movements

Same as Vibration test but the IMUs will be moved (including rotations) by hand by very small amounts. The IMUs will be returned to the exact initial position by the end of the test. Vibration and Small movements tests should also be combined.

Moving

Navigation algorithm will be run for 20 seconds like in Stationary test but the IMUs will be moved along a line. Difference between actual and measured velocity and displacement should correspond to the drift observed in the previous tests. Various methods for moving the IMUs will be tried to provide various levels of vibration and lateral movement, different acceleration profiles, and different accuracies of the actual distance and velocity.

6.12.5 Motor Control Test

Objectives:

- Functionality
 - Speed Control
 - Torque Control
 - Reading Sensors
- Speed Accuracy
- Response Time

Functionality

To begin with, we will test simple functionality of the motor controllers. That is, to test that we are able to control the speed and torque of the motor. We will also test that we are able to read from the built-in hall effect sensors among others.

Speed Accuracy

Once basic functionality is established, a command for various speeds will be sent to the motor controller and the actual output speed will be measured using a tachometer for comparison. This will allow us to determine the speed accuracy of the motor controller.

Response Time

The time delay between sending a speed set command to the motor controller and the motor reaching this target speed will be measured such that the motor response time can be calculated.

6.12.6 BMS Test

- Functionality
 - Temperature
 - Current
 - Battery Voltage
 - String Voltage

Functionality

A functionality test will involve polling the BMS system for various measurements such as temperature, current output, overall battery voltage and string voltage. These will then be measured manually using a thermometer and multimeter respectively to verify that these readings are indeed correct.

6.13 Cost Breakdown

Components/Materials	Quantity Required	Cost (£ per unit)	Total Cost (£)
ATSAMC21J18A	6	4.65	27.90
SAM C21 Xplained Pro	6	47.73	286.38
35-way AMPSEAL Automotive Plug Assembly	10	10	100
Shielded Multicore Signal Cable (30m)	1	146.08	146.08
Phoenix Contact Classic COMBICON connectors	50	1.84	92
MOLEX C-GRID III connectors	50	1.07	53.50
VL6180X SATEL (pack of two)	10	12.89	128.90
VL53L0X SATEL (pack of two)	5	17.21	86.05
KEYENCE LR-W500 (purchased last year)	2	-	-
MPU9250 IMU	8	8.85	70.80
Tachometer	4	17.86	71.44
Magnetic Field Strength Sensor	2	115	230
Hall Effect Sensor	10	1.13	11.30
PCB Layout Package - Sponsored by Altium	1	-	-
Raspberry Pi 3 (purchased last year)	2	-	-
Total			1304.35

Table 34: Controls cost breakdown.

6.14 Timeline

Action	Deadline
All Sensors Selected	January
Full Control System Schematic	End of January
1 st Generation PCBs for Control Nodes	Early March
PCBs Testing and Modification	March–April
Final PCB Design	May
1st Control Network Prototype	May
Final Control Network Design	Mid-June
Final Testing	Mid-June–End of July

Table 35: Controls timeline.

7 Software Systems

7.1 Introduction

A central pillar of the Hyperloop concept is its ability to expedite and coordinate the mass transportation of people and freight *autonomously*. The development of an autonomous vehicle demands revolutionary computational control and navigation systems, and necessitates an intimate intersection of powerful hardware with disruptive, intelligent software. Poddy the Second boasts innovative software solutions to the problem of autonomously navigating a passive Hyperloop tube, while showcasing an uncompromising commitment to passenger safety. The sections which follow document the development of the software systems which aim to govern the safe operation of our prototype pod in the next iteration of the SpaceX Hyperloop Pod Competition.

7.2 Navigation

7.2.1 Introduction

Our onboard navigation system serves to determine the acceleration, velocity, and displacement of our pod in real-time, and make such values available to all subsystems which require this information — such as braking and telemetry subsystems.

To achieve this, our system utilises an array of microcontrollers and sensors, including inertial measurement units (IMUs), proximity sensors, optical sensors (tasked with counting reflective stripes), and gyroscopes to capture and process physical data, which subsequently informs the safe guidance of the pod through the Hyperloop tube.

This section of the document aims to outline, in detail, the process by which our system arrives at the accurate calculation of the pod's motion parameters.

7.2.2 Summary

Determining the velocity and orientation of the pod as a function of IMU data alone introduces inaccuracies into the calculated values. In light of this, our navigation system combines measurements from multiple sources.

Onboard gyroscopes serve to determine the proportion of measured acceleration attributable to gravitational acceleration, before compensating for this component in the final calculated value. This acceleration value is subsequently integrated

twice to yield a value for the displacement of the pod through the Hyperloop tube.

Performing multiple integration operations on acceleration data introduces drift, where the calculated value of the pod's displacement increases beyond the actual value, out of phase with the motion of the pod. To counteract this, our system employs proximity sensors in conjunction with optical sensors to eliminate this degree of drift in the calculated value of displacement.

This range of sensory inputs, working in concert with noise-reduction digital filtering, enables our navigation system to accurately and reliably calculate our pod's parameters of motion, and facilitate the safe delivery of our pod to the end of the Hyperloop tube without collision.

7.2.3 Conceptual Solution

It was decided to use both gyroscopes and accelerometers (combined in IMUs). Assuming that the tube is perfectly straight and level, it would be possible to measure acceleration along the axis of the Hyperloop tube alone. However, if this assumption is inaccurate and the pod tilts during the run, there will be a component of \mathbf{g} (gravitational acceleration) aligned with the axis along which the acceleration of the pod is measured. Such offsets, however small, would quickly compound as a consequence of numerical integration, thus inducing a significant error in the calculated values for pod velocity and displacement. This error was deemed to necessitate the use of gyroscopes in order to measure the orientation of the pod accurately.

To calculate the orientation, velocity, and displacement of the pod, it is necessary to integrate angular velocity, acceleration, and (translational) velocity, respectively. Numerical integration yields accurate results for a short period of time, however, as time proceeds, the results begin to *drift* beyond the accurate value representative of the pod's true motion. To counteract this effect, proximity sensors are employed to measure the distance to the ground from the four corners of the pod, in conjunction to the distance to the rail from each end of the pod. This data-set is sufficient to fully determine the orientation of the pod, in accompaniment with the velocity and displacement of the pod in the vertical and horizontal (left-right) axes. The data acquired from proximity sensors is susceptible to noise, and the update-cycle of the optical sensor is infrequent, hence these values merely complement the data acquired from the IMUs to constitute a drift-resolution mechanism — the IMUs represent the chief source of navigation data.

The navigation software represents rotation in the form of a mathematical model

named a *quaternion*. This was deemed advantageous when compared to other rotation models, such as rotation matrices and Euler angles, for two primary reasons. One such reason is that they can be more readily interpolated than alternative models, which is necessary when combining orientation estimates from multiple sources (please see stage 2 of the navigation algorithm below). A further advantage of quaternions is their minimal representation - while rotating a vector using a quaternion requires more operations than would be necessary to undertake the same rotation using a rotation matrix, composing rotations with quaternions is a less computationally-taxing process. The algorithm outlined hereto uses composition extensively, hence the decision to use quaternions affords us a computationally cheaper process.

7.2.4 Navigation Algorithm

Let $\omega'(t)$ represent the body angular velocity pseudovector of the pod as a function of time. This is measured by the on-board gyroscope, and hence evaluated for $t \in \{t_0, t_1, t_2, \dots\}$ where we have the general recurrence relation

$$t_i - t_{i-1} \approx \frac{1}{8000} \text{ seconds (s)}.$$

Similarly, let $\mathbf{a}'(t)$ be the acceleration vector measured at time $t \in \{t'_0, t'_1, t'_2, \dots\}$, where we have

$$t'_i - t'_{i-1} \approx \frac{1}{1000} \text{ seconds (s)}.$$

Lastly, let $\mathbf{x}_p(t)$ be the displacement vector estimated from the combination of proximity sensor and optical sensor data at time-points $t \in \{t''_0, t''_1, t''_2, \dots\}$. The period $t''_i - t''_{i-1}$ is expected to be approximately $\frac{1}{50}$ seconds, but will vary widely for the stripe counter (optical sensor) component.

The inputs $\omega'(t)$, $\mathbf{a}'(t)$, and $\mathbf{x}_p(t)$ are used to calculate the orientation quaternion $\mathbf{r}(t)$ in addition to pod acceleration vector $\mathbf{a}(t)$, velocity vector $\mathbf{v}(t)$, and displacement vector $\mathbf{s}(t)$ in the frame of reference of the Hyperloop tube. (All vectors are represented as row vectors.)

The calculation consists of several stages:

1. The most frequent is the update of the orientation quaternion, which occurs upon the availability of every new angular velocity reading (8 kHz). Given $\omega'(t_{i-1})$, t_i , and $\mathbf{r}(t_{i-1})$, the angle-axis representation of the rotation undertaken by the pod is calculated as $r_i^{i-1} = (\cos(\frac{\varphi}{2}), \frac{\theta}{\varphi} \sin(\frac{\varphi}{2}))$, where $\varphi = |\theta|$ is the angle of rotation. Finally, an updated total orientation quaternion is evaluated as $\mathbf{r}(t_i) = \mathbf{r}_i^{i-1}(t_{i-1})$;

2. When a new orientation estimate becomes available from the proximity sensors (quaternion $\mathbf{p}(t)$), $\mathbf{r}(t)$ is adjusted using Quaternion SLERP (Spherical Linear Interpolation) as $\mathbf{r}(t) := \mathbf{r}(t)(\mathbf{r}(t)^{-1}\mathbf{p}(t))^c$, where the real constant $0 < c < 1$ is the empirically tuned weight of the proximity sensors' orientation estimate;
3. When a new measurement of acceleration is taken, it is transformed into the Hyperloop tube's frame of reference as $\mathbf{a}(t) = \mathbf{r}(t)\mathbf{a}'(t)\mathbf{r}(t)^{-1} - g$, where g is the gravitational acceleration measured immediately before the run commences. A three-dimensional vector (namely \mathbf{a} and \mathbf{a}' in this case) may be identified via the appropriate isomorphism;
4. The velocity is subsequently calculated from this value of acceleration as $\mathbf{v}(t'_i) = \mathbf{v}(t'_{i-1}) + \Delta\mathbf{a}t$, where $\mathbf{a} = \frac{1}{2}(\mathbf{a}(t'_i) + \mathbf{a}(t'_{i-1}))$ is the estimated acceleration during time $\Delta t \approx t'_i - t'_{i-1} = \frac{1}{1000}$ s;
5. The velocity is periodically adjusted using proximity and optical stripe counter data as $\mathbf{v}(t''_i) := \mathbf{v}(t''_i)C + \frac{\Delta\mathbf{x}_p}{\Delta t}(I - C)$, where $\Delta\mathbf{x}_p = \mathbf{x}_p(t''_i) - \mathbf{x}_p(t''_{i-1})$ is the change in displacement during time $\Delta t = t''_i - t''_{i-1}$, where I is the identity matrix, and C is a constant diagonal weight matrix (similar to the constant c in stage 2);
6. The displacement of the pod through the Hyperloop tube can thence be calculated from the velocity as $\mathbf{x}(t'_i) = \mathbf{x}(t'_{i-1}) + \mathbf{v}t$, where $\mathbf{v} = \frac{1}{2}(\mathbf{v}(t'_i) + \mathbf{v}(t'_{i-1}))$ is the estimated velocity during time $\Delta t = t'_i - t'_{i-1} \approx \frac{1}{1000}$ s;
7. The displacement is periodically updated from proximity and stripe count data as $\mathbf{x}(t) := \mathbf{x}(t)C + \mathbf{x}_p(t)(I - C)$, where I is the identity matrix and C is a constant diagonal weight matrix.

Nota bene: while C is a convenient mathematical notation, the software implementation of this mathematical procedure will employ three separate scalar constants in order to perform the calculations in a component-wise capacity. This will prove especially useful for separating the proximity sensor updates from optical sensor updates, as these are likely to occur at different time-stamps.

7.2.5 Filtration Technique

Our navigation system uses digital filtering to reduce the noise of the data acquired from sensory inputs. The team has decided to use a Kalman filter due to its ability to 'smooth' data in a more dynamic and adaptive capacity than is possible with low-pass filters or exponential moving average filters. This will be used in concert with a complementary filter, tasked with improving the reliability of sensor data. Figure 99 illustrates the processing and filtering of data in the form of a flowchart.

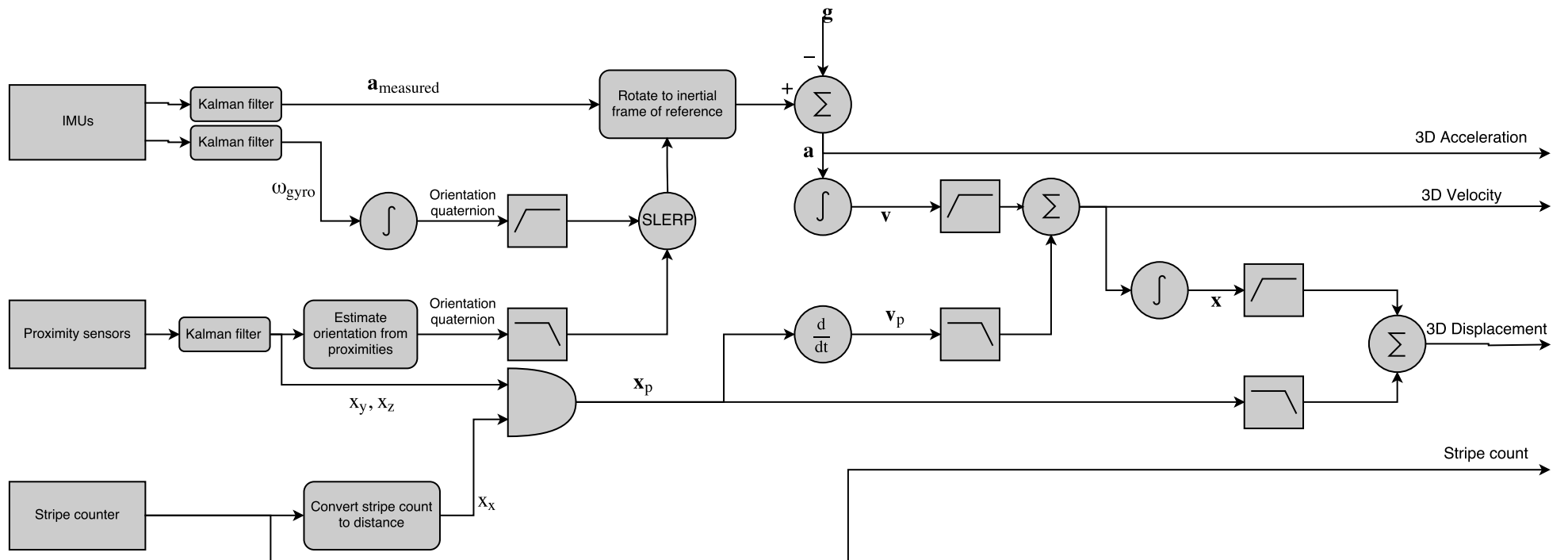


Figure 99: Navigation algorithm.

7.2.6 Scalability

The navigation system documented hereto is independent of the Hyperloop tube, thereby rendering our pod as a fully autonomous vehicle. Our pod is thus capable of operating successfully in an entirely passive tube, increasing the ease at which the Hyperloop concept could be up-scaled for mass-transportation purposes (attributing navigation systems to the tube infrastructure would be costly and increase large-scale development time).

7.2.7 Testing

The hardware of the navigation system will undergo extensive testing, as afore-detailed in the *Controls Module* section of this design package. The navigation algorithm will be tested upon this hardware platform to ensure that the numerical values calculated are in phase with physical reality. Since the algorithm is based upon that of last year's competition entry — which successfully passed exhaustive testing — we expect this year's test results to be encouraging, bearing identical results beyond improved drift resolution.

7.3 Communications

7.3.1 Introduction

The software communication system employs a range of solutions to facilitate remote monitoring and control of the pod during the Hyperloop run. The telemetry system is tasked with ensuring that emergency commands can be received and responded to by the pod in real-time, while simultaneously transmitting information from battery management systems and navigation systems for review on the Mission Control system. This section of the design package details the operation of the software communication system.

7.3.2 Summary

The telemetry system is implemented in C++ and uses TCP/IP sockets to send and receive data packets between the pod and the Mission Control system - this constitutes the arterial connection between the pod and the outside world. The data packets can take the form of pod parameters, such as battery temperature and pod velocity, being sent for display on the Mission Control laptop, or emergency commands such as “STOP” sent from Mission Control to the pod. Each pod parameter is associated with a unique code which is concatenated to the beginning of the data packet as a prefix. The Mission Control system analyses the initial data elements of each received packet to ascertain the physical quantity it

represents and display the numerical value in the appropriate field on the graphical user interface (GUI).

The Mission Control system is implemented in Java and, as such, runs on the Java Virtual Machine (JVM). This system enables the user to issue real-time interrupts to the pod, which transition the pod's state machine into the emergency state should a safety-critical error occur, such as a battery over-temperature warning. The user thus maintains full control over the pod should the autonomous systems fail or an unforeseen issue arise. The Mission Control system also relays relevant data (namely: *status*, *position*, *velocity*, *acceleration*, and *team ID*) to a SpaceX server in real-time in the form of a UDP datagram. Battery safety can be monitored remotely, as the Mission Control system displays battery temperatures, currents, voltages, and charge levels to the user. Should these values fall outside the safe operating range, the relevant numerical value will be displayed in red on the GUI in order to notify the user. One may then proceed to issue the "KILL POWER" command to the pod, which transitions the pod into the emergency state (also called 'state 0' - please see the Section 7.4 of this document) which disconnects the high-power batteries.

7.3.3 Considered Solutions

The team considered using the User Data Protocol (UDP) connection protocol to facilitate communication between the pod and the mission control system, however we decided to use TCP due to its robustness and data-delivery guarantee. Other implementation environments were also considered, but C++ proved to be best-suited for interaction with the Controls architecture, and Java the best for GUI development.

7.3.4 Chosen Solution

The software communications architecture emulates the form of a client/server relationship, where the pod-side telemetry system acts as a C++ TCP/IP client, and the Mission Control system as a Java server. The communication protocol is independent of programming environment, thus the two systems can communicate seamlessly irrespective of the differing implementation languages.

TCP/IP is a connection-oriented network protocol suite, meaning that a connection must first be established before the client and server can exchange data. TCP is a reliable protocol because it incorporates transmission error-detection into the protocol itself, ensuring not only that all data packets are delivered, but also that they are delivered in the correct order - this is not true of UDP. This is achieved

by assigning a unique sequence number to each piece of data that is transmitted. For each data segment sent, the receiving client/server must return an acknowledgement (ACK) within a specified period. If an ACK is not received by the sender, the data is re-transmitted. TCP is also full-duplex, meaning that data can be both sent and received over the socket simultaneously. This was a key design consideration, as the pod must be capable of continuously sending pod parameters to Mission Control while also listening for emergency commands. If the telemetry connection is lost during the run, the pod is designed to transition to the emergency state and deploy the power-redundant emergency brakes — this is because, without a telemetry connection, the emergency brake command cannot be issued to the pod from Mission Control. All communications are also saved to a text file for analysis post-run.

Key data on the pod's state will be forwarded to a SpaceX computer system via a UDP socket, as required by the competition specification. A datagram containing *status*, *position*, *velocity*, *acceleration*, and *team ID* parameters will be pushed to IP address 192.168.0.1 using port number 3000. UDP is a connectionless datagram protocol, and facilitates faster transmission than TCP/IP as it does not attempt to recover lost packets, and hence does not lose time detecting and re-transmitting dropped packets as is the case with TCP/IP. Figure 100 illustrates this.

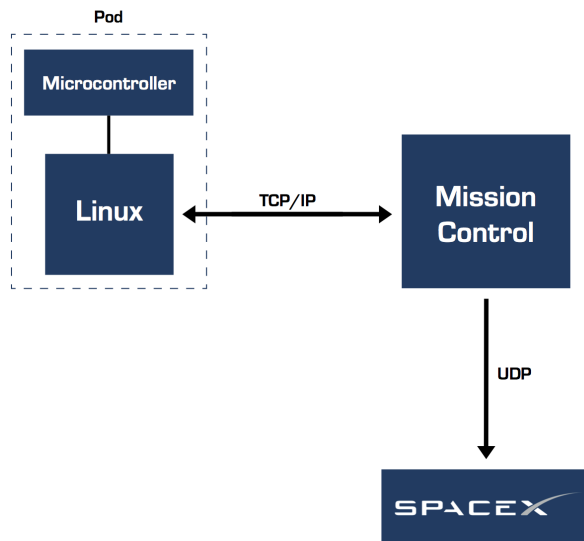


Figure 100: Communications Flow Chart

7.3.5 Safety

If safety-critical pod parameters deviate from their safe operating ranges, the Mission Control system will graphically notify the operator who can issue an emergency signal to the pod. The TCP connection will guarantee that these commands reach the Linux computer which controls the emergency brakes and power connections. As previously explained, the protocol can confirm that the pod has received the command and the request will be retransmitted in the event that it is not received. Should the telemetry connection fail, the pod will transition to the emergency state as a safety precaution.

7.3.6 Testing

Rigorous testing has been undertaken to ensure that the telemetry system can reliably transmit bi-directional data in real-time and respond to emergency interrupts. A Raspberry Pi computer running the pod-side communication code successfully communicated with the Mission Control system running on a team laptop over a direct ethernet connection and the university WiFi network. When an emergency command was issued from Mission Control, while receiving the pod data-stream, the Raspberry Pi received this signal with immediate effect.

The UDP datagram transfer has also been tested with a custom UDP server, simulating the SpaceX computer. The UDP receiver was executed on an Amazon Web Services machine, running Amazon Linux AMI 2017.03 on a 2.3GHz Intel Xeon-E5 processor. Datagrams of critical pod parameters were transmitted successfully with no notable packet losses.

The software communication systems are based heavily upon the architecture of last year’s design, which succeeded all tests undertaken. Such tests will be reiterated at the appropriate point in the development cycle — please see Section 7.5 of this design package for more information on the software development timeline.

7.4 State Machine

7.4.1 Design Constraints

An initial challenge faced by the team while designing the software was the embedded system's inherent difficulty in describing its complex processing behaviour, especially of critical failures in the system. A potential implementation should:

- be capable of responding to internal and external events;
- be flexible and modular, facilitating change to the logic-flow of the program without impacting the overall system;
- ensure that every possible state/condition (especially edge conditions) of the pod and every event are handled by the system;
- be able to precisely communicate the current state of the pod to a designated SpaceX server;
- ensure that the pod can only be in one state at any given time.

7.4.2 Design Decisions

Ultimately, the team decided to use the *Finite State Machine* model to precisely capture the system's behaviour. This solution was chosen because the use of such a state machine greatly simplifies the central coordination of the pod's complex system of sensors and actuators. We can also prevent “*spaghetti code*” with convoluted conditional logic, where each branching point requires a complex expression and transitioning to states requires modifying many variables, which can easily lead to inconsistencies and unwanted side effects. Another advantage is the flexibility and modularity of the model, which permits the addition and removal of new states over time — the state machine can scale seamlessly with the increasing complexity of the pod systems without affecting the overall functionality of the system.

The state machine runs on a microcontroller which is connected to all pod control systems via CANBUS. The microcontroller is directly connected to the pod's power redundant brakes, thus in a scenario where the CANBUS is inactive the pod reserves the ability to stop promptly. The microcontroller is also directly connected to the Linux machine which governs communication between the pod and the Mission Control system. This is to facilitate the prompt response to emergency commands, in addition to the transmission of pod information to the operator and SpaceX.

7.4.3 State Diagram

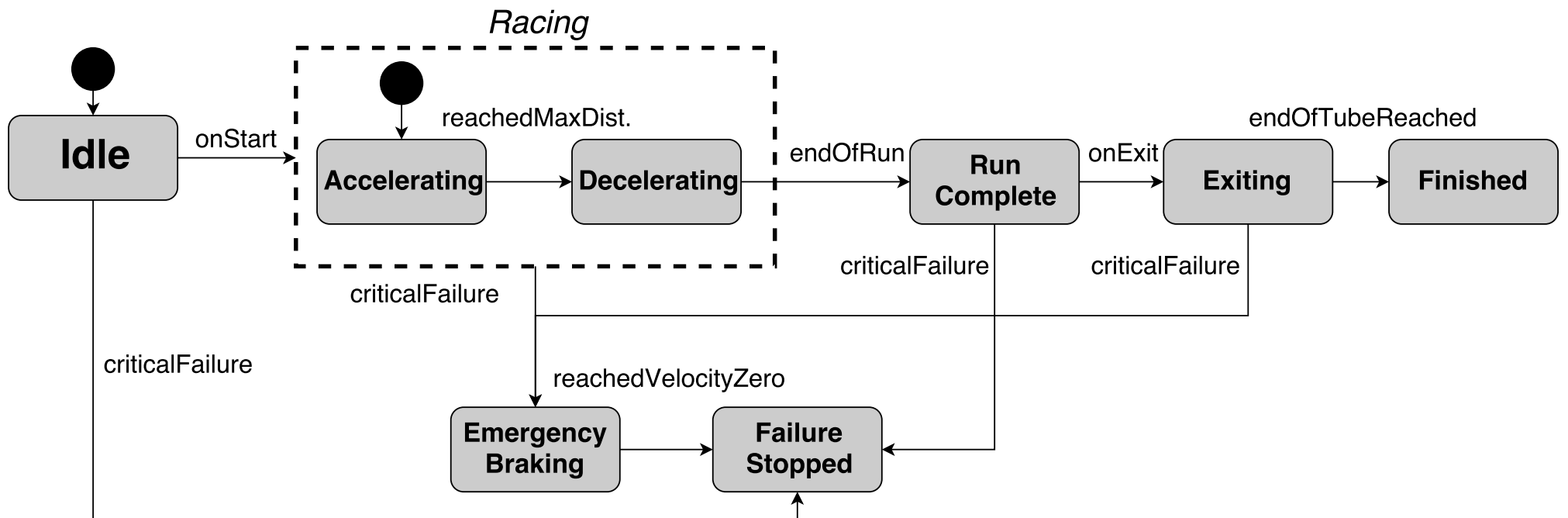


Figure 101: State machine diagram.

7.4.4 States

State	Description	Systems
Idle	Initial state	All dynamic systems in standby.
Racing/ Accelerating	Accelerating state	Propulsion system provides maximum acceleration.
Racing/ Decelerating	Decelerating state	Propulsion system provides maximum deceleration.
RunComplete	Pod has completed the run and reached velocity zero.	All dynamic systems in standby.
Exiting	Pod moving with low velocity towards the end of the tube.	Very low power provided to propulsion system.
Finished	Pod is stationary and has reached the end of the tube	All dynamic systems in standby.
EmergencyBraking	Power-redundant emergency brakes are applied to make the pod stop as quickly as possible.	Emergency brakes deploy, power cut to propulsion system.
FailureStopped	Pod is not moving as a result of emergency braking or a failure in a static state. Manual intervention required.	Emergency brakes deploy, high power battery cut.

Table 36: Pod states.

7.4.5 Events

Event	Current State	Next State	Transition Criteria
onStart	Idle	Accelerating	Permission is given by SpaceX staff.
reached MaxDistance	Racing/ Accelerating	Racing/ Decelerating	Distance/position sensors have detected that the pod has reached the maximal distance which is dynamically computed on the fly, taking into account the safety-critical maximal deceleration of 1.5G.
endOfRun reached	Racing/ Decelerating	RunComplete	Distance/position sensors have detected that the pod has reached the end of the run and that the velocity is zero.
onExit	RunComplete	Exiting	Permission is given by SpaceX staff.
endOfTube Reached	Exiting	Finished	Distance/position sensors have detected that the pod is at the end of the tube (security margin included).
criticalFailure	1. Idle, Racing, Exiting 2. RunComplete	1. Emergency Braking, 2. FailureStopped	<ul style="list-style-type: none"> • IMU failure • Battery temperature critical ($> 70^{\circ}\text{C}$) • Loss of telemetry • Low power battery voltage ($< 15V$) • High battery voltage ($> 200V$) • Low power battery current ($< 30A$) • High power battery current ($> 900A$) • Navigation fails • Pod is unstable - excessive vibrations • Calculated displacement in tube is not feasible • Power is lost • Motor error (E.g. unresponsiveness) • Last chance to brake/maximal acceleration period exceeded • Breach in the CANBUS • Failure of sensors • Master Control Unit disconnected
reached VelocityZero	EmergencyBraking	FailureStopped	Emergency braking is completed and the velocity sensors indicate that the pod is no longer in motion.

Table 37: Considered possible events with transition criteria.

7.4.6 Testing

The team uses YAKINDU Statechart Tools to test the state machine model. The software provides an integrated modelling environment with simulations allowing to check dynamic semantics, set breakpoints on transitions and debug logic errors. Additionally, the team is building a prototype pod to test all subsystems and their communication. This will let the team test the interaction of the event-driven state machine with all software modules, such as navigation and motor control.

7.5 Software Development Timeline

The development timeline for the software systems in their totality is tabulated overleaf in the form of a *Gantt chart*. Software development is inherently iterative and non-linear, thus time has been allocated to re-iterate elements of the development process should new information come to light as a consequence of testing.

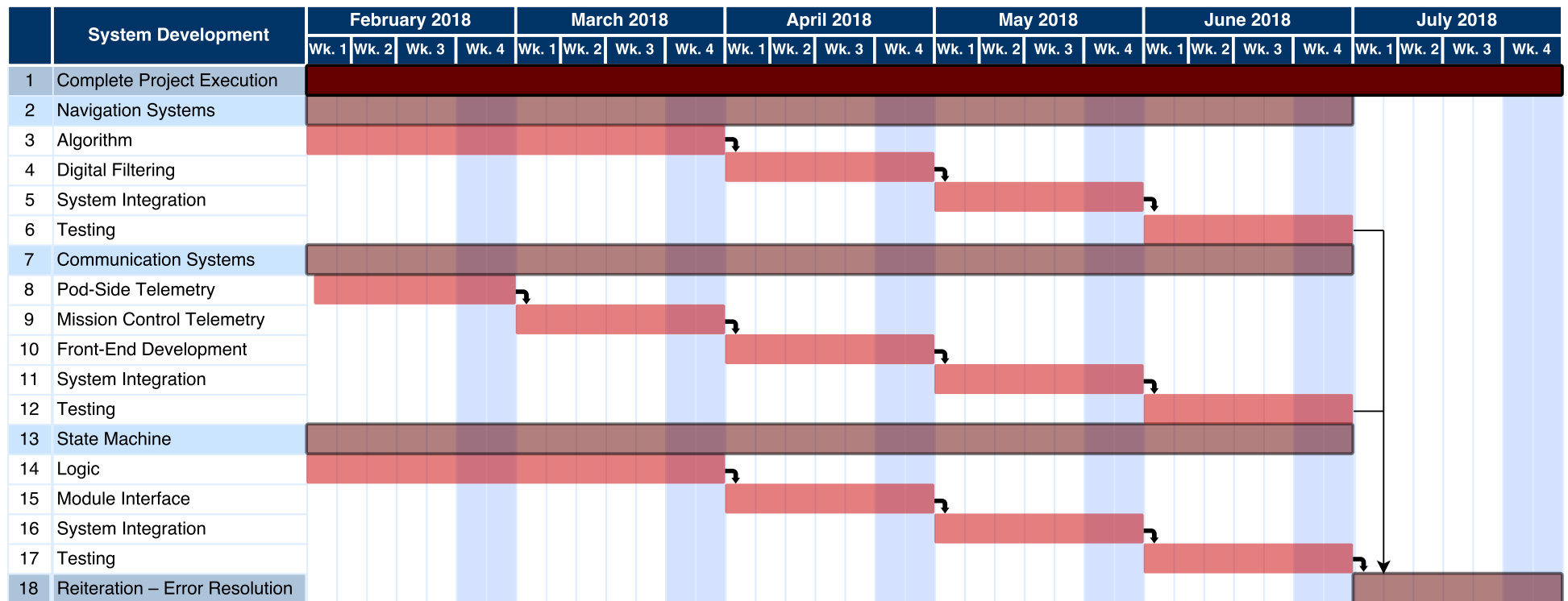


Figure 102: Software systems timeline.

8 Structure



8.1 Carbon Fibre

Metals are for Victorian times.

Dr Austin Lafferty
Postdoctoral Student
Research Institute of Materials and Processes
The University of Edinburgh

The transport industry is going through a shift toward composite materials, be it in the automotive industry where all high performance cars and BMW's new i Series now have a carbon fibre chassis, or the aerospace industry with Rocket Lab's Electron or SpaceX's BFR liquid oxygen tank. Hyperloop pods, once made commercially available, will most likely be manufactured with a carbon fibre monocoque given it is a lightweight, high performance material. With this in mind, it only makes sense for HYPED to push its use of carbon composites as well, given its suitability to our application.

However, designing a carbon fibre monocoque takes years of experience, and carbon fibre in general is highly versatile yet subtle material to work with, both in its anisotropic nature, diverse manufacturing methods, and plethora of applications. The goal for HYPED as a team is to gain the valuable experience in working with carbon fibre over this and the coming years, fully aware that such experience is not gained overnight.

In speaking with our university our team got authorisation for a small handful of our members to have formal training and full access to the composites lab, putting us in the position to gain the experience and have access to the tools necessary to manufacture our parts.

Carbon Fibre Reinforced Polymer (CFRP) will be used in our three core structural parts: the Chassis, Pressure Vessel, and Shell, as well as for the Dynamic Module Plate which was detailed earlier. For their theoretical design and simulations, our team has used material values [12]. Floreani's thesis details a student project based on the manufacturing of a carbon fibre part that plays a structural role. The carbon fibre used for his project has been sourced through sponsors, and the values used in his simulations were derived from interpolations of values given by the supplier of the material, taking into account the fact that he did not have access to an autoclave and therefore could not achieve ideal properties. Our simulations have been based on the same values, but it is important to note that these are simply representative values showing the feasibility of our designs, using a safety factor of two wherever possible. Once HYPED has secured their own supply of carbon fibre, and before undertaking the manufacturing of our parts, the team will derive material properties from physical testing of samples manufactured in house. These will allow our team to make new simulations, finalize component geometries, and then carry on with manufacturing. All these later simulations will adopt a safety factor of two, with no exceptions made.

Following is some information on CFRP and how it will be implemented in our designs, going from resin to weave to the layup itself.

Selecting the exact resin used is critical in working with carbon fibre, given it is what establishes the general material properties. The resin is what forms the matrix binding the fibres, and gives the material both its compressive strength and in and out of plane stiffness. Toughness, recyclability and flexibility are not desired therefore a thermoplastic matrix can be dismissed; they are also slightly difficult to use in manufacturing. However, a thermoset such as epoxy resin or PEEK are standard fibre matrices that can be used in our case, and can be acquired easily. PEEK and epoxy resins are compared in Table 38.

	σ (Mpa)	E (Gpa)	ν	ρ (gcm $^{-3}$)	\mathcal{L}/kg
PEEK	90	3.6	-	1.32	1–7
Epoxy	85	10.5	0.3	1.4	3–5

Table 38: PEEK and epoxy resin comparisons.

Strain is something we want to avoid at all costs given deformation in certain components such as the Chassis or Dynamic Module Plate would lead to displacements of critical systems including the brakes and Halbach wheels, potentially leading to catastrophic failure. Therefore epoxy resin is the best matrix choice due to its high Young's modulus.

Lamina properties are approximated by a set of equations derived in Appendix A.4.1. From these are obtained values for the longitudinal modulus, 138GPa, and the transverse modulus, 24GPa approximately, although this assumption was made by using the equation for the rule of mixtures and is treated as a worst-case value. More accurate properties can be assumed using the Halpin-Tsai equation or by material testing. The in plane Poisson's ratio obtained is 0.26. These equations define microscopic properties in a fibre matrix, and can roughly describe laminates and therefore weaves by assuming unidirectional properties. This gives a rough estimation for the material strength within a layup, although empirical determination of these properties through testing of samples will yield the most accurate results.

At a macroscopic level, carbon fibre can be classified in a few different categories including unidirectional fibres, and weaves or fabrics. Unidirectional fibres refer to laminates made up of fibres oriented in a single, continuous direction. These have a very high tensile strength but limited lateral strength, which is compensated for in unidirectional fibre layups by implementing several laminae in various orientations. On the other hand, fabrics or weaves are carbon fibres wound together by weaving bundles, or tows, of unidirectional fibres to create a weave, the orientation of which affects the material properties. Plain weaves have the advantage of being resistant to fabric distortion during layup, which makes it easier to maintain uniform properties throughout a component. However, the strength of a composite fabric is roughly proportional to the length of tow in the in-plane direction, meaning a 2×2 twill weave has better properties than a plain weave given less of the material is 'spent' weaving over or under other tows. 2×2 twill weaves also have the advantage, due to their composition, of being more drapable, meaning they are easier to lay up in tight geometries with small radii. Finally, a weave such as a 4H satin would be ideal for parts such as the pressure vessel, as it could be used to maximise its performance in the hoop direction where it is needed the

most. See Figure 103 for an illustration.

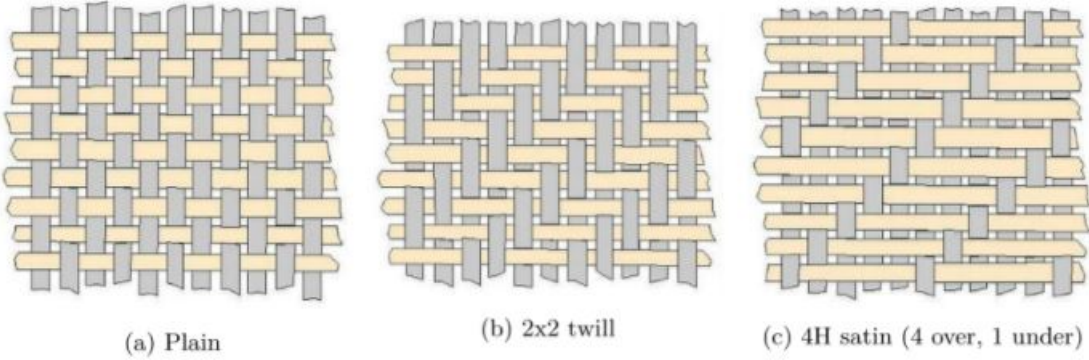


Figure 103: Carbon Fibre weave patterns [13].

Nonetheless, depending on the carbon fibre secured through suppliers or sponsors, it is possible that all our parts end up being manufactured with a same fabric, in which case a 2×2 twill weave would be a good solution. Ideally, this would be a prepreg roll given prepreg layup offers a few advantages over other manufacturing methods, such as wet layup and resin infusion. In fact, wet layups make it difficult to work on large parts as the resin tends to start curing and imperfectly so before the layup is finished and the part is put into an oven. On the other hand, resin infusion is a highly technical method and requires much experience to obtain a good result. However, prepreg — pre impregnated — rolls allow for a layup on large parts while offering good results given the resin has been previously impregnated into the fabric through well defined industrial processes. One disadvantage prepreg rolls bring is that they must be refrigerated at around -20°C , although it is well worth the trouble.

Once the weave is determined, CFRP can follow various layups. For most of our components the layup will be such that quasi-isotropic properties can be obtained. To do so, the weaves must be arranged in certain layups depending on the amount of layers necessary. These will be representatively resumed in Table 39 — adding more layers is obviously possible.

Number of Layers	4	6	8
Layer Orientation ($^{\circ}$)	0, -45, 45, 90	0, 45, 90, 90, 45	0, 45, -45, 90, 90, -45, 45, 0

Table 39: Weave layup arrangements.

The minimum number of layers that will be used in any of our parts is 4 to ensure even at their thinnest, parts will unlikely be prematurely damaged.

The manufacturing process for any composites is primarily defined by the geometry and properties required from the design. The relevant design parameters are summarised in Table 40, overleaf.

Process	Production Speed	Cost	Strength	Size	Shape	Raw Material
Filament Winding	Slow to fast	Low to high	High	Small to large	Cylindrical and axisymmetric	Continuous fibres with epoxy and polyester resins.
Pultrusion	Fast	Low to medium	High (along longitudinal direction)	No restriction on length; small to medium size cross section	Constant cross section	Continuous fibres, usually with polyester and vinylester resins
Hand lay-up	Slow	High	High	Small to large	Simple to complex	Prepreg and fabric with epoxy resin
Wet lay-up	Slow	Medium	Medium to high	Medium to large	Simple to complex	Fabric/mat with polyester and epoxy resins
Spray-up RTM	Medium to fast	Low	Low	Small to medium	Simple to complex	Short fibre with catalysed resin
	Medium	Low to medium	Medium	Small to medium	Simple to complex	Preform and fabric with vinylester and epoxy
SRIM	Fast	Low	Medium	Small to medium	Simple to complex	Fabric or preform with polyisocyanurate resin
Compression molding	Fast	Low	Medium	Small to medium	Simple to complex	Molded compound (e.g. SMC, BMC)
RTM	Medium	Low to medium	Medium	Small to medium	Simple to complex	Preform and fabric with vinylester and epoxy
Stamping	Fast	Medium	Medium	Medium	Simple to contoured	Fabric impregnated with thermoplastic (tape)
Injection molding	Fast	Low	Low to medium	Small	Complex	Pallets (short fibre with thermoplastic)
Roll wrapping	Medium to fast	Low to medium	High	Small to medium	Tubular	Prepregs

Table 40: Manufacturing process selection criteria. [14].

Implementing carbon fibre at such scales will be a first for the HYPED team, but the necessary time will be taken to learn how to work the material and get the best results from it. The more experienced members amongst us will help in manufacturing our carbon fibre parts, while working within our University's composites department.

As mentioned previously, material strength, specifically in the case of carbon fibre, depends on a wide array of variables. However, for the sake of analysing simulation results, a material strength had to be defined; one that our team could realistically expect to get in sourcing carbon fibre [12], our maximum tensile stress was assumed as 561MPa, while the maximum compressive stress is taken as 406MPa. Overall, the maximum stress was therefore estimated to be 406MPa. These values are from Cytec's 2×2 Twill T300 weave.

8.2 Chassis

8.2.1 Introduction

The Chassis is the base of our design, both the primary structural component and the part to which all other components are appended. In addition to bringing a structure to our pod and carrying the payload, the chassis' role is to integrate and organise all power, propulsion, dynamic and control systems. Specifically in the scope of a competition, this requires a serviceable design that ensures ease of access to components, all the while remaining as weight efficient as possible and structurally able to withstand all the loads to which it will be subjected. With safety, adaptability, scalability, and performance in mind, the concept of a modular design was embraced. The key aspect is that the chassis was designed around the concept of modularity, and so around the modules it would have to house. As such, the chassis' design was virtually fixed one month after designs started, giving the flexibility to build systems around it knowing it would remain the same. This allowed for whole modules or components to be revamped at mature design stages since others could be reallocated in accordance to this. This modular design will also help streamline the manufacturing process as subsystems do not depend on the completion of other parts, and will allow us to test and improve upon module designs when possible as modules do not strictly depend on one another. In fact, as designs are built, tested, and iterated upon, all modules will be quick and easy to disassemble from the chassis so that there is no safety hazard posed by working on various parts within the pod at the same time. This will also offer maximum flexibility in improving on modules as time and resources allow. However a modular design also comes with its drawbacks. The main drawback that comes to mind is the idea that modularity offers practicality at the expense of performance,

suggesting a chassis that might not offer satisfiable strength due to its geometry. Generally speaking, the chassis' geometry has not so much been optimised for efficiency, but has a straightforward orthogonal structure for the sake of modularity and operability. Nonetheless, our chassis will be made of carbon fibre, with the idea that varying geometries would not cause a significant change in mass relative to the pod's mass as a whole, and therefore having a modular design is clearly more of an advantage than it is a drawback.

Our team's design in the PDB detailed an aluminium chassis, however the design now focuses on carbon fibre. The reason for this is that carbon fibre is a highly technical and expensive material to use in manufacturing, and the team chose aluminium as a safer bet on what was doable given our expertise, resources, and expectations at the time. However, after speaking at length with the composites department of our university as well as Masters and PhD students with experience in composites, taking on the design and manufacturing of carbon fibre parts was deemed within our reach, and well worth the challenge. In the case of the chassis, an aluminium part is a safer bet and easier to work with given that composites involve inserts, drilling, or bonding in attaching modules which complicates the design and manufacture of our part. However, the mass savings of an order of magnitude, from tens of kilograms to just a few, means that our design when using composites remained one capable of offering high performance in terms of strength to weight ratio, and worth the added trouble.

8.2.2 Summary

Table 41 outlines the design specifications of the chassis in weight, dimension and material.

Item	Length (mm)	Height (mm)	Width (mm)	Thickness (mm)	Mass(kg)	Material
Outer U-Channels ($\times 2$)	3000	216	60	12	21.9	Carbon Fibre
Inner U-Channels ($\times 4$)	750	216	60	12	5.48	Carbon Fibre

Table 41: Chassis design specifications.

As mentioned previously, the end design of our chassis uses carbon fibre reinforced polymer as its core material. However, to make room for any contingency, our choice is to build a proto-prototype out of glass fibre reinforced polymer — GFRP. Our partnership with the company with which we built the shell last year has also been secured for this year, meaning it is well within our capabilities to manufacture such a part, and to high standards. The aim is therefore to build the chassis out of GFRP early on so as to have it in our lab and use as a physical housing to design all of our modules, while also gaining valuable experience so that the CFRP chassis is then manufactured to the highest standards. Since GFRP and CFRP are cousin materials, the experience gained in building the former chassis will be transferable. The following design is characterised with a CFRP chassis in mind, but applies to the glass fibre part as well.

8.2.3 Considered Solutions

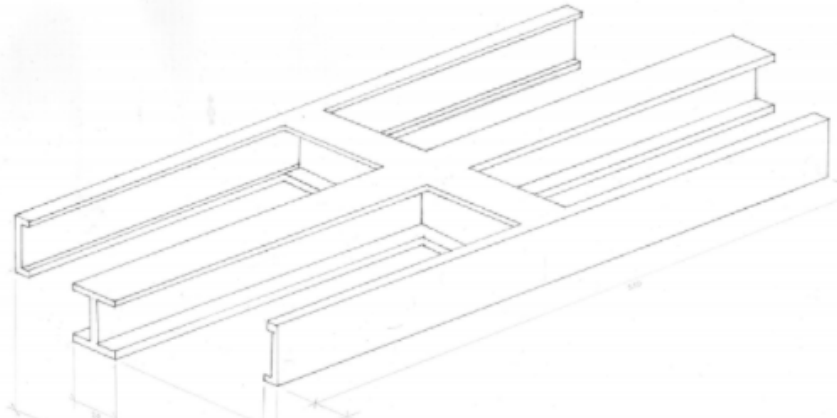


Figure 104: 1st chassis iteration dimensions: 2500mm×1000mm×100mm.

As seen in Figures 104 and 105, the chassis design evolved over time from less to more functional, keeping the same idea focused around the housing of modules, and manufacturability. Dimensions evolved as well, as the chassis was made thinner and longer to adapt for the positioning of levitation while keeping a big enough inner volume to house all of the pod's systems. The geometry of the chassis is widely based on beam-like U sections, as these offer good resistance in bending and torsion. The iterations through which the design went were largely based on the massive battery the chassis would have to house, and the accessibility of various modules or lack thereof. The modules gained more and more importance in the design, and grew increasingly larger, to the extent that they will play a quasi-structural role in the final design.

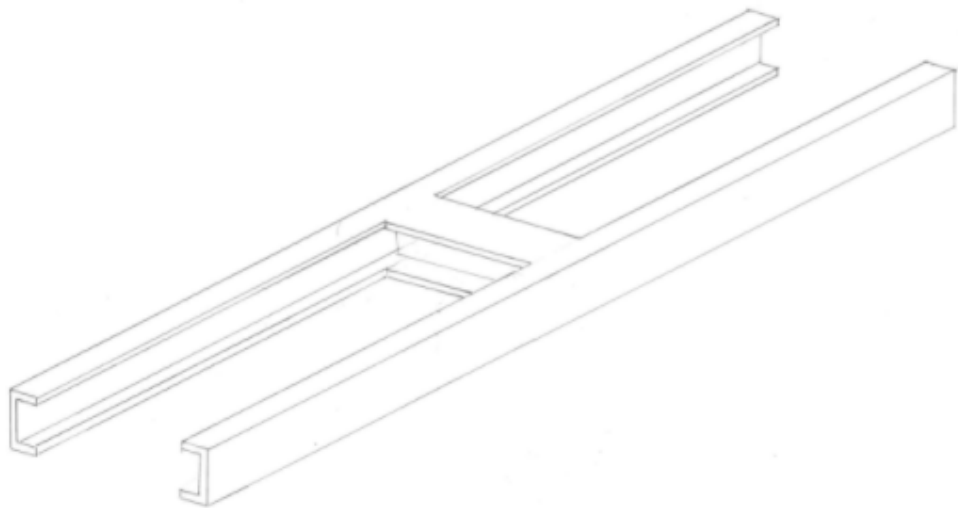


Figure 105: 2nd chassis iteration dimensions: 3000mm×1000mm×200mm.

8.2.4 Chosen Solution

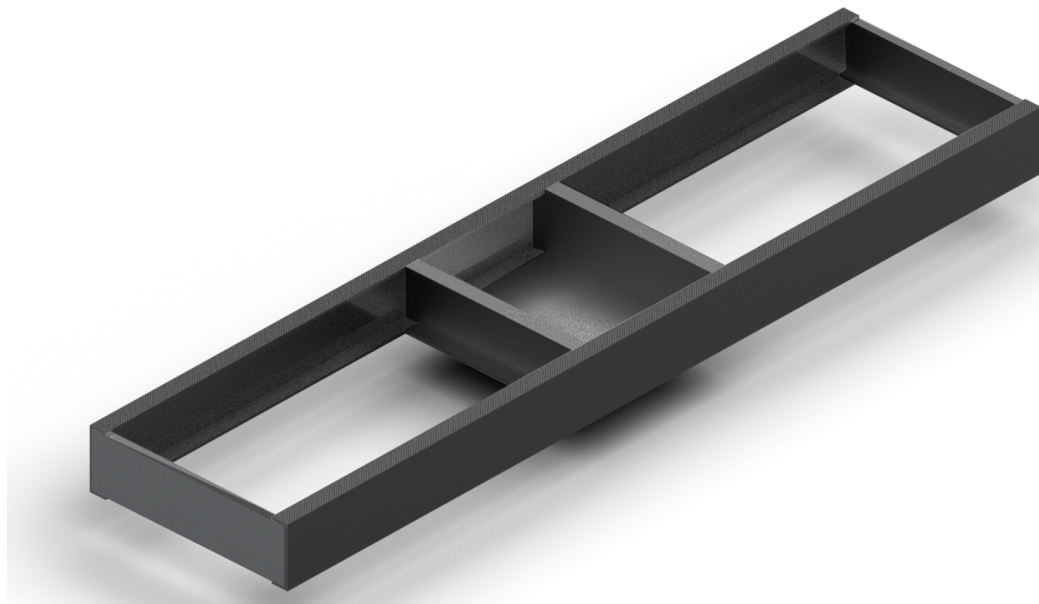


Figure 106: Final Chassis iteration dimensions: 3000mm×750mm×216mm.

Past this stage, one single major modification was made due to the shifting power requirements of our pod. Earlier plans were to have the battery split into two

modules on either side of the central I beam, but during the first few months of designing our pod our target power requirements rapidly increased from 4.75kWh up to 6.34kWh. This made for a battery so large that splitting it in two less and less of a justifiable design choice, which led to ‘splitting’ the central I beam into two parts, with the battery pack in the middle. This led to a chassis design as seen in Figure 106.

When the concept of modules comes into play, their attachment method to the chassis must also be considered. The initial idea was to have modules mount onto rails within the chassis allowing for quick insertion and removal of these; however, this was quickly discarded. When working with carbon fibre, bonding epoxies can also be used, but this would mean once placed modules would no longer be removable, which would defy the whole purpose of our design. As a result, the solution that was adopted is to bolt modules to the chassis. This allows for a secure connection while enabling the quick removability of modules.

8.2.5 Simulations

The worse case scenario for the chassis was defined as follows: full acceleration (or deceleration) of 2g, payload under the form of a 140kg pressure vessel, and 2mm bumps at opposite corners simultaneously while levitating. This is when all emergency brakes and Halbach wheels are engaged in braking, in addition to imperfections in the track. The edges of the bottom plate are fixed, and a safety factor of 2 is included. Figure 107 shows that the maximum displacement due to two 2mm bumps in opposite corners in addition to the force induced by the payload is about 3.5mm, which is acceptable.

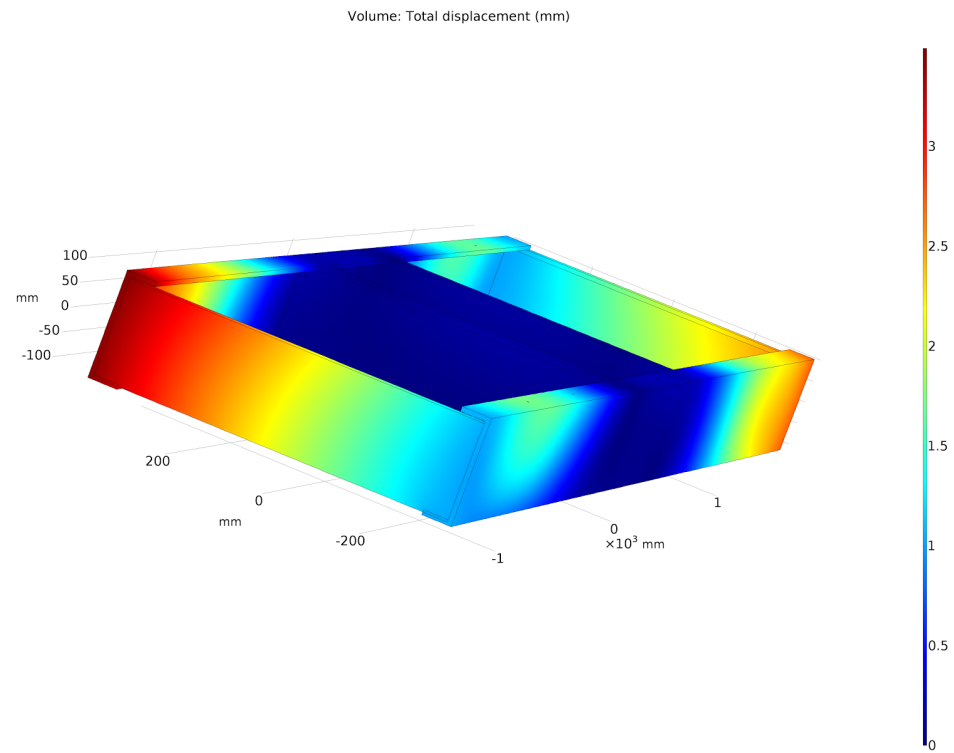


Figure 107: Induced displacement in mm.

Furthermore, obtaining principal stresses in all directions has shown that the greatest stress will be induced in the vertical direction, and will be of about 550MPa. This is greater than the maximum stress that was defined by our example of 2×2 twill T300 fabric, but remains within the range of performance offered by carbon fibre, which is around 600MPa. However, our team will run further simulations on the chassis using Abaqus, a simulation software that enables better definition of carbon fibre before undertaking manufacturing.

Another design scenario was defined as a frontal crash, one that our chassis would have to withstand. Given that the chassis was designed for bearing the loads from modules specifically, our team chose to give the front shell a structural role so that it could mitigate the loads on the chassis in the event of a frontal collision. As seen in the specific Shell section, the front was structurally designed so that it could bring the pod to a full stop in the event of a 7ms^{-1} frontal crash, before the chassis itself were to hit the obstacle. This avoids any major damage or stresses to be induced on either of the modules or the pressure vessel. Furthermore, a simulation was carried out on the chassis to show that in such a crash it would not fail. This can be seen in Figure 108, where the highest stress is in the direction

of the chassis' length, at about 95MPa, whereas material strength stands at a few hundreds of MPa.

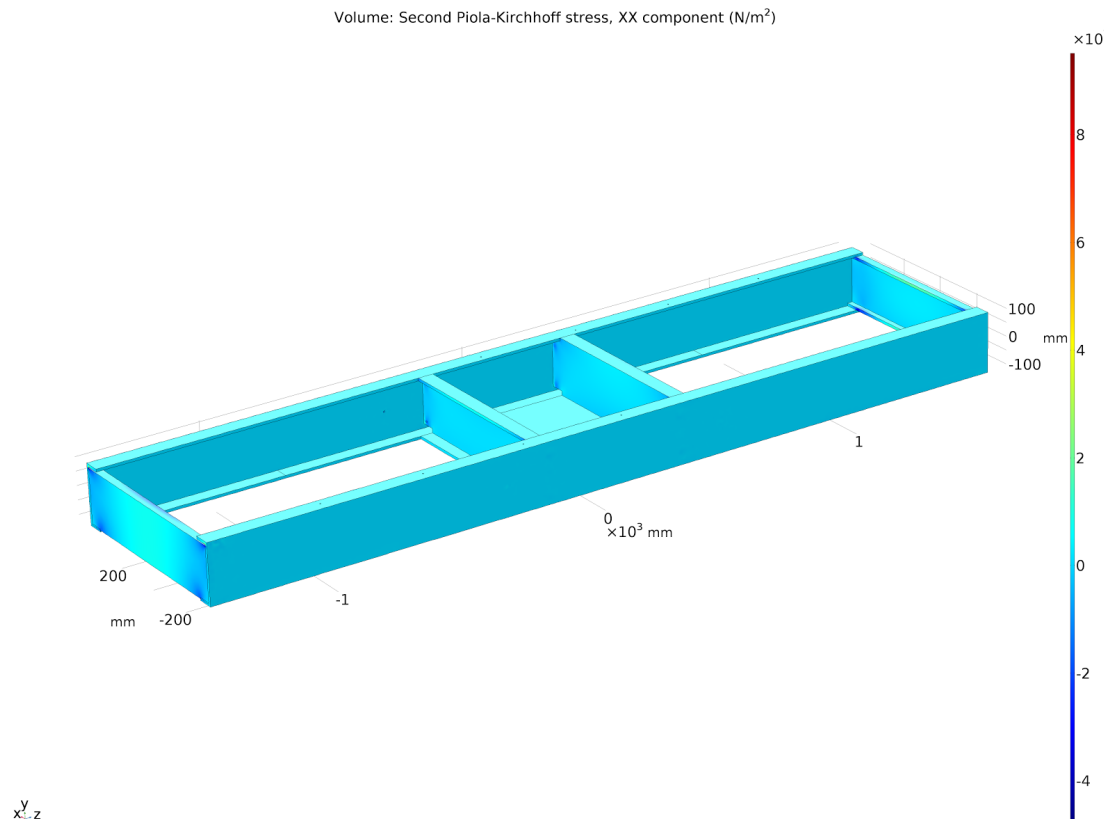


Figure 108: Stresses induced on the chassis.

8.2.6 Safety

The chassis will be made from between eight and twelve laminae of carbon fibre, depending on the material properties obtained through testing, and simulations taking the safety factor of two into account. However, if there is a fracture of a number of fibres in a particular lamina, it will not propagate throughout the structure as all neighbouring fibres will be held strongly by the matrix the resin forms. The manufacturing process of the chassis, bagged in a vacuum-seal, will ensure there are virtually no air bubbles in the component, and it will therefore not be of concern in a vacuum environment.

8.2.7 Scalability

Although the chassis would likely undertake a significantly different form in a scaled design, if ever similar beams were used they would likely be made in a pultrusion process, given their simple and constant geometry, and not by hand layup as the team intends to make them. Pultrusion is a process whereby fibres are extruded through a metal section and infused with resin making for an accurate section, although with orthotropic properties. This production method is much more scalable than hand lay-up.

Given the different manufacturing process of a scaled chassis, and its increasing returns to scale, the cost of a scaled chassis cannot be estimated without contacting manufacturers of pultruded composite members. Size and weight of the chassis can be considered to increase roughly linearly with an increase in the size of the pod, making a 7m long pod around 63kg, without accounting for any metal inserts or reinforcements, which would likely be necessary. A longer chassis would also likely be made thicker to withstand the larger forces to which it would be subjected due to the moments that would be created. Close and regular inspection may have to be done on such a chassis given CFRP is a fragile and brittle material.

8.2.8 Cost Breakdown

A minimum of two chassis will be made, one from glass fibre and the other from carbon fibre. The GFRP chassis will be made with a company that sponsors us through materials, only covering costs for labour hours they incur. However, while last year the bulk of the technical manufacturing was done by them, this year HYPED expects to do all the labour and only pay for consulting and learning hours. This should not amount to more than £1000.

On the other hand, the CFRP chassis will not be possible to manufacture in house, given the university does not have a large enough oven or autoclave to bake such a large part. The team will still attempt have the chassis manufactured by its members, but will depend on external facilities to do so. The carbon fibre sheets themselves will also hopefully be obtained through sponsorship. However, assuming the team may have to source its own CFRP, the material cost for the carbon fibre chassis is expected to reach £2000, and renting the facilities or getting it manufactured externally may amount to £2000 as well.

The total best case cost of the chassis with the static components it includes is therefore estimated at £5000. Table 42 is a summary of the estimated best and worst case cost estimates to manufacture the chassis.

Component	Subcomponent	Cost (£)
Mould	Pultruded	50
GFRP Chassis	Labour Hours	1000
	Material	0
CFRP Chassis	Labour & Renting Facilities	2000
	CFRP	1500
	Resin	500
Best Case Total		5050
Worst Case Total		8050

Table 42: Chassis cost breakdown.

8.2.9 Manufacturing

The manufacturing of the chassis will be done using a pultruded glass fibre ‘U’ channel as the master. A female mould will be made from its outer shape so that composite materials can then be laid up in it and cured. The pultrusion process is when long fibres are pulled through a heated metal die forming a composite beam with constant cross section. The value of this is that it makes for an accurate part which is needed for our master. In theory, our team could also manufacture a master from an epoxy block, but working with a pultruded member will produce just as good results in less time, and likely for lower costs. The geometry of the mould should be such that the channels produced with it will have a height of at least 200mm, providing for an equal or greater inner volume of the chassis to what was designed. A close available standard size channel found from a manufacturer is 240m high, which would make for a part height of 240mm, 40mm greater than designed, leaving more room for modules within the chassis. The flange width of the standard pultruded channel is 72mm, giving enough length to work with for the chassis’ flanges. As the team continues to look into potential pultruded member providers, the most appropriate available member will be selected. To manufacture the I beam battery housing, the same fibreglass section will be used to create a shorter mould with an extended web on each end that will slot in and be secured to the U-channels.

As mentioned previously, the team will start by manufacturing a proto-prototype out of GFRP before going on to build the CFRP chassis. The rationale behind this is to have the first chassis as a backup given the team has a partner in fibreglass manufacturing and making a chassis out of this material can be considered a safe option. For both parts of either material the first step will be to make small samples of $250 \times 25 \times 2$ mm that will be tested at machines from our university so

that material properties can be empirically obtained. These properties will then be used to create a custom material in simulations from which the thickness needed from composites will be obtained. Only then will the team undertake the actual manufacturing of the parts, with a safety factor of two.

8.2.10 Testing

Testing Each member produced will undergo mechanical testing to determine its resistance to the loads it will experience, including maximum acceleration load, imperfections in the track floor, and reaction forces from the levitation and payload. The chassis will then undergo these testings once assembled, and members are bolted together.

Regarding the bolting of parts, tests will be carried out with bolts using washers as well as big Head bolts to assess how they perform under load before deciding which ones to use in our final design.

8.2.11 Timeline

A timeline for the chassis manufacturing and testing can be seen in Table 43.

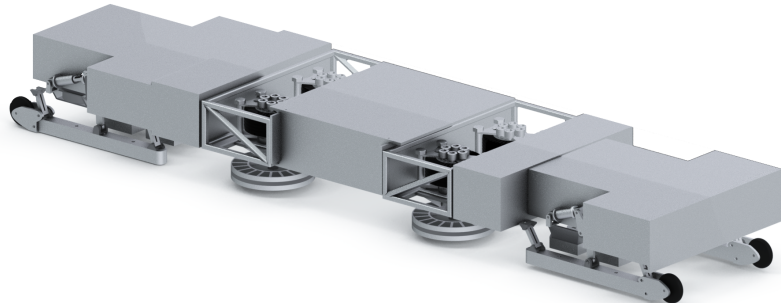
January	Making GFRP samples, obtention of material properties, redesign of GFRP chassis in accordance, sourcing of CFRP supply.
February	Obtention of CFRP supply, manufacturing of GFRP chassis, testing of GFRP chassis, making CFRP samples, obtention of CFRP material properties, redesign of CFRP chassis in accordance.
March	Manufacturing of small-scale CFRP members for testing, validation of theory and simulations through test or otherwise addition of safety factor in design in accordance.
April	Manufacturing of CFRP chassis, testing of CFRP chassis.
May	Further testing of chassis, use in early assembly.

Table 43: Chassis timeline.

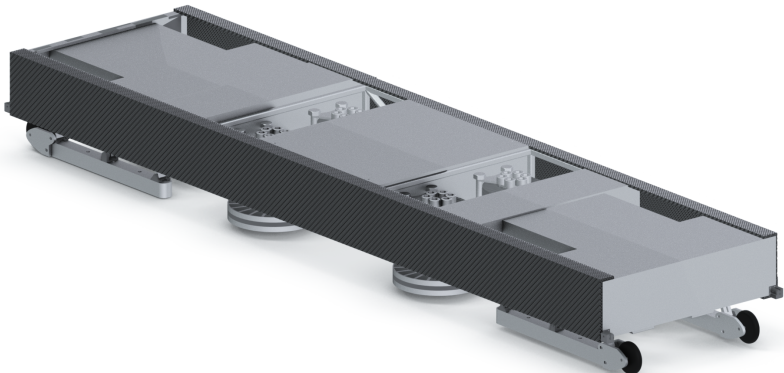
The following three figures illustrate the chassis being fitted with the dynamic, electronic and power modules:



(a) Chassis without module casings.



(b) Dynamic, power and control modules arranged in the shape of the chassis.



(c) Chassis complete with modules.

8.3 Pressure Vessel

8.3.1 Introduction

As was the case last year, a self-imposed design constraint — and the major design constraint for us — is to have a full-size dummy as our payload. This dummy has the size and weight of a 95th percentile Scottish male. Last year this constraint was took to the letter, as our dummy just barely fit lying flat in our pod, which ended up looking like a very, very fancy, expensive, and complex coffin. However, this year's aim is to create a liveable environment, which starts with a decent sitting position akin to a 'zero gravity' lounge seat, and involves a pressurized environment so that our dummy can cruise in the comfort of one atmosphere. This will help promote the Hyperloop concept as a whole, and makes the challenge of building a pod that much more interesting for us at HYPED.

8.3.2 Summary

The main constraints when designing the pressure vessel were to optimize its size in order to reduce its overall weight and manufacturing costs while still being able to house all its internals, namely the dummy, seat, and pressure sensors. After some iterations with the dummy and seat positioning angles in CAD, the dimensions of the vessel were set to $2000 \times 750 \times 700\text{mm}$ (length \times width \times height), allowing some clearance for the dummy's head and feet. The pressure vessel will be about 50kg depending on the exact number of laminae used in manufacturing.

Given the pressure vessel will be around 50kg, the dummy weighs 75kg, and around 15kg will be divided between the mounts and seat, the total payload (full pressure vessel) will amount to roughly 140kg.

8.3.3 Considered Solutions

After careful evaluation of different plausible materials with which to build the pressure vessel — including aluminium, PVC U, fibreglass and carbon fibre — CFRP was chosen not only due to its weight savings, but because a commercial Hyperloop pod would most likely be made from composites, and it only made sense to build our own pressure vessel from carbon fibre. Table 44 gives a summary of the different options considered — it is worth noting that even though the PVC U gives a better weight rating, its tensile strength is lower than that of carbon fibre and so a higher thickness of it would be required.

Material	ρ (gcm ⁻³)	Total Mass (kg)
Carbon Fibre	1.7–2	45–50.9
Aluminium	2.7	68.74
PVC U	1.3–1.5	34.3–39.6
Fibre Glass	2.1–2.7	55.44–71.28

Table 44: Considered materials for pressure vessel.

8.3.4 Chosen Solution

Our design is that of a flat-bottomed cylindrical vessel. This optimizes the space available inside it in order to fit our dummy and seat. Corners of the pressure vessel need to be filleted so as to have a good stress distribution, and radii of 50mm have proved to be sufficient as well as fairly easy to manufacture. Since curvature is still preferable our design has a semi-circle-shaped cross section at the top. It should be noted symmetry is beneficial in the strength of a vessel and the vessel is therefore symmetric in the front and side planes.

Using a hoop stress formula (hoop stress $\sigma_h = \frac{\Delta pr}{t}$, Δp is pressure, r is radius, t is thickness) and using a pressure difference of over 1atm for the sake of contingency, it was found that a wall thickness of 1mm would be enough to withstand the pressure differential. The non-trivial geometric simplifications used to model our pressure vessel to the simpler shape required for the hoop formula, led to the decision of increasing the wall thickness to 2–3mm to have a good safety margin.

Seat

Despite its seemingly trivial purpose, the seat design choice was one of the biggest constraints for the design of the pressure vessel as a whole and by extension, the entire pod. Primary design drivers for the seat include weight, cost, ease of manufacturing, and passenger safety and comfort, including position and orientation. The seat will face the direction of travel.

Seat sizing was driven by the size of the dummy. The chosen dummy represents a 95th percentile Scottish adult male; it is 185cm tall and weighs 75kg and the seat and dummy dimensions are given in Table 50 given in Appendix A.4.2. By designing the seat for a dummy of this size, it is ensured that the pod will fit the majority of the population. A major decision in deciding on a seat was whether to manufacture a seat in house, or to purchase a seat designed for motor racing. It was decided that the seat would be manufactured in house so that the dimensions and shape are exactly as required. The angles of the seat design were designed to minimise the space required, and to provide passenger comfort. A brief IDL

(Interactive Data Language) script was used to optimise the seat shape, and bearing scalability in mind, a reclining position was specified with a back angle of 35° . Figure 110 illustrates this.

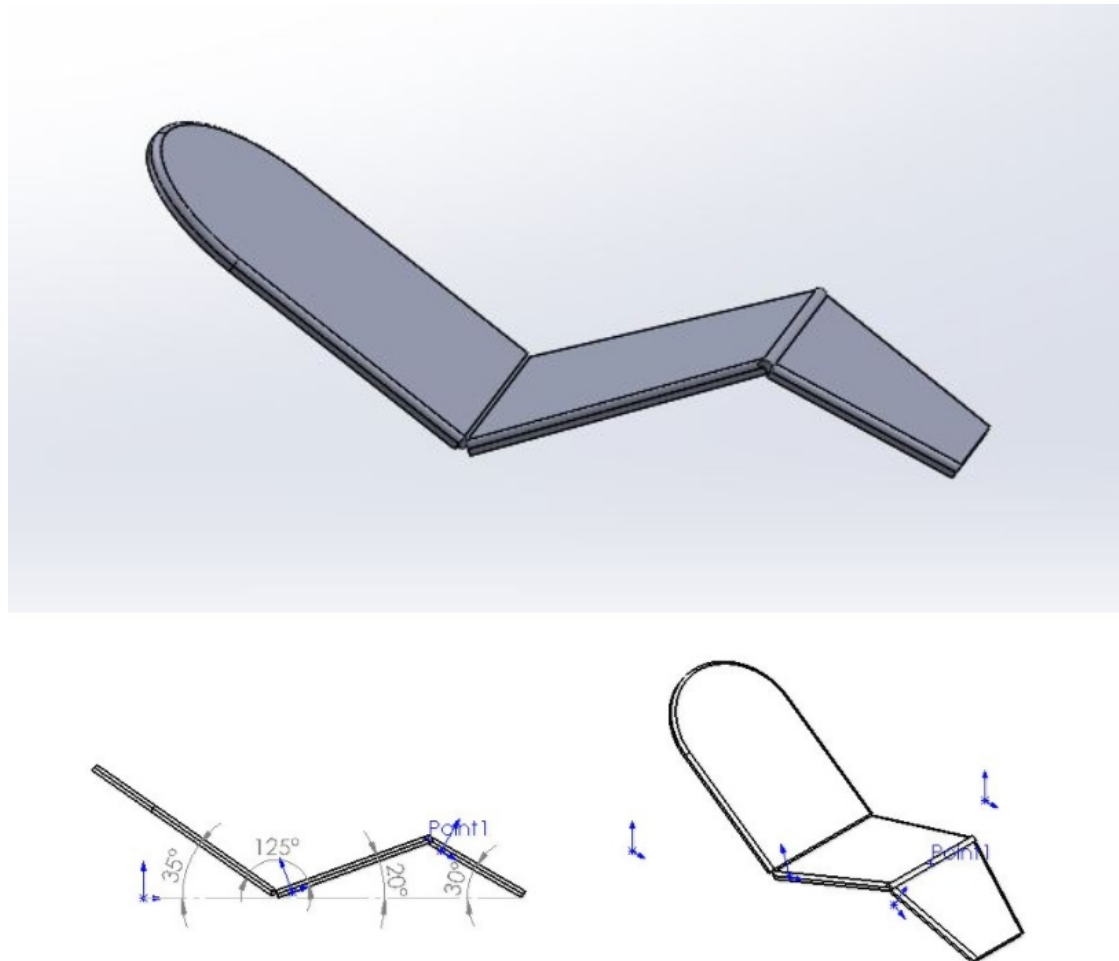


Figure 110: Top: A CAD design of the pressure vessel seat. Bottom: diagram of the angles chosen of the pressure vessel seat.

Different seat insertion methods were considered. Ultimately it was decided the best option was to have the seat removable from the vessel via rails through the rear hatch as the dummy's weight is significant at 75kg and is safer to glide into place rather than carry onto the seat. A five-point racing harness will be used to restrain the dummy in the seat, as is standard in motor racing. This will be fixed to the seat support system, and will act to restrain the dummy against movement caused accelerations, decelerations, vibrations, and in any hypothetical crash scenario.

Whilst no detailed design has been conducted at this stage given its secondary importance, the seat could be supported by a frame consisting of tubular members. These will connect the seat with the skis on which it will be inserted in the pressure vessel. The frame is to be able to support any loading caused by the seat in all possible scenarios, whilst being as light as possible. The seat, and mechanisms have been included to demonstrate the feasibility, and scalability of Hyperloop as a viable transport option. The designs have been carried out to ensure passenger comfort and safety as well as to be lightweight and easy to manufacture.

Hatch

The main considerations for the pressure vessel hatch were its design, the sealing, enclosing mechanism, and the hinge mechanism.

Multiple options for the hatch design were considered. The main constraint was that a hatch was needed for access to assemble all the inner pod sub-systems, including the seat and dummy. This meant at least one hatch was needed on the end of the pod, for access to fit the seat in. Having one or two falcon wing style doors on either side of the pod was considered, but for now dismissed. Our design will have a single hatch at the tail end of the pod.

This end hatch must have the same cross section as the pressure vessel's main body so that the seat could be slid in easily on rails without any obstacle at the "entrance". The area would also determine the pressure force acting on the door. The dimensions were therefore decided to be height 620mm, width 650mm with a curved lip of radius 50mm, and a flat lip of width 30mm, seen in Figure 111 alongside the opened hatch.



Figure 111: Pressure vessel with hatch.

For the seal design, multiple aspects had to be considered thoroughly, as this component will be the main influencer of performance of the pressure vessel. A seal material had to be chosen, considerations for this included the temperature limit of the material, its compression recovery, the pressure tolerance range and most importantly its gas impermeability. Various rubber properties were examined and it was decided that butyl rubber is best suited the requirements due to its use in vacuum applications and high gas impermeability found in [15].

To maintain an airtight seal, the rubber has to be in compression. Clamp latches were chosen to provide this compressive force. The amount of force to keep the seal in compression depends on the hatch size and pressure differential, as well as the compressibility of the rubber, and by using the simple $P = \frac{F}{A}$ calculation, the force on the hatch door was calculated to be roughly 37kN. Three to five latches around the circumference of the hatch will be enough to clamp it down, depending on the exact force rating of the latches that end up being used in our design. One part of the latch will be attached to the hatch door, and the other will be attached to the pressure vessel. The latches will be similar in design to Figure 112.



Figure 112: Pressure vessel hatch latch.

For the seal and its attachment to the pressure vessel, the main constraint is defined by our ability to manufacture the carbon fibre into intricate geometries. A common seal design for vacuum chambers consists of making a groove around the circumference of the vessel body and fitting a rubber O-ring or rubber seal into the groove. This ensures the rubber is in compression. However due to the nature of carbon fibre, scoring it will result in fracture of the fibres which is undesirable for the pressure vessel. Therefore, the team had to come up with an alternative design within our current known manufacturing limits of carbon fibre. Many designs were considered, including a rubber seal with a circular profile attached to either side of the vessel's walls with rubber flanges, as well as having an aluminium insert supporting a rubber seal between the two components. Finally, a wedge shape

plug door design was decided on, where both ends of the pressure vessel and hatch were wrapped around an aluminium insert to create a wedge shaped cross section. The rubber seal will be attached to the circumference of the pressure vessel with epoxy. The profile of the rubber seal will have a hole running through it to increase the compressibility of the seal, see Figure 113.

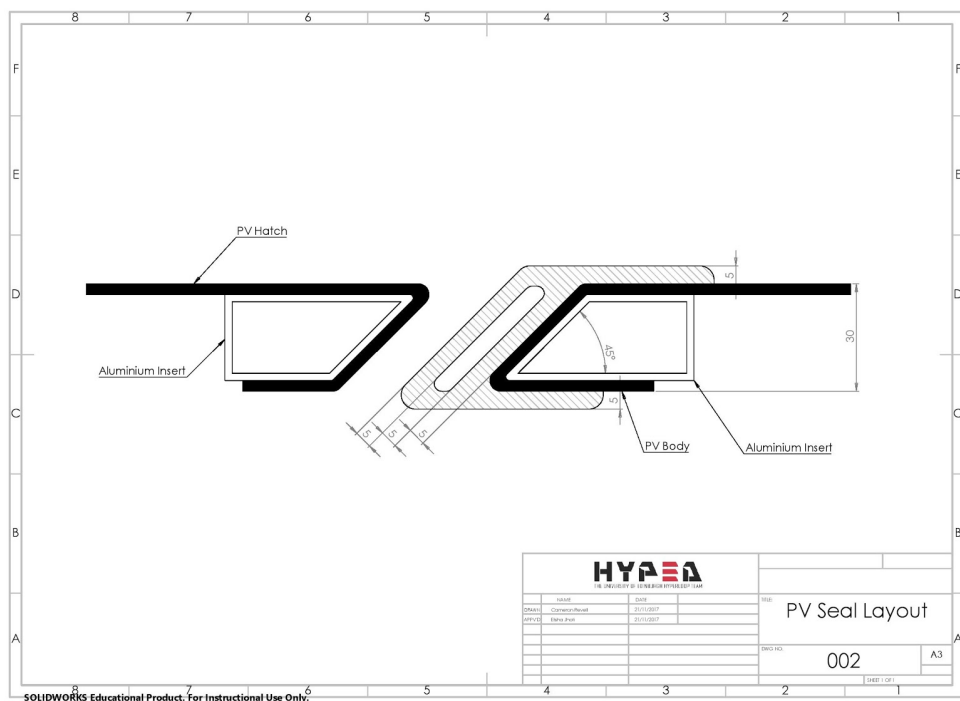


Figure 113: Seal layout.

Please note that our design will not use aluminium inserts as suggested in the figure, but a carbon fibre frame instead. This is because aluminium tends to react with carbon fibre causing galvanic corrosion, and there is a difference in thermal expansion properties between the two making them non-ideal materials to work with together.

The hatch will open outwards, as there is not enough space inside the pod for it to open inwards. The hinges will also be on the inside of the pod so as not to interfere with the interface between the pressure vessel and end cone.

The hinge can be either at the top or on one of the sides, if at all. In the case the hatch opens upwards, two options for supporting it have been considered; gas struts and a torsion bar. The gas struts were decided to be impractical as there

would be nowhere to fix the end attached to the pressure vessel that would not interfere with the seal. A torsion bar was also considered, as used in the DMC DeLorean vehicle. When opening the hatch, the bar would allow for rotation around the horizontal axis, and pre-stressing the torsion bar would also allow the hatch to stay open. The torsion bar would also make the hatch rise automatically reminiscent of a car trunk. In the end, a torsion bar was deemed unnecessary weight and it was decided to just have hinges with a large opening angle so the hatch could rest on the roof of the pressure vessel. After a search of various suppliers, it was decided to use 150° opening angle concealed blum style cabinet hinges, as a pair of these hinges would be able to bear a load of 5kg, the maximum upper limit of the door mass. Forces coming from the pressure difference will also have to be taken into account when choosing the hinge.

Chassis Mounting

As for the rest of the pod, it is important that the pressure vessel be easily removable from the pressure vessel. Rail mountings or mounting the pressure vessel on a set of brackets were considered, but simple bolting through the pressure vessel was chosen as the most straightforward option, although this does bring up the concern of air leakage. The advantage of bolting is that it enables a secure connection, and as the pressure vessel will be in direct contact with the chassis all along its length, forces will act through the entirety of the contact area through reaction and frictional forces. The potential leakage will be remedied by using flat rubber seals, much like washers, atop which metal washers will be placed so as to keep these under compression by the nut or bolt head. Figure 114 illustrates this.

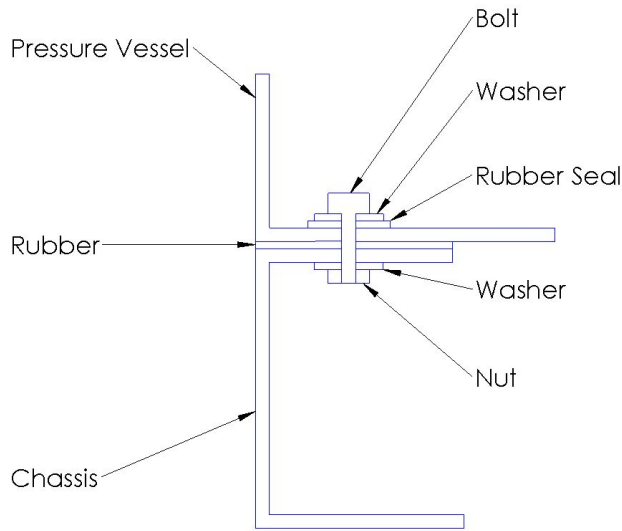


Figure 114: PV-chassis mounting diagram.

Regarding the bolts, shear stresses are the main issue in this case. However, by a simple application of $F = ma$ it can be seen that in order for the 140kg loaded pressure vessel to accelerate at 2g, the shear force would be about 2.7kN. In this design the shear force is distributed between shear force directly on the bolts and friction that will arise due to contact between the pressure vessel and the chassis. The shear capacity of single grade 2 M10 bolt is in the region of 18kN, which is amply capable of bearing the load. Furthermore, the rubber seen between the pressure vessel and the chassis makes so that when the vessel is tightly bolted down, its mounts can be considered as the entirety of the contact area between both components. This is what is used as boundary conditions in simulations. The base of the pressure vessel will be made thicker than the rest to accommodate for the stresses that will accumulate near the bolts.

Livability

The primary goal of the pressure vessel is to provide a strictly liveable environment for our dummy, including appropriate temperatures, pressures, and carbon dioxide levels. Nonetheless, if time allows the team may undertake secondary, non-essential improvements on the vessel such as adding lighting and a public announcement sound system to mimic a true passenger cabin. The addition of a display from a camera feed at the front of the pod could be interesting as well, but any of this would be done only once all the rest is finished.

Inside the pressure vessel, there will be sensors measuring the air pressure, carbon

dioxide content, and temperature. This will allow us to ensure that the pressure vessel does not leak air, that the air is breathable, and both pressure and temperatures are appropriate. The sensors would be mounted on the floor of the vessel, at the back, under the seat. This allows for easy routing of the cables through the floor of the pressure vessel to the controls module in the chassis. Collected data will be transmitted in real time back to mission control.

An illustration of the loaded pressure vessel is seen in Figure 115.



Figure 115: Loaded pressure vessel.

8.3.5 Simulations

Most simulations in this report have been done using COMSOL, however Abaqus was used to simulate our pressure vessel given it allows for a better definition of carbon fibre as a material, down to the amount of layers used. Simulations carried out on the pressure vessel show its behaviour under an atmosphere of pressure differential between the inner and outer pressures. Figure 116 shows that in these conditions the maximum displacement would be of 10mm.

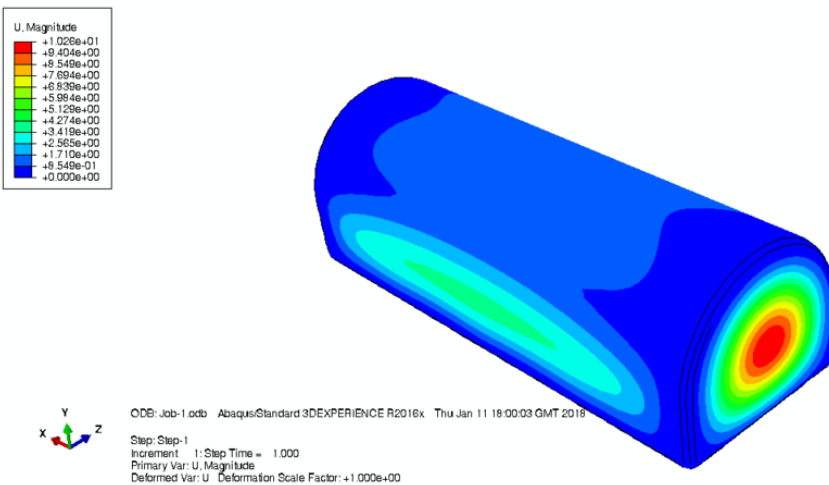


Figure 116: Induced displacement in mm.

A displacement of this magnitude can be worked with, but the team will optimise the pressure vessel's design so as to minimise it.

Regarding the stresses on the pressure vessel, those in the X direction (along the length) have proven to be the highest, at just under 300MPa, as seen in Figure 117.

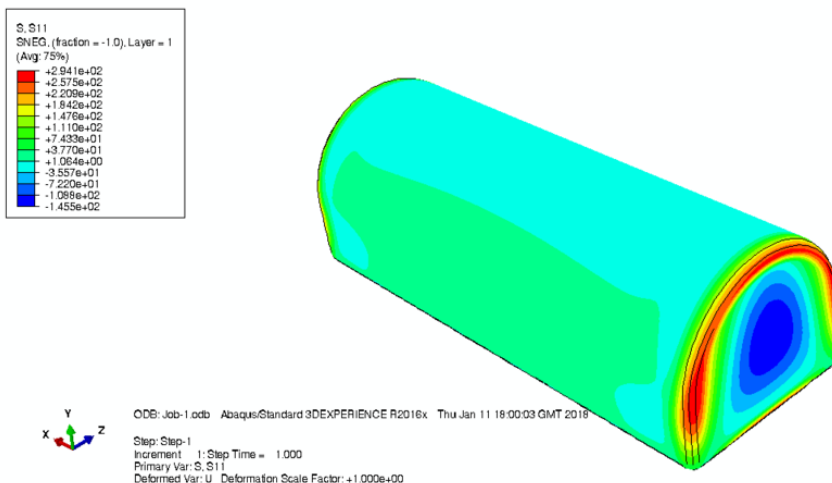


Figure 117: Longitudinal stress in MPa.

This stress is within material properties, but has been obtained for simulations using 16 layers of carbon fibre. While it is possible to manufacture our pressure vessel using so many layers, due to the uneven distribution of stresses there is room to optimise our design so as to add reinforcements only where needed. Further simulations will also need to be carried out in order to account for the added stress of the bolts during maximum acceleration, including a safety factor of two. In the above simulation, the pressure vessel mount has been approximated to the entirety of the bottom plane, so it is likely that reinforcements will be needed for the bolts as well. These optimised and more accurate simulations will all be undergone before the part is manufactured.

8.3.6 Safety

A small scale prototype of the pressure vessel will be made in house to ensure the parts' performance is in accordance with our models and expectations. The final part will also be tested at the nominal operating pressure plus a safety margin to ensure it will function properly in a vacuum, and there will be a relief valve to ensure the pressure vessel never endures a higher pressure differential than that for which it has been tested. The final part will be tested either by locking it closed while pumping it up to 2bar through a valve at its surface, or locking it at one atmosphere and putting it in a vacuum chamber larger than itself.

8.3.7 Scalability

The pressure vessel is the main element on our pod showing that HYPED thinks about this competition with the true Hyperloop concept in mind. Building this pressure vessel and incorporating it as a driving design constraint for the pod as a whole shows the focus that HYPED has on scalability.

Whether or not our team pursues with a 2×2 twill weave for this component, it is possible that a full-scale model would be manufactured through filament winding or an asymmetric weave such as a 4H satin, at least for the central part of the vessel. However, following is a more technical analysis of the scalability of this component.

Expressions for the hoop and shear stress in the wall due to torsion in generic cylindrical pressure vessels are given in the two equations below.

$$\text{Hoop Stress} = \sigma_h = \frac{\Delta pr}{t}$$

$$\text{Shear Stress} = \tau_s = \frac{\text{torsion} \cdot r}{l}$$

Where we have the terms in σ_h described in Section 8.3.4. For τ_s , l is given by the length of the cylindrical pressure vessel.

As the cross section of the pod increases, the hoop stress increases proportional to the inverse of the square of cross-sectional area of the pod, see Figure 118. Therefore, as the scale of the Hyperloop increases, the geometry is more efficient.

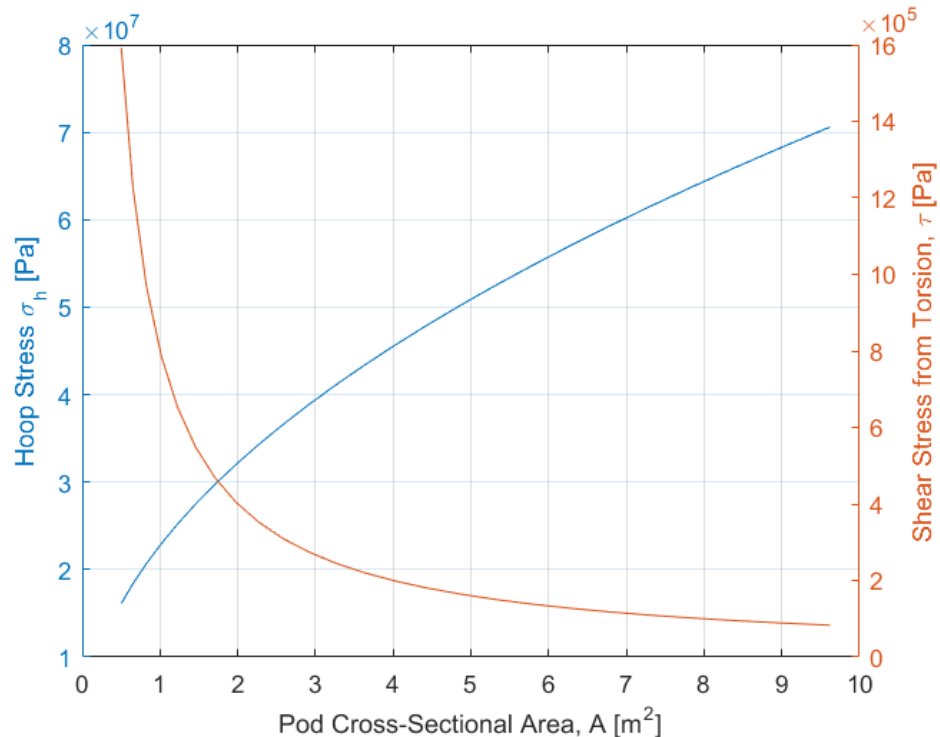


Figure 118: Cross-sectional area against hoop and shear stress of general cylindrical pressure vessel.

Similarly, the relative effects of torsion are far more pronounced in a small-scale pressure vessel, and whilst a larger scale pod will develop more significant bending moments, these can be easily compensated for by using stringers and other structural reinforcements built into the vessel. Significant work could be invested

into re-designing a more efficient pressure vessel-shell interface. The small discontinuities in our design between these components would be amplified in a larger pod and could create aerodynamic issues given the Mach numbers reached on a full-scale system. For a large-scale design, a single, continuous pressure vessel that incorporates aerodynamic elements would be far more efficient, and improve the aesthetic value of the pod.

In industry today, there is no reason why a pressurised composite transport cannot be used, with Boeing's 787 Dreamliner incorporating up to 50% composite material by weight and 80% by volume [16]. Therefore, future iterations of the design may even dispose of the need of external structural elements and be based on a monocoque structure, combining the roles of the chassis, shell, and pressure vessel into one. Regardless, working on a design that separates the pressure vessel from the chassis makes the modular system more operable and adjustable, and generally better suited in the scope of this competition.

8.3.8 Cost Breakdown

Component	Price (£)
Pressure vessel material	2000
Epoxy block	1000
Facility Usage	3000
Latches, Hinge, Valves & Inserts	500
Total	6500

Table 45: Pressure vessel cost breakdown.

8.3.9 Manufacturing

As for the chassis and shell, our aim for this year was to introduce composites in the pressure vessel, and more specifically CFRP. This material is just as relevant to the pressure vessel as it was when speaking of the chassis. In fact, today's highest end pressure vessels, used to contain and transport high pressure gases, are what the industry calls Type V pressure vessels, which are all-composite. These are filament-wound, meaning that the carbon fibre is used directly from tows, and not made into a weave. This is a very efficient use of the material, as it is almost exclusively used in tension which is where it performs best. These pressure vessels are usually cylindrical shaped with hemisphere ends, which is one of the most efficient designs in dealing with inside pressure, which can go up to a few tens of atmospheres.

Given the stress in the pressure vessel's walls is calculated in terms of gauge pressure, and that our vessel will have to maintain one atmosphere at most, it will be dealing with nowhere near the pressures to which industrial Type V vessels are subjected. As a result, the design can have more of a free geometry, and not be strictly cylindrical. Furthermore, the pressure vessel design can very well be made out of a twill weave and not filament winding, given filament winding is a very technical process requiring expensive machinery, and a weave layup will be up to our performance requirements.

The pressure vessel's structure is different to other components given in its central area it will experience two times the loads, in the hoop direction compared to the longitudinal direction, and therefore we could justify using an asymmetric weave such as a 4H Satin.

Axisymmetric composite pressure vessels are typically filament wound around a mandrel. However, even with simple variations in an axisymmetric design, such as an ellipse, the concentration of material deposited onto the mandrel varies, resulting in a range of material properties. Since the HYPED pressure vessel is not axisymmetric, this manufacturing technique is not valid.

The most valid approach lies in laying up a series quasi-isotropic laminate into a pair of moulds and then curing in an autoclave. The moulds will be manufactured from two masters, which will be manufactured by CNCing an epoxy block.

This method is not the fastest method and will incur significant costs, notably external labour, epoxy and the hiring of an autoclave, but will allow for even layup and implementation of unique design features, such as the seal, which filament winding could not manage. Due to the scale of the pressure vessel, it is unlikely the team will be able to manufacture in house and will instead attempt to use external facilities.

The design of pressure vessel components has been undertaken with a view towards manufacturability. The first stage in the manufacture of the pressure vessel will be to manufacture the individual parts that are required. The largest and most complex of these will be the core shell of the pressure vessel. This carbon fibre piece will be manufactured from a single epoxy mould. The seals and latches will be attached around the rim, and a hole will be inbuilt in order to run sensor wiring to the main control module. The holes and their respective vacuum seals for the bolts in the vessel-chassis attachment interface will also be added.

The other major carbon fibre part to be manufactured is the hatch, again this will be made from a single epoxy mould before being finished with latch hooks attached around the rim.

The seat sections will be constructed again using carbon fibre, before having aluminium attachment points fitted. The seat support could be fabricated using aluminium pipe sections bolted to the seat. Skis will be fitted, allowing the seat to roll on the internal pressure vessel rails.

Assembly of the component parts should not prove too challenging. The seat assembly will slide into the vessel on rails, and bolts through the rails and skis will secure it in place. The hatch will be attached to the pressure vessel using an internal hinge discussed previously, and will be secured shut using latches.

8.3.10 Testing

The pressure vessel could be tested by reversing the pressure differential, i.e. adapting a pump interface and increasing its internal pressure to 2atm, or by testing it within a vacuum chamber larger than itself. In the case it is tested by increasing the interior pressure, an additional valve will have to be added to the design during the manufacturing stage so that the vessel may be pumped up to the appropriate pressure.

The team may undertake to build a vacuum chamber larger than the pressure vessel to test it as long as all other pressure-sensitive systems on the pod, the chamber could made out of unplasticized polyvinyl chloride (PVC U). This PVC U would be capable of sustaining a pressure differential of over 10^3Pa — from 1bar to 500Pa — and would be large enough to accommodate the largest of our subsystems, namely, the pressure vessel.

All our subsystems will be individually vacuum tested in the chamber in the range of 500–1000Pa, adding a margin of about 360Pa given the SpaceX test track is said to go down to 860Pa at its lowest pressure.

8.3.11 Timeline

Table 46 details the plan for manufacturing and testing of the Pressure Vessel.

January	Design of a small-scale prototype pressure vessel.
February	Manufacturing of small-scale prototype.
March	Testing of prototype, redesign of full pressure vessel according to prototype performance with respect to expectations from models and simulations.
April	Manufacturing of full pressure vessel.
May	Testing of pressure vessel.
June	Use of pressure vessel in Pod assembly.

Table 46: Pressure vessel timeline.

Once the team's CFRP supply is obtained circa mid-February 2018, a small scale prototype will be built so as to gain experience in manufacturing and adding inserts in the manufacturing process. This part will then be tested to failure in order to determine how accurately it follows our models and predictions. Once this is done, and depending on the results obtained, the full-size pressure vessel may be redesigned slightly, and then manufactured by our team externally. For the same reason as detailed in the Chassis Timeline section, manufacturing may be carried out in April. Following this, all testing should be carried out by the end of May.

8.4 Shell

8.4.1 Introduction

The shell is but a manifold that covers the outer layer of the pod. In the initial stages of the competition several sketches, from an aerodynamic and an aesthetic point of view were made and scrutinized. In order to design a suitable shell for the conditions in which the pod would be travelling, the team needed to consider various factors such as aerodynamics, functionality, manufacturability, safety — both for the pod and cargo — cost, and aesthetics. The team also had to tailor the shell with respect to other components on the pod, most notably the chassis and pressure vessel. The pressure vessel is part of the outer body of the pod, therefore speaking of the shell is referring to a symmetrical set of front and rear end cones alone.

Due to the low pressure environment of the Hyperloop, the decisive factors in the design are primarily manufacturability, cost and safety rather than aerodynamics. Nonetheless, the latter still played a role in design choices, and was of course still considered. Throughout this section, decisions were made based on this rationale.

Given the geometry of the chassis which is based primarily on modularity, it is poorly optimised for a crash scenario. As a consequence, the shell will play a significant role in such a scenario, acting as a crumple zone so as to avoid any major damage to the chassis and other internal components including the battery in the case of a collision.

8.4.2 Summary

The width of the shell is defined by that of the chassis, while its height is defined by that of the chassis added to the pressure vessel height, giving a total width of 750mm, height of 916mm, and length of 850mm for each end cone — 550mm covering the chassis, and 300mm serving as a crumple zone. The mass of an individual cone will depend on the exact final layup, but will likely be around 3kg.

8.4.3 Considered Solutions

Reading through fluid mechanics theory was done in order to find a good starting point for a streamlined shell. This brought forth the understanding that aerofoils are ideal examples of streamlined bodies, as they reduce the drag caused by the adverse pressure gradient to such an extent that virtually the only remaining friction loss is through the body's skin friction. As a result, the team looked into various aerofoil curves literature [17]. The authors have focused particularly on some aerofoils for which simulations have been carried out, and some results are summed up in Figure 119. The main constraint imposed on the curve choice was to get the least lift possible given during an emergency braking scenario it is crucial for the centre of mass to be as low as possible. In an open-air test, this may be important.

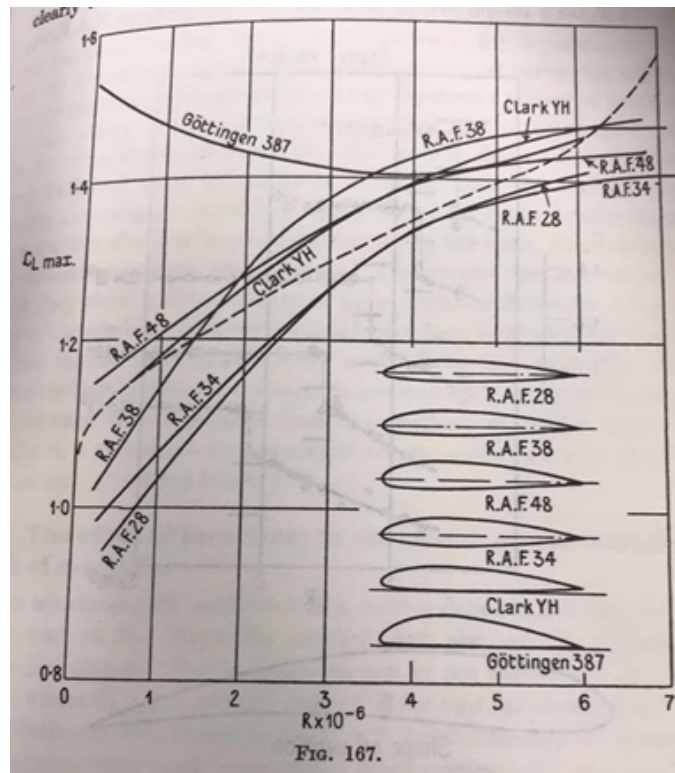


Figure 119: Lift coefficient against Reynolds number on several aerofoils.[17]

Looking at Figure 119 above one can see that there is a plot of several curves associated with 6 aerofoils. The curves detail their lift coefficient, where C_L is defined as the lift force per unit span, with respect to the fluid's Reynolds number. The team has noticed a slight mistake in the labelling of the graph as the horizontal axis should be labelled with $R \times 10^6$ and not as $R \times 10^{-6}$, as can be readily understood from the explanation of the graph that is given by Goldstein in the text Modern Developments in Fluid Dynamics. Unfortunately it was not possible to locate any *errata corrigere*.

Concerning our design and its environment, the Reynolds numbers that come into play are in the order of 10^1 to 10^2 (see Appendix A.4.3). On the graph it is seen (if aware of the labelling error) that the RAF.28 aerofoils maximum lift falls as the Reynolds number decreases. The RAF.28 was therefore an curve option, not only for being an aerofoil with its beneficial aerodynamic properties, but also in efforts to reduce the upward lift force the pod will experience in the tube. The CAD design of the RAF 28 end cone is shown in Figure 120.



Figure 120: RAF.28 nose cone.

Designing the tail end of the pod also came into play. Initially, for aerodynamic purposes, the team considered having a tapered tail end cone that would provide a more streamlined shape for the pod's body in further efforts to reduce air drag — as explained above for one of the teams' choice of nose cone design following the RAF.28 aerofoil. An example of this can be seen in Figure 121, which corresponds to the the RAF.28 aerofoil tail. Other asymmetric ideas followed from that and although these options were more optimal in terms of aerodynamic performance, the team then had to look at the manufacturing constraints that would be involved in the coming months of building our end cones.



Figure 121: RAF.28 tail end cone.

Specifically when thinking about manufacturing, the idea of symmetric end cones gained traction. This would mean that the tail end cone would be an exact replica of the nose end cone. The rationale behind this idea was largely based off of the more realistic constraints of manufacturing and the cost of building carbon fibre end cones including their moulds. Thus, adopting a symmetric shape for the pod would reduce manufacturing time and cost as the team would only need to build one nose cone mould and the process would be the same for both the nose and tail end cones in terms of layering the carbon fibre, also reducing the chance of mistakes being made.

8.4.4 Chosen Solution

Design

As will be detailed later on, the RAF.28 curve was dismissed on the basis that it would not serve well as a crumple zone in the case of a crash. Coming from last year's design and founded on research in fluid mechanics and nose cones, the team has based this year's design on the Haack Series profile curve. This curve was mathematically derived in attempts to minimize drag force acting on a body using such a design and was a clear choice for our profile curve due to its effective use in aircraft design, since they experience varying speeds similar to those a commercial Hyperloop is looking to achieve. The curve is parameterized and defined as

$$\theta = \arccos\left(1 - \frac{2x}{L}\right)$$

$$y = \frac{R}{\sqrt{\pi}} \sqrt{\theta - \frac{\sin(2\theta)}{2} + C\sin^3(\theta)}.$$

Where x and y are the usual Cartesian coordinates, L is the total length of the profile curve, and R is the height of the profile curve.

C is known as the Haack Series Coefficient and dictates the curvature. Specific values of C have also grown in significance throughout the lifetime of the equation, namely $C = \frac{1}{3}$ and $C = 0$. Evidence published on a number of different nose cone designs [18] shows experimental tests that establish theoretical predictions on the optimised curves that are obtained in reality. For a value of $C = \frac{1}{3}$, the equation is known as the LV-Haack model, minimising the drag force for a given length and volume, with values based off the design of the end cone. For $C = 0$, the equation is known as the Von Karman Ogive — henceforth referred to as the Von Karman — minimises the drag force for a given length and height of the profile curve. Because of the increasing length of the chassis as designs progressed, the length

and height of the nose and tail end cones became more of a priority so as to minimize total pod length while keeping a justifiable profile in terms of aerodynamics. The value of $C = 0$ optimises this length while keeping a low drag coefficient of 0.10 at our estimated speeds. This is particularly true at scaled Hyperloop speeds north of 1200kmph, as another paper suggests [19]. The paper details, shown in Figure 122, that for speeds of around Mach 0.9 the Von Karman, labelled as V.K., performs at its best. The LV-Haack Model is ever so slightly more superior in this range but as explained above, the Von Karman is a far better fit for the design in terms of the height and length constraints. Based off of the constraints of our design and of its superiority, a value of $C = 0$ has been used in the design of the Von Karman profile curve for the pod.

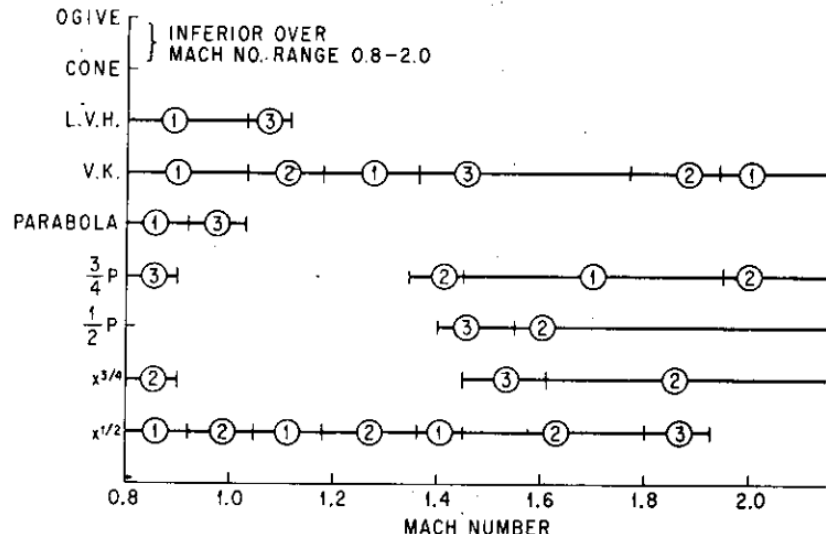


FIG. 3-12. Qualitative drag comparison of nine nose shapes ($l/d = 3.0$). (1) Best (least drag). (2) Better. (3) Good.

Figure 122: Various levels of superiorities of nose cone profile curves given the Mach number from 0.8–2.

Hence, the team considered two profile curves to govern our nose cone. The task was then to decide upon the overall design of the cone in terms of dimensions and shape. The Von Karman was plotted in Matlab while the RAF.28 coordinate points were taken from an aerofoil coordinates database [20] created by the department of aerospace engineering at the university of Illinois Urbana-Champaign. This gave the team the required data points to plot each of the profile curves into SolidWorks. Alongside this, further curves and sketches were made in attempts to create as smooth a nose cone as possible to ensure that their aerodynamic proper-

ties were upheld. The CAD designs of the following nose cones implemented the boundary surfacing and lofted surfacing tools in SolidWorks so as to follow the guide curves of the cross section and profile curves chosen. Two early iterations of the nose cone, which followed the Von Karman profile curve can be seen in the Appendix A.4.4.

After further edits made on the CAD design the surface was smoothed out allowing a more streamlined flow around the pod. The final end cone design can be seen in Figure 123.

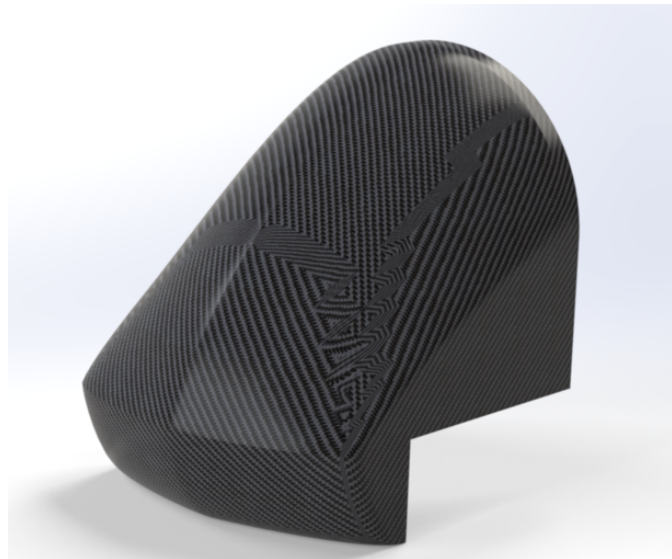


Figure 123: Von Karman nose cone.

The most costly part of the manufacturing process will be making the female mould from high quality materials. Approximately, the total cost of a single carbon fibre nose cone is £3000. This encompasses the female and male moulds required as well as the time taken by the CNC machine to shape the mould material — likely an epoxy tooling block — to desired dimensions, and the materials and necessary tools. By having an asymmetric pod, the total cost of the shell sub team's components would be roughly double, at around £6000. Having a symmetric pod therefore makes sense for weight distribution, regarding the manufacturing process, and due to cost and time constraints.

Structure

As with all crumple zones, the purpose of the pod's crumple zone is to control the deformation of the cone during a crash such that the passenger is safely decelerated and the crushing does not advance as far as the chassis or the pressure vessel — protecting all other technical components. The shell has structurally been designed for a crash at 7ms^{-1} , the standard for a mechanical engineering student automotive competition.

As the flatness of the front face of a nose cone increases, the crushing force will spread out over a wider area which increases the chance of the cone breaking at the bases and damage being done to the rest of the pod. Therefore, the best design is the one with the highest curvature around the contact point or tip, as the high pressure at this point will reduce the propagation of fractures and allow progressive crushing to occur. Having a tip with a small curvature also serves as a triggering mechanism which helps cause failure through small and progressive fractures, which are desired, rather than catastrophic failure at the base. This was the main driver towards choosing the Von Karman over the RAF.28 nose cone.

The nose cone will be made with a non-homogenous layup specifically to serve its structural purpose. Having a small number of carbon fibre layers at the tip will also help to trigger the crumpling as the peak will take most of the initial impact. The remainder of the crumple zone will be reinforced with more layers in order to increase the rate of energy absorption and safely decelerate the pod to rest before the crushing reaches the chassis. The exact lay up of the carbon fibre is detailed further on.

In designing the crumple zone, the team had to ensure that the crushing doesn't advance as far as to the chassis or pressure vessel in an off-nominal crash of 7ms^{-1} (assumed to be completely plastic). Therefore, the crush length had to be calculated. An expression for the crushing force required to progress the crush by an infinitesimal distance dx was derived by balancing the work done by the force and the energy absorbed by the mass of material destroyed m (with specific energy absorption (SEA) e_a)[21]:

$$\int F dx = -e_a m = -e_a \int P(x) n(x) \rho_{gsm} dx = -E_a.$$

Where E_a is the energy absorbed, $P(x)$ is the perimeter of the cross section of the nose cone at a distance x from the peak, $n(x)$ is the number of carbon fibre layers at the cross sectional position, x and ρ_{gsm} is the area density of the material in gm^2 [21]. Therefore, using Newton's 2nd law $F = ma$ we have

$$a = \frac{F}{M} = -\frac{e_a \rho_{gsm}}{M} \int P(x) N(x) dx,$$

where M is the mass of the pod estimated at 500kg.

For our purposes, using a ρ_{gsm} of 200gsm (area density, grams per square meter) is sufficient and the SEA was estimated to be 15kJkg^{-1} , [22].

A MATLAB script created by Gray [21] was used to calculate the deceleration over distance along the end cone coupled with the energy absorbed allowing us to determine the crush length. The perimeter of 22 cross sections at various points along the nose cone were measured using SolidWorks and is shown in Appendix A.4.5, alongside the data inputted into the MATLAB script in Figure 141. Figure 124 is a graph of the deceleration and energy absorbed against the distance along the nose cone for an optimal ply distribution of 4, 6, 8, and 10 layers starting at 0, 50, 125, and 175mm respectively from the tip of the cone.

The MATLAB script was run three times using the different ply distributions shown above. The optimal distribution was found to be xplies2 due to it resulting in the lowest average acceleration and a crush length of roughly 250mm which brings the pod to rest well before the crushing reaches the chassis or pressure vessel.

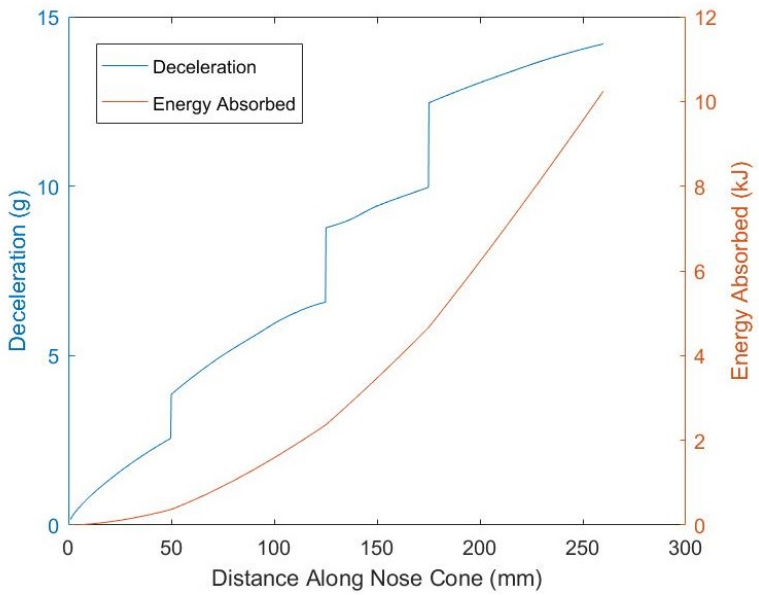


Figure 124: Deceleration and energy absorption against distance along nose cone.

The crush length corresponds to the distance along the nose cone where the energy absorbed equals the energy of the crash ($\approx 10\text{kJ}$ assuming an impact speed of 7ms^{-1}) which can be read off the graph as roughly 250mm. One can also see that the peak deceleration is approximately 15g.

8.4.5 Mounting

The shell mounting to the chassis and pressure vessel will be at five different points, using a pin-type mechanism where bolts will be screwed onto threaded inserts locking the shell onto the pod body. Figure 125 describes the locations of the 5 mounting points, each with their male and female counterparts. The image on the right illustrates the mounting method used to fix each end cone onto either side of the chassis.



Figure 125: Left: overview of the mounting method of shell-chassis & pressure vessel. Right: up close figure of attachments for shell-chassis.

8.4.6 Simulations

Simulations have been run on a pod assembly using the Von Karman end cones both at the nose and tail. Two computational fluid dynamics (CFD) scenarios have been defined; one simulating the run at an atmosphere, and the other at 860Pa which is defined as the minimum pressure in the SpaceX tube.

The highest stresses induced on the shell and pod as a whole occur in the atmospheric run; as Figure 126 shows these would not surpass 70kPa, so are well under the strength of the material which is in the order of a few hundreds of MPa, depending on the exact fabric and resin system used.

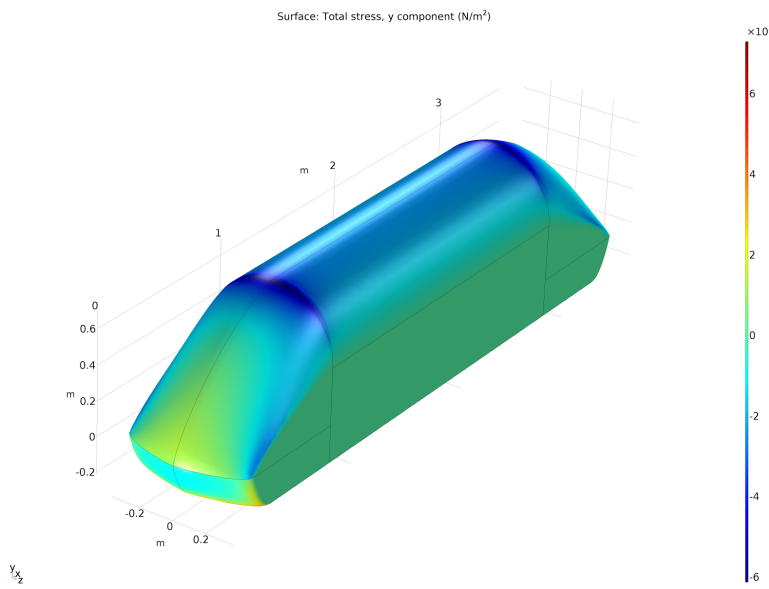


Figure 126: Relative stresses in atmospheric run.

The highest stresses induced by the flow is in the vertical direction.

The Figures 127 and 128 represent the streamlines and relative fluid velocities for the atmospheric run and the run at 860Pa respectively.

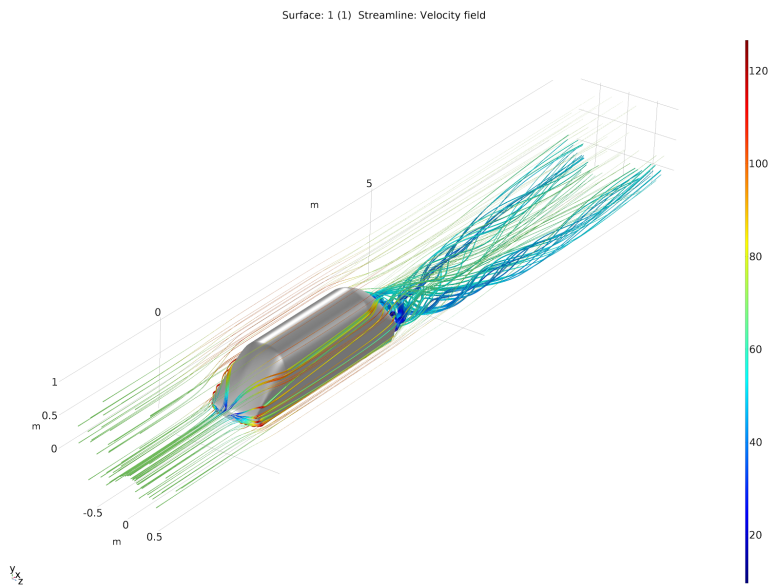


Figure 127: Relative fluid velocities in atmospheric run.

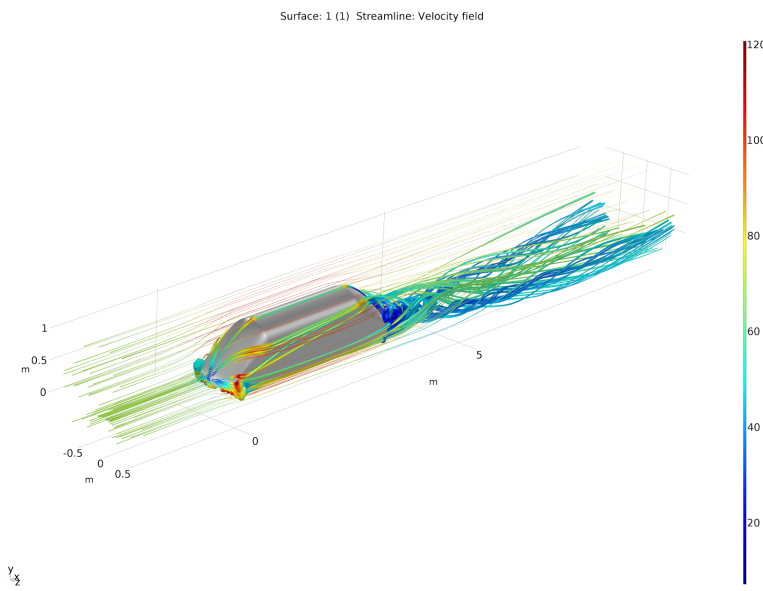


Figure 128: Relative fluid velocities in 860Pa run.

The most important point to note from the streamline plots is that there is no significant separation at the front of the pod where the shell joins the pressure vessel. The drag coefficient at an atmosphere is 0.10, while the drag coefficient at low pressure is 0.15. The small difference between the coefficients at both pressures and the relatively small drag coefficients to start with suggest that our pod would fare well in a tube breach resulting in rapid pressurisation; more on that at the end of this section. Anecdotally, our obtained drag coefficients are nearly twice as small as was the case for last year's design we achieved.

Following are plots of the relative pressure differences for both runs, at one atmosphere and 860Pa respectively.

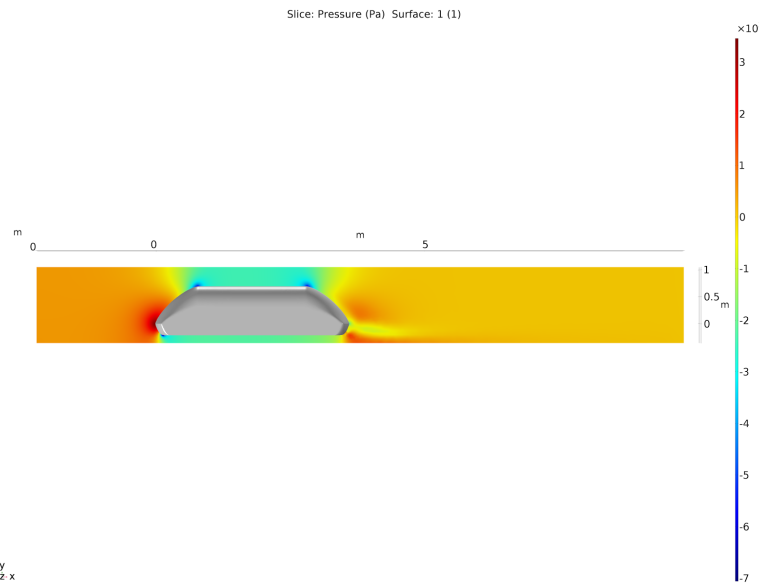


Figure 129: Relative pressure differences in atmospheric run.

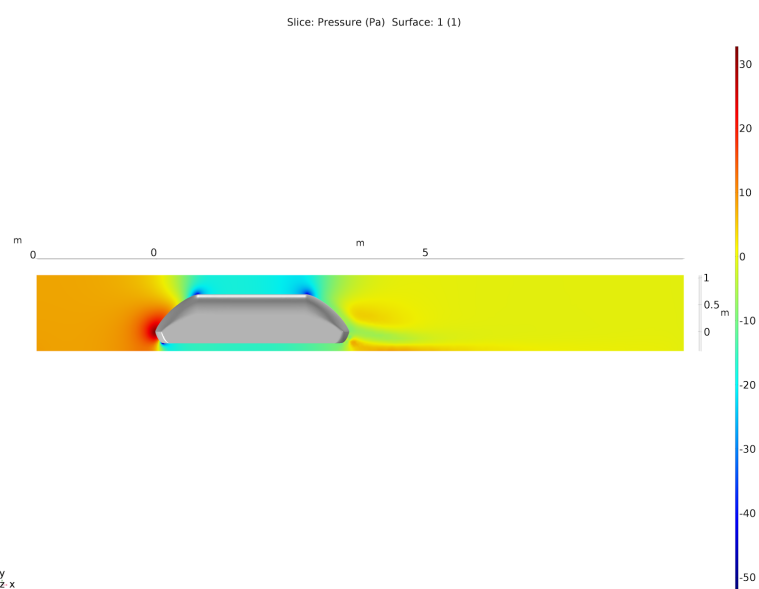


Figure 130: Relative pressure differences in 860Pa run.

As shown, the maximum relative pressure difference around the pod is around approximately 85Pa at most. This logically occurs at the atmospheric run. Thus, overall pressure differences are negligible, validating our choices in the design.

Finally, another simulation was made at 430ms^{-1} with a pressure of 1 atmosphere. This models a breach in the tube resulting in rapid pressurisation, where the speed of the pod is added to the air's speed of propagation, around the speed of sound. The following figure shows the maximum total stress in the fibres to be about 300kPa which, while higher than stresses found in previous simulations, remains at three orders of magnitude smaller than the material strength.

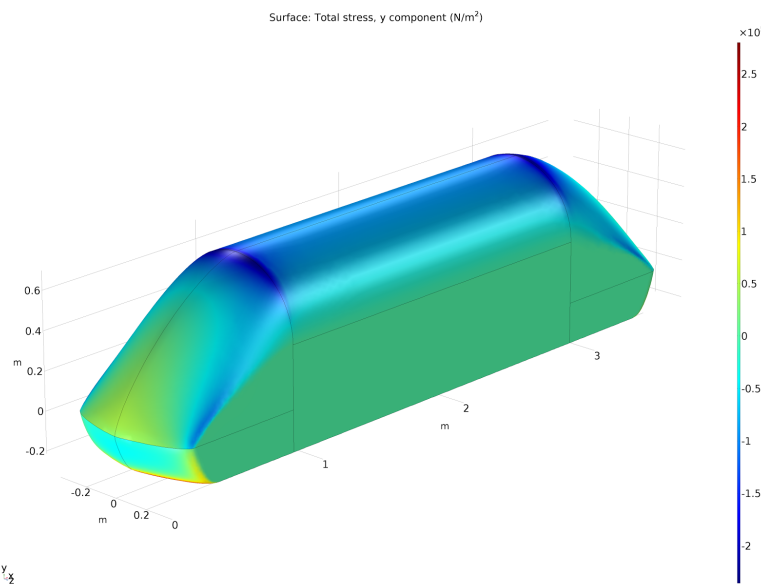


Figure 131: 430ms^{-1} atmospheric run to test potential event of de-pressurisation in tube.

Our pod would therefore not be very much affected by a rapid pressurisation of the tube.

8.4.7 Safety

The shell will be physically tested, ensuring its crumple zone purpose is successfully carried out without catastrophic failure. Being mounted onto the pod at five different points ensures a certain redundancy whereby two or three mounting points can fail — highly unlikely — before the shell falls off. These will also all be tested under load in advance.

8.4.8 Scalability

It is uncertain whether a scaled Hyperloop design would have isolated end cones such as in our design, yet is a possibility nonetheless. Assuming so, a scaled design would weigh about 50kg. The cost would depend on the exact manufacturing procedure, although if the shell were made from a corrugated sandwich as mentioned in the Dynamic Module Plate section, these costs would remain relatively low.

8.4.9 Cost Breakdown

Component	Price (£)
CFRP (including test units)	3000
Resin	1000
Facility Usage	2000
Total	6000

Table 47: Shell cost breakdown.

8.4.10 Manufacturing

A first male master mould will be made by CNCing an epoxy tooling block to the desired geometry. From this mould, will be made two female moulds out of carbon fibre with tooling resin — these will be used to lay up the final parts. The reason why female parts must be used to make our end cones is because a good surface finish can only be obtained where the end part is in contact with the mould, therefore given the shell needs a good surface finish on its exterior face, a female mould is used. It may seem circuitous to CNC a male mould to make a set of CFRP female moulds to then make a part, but this is because a female mould directly made from an epoxy block would not be able to withstand the temperatures at which CFRP cures. The CFRP female moulds will therefore be precured on the male block, then removed from the block so they finish curing in an oven.

Once these two moulds are ready, they will be bolted together through their flanges which lie on their symmetry axis so that the carbon fibre can then be laid up in them. Once the layup is done, the part will be bagged and vacuum sealed so as to apply even pressure on its surface, and then cured in an oven or an autoclave if possible. Once the part has been cured, it can easily be removed from the female mould since both of these can be unbolted and separated — this is the advantage of having the mould in two pieces rather than one. The part is then finished.

8.4.11 Testing

Given the shell's structural significance, it will go through physical testing to ensure it meets its design requirements. Despite deriving the exact layup in terms of layers analytically, our team intends to start by manufacturing three sample end cones with the nominal layup and two additional cones, one with more layers and the other with less, so as to empirically determine which layup is optimal in a real-world design. The end cones will be tested in a frontal crash at 7ms^{-1} , with the same mounting method that is intended to be used in our final design.

8.4.12 Timeline

January	Design refinement and optimisation, including aesthetics.
February	CFRP material testing (valid for all CFRP parts).
March	Redesign from experimentally obtained material properties (valid for all CFRP parts).
April	Manufacturing of three test cones, crash testing.
May	Manufacturing of two end cones for pod.
June	Testing in terms of mounts, assembly.

Table 48: Shell timeline.

A Appendices

A.1 Loading Plan

The magnets being used can pose a large danger when being handled, due to their extremely high field strength. Therefore the following procedures must be followed when handling the magnets.

A.1.1 Procedure

- Four people and a forklift are needed: person A, B, C, safety officer.
 - All of them should wear protective gloves, glasses and steel-toe safety boots
 - None of the persons should be allergic to nickel (magnets contain nickel)
 - All persons will be checked by the safety officer that they dont have any magnetic materials or electronic devices on their persons.
 - One person should be designated as a safety officer to observe and will call a stop to the procedure in case of anything off nominal.
 - Person A is responsible to clear the path through which the magnets and people involved in the procedure will move.
 - Person A is responsible to show them the predesignated route.
1. The pod will be placed on the forklift.
 2. Person B and C will ensure that the pod is placed safely and is stable on the forklift.
 3. At the signal of the safety officer forklift will lift up the pod.
 4. At the signal of the safety officer, forklift will move the pod along the pre-designated route.
 5. The safety officer will be checking that none of persons A, B or C are in the way of the route or at risk from falling pod.
 6. Person A should check continuously that the path is clear and nobody approaches the route.
 7. Upon reaching the destination, the safety officer will check that the pod is properly aligned and give the signal to lower it
 8. Person B and C will be checking that the pod is lowered from the forklift safely.
 9. The pod is now placed in the new location.
 10. Safety officer must check that everything on the pod has remained the same as before and there is no any damage on any component of the pod.

A.2 Propulsion Appendix



Figure 132: HPEVSAC-35 Motor.

As mentioned previously, this motor is far too big to be integrated within the chassis and would have to stick out - most likely from the top. However, it was still considered as a highly reliable and inexpensive option until something better was found. A graph for the motor torque, speed, power, voltage and current can be seen below [23]. It matches our requirements very well - 175 Nm of peak torque, 8000 rpm peak speed and 47 kW maximum power.

However, another thing to consider is the low voltage and therefore high current coming from the battery. Recall that there are a total of four motors on the pod, where all motors are powered from a unified high power battery system. Power management at such a high amperage (2600 A) becomes excessively difficult, large, expensive and inefficient. A higher voltage option would have been preferred. While the referenced model is meant to be air-cooled, conversations with the manufacturer suggested that liquid-cooling is possible and common practise.

Brushless DC motor (BLDC)

With recent advances in power control electronics, brushless DC motors have become more common for high power applications. BLDC motors are generally very compact and power dense. Particularly the outrunner configuration works well for our physical requirements - where the rotor spins with the outer casing and the stator is placed on the inside. This achieves a flat disc shape, much like a pancake - in other words, much shorter but somewhat wider than other motors of the same rated power.



Figure 133: Alien Power Systems 20080 Outrunner Paramotor.

The Alien Power Systems 20080 Outrunner Paramotor is a 45 kW motor with a very appealing physical shape and size for our applications, as well as an affordable price. However, this motor can only achieve 71 Nm of torque according to the manufacturer and while it is possible to achieve higher values with custom windings, that would drop the already low maximum speed of 6000 rpm. It is clear that the torque-speed characteristics desired for paramotor applications (constant torque) are not ideal for ours. As with the induction motor from the previous section, the low-voltage and high-current input of this motor is not ideal for power management circuitry. Additionally, liquid-cooling is not available for this motor and would have to be implemented in-house.

The Equipmake APM200 traction motor



Figure 134: Equipmake APM200 motor.

The motor comes as a very complete package and achieves impressive specifications at a mass of only 40 kg - 2475 Nm of peak torque with the gearbox, 10000 rpm maximum speed and 220 kW of peak power. However, this motor would require the team to develop a drivetrain in-house and redesign the chassis so that the drivetrain and motor fit inside. It was decided that with the time available, this is unlikely to be the best option [24].

YASA-400 motor



Figure 135: YASA-400 motor.

The advantage of this motor is that it would fit within the C-beam of the chassis and it matches our requirements perfectly - 360 Nm of peak torque (180 Nm per wheel), 7500 rpm maximum speed and 90 kW peak power (45 kW per wheel).

The motor is equipped for liquid-cooling. The motor does not include an inverter/controller or a cooling system, making it rather expensive [25].

Custom Motor Figures

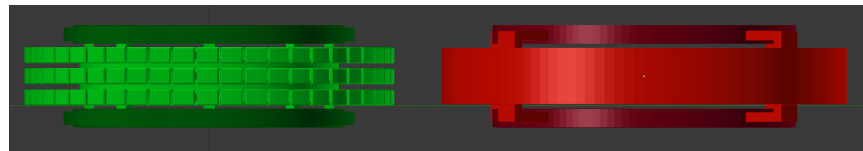


Figure 136: Custom motor stator (left) and rotor (right).

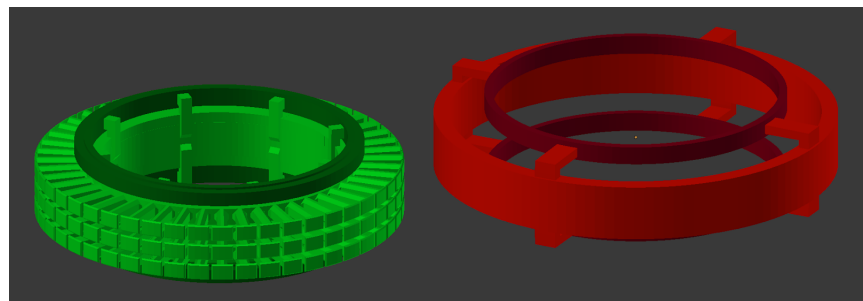


Figure 137: Custom motor stator (left) and rotor (right).

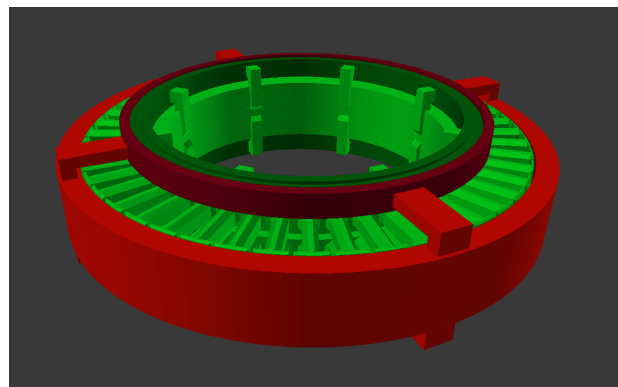


Figure 138: Custom motor.

Prototype Motor

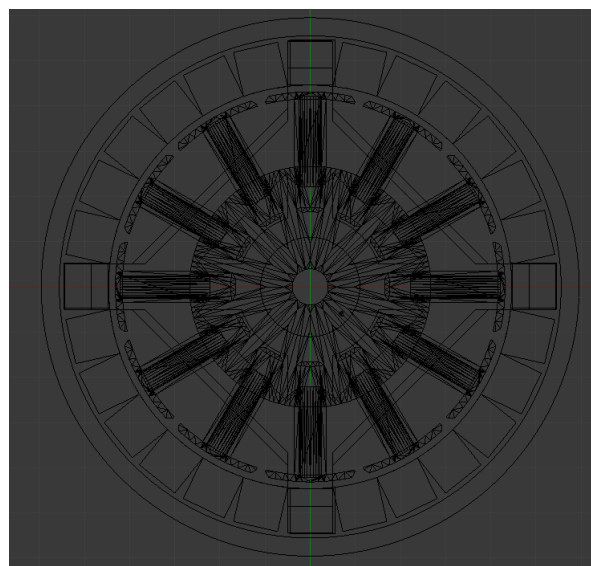


Figure 139: Prototype Motor.

A.3 Dynamic Module Appendix

Material	Density	Young's Modulus	Poisson Ratio	Strength
(a) Foam	ρ_f (g/cm ³)	E_f (MPa)	v_f	Shear Strength τ_{fc} (MPa)
Rohacell 31 (R31)	0.031	36	0.2	0.3
Rohacell 51 (R51)	0.051	70	0.3	0.8
H100	0.1	120	0.32	1.6
H200	0.2	280	0.32	3.3
(b) Base Material	ρ_s (g/cm ³)	E_s (GPa)	v	Compressive Strength σ_γ (GPa)
304 stainless steel	7.9	210	0.3	210
Ti-6Al-4V	4.43	114	0.3	1070
GFRP	1.77	30	0.18	350
CFRP	1.55	110	0.32	870

Table 49: Mechanical Properties of (a) polymer foam and (b) base material of corrugated strut[8].

A.4 Structure Appendix

A.4.1 Lamina Properties

Overall Lamina properties cannot be determined until precise volumetric fraction, V_f , of the fibres is known. Park Electrochemical Corporation [26] quotes average resin content by volume for prepgs of approximately 42%, which is the value used to determine initial lamina properties. We have,

$$\text{Longitudinal Modulus} = E_1 = E_f V_f + E_m (1 - V_f) = 138.39 \text{ GPa},$$

$$\text{Transverse Modulus} = E_2 = \frac{E_f E_m}{(1 - V_f) E_f + V_f E_m} = 23.95 \text{ GPa},$$

$$\text{In plane Poisson's ratio} = v_{12} = v_f V_f + v_m V_m = 0.26,$$

$$\text{Lamina Density} = \rho_f V_f + \rho_m V_m = 1.6378 \text{ g cm}^{-3},$$

where,

ρ_f = density of fibres,
 ρ_m = density of matrix,
 V_f = volumetric fraction of fibres,
 V_m = volumetric fraction of matrix,
 E_f = Young's modulus of fibres (longitudinal),
 E_m = Young's modulus of matrix,
 v_f = Poisson's ratio of fibres,
 v_m = Poisson's ratio of matrix.

A.4.2 Seat & Dummy Dimensions

	Length (mm)	Maximum Width (mm)	Height (mm)
Seat	1735.72	580	429.503
Dummy	1850	550	N/A

Table 50: Seat & Dummy Dimensions

A.4.3 Reynolds Number Calculation

We want to find the Reynolds number for the pod with given length, $L = 3.6\text{m}$, given that the pod is to be travelling approximately at velocity $U = 100\text{ms}^{-1}$.

In the SpaceX track, that according to the SpaceX Hyperloop Track Specifications will be emptied of the contained atmospheric air until a pressure $P_2=861.8446\text{Pa}$ is reached in the tube. Considering that this study is dealing with a very low gas pressure, it can be considered to behave like an ideal gas. Hence, the Ideal Gas Law can be used to determine the final temperature T_2 of the gas inside the track. We use the simple ideal gas law equation,

$$\frac{T_1}{P_1} = \frac{T_2}{P_2},$$

and given the initial atmospheric pressure and temperature

$$P_1 = 101325.93\text{Pa} \quad \& \quad T_1 = 288.15\text{K},$$

before the pumpdown. Finally, it is calculated that

$$T_2 = P_2 \frac{T_1}{P_1} = 2.45\text{K}.$$

Subsequently, it is necessary to find an estimate for the viscosity of the fluid. Since an experimental measurement is not possible, the best theoretical estimate is given by Sutherland's formula

$$\mu = \mu_0 \frac{T_0 + C}{T_2 + C}.$$

Where μ is the calculated value of viscosity of the low pressure air, μ_0 is the viscosity of air, which is approximated to $\mu_0 = 18.6\text{Pas}$ from [27] and $T_0=300\text{K}$ is the temperature at atmospheric pressure 1atm. C is Sutherland's constant and is given by $C=120\text{K}$ according to [28]. Thus,

$$\mu = \mu_0 \frac{T_0 + C}{T_2 + C} = 63.8\text{Pas}.$$

And as a penultimate step, the density of the dry low pressure fluid is calculated by

$$\rho = \frac{P_2}{R_{specific} T_2}$$

Where $R_{specific}=287.058\text{Jkg}^{-1}\text{K}^{-1}$, according to [29], is the specific gas constant for dry air. So it is deduced that

$$\rho = \frac{P_2}{R_{specific} T_2} = 1,225\text{kgm}^{-3}.$$

And finally the Reynolds number at this air pressure is

$$Re = \frac{\rho U L}{\mu} = 6.9$$

The same calculations above were made using atmospheric pressure to give us an estimation of the reynolds number of $Re = 813.2$. This number will be used for open air tests.

A.4.4 Previous Nose Cone Iterations & Simulations

As seen from Figure 140, there was certain difficulty with ensuring that the nose cone was as smooth a surface as possible, while still acting flush with the horizontal and cuboid 'U' channels of the chassis.

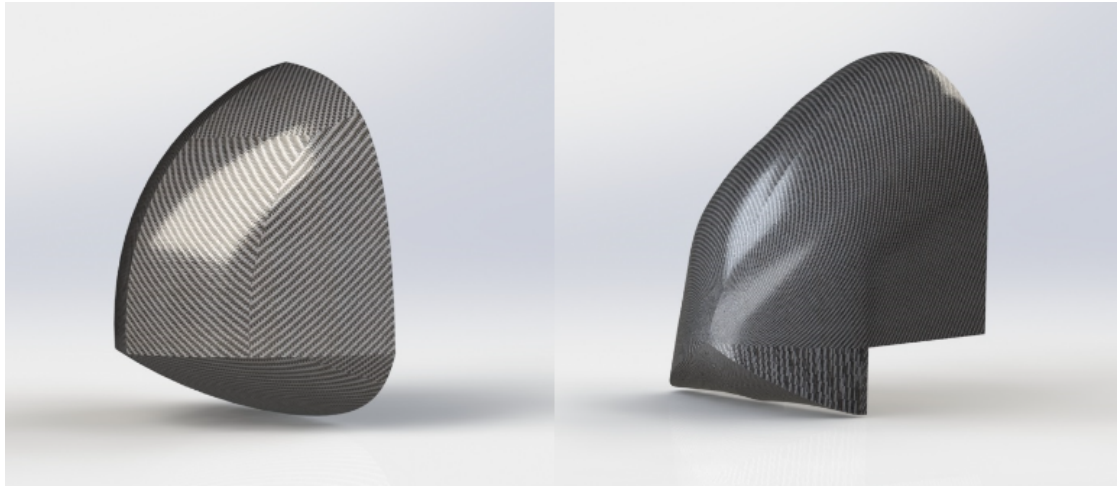


Figure 140: Left: 1st nose cone iteration. Right: 2nd nose cone iteration.

A.4.5 Crumple Zone Data

The MATLAB script created by Gray takes an interval I of 1000 evenly spaced points between the first and last distance measurements taken along the nose cone using the function `linspace'` including the endpoints. It then loops through all points, and uses the `interp'` function to estimate values between each of these points so as to form a continuous shape-preserving piecewise cubic polynomial describing the variation of perimeter along the nose cone. Then, for each distance x in this interval I , it locates the largest distance along the nose cone where the number of plies increase, while making sure that this distance is smaller than the point x in I . By doing this, it determines the number plies needed, out of the possible number of plies taken into account. The script then uses trapezoidal integration to evaluate the integrals for the deceleration and energy absorbed as given above. Using these results, after the loop is completed, a plot is created displaying the deceleration and absorbed energy against the distance along the nose cone.

The MATLAB script [21] has the following input values: the estimated mass of the pod, m , the gsm (area density) of the carbon fiber and the specific energy absorbed SEA. It also takes in the set of perimeters $P(x)$ given by the distance along the nose cone at x , and lastly the number of plies used given the distance along the nose cone. The team's input data can be seen in the figure below.

	A	B	C	D	E	F	G	H
Crumple Zone Deceleration Estimator Input Data								
1								
2	Distance (m)	Perimeter (m)						
3	0.001	0.06874	gsm (kgm ⁻²)	0.2				
4	0.002	0.10934	mass (kg)	500				
5	0.003	0.14466	SEA (kJ/kg)	15				
6	0.004	0.17554						
7	0.005	0.20454						
8	0.01	0.33288	xplies1 (m)	nplies1	xplies2 (m)	nplies2	xplies3 (m)	nplies3
9	0.015	0.44558	0	4	0	4	0	4
10	0.03	0.73492	0.05	6	0.05	6	0.1	6
11	0.045	0.97747	0.1	8	0.125	8	0.2	8
12	0.06	1.18563	0.15	10	0.175	10		
13	0.075	1.36486	0.2	12				
14	0.09	1.51806	0.25	14				
15	0.105	1.66544	0.3	16				
16	0.12	1.76988						
17	0.135	1.83223						
18	0.15	1.92379						
19	0.165	1.99318						
20	0.18	2.05703						
21	0.195	2.11583						
22	0.21	2.16988						
23	0.235	2.25449						
24	0.26	2.32143						

Figure 141: Input data for deceleration & energy absorption calculator.

‘xplies’ denotes the positions of ply increase and ‘nplies’ denotes the number of plies at the corresponding position. E.g. xplies 3 has 4 plies at $x = 0$, i.e. at the tip, and thickens by 2 layers at 100mm and again at 200mm.

References

- [1] Simon, E., 2005. *Evaluation of Lithium Polymer Batteries*, ESA/ESTEC, NASA Battery Workshop.
- [2] Balaguer, D., Escolano, 2014–2015, *Thermal analysis of a LiFePo₄ Battery*, Escola Tècnica Superior d'Enginyeria Industrial de Barcelona.
- [3] Reid, C., 2007, *Lithium Iron Phosphate Cell Performance Evaluations for Lunar Extravehicular Activities*, NASA Glenn Research Center, 10th Electrochemical Power Sources R&D Symposium, Williamsburg, VA. Available at: <https://ntrs.nasa.gov/archive/nasa/casi.ntrs.nasa.gov/20070032058.pdf>
- [4] Available at: <http://www.batteryblocs.com/>
- [5] Post, R. E., and Ryutov., D., 1996. *The Inductrack Concept: a New Approach to Magnetic Levitation*. The Lawrence Livermore National Laboratory. UCRL-ID-124115.
- [6] Arx Pax Labs Inc, 2016. *Hover Engine HE3.0 Datasheet*, Revision 2.0. Available at: <http://hover.arxpax.com/wp-content/uploads/2016/09/HE3.0-Datasheet-Rev2.pdf>
- [7] Wildwood Brake Pads Information. Available at: <http://www.wilwood.com.brakepads/BrakePadsApp.aspx?compound=PolyMatrix%20>
- [8] Han B. et al, 2015. *Foam filling radically enhances transverse shear response of corrugated sandwich plates*. Materials and Design Vol.77, p.132-141.
- [9] Yan, L.L. ; Yu, B. ; Han, B. ; Chen, C.Q. ; Zhang, Q.C. ; Lu, T.J., 24 September 2013, *Compressive strength and energy absorption of sandwich panels with aluminium foam-filled corrugated cores*. Composites Science and Technology, Vol.86, p.142-148.
- [10] Grigorie, L. T., Botez, R. M., 2010. *Modelling and Numerical Simulation of an Algorithm for the Inertial Sensors Errors Reduction and for the Increase of the Strapdown*. Available at: <http://www.tcsme.org/Papers/Vol134/Vol134No1Paper1.pdf> [Accessed 10 October 2017].
- [11] RF Wireless World, 2012. *TVS diode Basics*. Available at: <http://www.rfwireless-world.com/ApplicationNotes/TVS-diode.html> [Accessed 26 December 2017].

- [12] Floreani, C., 2016. *Design and Manufacturing of Carbon-Fibre Composite Nose Cone Assembly and Impact Attenuator for Formula Students Competition*, Masters Dissertation, University of Edinburgh.
- [13] Carbon Fiber - All Patterns Explained, 2015. Available at: <http://www.carbon.ee/en/n/carbon-fiber-all-patterns-explained>
- [14] Mazumdar, S., 2002. *Composites manufacturing*. Boca Raton, Fla. CRC Press.
- [15] Delta Rubber, *Rubber Selection Guide*, <https://shop.deltarubber.co.uk/rubber-selection-chart.pdf>
- [16] Hale, J., 2017. *AERO - Boeing 787 from the Ground Up*. Available at: http://www.boeing.com/commercial/aeromagazine/articles/qtr_4_06/article_04_1.html
- [17] Fluid Motion Panel, Edited by Goldstein, S., 1938. *Modern Developments in Fluid Dynamics*, Aeronautical Research Committee, Oxford At The Olarendon Press, Vol. 1 & 2.
- [18] Perkins, E., Jorgensen, L., Sommer, S., *Investigation of the drag of various axial symmetric nose shapes*, Report 1386, National Advisory Committee For Aeronautics, p.1245-1246.
- [19] Chin, S., 1961. *Missile Configuration Designs*, The Martin Company, Orlando, FL, p.27. Available at: https://aerocastle.files.wordpress.com/2012/04/missile_configuration_desig.pdf
- [20] Applied Aerodynamics Groups, *UIUC Aerofoil Coordinates Database*, Department of Aerospace Engineering, University of Illinois Urbana-Champaign. Available at: http://m-selig.ae.illinois.edu/ads/coord_database.html
- [21] Gray, A.C., *Design, Manufacture and Testing of a Composite Crash Structure for a Formula Student Car*, Masters Dissertation, University of Edinburgh.
- [22] Savage, G., Bomphray, I., Oxley, M., 2004. *Exploiting the fracture properties of carbon fibre composites to design lightweight energy absorbing structures*, Engineering Failure Analysis, Volume 11, Issue 5, p.677-694, ISSN 1350-6307. Available at: <https://doi.org/10.1016/j.engfailanal.2004.01.001>
- [23] Thunderstruck Motors AC-34 and AC-35 Systems. Available at: <http://www.thunderstruck-ev.com/ac-34-w-1238-5601-clone-en-2.html>

- [24] Equipmake APM 200 motor. Available at: <http://equipmake.co.uk/apm200-motor/>
- [25] YASA 400 motor. Available at: <http://www.yasamotors.com/products/yasa-400/>
- [26] Park's E763 modified epoxy system. Available at: <https://parkelectro.com/aerospace-products/e-761-2/>
- [27] Lide, D. R., 2005. *CRC Handbook of Chemistry and Physics*. 86th ed. Boca Raton (FL): CRC Press. ISBN 0-8493-0486-5.
- [28] Crane, 1982. *Flow of fluids through valves, fittings, and pipe*, Technical Paper No.410 M., Metric Edition.
- [29] Olson, Wayne M., 2000. *AFFTC-TIH-99-01 Aircraft Performance Flight Testing*, Technical Information Handbook, Air Force Flight Test Center, Edwards Air Force Base, California, United States Air Force.